

CCMS-92-17
VPI-E-92-16

CENTER FOR COMPOSITE MATERIALS AND STRUCTURES

LANGLEY
GRANT
IN-24-CR
135330
p. 264

Analysis and Optimal Design of Pressurized, Imperfect, Anisotropic Ring-Stiffened Cylinders

R. Ley
Z. Gürdal
E. Johnson
J. H. Starnes, Jr.

Virginia
Tech
VIRGINIA POLYTECHNIC INSTITUTE
AND STATE UNIVERSITY

BLACKSBURG, VIRGINIA
24061

(NASA-CR-191375) ANALYSIS AND
OPTIMAL DESIGN OF PRESSURIZED,
IMPERFECT, ANISOTROPIC
RING-STIFFENED CYLINDERS Report,
Sep. 1987 - Jun. 1992 (Virginia
Polytechnic Inst.) 264 p

N93-18774

November 1992

Unclass

G3/24 0135330

College of Engineering
Virginia Polytechnic Institute and State University
Blacksburg, Virginia 24061

November 1992

VPI-E-92-16
CCMS-92-17

***Analysis and Optimal Design of Pressurized, Imperfect,
Anisotropic Ring-Stiffened Cylinders***

R. Ley¹
Z. Gürdal²
E. Johnson³
J. H. Starnes, Jr.⁴

Performance period:
September 1987 - June 1992

Grant NAG-1-343

Prepared for: Aircraft Structures Branch
 National Aeronautics and Space Administration
 Langley Research Center
 Hampton, VA 23665-5225

¹ Graduate Student, Department of Engineering Science and Mechanics
Virginia Polytechnic Institute and State University

² Associate Professor, Department of Engineering Science and Mechanics
Virginia Polytechnic Institute and State University

³ Associate Professor, Department of Aerospace and Ocean Engineering
Virginia Polytechnic Institute and State University

⁴ Head, Aircraft Structures Branch, NASA Langley Research Center,
Hampton, VA

ANALYSIS AND OPTIMAL DESIGN OF PRESSURIZED, IMPERFECT, ANISOTROPIC RING-STIFFENED CYLINDERS

ABSTRACT

Development of an algorithm to perform the structural analysis and optimal sizing of buckling resistant, imperfect, anisotropic ring-stiffened cylinders subjected to axial compression, torsion, and internal pressure is presented. The structure is modeled as a branched shell. A nonlinear axisymmetric prebuckling equilibrium state is assumed which is amenable to exact solution within each branch. Buckling displacements are represented by a Fourier series in the circumferential coordinate and finite elements in the axial or radial coordinate. A separate, more detailed analytical model is employed to predict prebuckling stresses in the flange/skin interface region.

Results of case studies indicate that a nonlinear prebuckling analysis is needed to accurately predict buckling loads and mode shapes of these cylinders, that the rings have a greater influence on the buckling resistance as the relative magnitude of the torsional loading to axial compression loading is increased, but that this ring effectiveness decreases somewhat when internal pressure is added.

The enforcement of stability constraints is treated in a way that does not require any eigenvalue analysis. Case studies performed using a combination of penalty function and feasible direction optimization methods indicate that the presence of the axisymmetric initial imperfection in the cylinder wall

can significantly affect the optimal designs. Weight savings associated with the addition of two rings to the unstiffened cylinder and/or the addition of internal pressure is substantial when torsion makes up a significant fraction of the combined load state.

Assumption of criticality of the stability constraints and neglect of the stress constraints during the optimal sizing of the cylinders produced designs that nevertheless satisfied all of the stress constraints, in general, as well as the stability constraints. Subsequent re-sizing of one cylinder to satisfy a violated in-plane matrix cracking constraint resulted in an optimal design that was 49% heavier than the optimal design produced when this constraint was ignored.

The additional internal pressure necessary to produce a violation of a stress constraint for each optimal design was calculated. Using an unsymmetrically laminated ring flange, a substantial increase in the strength of the flange/skin joint was observed.

ACKNOWLEDGMENTS

This work was supported by the NASA Langley Research Center under grant NAG1-343, the NASA-Virginia Tech Composites Program, with Dr. James H. Starnes, Jr. as Technical Monitor. The work was completed during the research residency of the first author at NASA Langley Research Center. The first author would like to thank Dr. Raphael T. Haftka of Virginia Tech, Dr. Mel Anderson of Old Dominion University, and Dr. Michael P. Nemeth of NASA Langley Research Center for their key comments.

TABLE OF CONTENTS

	<u>Page</u>
ABSTRACT	ii
ACKNOWLEDGMENTS	iv
TABLE OF CONTENTS	v
LIST OF TABLES	ix
LIST OF FIGURES	x

CHAPTER

1	INTRODUCTION, OBJECTIVE, AND BACKGROUND INFORMATION.....	1
	1.1 Introduction	1
	1.2 Objective.....	3
	1.3 Background Information.....	4
	1.3.1 Mathematical Models of Stiffened Shell Structures....	4
	1.3.2 Equilibrium and Buckling Analyses of Stiffened Cylinders.....	4
	1.3.3 Structural Optimization and Mathematical Programming	6
2	REVIEW OF PERTINENT LITERATURE.....	9
	2.1 Shell Theories	9
	2.2 Analysis of Unstiffened and Stiffened Cylindrical Shells	12
	2.2.1 Unstiffened Isotropic Cylindrical Shells	12
	2.2.2 Unstiffened Anisotropic Cylindrical Shells.....	14
	2.2.3 Stiffened Isotropic Cylindrical Shells.....	17
	2.2.4 Stiffened Anisotropic Cylindrical Shells	19
	2.2.5 Stresses and Strains Adjacent To Stiffeners.....	20
	2.3 Design of Unstiffened and Stiffened Cylindrical Shells	24
	2.3.1 Stiffened Isotropic Cylindrical Shells.....	24

	2.3.2	Unstiffened Anisotropic Cylindrical Shells.....	28
	2.3.3	Stiffened Anisotropic Cylindrical Shells.....	30
	2.3.4	Shell Design Based On A Geometrically Nonlinear Analysis.....	32
	2.4	Summary.....	35
3		PROBLEM STATEMENT, ASSUMPTIONS, AND GOVERNING EQUATIONS.....	36
	3.1	Problem Statement.....	36
	3.2	Analytical Model and Assumptions.....	36
	3.3	Governing Equations.....	39
	3.3.1	Strain-Displacement Equations.....	39
	3.3.2	Stress-Strain Equations.....	41
	3.3.3	Equilibrium Equations and Boundary Conditions.....	42
	3.3.4	Compatibility Equations.....	44
4		STRUCTURAL ANALYSIS OF THE AXISYMMETRIC PREBUCKLED EQUILIBRIUM STATE.....	46
	4.1	Solution To The Equations Governing The Geometrically Nonlinear Axisymmetric Response Of Cylindrical Shell Segments.....	46
	4.2	Solution To The Equations Governing The Geometrically Linear Axisymmetric Response Of Annular Plate Segments.....	51
	4.3	Determination of Constants of Integration.....	60
	4.4	Stress Analysis at the Ring Flange/Cylinder Wall Interface....	64
5		BUCKLING ANALYSIS.....	79
	5.1	Solution Methods.....	79
	5.2	Finite Element Model of the Second Variation of the Total Potential Energy of a Laminated Cylindrical Shell.....	86

5.3	Finite Element Model of the Second Variation of the Total Potential Energy of a Laminated Annular Plate	95
5.4	Finite Element Model of the Second Variation of the Total Potential Energy of the Ring-Stiffened Cylinder: Assembly of Global Stiffness and Geometric Stiffness Matrices	100
5.5	Formulation of the Nonlinear Buckling Eigenvalue Problem ...	107
6	OPTIMAL DESIGN ALGORITHM	109
6.1	Introduction	109
6.2	Quadratic Extended Interior Penalty Function Method	111
6.3	Method of Feasible Directions	113
6.4	Design Variables	116
6.5	Stress Constraints	119
6.6	Buckling Constraints	121
6.6.1	LDL ^T Decomposition of $[K(n_i) + K_G(n_i; \lambda)]$	122
6.6.2	Equivalent Constraint Formulation	123
6.7	Sensitivity Analysis	127
6.8	Convergence Criteria	128
7	RESULTS AND DISCUSSION	133
7.1	Buckling Analysis Case Study	133
7.2	Description of Optimal Sizing Case Study and Discussion of Algorithm Performance	137
7.3	Optimal Design Case Study Results	141
7.3.1	Unstiffened Cylinder Case Studies	142
7.3.2	Ring-Stiffened Cylinder Case Studies	145
7.3.2.1	Discussion of Optimal Design Details	145
7.3.2.2	Discussion of Optimal Weight Trends	147
7.4	Stress Constraints	150
7.4.1	Ring Flange/Cylinder Skin Interface Stresses	151

7.4.2	Results of Stress Analyses of Optimal Cylinders	153
7.4.3	Internal Pressure To Failure	155
8	CONCLUDING REMARKS AND RECOMMENDATIONS FOR FUTURE WORK	158
8.1	Concluding Remarks	158
8.2	Recommendations For Future Work	160
	REFERENCES	163
	NOMENCLATURE	176

<u>APPENDIX</u>	<u>Page</u>
A	LAMINA STRESS ANALYSIS OF PREBUCKLED CYLINDRICAL SHELL SEGMENT
	223
B	FORMULATION OF EQUILIBRIUM EQUATIONS GOVERNING THE RESPONSE OF A RING FLANGE AND ATTACHED SKIN AS A SYSTEM OF FIRST ORDER ORDINARY DIFFERENTIAL EQUATIONS
	229
C	ELEMENT STIFFNESS AND GEOMETRIC STIFFNESS MATRICES FOR A CYLINDRICAL SHELL FINITE ELEMENT
	236
D	ELEMENT STIFFNESS AND GEOMETRIC STIFFNESS MATRICES FOR AN ANNULAR PLATE FINITE ELEMENT
	239
E	LDL ^T DECOMPOSITION OF A SYMMETRIC MATRIX
	245

LIST OF TABLES

<u>Table</u>	<u>Page</u>
1 Nomenclature.....	176
7.1.1 Assumed Material Properties of Graphite-Epoxy Tape.....	186
7.1.2 Assumed Material Properties of Graphite-Epoxy Cloth.....	186
7.1.3 Assumed Material Properties of Ductile Adhesive.....	186
7.2.1 Description of Design Variables, Side Constraints, and Initial Designs ...	187
7.2.2 Load / Imperfection Case Identification.....	188
7.3.1 Optimal Designs of Unstiffened Cylinders.....	189
7.3.2 Optimal Design of Strap-Stiffened Cylinders.....	190
7.3.3 Optimal Design of "T" Ring-Stiffened Cylinders.....	190
7.3.4 Active Constraints and Corresponding Lagrange Multipliers For Unstiffened Cylinder Designs.....	191
7.3.5 Active Constraints and Corresponding Lagrange Multipliers For Strap-Stiffened Cylinder Designs.....	192
7.3.6 Active Constraints and Corresponding Lagrange Multipliers For "T" Ring-Stiffened Cylinder Designs.....	192
7.4.1 Minimum Stress Constraint Values For Strap-Stiffened Cylinder Optimal Designs.....	193
7.4.2 Minimum Stress Constraint Values For "T" Ring-Stiffened Cylinder Optimal Designs.....	194
7.4.3 Internal Pressure To Failure For Strap-Stiffened Cylinder Optimal Designs.....	195
7.4.4 Internal Pressure To Failure For "T" Ring-Stiffened Cylinder Optimal Designs.....	196

LIST OF FIGURES

<u>Figure</u>	<u>Page</u>
1.1.1 Ring-Stiffened Cylinder And Imposed Loads	197
3.2.1 Typical Cylindrical Shell Lamina	198
3.2.2 Typical Annular Plate Lamina	198
3.2.3 Cross Section Of Ring-Stiffened Cylinder	199
3.3.1 Typical Conical Shell Segment	200
4.3.1 Prebuckling Equilibrium And Compatibility	201
4.5.1 Ring/Shell Bonded Joint	202
5.2.1 Cylindrical Shell Finite Element	203
5.3.1 Annular Plate Finite Element	204
5.4.1 Cylindrical Shell Finite Element / Annular Plate Finite Element Junction	205
7.1.1 Buckling Analysis Example Problem	206
7.1.2 Buckling Interaction Diagram For Unstiffened Cylinder	206
7.1.3 Buckling Interaction Diagram For Ring-Stiffened Cylinder	207
7.1.4 Effect Of Adding Rings To Unpressurized, Perfect Cylinder	207
7.1.5 Effect Of Adding Rings To Unpressurized, Imperfect Cylinder	208
7.1.6 Effect Of Adding Rings To Imperfect, Pressurized Cylinder	208
7.1.7 Case "A" Buckling Mode Shape Of Perfect Ring-Stiffened Cylinder	209
7.1.8 Case "A" Buckling Mode Shape Of Imperfect Ring-Stiffened Cylinder ..	209
7.1.9 Case "A" Normalized Prebuckling Radial Displacement	210
7.2.1 Optimal Sizing Case Study Configurations	211
7.3.1 Effect of Mechanical Loading on Optimal Designs of Perfect, Unpressurized Unstiffened Cylinders	212
7.3.2 Effect of Mechanical Loading on Optimal Designs of Imperfect, Unpressurized Unstiffened Cylinders	212

<u>Figure</u>	<u>Page</u>
7.3.3 Effect of Mechanical Loading on Optimal Designs of Imperfect, Pressurized Unstiffened Cylinders	213
7.3.4 Effect of Imperfections and Pressurization on Weights of Optimal Unstiffened Cylinders	213
7.3.5 Effect of Mechanical Loading on Optimal Designs of Perfect, Unpressurized Strap-Stiffened Cylinders.....	214
7.3.6 Effect of Mechanical Loading on Optimal Designs of Imperfect, Unpressurized Strap-Stiffened Cylinders.....	214
7.3.7 Effect of Mechanical Loading on Optimal Designs of Imperfect, Pressurized Strap-Stiffened Cylinders	215
7.3.8 Effect of Mechanical Loading on Optimal Designs of Perfect, Unpressurized "T" Ring-Stiffened Cylinders	215
7.3.9 Effect of Mechanical Loading on Optimal Designs of Imperfect, Unpressurized "T" Ring-Stiffened Cylinders	216
7.3.10 Effect of Mechanical Loading on Optimal Designs of Imperfect, Pressurized "T" Ring-Stiffened Cylinders	216
7.3.11 Comparison of Strap-Stiffener Weights With "T" Ring Stiffener Weights	217
7.3.12 Effect of Imperfections and Pressurization on Ring Weights of Optimal Unpressurized "T" Ring-Stiffened Cylinders.....	217
7.3.13 Effect of Imperfections and Pressurization on Weights of Optimal Strap-Stiffened Cylinders	218
7.3.14 Effect of Imperfections and Pressurization on Weights of Optimal "T" Ring-Stiffened Cylinders	218
7.3.15 Weight Savings Due To Addition Of Rings.....	219
7.3.16 Effect of Imperfections and Pressurization on Weight Savings Due To The Addition of "T" Ring Stiffeners.....	219

<u>Figure</u>	<u>Page</u>
7.4.1 Typical Ring Flange/Cylinder Skin Adhesive σ_{zz} Peel Stress Distributions	220
7.4.2 Typical Ring Flange/Cylinder Skin Adhesive τ_{xz} Shear Stress Distributions	220
7.4.3 Typical Ring Flange/Cylinder Skin Adhesive τ_{yz} Shear Stress Distributions	221
7.4.4 Effect of Strap Stacking Sequence On Internal Pressure To Failure of Optimal Strap-Stiffened Cylinders	221
7.4.5 Effect of Neglect of Matrix Cracking Failure On Internal Pressure To Failure of Optimal Strap-Stiffened Cylinders	222
7.4.6 Effect of Neglect of Matrix Cracking Failure On Internal Pressure To Failure of Optimal "T" Ring-Stiffened Cylinders	222

LIST OF TABLES

<u>Table</u>	<u>Page</u>
1 Nomenclature.....	176
7.1.1 Assumed Material Properties of Graphite-Epoxy Tape.....	186
7.1.2 Assumed Material Properties of Graphite-Epoxy Cloth.....	186
7.1.3 Assumed Material Properties of Ductile Adhesive.....	186
7.2.1 Description of Design Variables, Side Constraints, and Initial Designs ...	187
7.2.2 Load / Imperfection Case Identification.....	188
7.3.1 Optimal Designs of Unstiffened Cylinders.....	189
7.3.2 Optimal Design of Strap-Stiffened Cylinders.....	190
7.3.3 Optimal Design of "T" Ring-Stiffened Cylinders.....	190
7.3.4 Active Constraints and Corresponding Lagrange Multipliers For Unstiffened Cylinder Designs.....	191
7.3.5 Active Constraints and Corresponding Lagrange Multipliers For Strap-Stiffened Cylinder Designs.....	192
7.3.6 Active Constraints and Corresponding Lagrange Multipliers For "T" Ring-Stiffened Cylinder Designs.....	192
7.4.1 Minimum Stress Constraint Values For Strap-Stiffened Cylinder Optimal Designs.....	193
7.4.2 Minimum Stress Constraint Values For "T" Ring-Stiffened Cylinder Optimal Designs.....	194
7.4.3 Internal Pressure To Failure For Strap-Stiffened Cylinder Optimal Designs.....	195
7.4.4 Internal Pressure To Failure For "T" Ring-Stiffened Cylinder Optimal Designs.....	196

Chapter 1

INTRODUCTION, OBJECTIVE AND BACKGROUND INFORMATION

1.1 Introduction

Significant advancement in the state-of-the-art of analysis and design of advanced composite materials and structures has led aerospace vehicle manufacturers to incorporate increasing amounts of composite structure into new vehicle designs. Motivated by the potential for significant weight savings and the possible replacement of complicated structural assemblies by single, co-cured composite components, design engineers and researchers today seek to incorporate composite materials into primary load-bearing structure. One candidate for such an application is the fuselage of next-generation transport aircraft, a stiffened cylindrical shell. The problem that confronts the manufacturer is to determine the material distribution among the cylinder skin and stiffening elements resulting in a weight-efficient vehicle that can withstand the imposed loads. Using laminates made of advanced composite materials, the designer has much more flexibility than he has with metals in that he can tailor the strength and stiffness of individual structural components by varying the ply orientations and/or thicknesses of the layers comprising the laminate. This type of tailoring, along with optimum sizing of the stiffening elements, yields a very efficient structural design. Since the cost of composite structure fabrication today is still relatively high, it is prudent to take advantage of this tailorability and use composites to their full potential. However, many important technological issues must still be resolved. In their report, Jackson, et. al.¹ propose a full scale analysis, design and test effort to qualify advanced composite structure for use in the fuselage of both civil and military transport aircraft. They present an exhaustive list of technical issues which would need to be addressed before such structure could be qualified for flight. Dickson and Biggers² addressed many of these issues while successfully designing and building a full scale advanced composite stiffened panel. Industrial interest in design optimization of such panels led to the development

by Bushnell^{3,4} of PANDA and PANDA2 , two computer programs which aid the engineer in the design of minimum weight stiffened panels.

The work described in this document outlines the development of a methodology to perform the structural analysis and minimum weight structural sizing of the laminated fiber reinforced composite stiffened cylinder depicted in Fig. 1.1.1. The problem can be described as follows. First, the structural analysis must contain sufficient detail to provide reliable estimates of response quantities that constrain the design. For example, as will be discussed in section 2.2, details such as initial geometric imperfections and the deformation of stiffener cross-sections, phenomena typically ignored or addressed in only an approximate manner, can have a significant effect on the buckling loads of shell structures. These buckling loads generally represent critical constraints on the design of thin-walled structures. Second, the structural analysis must be made efficient enough to be incorporated into a structural sizing algorithm which may require the performance of several hundred structural analyses. Actual incorporation of the structural analysis into a structural sizing algorithm represents the final step in the process.

1.2 Objectives

Current computer programs written for optimal sizing of stiffened cylinders suffer from one or more of the following simplifying assumptions

1. A linearized prebuckling equilibrium state.
2. Modeling the stiffeners as beam elements.
3. A perfect bond of zero thickness between the shell wall and stiffener attachment flange.

These commonly made assumptions constitute serious deficiencies for optimal design, as will be discussed in greater depth in section 2.2. The main purpose of the present study is to investigate the optimal sizing of anisotropic, ring-stiffened cylinders using a structural analysis devoid of these deficiencies. Several objectives will be met as part of this investigation. The first objective of the present study is to develop an efficient structural analysis to predict prebuckling deformations, prebuckling stresses, and buckling loads of anisotropic, ring-stiffened circular cylindrical shells subjected to axial compression, torsion, and internal pressure loadings. The structure is modeled as a branched shell. A nonlinear axisymmetric prebuckling equilibrium state is assumed which is amenable to exact solution within each branch. Axisymmetric geometric imperfections are included. The second objective is to implement the structural analysis into a structural sizing algorithm that will be used to develop minimum weight ring-stiffened cylinders for a future experimental investigation. The effects of initial geometric imperfections and pressurization on the minimum weight designs are investigated. The final objective is to evaluate local stresses in the area adjacent to the ring-to-shell interface of the optimal designs. The effects of an imperfect, geometrically nonlinear prebuckling equilibrium state and internal pressurization on optimal stiffened shell designs, and on the ring/shell interface stresses in these designs, are technical issues expected to directly affect the fuselage designs of next-generation transport aircraft.

1.3 Background Information

1.3.1 Mathematical Models of Stiffened Shell Structures

As described in the text by Niu⁵ three major buckling modes constraining the designs of stiffened shell structures such as an aircraft fuselage are; local instability of the stiffener segments, panel instability, and general instability. Local instability involves buckling of the individual parts of the stiffeners (flanges, webs, etc.), panel instability implies buckling of the shell in the panel length between two rings, and general instability implies that the rings, not being rigid enough to enforce node lines along their lines of attachment to the shell, buckle along with the rest of the cylindrical shell. Traditionally, these three types of instability are analyzed as separate phenomena. Local instability is evaluated by modeling a stiffener flange or web as a plate segment having boundary conditions assumed to result in conservative buckling load estimates such as simple as opposed to clamped or elastically restrained supports. Panel instability is evaluated by smearing the stiffnesses of any longitudinal stiffeners into an equivalent orthotropic shell layer and treating the shell segment between rings as a simply supported monocoque cylinder. General instability has been traditionally evaluated by smearing both the stringer and ring stiffnesses out over the entire shell surface. With the advent of more powerful computers and analytical techniques, the smeared model is slowly giving way to models which treat the stiffeners as discrete elements.

1.3.2 Equilibrium and Buckling Analyses of Stiffened Cylinders

A significant amount of literature devoted to the study of buckling of shells describes the advantages and disadvantages of calculating buckling loads based on "classical" and "nonclassical" theories. In his survey paper, Bushnell⁶ provides an excellent explanation of these two types of theories. In the "classical" type of analysis, the primary (or prebuckled) equilibrium state of the structure is assumed to be free of any bending deformations (rotationless). This greatly simplifies the analysis. In the classical buckling analysis of cylindrical shells, effects of the boundaries on the prebuckled

equilibrium state are ignored and the shell is assumed to be perfectly smooth (free of any initial geometric imperfections) so that a pure membrane state of stress can be assumed to exist in the unbuckled cylinder. However, the effects of boundary conditions are considered in the solution of the equations governing the stability of the structure; hence, there is an inconsistency between the buckling analysis and the analysis of the prebuckled equilibrium state. This inconsistency can be eliminated by abandoning the assumption of a pure membrane prebuckled equilibrium state - a characteristic of many "nonclassical" theories. In an axisymmetrically loaded cylindrical shell, bifurcation buckling can occur from an axisymmetric prebuckled equilibrium configuration into a general asymmetric configuration. The axisymmetric prebuckled equilibrium state may include a substantial amount of bending, especially if geometric imperfections in the shell wall are accounted for. Substantial bending in the presence of membrane loading means that the deformation is a nonlinear function of the applied load; hence, the equations governing the stability of the axisymmetric equilibrium configuration are nonlinear functions of the applied load - *a nonlinear buckling eigenvalue problem*. This type of eigenvalue problem is in contrast to the linear buckling eigenvalue problem generated when the prebuckling equilibrium state is assumed to exhibit geometrically linear behavior as in the case of classical buckling of a cylindrical shell. The load-displacement curve describing the nonlinear prebuckled equilibrium state may contain points at which bifurcation occurs (intersection of equilibrium paths), or the curve may reach a relative maximum. This relative maximum is referred to as a limit point. For elastic, conservative systems, buckling occurs either at a bifurcation point or a limit point.

A major factor complicating the theoretical analysis of both the prebuckling equilibrium state and the stability of shells is the complexity of the governing equations. Unlike plates, coupling between flexural and membrane behavior cannot be ignored even when the deformations are extremely small; furthermore, there is no universally accepted set of equations governing shell response as there is in the case of plate the-

ory. The form of the strain-displacement equations is a particular focal point of controversy; researchers tend to disagree as to which terms in these equations must be retained and which ones can be neglected. The result of this controversy is a large number of theories ranging from the most complicated (Flügge's) to the simplest (Donnell - Mushtari - Vlasov). As will be discussed in Chapter 2, the literature is replete with information to help guide those interested in selecting an appropriate theory for a particular problem.

In most applications, a thorough prebuckling stress analysis is warranted in addition to the buckling analysis. Under certain types of loads, thin shells can exhibit regions of high local stress. In metals, yielding of the material occurs relieving these stresses; however, in brittle materials, such as advanced composites, stress relief must come from other sources such as transverse matrix cracking, local fiber failure and delamination. Experimental work, such as that reported by Starnes, et. al.⁷, indicates that the region adjacent to skin/stiffener attachment areas warrants special attention since this is typically a region where high local stresses occur. It is, therefore, possible that a certain configuration might fail due to such a stress concentration before buckling occurs, requiring a thorough and accurate prebuckling stress analysis to predict such a failure.

1.3.3 Structural Optimization and Mathematical Programming

Engineers originally relied on fully stressed and/or simultaneous failure mode design philosophies in order to develop minimum weight designs. Then Schmit⁸ presented a landmark paper in 1960 proposing the application of nonlinear mathematical programming techniques to develop minimum weight structural designs satisfying a specified set of constraints with the aid of a digital computer. He coined the term structural synthesis (today more commonly referred to as structural optimization) to describe the procedure and showed that in many cases the fully stressed / simultaneous failure mode design approaches did not produce truly optimum designs. Engineers gen-

erally apply structural optimization techniques to either minimize weight or maximize performance, which becomes the objective function of the mathematical programming problem. The constraint set reflects other structural requirements or restrictions that need to be imposed to achieve a usable design. Mathematical programming (MP) techniques used to solve structural optimization problems are of one of two types - indirect techniques and direct techniques. Indirect techniques involve replacing the constrained minimization (or maximization) problem with a set of unconstrained problems. These are called sequential unconstrained minimization techniques or SUMT and include the penalty function methods. Direct MP techniques deal with the objective and constraint functions individually. In either MP technique a method must be chosen to minimize or maximize a nonlinear function of several variables. Newton's method, certainly the most well-known, requires formulation of the Hessian matrix (second derivatives of the objective function and constraints with respect to the design variables); hence, it is called a second order method. Since second derivatives tend to be computationally expensive to calculate, first order methods involving only first derivative (gradient) information tend to be more popular. Derivative information is generally obtained exactly, or approximately using finite differences. If it is not feasible to calculate any derivative information at all, a zero order method, requiring function evaluations only, may be used.

The optimum designs generated by a structural optimization algorithm may or may not be unique. The design variables and the constraints define what is known as a design space. If this design space is convex, then only one point in this space will satisfy the conditions of optimality and the optimum design is called a *global optimum*. The necessary conditions are generally referred to as the Kuhn-Tucker conditions. (See section 5.1 of Ref. 9. A discussion of the Kuhn-Tucker conditions is presented in section 6.8). This is true, for example, of problems where the objective function and all the constraints are linear functions of the design variables. For problems where the objective function and/or the constraints are nonlinear functions of the design variables,

convexity of the objective function and constraints need to be established. Many structural optimization problems result in a design space which is generally nonconvex. In this case many points satisfying the Kuhn-Tucker conditions may exist in the design space. Of these points, the one resulting in the true extremum of the objective function is the global optimum; the other points are called *relative optima* or *relative minima*. *Alternative optima* or *alternative minima* are points in the design space satisfying the Kuhn-Tucker conditions yielding the same value of the objective function as other optima.

Chapter 2

REVIEW OF PERTINENT LITERATURE

2.1 Shell Theories

A wide variety of different theories exists upon which to form the basis of a thin shell structural analysis. The publication by Leissa¹⁰ contains an excellent comparison of the various theories used in linear shell analysis. Such a comprehensive discussion of the various geometrically nonlinear theories has yet to be published. Of the theories employed in the analysis of circular cylindrical shells, the three most commonly used are (in order of decreasing complexity): the theory of Flügge¹¹, the theory of Sanders¹², and the theory of Donnell^{13,14} (also known as Donnell-Mushtari-Vlasov or DMV theory). These theories diverge widely in their treatment of the shell strain-displacement equations and the expressions for the force and moment resultants. Flügge's theory has been criticized on the grounds that the equations keep the numerically small terms of order h/R_α (h is the shell thickness and R_α is a radius of curvature). Recognition of the complexity of Flügge's equations and a desire to generate a practical solution to the problem of the buckling of a long thin-walled cylinder under torsional loading led L.H. Donnell to propose a relatively simple set of equations governing the response of circular cylindrical shells. These equations are almost exactly the same as those governing the response of a flat plate except for the presence of a term W/R in the expression for the circumferential strain and a term N_y/R in the equation expressing equilibrium of forces normal to the shell surface (W is the radial displacement, N_y is the circumferential stress resultant, and R is the cylinder radius). One important aspect of Donnell's equations is that in the strain-displacement equations and the expressions for the stress resultants and stress couples, the following approximation is made

$$1 + \left(\frac{z}{R}\right) \approx 1 \quad (2.1.1)$$

where z is a coordinate in the through-the-thickness direction. Thus, the through-the-

thickness variation of the lengths of the circumferential fibers is neglected. Donnell states in his paper that should any of the terms neglected in his theory be retained these terms would be multiplied by either $k(h/R)^2$ or $(1/n)^2$, where h is the shell thickness, k is a material property-dependent constant of order 1, and n is the number of circumferential waves in the buckling mode shape. Thus it would appear that DMV theory would be adequate for thin shells with large n . Donnell achieved excellent correlation of his theory with experiments. Some insight as to why this was so was provided by the work of Marguerre¹⁵ on shallow cylindrical panels. Published about the same time as Donnell's paper, Marguerre's equations were strikingly similar. The similarity in the equations governing the response of Marguerre's shallow panels and the buckling of Donnell's cylinders, along with the good correlation Donnell achieved between his theoretically and experimentally determined buckling loads, can be attributed to the fact that the cylinder, buckled into a configuration containing many circumferential waves, behaves like a series of shallow shells linked at node lines. The inherent simplicity of DMV theory has made it the basis of many papers on the structural analysis of cylindrical shells up to the present day. In order to avoid the deficiencies of DMV theory without resorting to the complication of Flügge's equations, Sander's theory may be used. In Sander's theory, several terms involving the circumferential displacement and its derivatives in the strain-displacement equations that are ignored in DMV theory are retained.

In most practical applications, based on results published in the literature, use of a theory more complicated than DMV theory does not appear to be justified. In 1955, Hoff¹⁶ evaluated closed-form solutions for the linear bending response of isotropic cylindrical shells based on both Flügge and DMV theories. He showed that in the case of the axisymmetric response both theories were precisely equivalent for all values of geometrical parameters for which Flügge's theory was valid. Dong, Pister and Taylor¹⁷ extended this work to shells made of fiber composite laminates. Studying the linear, axisymmetric bending response of generally laminated cylinders, they showed that re-

sults based on DMV theory were practically the same as those based on Flügge's theory provided that the laminate was constructed of laminae having ratios of fiber direction Young's moduli to transverse direction Young's moduli (E_1/E_2) less than 1000. Unfortunately, no evidence of a study comparing the nonlinear axisymmetric bending response of cylindrical shells could be found in the literature. Most comparisons of various nonlinear shell theories that appeared in the literature have been performed in the context of solving the equations governing the *stability* of prebuckling equilibrium configurations.

Wu¹⁸ compared the buckling loads from an assumed membrane prebuckled state of laminated cylinders subject to combined loads of axial compression, torsion, and lateral pressure calculated using DMV theory to those loads calculated using Flügge's theory and found that, when the cylinder buckled into five circumferential waves or more, the difference in buckling loads predicted using the two theories was less than 3%. Most recently Simitses, et. al.^{19,20} compared the limit point loads of metallic and laminated cylindrical shells under axial compression calculated using a geometrically nonlinear structural analysis based on DMV theory to those calculated based on Sander's theory. In the special case of a shell made of a single layer of Boron/Epoxy with all fibers running in the hoop direction, buckling loads calculated using DMV theory were as much as 13% higher than those calculated using Sander's theory for cylinders having L/R ratios as low as 2. However, for most practically laminated shells they found negligible differences in the results based on the two theories for thin cylindrical shells whose postbuckled shapes contained four or more circumferential waves and whose L/R ratios were less than five.

2.2 Analysis of Unstiffened and Stiffened Cylindrical Shells

Efficient structural designs must be based on mathematical models which are realistic. This is especially true of designs generated in an automated structural optimization algorithm since the algorithms tend to exploit the simplifications in the model. Without adequate realism built into the model, large margins of safety may be necessary to insure that neglect of structural details does not result in unexpected failure of the as-designed structure. The citations below are included to provide some justification for the level of detail included in structural analysis used in this study. This discussion is not intended to be an exhaustive review of the literature pertaining to the analysis of cylindrical shells

2.2.1 Unstiffened Isotropic Cylindrical Shells

After publication of Donnell's paper in 1933 (Ref. 13), research focused on applying Donnell's equations to calculating buckling loads of isotropic cylinders subject to other types of loads, particularly axial compression, since it was felt that this would yield insight into the response of the compression side of a bent aircraft fuselage. Assuming a linear prebuckled equilibrium state, Seide and Weingarten²¹ showed in 1961 that the bending buckling load of an isotropic cylinder was nearly the same as the buckling load of the same cylinder under pure axial compression. Crate, et. al.²² extended the experimental work of Donnell in 1946 to isotropic cylinders loaded in torsion with internal pressure. They found that the pressure increased the buckling load significantly and published an interaction formula applicable to design. It is well-known that the correlation of the results of a classical buckling analysis to experimental results for cylinders subject to axial compression is too poor for such an analysis to be used as the basis for design. It is generally believed that there are two major reasons why this is so, one pertaining to the existence of initial imperfections and the other to the inconsistency of boundary conditions used in the prebuckling and buckling analyses. Donnell and Wan²³ showed, using the results of a large deflection analysis,

that small initial imperfections in the form of an initial stress-free radial displacement could result in buckling loads which are much lower than the classical value. In 1963, Koiter²⁴ showed that initial imperfections in the shape of the classical axisymmetric buckling mode,

$$W_0 = \mu \cos(q_0 x / R), \quad (2.2.1.1)$$

could reduce the axial compression buckling load by as much as 40% when μ , the imperfection amplitude, was as small as one-tenth of the shell wall thickness. In Eq. (2.2.1.1), x is the axial coordinate of the cylinder, R is the radius of the cylinder, $q_0^4 = 12(1 - \nu^2)R^2/h^2$, ν is Poisson's ratio, and h is the shell thickness. Koiter's results also indicate that the axisymmetric buckling mode imperfection shape is the most degrading shape of all possible harmonic, axisymmetric shapes. Hutchinson²⁵ extended Koiter's work by adding one asymmetric term to Koiter's axisymmetric buckling mode imperfection shape and calculating buckling loads of long cylinders subject to axial compression and internal pressure using DMV theory and ignoring the effects of the boundaries. Hutchinson concluded that internal pressure "ironed out" the asymmetric imperfections but not the axisymmetric ones, resulting in the axisymmetric imperfection having the dominant effect. An explanation for the degrading effect of axisymmetric imperfections can be found in the paper by Thurston²⁶. He points out that while the axial stress resultant remains fairly constant up to buckling, the circumferential stress resultant increases in a nonlinear manner. There is a strong coupling between this increasing circumferential stress resultant and asymmetric buckling modes which triggers premature buckling compared to classical linear theory. The bending of the shell wall with imperfections creates regions where the circumferential stress resultant may be compressive, which is an additional destabilizing effect.

Without including the effects of initial geometric imperfections, Stein²⁷ performed a theoretical buckling analysis from a geometrically nonlinear axisymmetric prebuckled state on a perfect cylinder under axial compression using DMV theory and showed that maintenance of consistent boundary conditions in the prebuckling and the buck-

ling analyses could result in buckling loads which are as much as fifty percent lower than those predicted using classical theory. He also showed that the addition of internal pressure tended to raise the buckling load up to the classical value. Almroth²⁸ added axisymmetric imperfections to Stein's analysis and allowed for elastic restraint at the shell boundaries. He evaluated imperfections that were nonperiodic functions of the axial coordinate as well as those that were periodic functions and concluded that the nonperiodic imperfections generally resulted in less dramatic drops in the buckling load. The work of Koiter, Stein, Almroth, and others led Tennyson, et. al.²⁹ to propose abandoning the inefficient practice of designing cylindrical shells using empirically estimated buckling load reduction factors in favor of basing designs upon an analysis of cylinders possessing axisymmetric wall imperfections. They showed, through theoretical analyses and experiments, that the Koiter type of imperfection shape (see Eq. (2.2.1.1)) with an amplitude equal to the root-mean-square of radial deviations from a pre-determined ideal shape measured in the cylinder wall, could adequately account for the effect of initial imperfections. They also included a two term asymmetric imperfection, similar to that of Hutchinson, in their theoretical analysis and concluded that the effect on the axial compression buckling load of the asymmetric term was relatively small compared to the effect of the axisymmetric component.

2.2.2 Unstiffened Anisotropic Cylindrical Shells

As the state-of-the-art of the analysis of unstiffened isotropic cylinders advanced, more and more attention began to focus on the behavior of cylindrical shells made of laminated fiber composite materials. Dong, Pister, and Taylor¹⁷ and Ambartsumyan³⁰ published some of the earliest work in the area of stress analysis of these shells, the former paying particular attention to the influence of bending-stretching coupling of the shell wall laminate on the response of the overall structure. The paper by Cheng and Ho³¹ presented the results of some of the earliest work performed in the area of buckling of generally laminated cylindrical shells. They performed a classical type of

analysis using a combination of Flügge's theory for the governing differential equations and DMV theory for the boundary conditions. Motivated by the work of Seide and Weingarten in the area of bending buckling of isotropic cylinders, Holston³² performed a similar analysis on cylinders made of laminated composite materials. He used linear anisotropic shell theory for the prebuckling analysis, ignoring the effects of boundary conditions, and applied both Flügge's theory and DMV theory to the stability problem. He concluded that the bending/compression interaction diagram was linear and that the buckling load of the cylinder under pure bending was very nearly equal to that of the cylinder under pure axial compression, a result similar to the one obtained for isotropic shells earlier (Ref. 21). Thus it appeared that the study of laminated cylinders under axial compression could provide information applicable to the study of the bending of a laminated composite cylindrical shell.

Card³³ studied the imperfection sensitivity of laminated cylinders subject to axial compression with the goal of finding the winding angle (α) of a balanced $\pm\alpha$ laminate configuration that yielded cylindrical shells with the lowest imperfection sensitivity. He used a geometrically nonlinear axisymmetric prebuckling analysis in order to study the effects of prebuckling boundary conditions that were consistent with those applied in the buckling analysis and concluded that for some laminate configurations this consistent approach yielded buckling loads which were as much as 25% below those calculated using classical theory. However, the results of the classical analysis for other laminate configurations were extremely close to the results obtained from his consistent analysis. The result of Card's buckling load and postbuckling coefficient calculations (postbuckling coefficients are an estimate of the slope of the postbuckled load-displacement curve at the bifurcation point, and are used as a measure of imperfection sensitivity) showed that a cylinder having a shell wall angle α equal to 45 degrees had the lowest imperfection sensitivity; furthermore, he concluded that the laminate configurations yielding the highest buckling loads generally were also the most imperfection sensitive. The results of a series of experiments qualitatively verified the

theoretical predictions, indicating that the disparity between buckling tests and theoretical predictions for anisotropic shells was comparable to that of isotropic shells for some laminates.

Work such as Card's led Tennyson, et. al.³⁴ to include the effects of an axisymmetric imperfection shape in their theoretical buckling analysis. They derived the classical axisymmetric mode shape for a generally laminated cylindrical shell, and used this as the imperfection shape in the analysis of cylinders with a $[\theta, 0, -\theta]$ laminate. Including imperfections with amplitudes as small as ten percent of the cylinder wall thickness in the analysis, they calculated buckling loads which were as much as 60% lower than the buckling loads calculated using the classical approach. Plotting the buckling load versus θ , with the imperfection amplitude as a parameter, they also demonstrated that the presence of initial imperfections negated the theoretical buckling load increase, resulting from a judicious choice of θ predicted based on classical theory. Buckling loads for imperfect cylinders proved to be insensitive to the lamination angle θ for the type of laminate under consideration. This correlated with Card's observation that the laminates of perfect cylinders that resulted in the highest buckling loads also resulted in structures having the highest imperfection sensitivity. Booton³⁵ extended Tennyson's work to study cylindrical shells under combined loads. He employed DMV theory, axisymmetric nonlinear prebuckling, an axisymmetric initial geometric imperfection of the same type as that used earlier by Tennyson, et. al.²⁷, and clamped boundary conditions in the prebuckling analysis consistent with those of the buckling analysis. The purpose of the study was to develop a general set of buckling interaction diagrams for various load combinations for use in the design of laminated cylinders. Booton found that the interaction diagrams could vary dramatically from one stacking sequence to another; furthermore, he found that in a few special cases the interaction diagram was convex toward the origin, rendering the commonly used approach of approximating the interaction diagrams with straight lines nonconservative. Perhaps more significant were the results of a series of experiments performed

as part of the study. He obtained excellent theoretical/experimental correlation, using his theoretical analysis to predict buckling loads which were typically within 10% of the corresponding experimentally observed values. Jones and Henneman³⁶ applied an analysis similar to Stein's²⁷ to study the effect of a geometrically nonlinear prebuckled state with consistent boundary conditions only (no imperfections included) on the buckling loads of cross-ply laminated cylinders subject to axial compression or lateral pressure (not in combination). They concluded that the effects were negligible for that particular family of laminates. In 1985 Simites, et. al.³⁷ published the results of their nonlinear structural analysis of simply supported four and six ply laminated cylindrical shells loaded in torsion and axial compression. They discovered that the lamina stacking sequence had a pronounced effect on the magnitude of the limit load and the imperfection sensitivity. The samples were more imperfection sensitive under axial compression than under torsion; furthermore, the laminates with the higher limit point loads were also more imperfection sensitive.

2.2.3 Stiffened Isotropic Cylindrical Shells

What is generally regarded as the earliest work in the theoretical analysis of stiffened metal cylinders was published by van der Neut³⁸ in 1947. Van der Neut calculated theoretical buckling loads of stiffened cylinders under axial compression using two different mathematical models. In the first model he smeared the stiffnesses of the rings into an equivalent orthotropic shell layer while in the second model he treated the rings as discrete curved beams. The stiffnesses of the longitudinal stiffeners were smeared in both models. Comparing the theoretical buckling loads calculated using both models, van der Neut concluded that the average number of rings lying within one half-wave length of the buckled mode shape must be greater than 2 for the buckling loads of the model with the smeared rings to be approximately the same as the corresponding buckling loads of the model with discrete rings. In many applications, such a close ring spacing is not practical. By including stiffener centroid eccentricity in his

model, van der Neut showed that placing the centroid at the shell wall middle surface in the theoretical analysis could result in large errors in the buckling load if the centroid of the stiffeners in the actual structure was offset from this middle surface. He also postulated that, due to the large number of circumferential waves in the buckle pattern, a cylinder under axial compression would possess almost the same buckling load as a cylinder subject to bending.

In 1950 Stein, et. al.³⁹ published the results of a theoretical and experimental study of simply supported ring-stiffened cylindrical shells under torsional loading. Using DMV theory to estimate the panel buckling loads in his analysis (assuming the rings possessed no torsional stiffness), he achieved good correlation (85%) with the experiments. Stein noted that the increasing the size of the rings tended to drive the buckling load up until the buckled mode shape possessed node points at the ring locations, noting that rings effectively resisted the formation of the diagonal buckles associated with torsional buckling. Block⁴⁰ conducted a theoretical study of similar ring-stiffened cylindrical shells subject to axial compression. He modeled the rings as discrete beam elements having centroids coincident with the shell wall midplane. Block concluded that use of such a detailed mathematical model was not justified; modeling the region between rings as an unstiffened, simply supported cylinder for panel buckling calculations and using the smeared technique for general buckling calculations produced adequate results for the particular cases studied. Haftka and Singer⁴¹ also modeled the rings as discrete beam elements in studying the buckling of ring-stiffened cylinders subject to axial compression and pressure loadings. In the axial compression case, they noted that unless the rings were extremely weak and their spacing extremely small panel buckling was the critical buckling mode; furthermore, adding rings to the unstiffened shell had a very small effect on the buckling load. This is because the buckled mode shapes of such structures typically possess many axial waves so that, unless the ring spacing is small, the rings tend to lie on node lines of the buckled waveform. Baruch and Singer⁴², using the smeared technique to calculate general buckling

loads only, studied stiffened cylindrical shells under external pressure loads. As van der Neut had concluded for such shells under axial compression, they concluded that it was very important to include stiffener eccentricity in the mathematical model. Block, Card, and Mikulus⁴³ drew the same conclusion for cylindrical shells under combined axial compression and pressure using the smeared technique. Still focusing on general instability only, Hutchinson and Amazigo⁴⁴ calculated postbuckling coefficients for stiffened cylindrical shells loaded in axial compression or external pressure using DMV theory and the smeared technique. They demonstrated that cylinders subject to axial compression stiffened with internal stringers only had near zero imperfection sensitivity while the same cylinders with internal rings only exhibited substantial imperfection sensitivity.

Bushnell⁴⁵ addressed the issue of how much detail to include in the mathematical model used to calculate buckling loads of stiffened shells of revolution. Using BOSOR4⁴⁶, a very accurate computer program based on a branched shell mathematical model, he showed that theoretical buckling loads and vibration frequencies could be unexpectedly sensitive to modeling details such as prestress deformations and out-of-plane stiffnesses of rings. He also noted that rings and stringers could exhibit significant prebuckling deformation leading to significantly unconservative buckling load estimates based on mathematical models which fail to account for this deformation.

2.2.4 Stiffened Anisotropic Cylindrical Shells

Many analysis codes (such as BOSOR4) now include the capability of analyzing laminated composite stiffened shells as well as isotropic stiffened shells; however, the state-of-the-art of the analysis of these stiffened shells is not as advanced as that of isotropic shells. The paper by Jones⁴⁷ presents the results of general buckling load calculations for fiber composite cylinders with composite stiffeners subject to hydrostatic pressure. The goal of this study was to observe the effects of stiffener eccentricity and the bending-membrane coupling induced by an unsymmetrically laminated shell wall.

Jones used the smeared technique and a classical buckling analysis based on DMV theory in his work assuming a membrane prebuckled state and ignored the effect of material bending and twisting coupling . He presented a single example which indicated that the axial compression buckling load was sensitive to the degree of membrane-bending coupling exhibited by the shell wall laminate. In 1975, Jones and Morgan⁴⁸ recognized that composite materials tend to possess different Young's Moduli in tension than in compression and modified Jones's analysis to include this phenomenon. They studied cylinders subjected to various combinations of axial loading and lateral pressure and found that the effect of the bilinear stress-strain relation on the buckling load was small for most practical materials

Wang and Hsu⁴⁹ studied the state of stress in prebuckled stiffened laminated cylindrical shells subject to combinations of internal pressure, temperature change, and axial load using a mathematical model with discrete beam elements representing the stiffeners. A few examples are included to demonstrate the capability of their analysis. One important detail shown on the charts that summarize the results of these examples is the existence of high strain gradients in the cylinder skin near the stiffening elements.

2.2.5 Stresses and Strains Adjacent To Stiffeners

As mentioned in section 1.3.2, proper characterization of the stresses in areas of high strain gradients may be important to the design of laminated composite structures. In the case of the composite ring-stiffened cylinder, the ring/skin interface is one such area. In the prebuckled equilibrium configuration, the rings must not separate from the skin. Since the thin shell may be loaded by a combination of tangential loads and normal pressure loads, a geometrically nonlinear prebuckling analysis is justified in order to accurately predict forces and bending moments at the ring/skin interface. It is assumed in the present study that the rings are adhesively bonded to the skin.

Wang and Biggers⁵⁰ developed an analysis code to be used in the design of flat

panels with adhesively bonded stiffeners. The stiffeners of such panels tend to separate from the skin when the structure is postbuckled and/or subject to normal pressure loads. To quantify this phenomenon, Wang and Biggers modeled the stiffener attachment flange and attached skin as orthotropic plates whose deformations are coupled through the presence of a thin, isotropic adhesive bond between them. They assumed that the transverse shear and normal stresses in the bond were constant through the thickness and that any tangential stresses could be neglected. The stiffener web and supporting skin were modeled as distributed springs. The results of this analysis showed that while the bond shear stresses (τ_{xz} and τ_{yz}) were more or less uniform across the step in thickness at the skin/flange interface, the bond normal stress (σ_{zz}) peaked sharply in this area. A narrow attachment flange resulted in a better design since wide flanges resulted in higher bond shear (τ_{xz}) stresses; furthermore, high ratios of flange thickness to skin thickness resulted in higher bond stresses and thus poorer designs. Wang and Biggers also showed that changing the lamina stacking sequence of both the flange and the skin could drastically affect the separation stresses. In one case, switching a zero and ninety degree ply within the stiffener flange laminate resulted in a forty-two percent increase in these stresses. Tsai⁵¹ presents an in-depth analytical and experimental study of the problem of stiffener pull-off in curved, postbuckled panels with co-cured stiffeners. He worked the problem using both a "maximum allowable pull-off strength" approach and a fracture mechanics approach to estimate the maximum strength of the specimens used in the experiments. Based on his experimental results, Tsai determined that the strain energy release rate calculated using the fracture mechanics approach was the controlling parameter for initiation of skin/stiffener separation and that a failure criterion based on this quantity could be used to determine skin-stiffener interface configurations resulting in maximum improvement in pull-off strength.

Hyer, et. al.⁵² performed a theoretical and experimental study of flat, stiffened panels loaded by normal pressure in order to evaluate the effects of stiffener geometry

and skin elastic properties on strain distributions in the skin/stiffener interface region. They observed that a significant amount of bending of the stiffener attachment flange and adjacent skin occurred due to pillowing of the skin and that the transition from low to high strains occurred in a very narrow region. They also found that geometrically nonlinear effects were important at pressures as low as 0.1 atm. and concluded that the stress state in the region was truly three dimensional. Decreasing the ratio of the bending stiffness of the stiffener attachment flange to that of the panel skin resulted in attenuation of the stresses in this three dimensional stress state without significantly affecting the global panel response since stiffener web height affected this response to a much greater degree. They also found that the addition of a small amount of in-plane biaxial tension load to the panel resulted in attenuation of the strain gradients. Cohen and Hyer⁵³ undertook the difficult task of attempting to rigorously characterize the complex three-dimensional stress state in the corner region where the skin and stiffener meet. They discovered that a stress singularity existed in this region and quantified its severity by calculating a stress intensity factor. By tapering the flange to meet the skin, they found that the magnitude of the stress intensity factor could be substantially lowered.

Boitnott⁵⁴ studied, both theoretically and experimentally, the stress state at the meridional edges of a long cylindrical panel subject to internal pressure using varying degrees of fixity at these edges in order to approximate the skin of an aircraft fuselage adjacent to a stringer. He employed nonlinear DMV theory to characterize the high bending gradients generated by pillowing of the skin under pressure at a supported edge. The high bending gradients resulted in severe local stress gradients at the supported edge which Boitnott concluded could only be accurately quantified using a geometrically nonlinear analysis. Boitnott also demonstrated that changes in the lamina stacking sequence could strongly influence the character of these stress gradients. The results of his experiments showed that laminated panels tended to fail earlier than metal panels of the same thickness since local yielding of the metal provided a

measure of strain relief near the supported edge.

2.3 Design of Unstiffened and Stiffened Cylindrical Shells

Past work completed in the area of design of stiffened cylindrical shell structures included results generated by either systematically varying different design parameters or by applying the techniques of structural optimization. There has not been a large amount of research devoted to the design of unstiffened, isotropic, circular cylindrical shells since only a single design variable, the shell wall thickness, is typically involved. Hyman and Lucas⁵⁵ studied buckling load maximization for designs where the wall thickness could vary along the length of the cylinder. They showed that substantial increases in structural efficiency could be realized using this technique. Most of the research in the area of minimum weight design of isotropic cylindrical shell structures has been devoted to such structures stiffened by rings and/or stringers.

2.3.1 Stiffened Isotropic Cylindrical Shells

As the state-of-the art of analyzing stiffened cylindrical shells advanced in the early 1960's, interest began to shift toward exploiting this advancement in order to develop more efficient structural designs. Most of the results generated in this time period were in the form of parametric studies which appeared at the end of papers primarily devoted to analysis. For example, in their paper on the analysis of stiffened cylindrical shells subject to external pressure loads, Baruch and Singer⁴² showed that locating stringers on the external surface of the shell wall resulted in higher general buckling loads than if the stringers were located on the internal surface. Block, Card and Mikulus⁴³ showed that, for stiffened cylinders under axial compression, both external stringers and external rings resulted in the highest general buckling loads. Considering that both of these observations were based on analyses employing the smeared stiffener technique, they could have ramifications in the design of unstiffened laminated composite cylinders; for example, a smeared set of stringers might approximate a thick layer of zero degree plies. In 1966, Singer and Baruch⁵⁶ presented the results of a large number of trade studies. They showed that while external stringers resulted

in higher general buckling loads, they also made the structure more imperfection sensitive. Perhaps their most important observation was that given an optimally designed structure, weight savings for a given load were less substantial than gains in the size of the general buckling loads for a given weight. Burns⁵⁷, analyzing stiffened cylinders subject to axial compression using a classical buckling analysis and the smeared technique, showed that use of both stringers and rings resulted in more efficient designs than stringers alone and that small amounts of internal pressure resulted in substantially lighter weight designs. This weight savings was so substantial that he proposed development of a fail-safe mechanism for an aircraft's fuselage which prestresses the rings to maintain skin hoop tension in the event of sudden cabin depressurization.

In the late 1960's designs based on parametric studies, such as Burns's, began to give way to designs based on systematic synthesis. Credit for the first publication of this type is generally given to Kicher⁵⁸. Schmit, Morrow, and Kicher⁵⁹ extended Kicher's early work, using the interior penalty function SUMT to design stiffened cylinders subjected to axial compression and lateral pressure. They used seven design variables (such as skin thickness, stiffener segment thicknesses, an stiffener segment lengths) and considered eleven separate failure modes (including local, panel, and general buckling) using classical buckling analyses and the smeared technique for the panel and general buckling analyses and classical flat plate buckling analyses for the individual stiffener segments, assuming they were simply supported at their edges. They concluded that minimum weight designs possessed internal rings and internal stringers, that use of the interior penalty function was effective, that consideration of multiple load conditions was important, that minimum gage design constraints (usually based on manufacturing considerations) resulted in substantial weight penalties, and that relative minima existed in the design space.

Simites and Ungbhakorn⁶⁰ and Simites and Aswani⁶¹ developed optimum designs using an approach that was different than the approach of Schmit, Morrow, and Kicher. They performed the design algorithm in two steps, minimizing the total weight

of stiffened cylinders subject to a single general instability equality constraint in the first step, generating sets of design curves, then using these curves in the second step to determine a final design satisfying all other constraints. Results of these studies showed that the extensional stiffness of the rings tended to be more important than bending stiffness as a design parameter while the bending stiffness of the stringers tended to be more important than the stringer extensional stiffness, leading to an optimum design consisting of rings of rectangular cross section and stringers of T shaped cross section. The designs were not unique, in general, and alternative optima existed. Simites and Giri^{62,63} employed this two-step design method in designing stiffened cylinders subject to combined loads with torsion included for the first time. They were careful to impose an upper bound on the ring spacing in order to justify smearing the rings in the general buckling calculations. In some cases, this constraint resulted in a substantial weight penalty. Other results included the observation that the addition of torsion resulted in heavier ring designs and tighter ring spacings with no substantial effect on stringer designs, that relative and alternative minima existed in the design space, and that stiffening in both directions resulted in the most efficient structure. Simites and Sheinman⁶⁴ studied the imperfection sensitivity of optimum designs of perfect cylinders. They concluded that accounting for initial imperfections was essential to the development of reliable optimum designs.

A greater proportion of work in shell design is being devoted to development of methodologies that are more fully automated than those used by Simites and his colleagues. Bronwicky, et. al.⁶⁵ applied an extended interior SUMT and a first order method using finite difference gradients for performing the unconstrained minimization, to the problem of developing designs of ring-stiffened cylinders subject to hydrostatic pressure. They chose maximization of the separation of the two lowest vibration frequencies as the objective function and used the smeared technique in their analysis. They also imposed buckling constraints based on their nonlinear vibration analysis by requiring a positive lower bound on the fundamental frequency. In many cases the op-

timization failed to converge. Pappas^{66,67} observed that Bronwicky's gradient-based optimization algorithm failed to address the possible occurrence of mode switching.

Mode switching can occur when a move made to a new point in the design space, while increasing the separation of the frequencies corresponding to the first two modes of the original design, may in fact result in a decrease in the separation of the frequencies corresponding to the first and third modes. If the second mode frequency of one design iteration corresponds to the third mode frequency of the previous iteration, mode switching has occurred. A similar problem can arise when attempting to maximize the lowest frequency. Pappas proposed two possible solutions to this problem: either continue using the first order optimization algorithm with added constraints to enforce separation of the higher vibration modes, or proceed as before using an optimization algorithm that does not rely on derivative information to determine search directions in the design space. Pappas actually combined these two proposed solutions, relying on direct search until the algorithm failed to find better designs, then using the method of feasible directions, a first order method, to perform a local search in the neighborhood of the best design found by direct search accounting for all critical and *near* critical vibration modes in the constraint set. Pappas showed that his technique could find optimum designs in the cases where Bronwicky's algorithm failed.

Kunoo and Yang⁶⁸ based their study of stiffened cylinder optimization on a more robust analysis in which they modeled some of the stiffeners as discrete beam elements. Such an analysis, they pointed out, tended to generate large order algebraic eigenvalue problems which remained prohibitively expensive to solve within a design optimization algorithm even after application of an efficient solution scheme; hence, they chose to use the simple one-term solutions from classical buckling theory and the smeared technique during the progress of the design optimization, then employ a more refined analysis to check the optimum design. Pappas and Moradi⁶⁹ pointed out that Kunoo and Yang "oddly" neglected to mention any problems associated with closely spaced eigenvalues. Studying the design of ring-stiffened cylinders subject to

external pressure loads, they showed that the process tended to generate a large number of nearly simultaneous buckling modes. The significance of this observation was that it became necessary to examine a large number of buckling modes and establish constraints for all the ones that were critical and near critical to avoid violating one constraint while moving to simultaneously lighten the structure and avoid violating another constraint. In a more recent study of optimum designs of stiffened cylinders under axial compression, Qiu⁷⁰ used a procedure similar to that of Schmit, Morrow, and Kicher⁵⁹, but simulated a postbuckled cylinder skin in the general and panel buckling load calculations by using a reduced modulus of elasticity for the skin. Qiu concluded that allowance for a postbuckled skin had a dramatic affect on the optimum designs.

2.3.2 Unstiffened Anisotropic Cylindrical Shells

The freedom to choose a lamination scheme makes the design of unstiffened laminated cylinders much more interesting than the design of unstiffened isotropic cylinders. While studying the classical buckling response of three layer laminated cylindrical shells (ignoring any bending-twisting or extension-twisting coupling exhibited by the laminate) subject to axial compression and internal pressure, Tasi⁷¹ performed efficiency studies which showed that the most efficient laminates were unsymmetric, with the layers possessing the highest axial stiffness located nearest the outside surface of the shell. This is similar to the efficiency of stiffened metal cylinders with external stringers. Simitses, et. al.³⁷ drew similar conclusions. The late 1970's through the present day have seen a tremendous increase in the application of formal optimization techniques to the design of unstiffened laminated cylindrical shells. Hirano⁷² based his designs on classical buckling of simply supported cylinders under axial compression using $\pm\alpha$ type laminates (see section 2.2.2) ignoring, as Tasi did, the presence of any bending-twisting or extension-twisting coupling. Hirano posed the design problem as an unconstrained maximization of the buckling load and used Powell's method (a zero-order method) to perform the optimization. The existence of many relative minima in

the design space required restarts from several initial points to locate the global optimum. The complexity of the problem made it impossible to determine what was truly the best design.

Nshanian and Pappas⁷³ conducted a very thorough study of the optimum design of symmetrically laminated cylindrical shells subjected to axial compression and lateral pressure. Their goal was to find a through-the-thickness piecewise constant or piecewise linear distribution of lamina orientation angles that would maximize the classical buckling load and lowest frequency of natural vibration, using the feasible directions optimization algorithm. The results of the study, obtained with a large number of computer runs, indicated that mode coalescence occurred for both the buckling and the vibration problem. For the buckling case, optimum designs possessed as many as twenty different modes with associated critical loads within three percent of each other. In some cases, when the authors considered too few buckling modes, the optimization failed to converge. This again demonstrated the need for consideration of higher buckling modes in the design algorithm. The main conclusions of the study were that the increase in buckling loads associated with the use of optimization was substantial and that the piecewise linear distribution of orientation angles through-the-thickness produced designs with higher buckling loads overall than those designs produced using the piecewise constant distribution. Onoda⁷⁴ extended the work of Nshanian and Pappas, providing complete freedom in the selection of the ply angle distribution through the thickness. Using direct search, with lamination parameters as design variables instead of lamina fiber orientation angles, Onoda concluded that shear-extension coupling should be negligible for the optimal laminate configurations and that a large number of alternative optima exist corresponding to both symmetric and asymmetric laminates. One of these optima consisted of an infinite number of infinitely thin layers arranged so that the shell was quasi-isotropic in its surface and quasi-homogeneous through its thickness. Sun⁷⁵ applied a different approach to solve the same problem as Onoda and showed this new approach to be superior to the direct search technique employed

by Onoda. Using a technique similar to that employed by Pappas^{66,67} and described in section 2.3.1, he first performed a random search of the entire design space to get a good initial point for a systematic search for the optimum design. He then applied Powell's method to converge on the optimum. Using several different initial points for the systematic search, Sun found his method generated global optima that were practically reproducible. Most recently, Hu and Wang⁷⁶ demonstrated the feasibility of using a commercial finite element code and the sequential linear programming technique to determine optimum lamina fiber orientation angles and hole geometries in shells with cutouts which maximize the buckling load of the shell from a linear prebuckled state.

2.3.3 Stiffened Anisotropic Cylindrical Shells

Most of the work in the area of design of stiffened laminated composite structure has been devoted to the study of stiffened flat and cylindrical panels. As mentioned in Chapter 1, PANDA³ and PANDA2⁴ represent the state-of-the-art in such design problems. Much of the information gleaned from the study of the optimum design of stiffened metal cylinders is applicable to cylinders made of laminated composites as well; however, the additional number of design variables and constraints possible in a stiffened laminated cylinder could result in a problem that would approach the capacity of even some of today's most powerful computers. This is not to say that examples of such designs studies are absent from the literature. As early as 1969, Chao⁷⁷ developed a code to produce minimum weight designs of orthogonally stiffened laminated composite cylinders using an analysis and a SUMT optimization algorithm very similar to that of Schmit, Morrow, and Kicher⁵⁹. The code is quite general, admitting combined axial compression, pressure, and torsional loads and including many different failure modes; however, the author fails to address such issues as the effects of anisotropy, mode coalescence and closely spaced buckling eigenvalues in the optimum designs. Example cases presented in the document served more to demonstrate the capabilities of the code than to report design trends; however, Chao did elaborate on his

discovery of alternative optima in the design space. He showed that when alternative optima existed the ply angles resulting in minimum weight generally did not result in a maximum buckling load. He reasoned that since the total weight was not a function of the layer orientation angles, derivatives of the buckling constraints with respect to these angles should be weighted in order to drive the design to the alternative optima having the higher buckling loads. Chao implemented this in his code with some success.

Agarwal⁷⁸ studied the design of cylinders loaded in axial compression only. In addition to unstiffened laminated cylinders, Agarwal considered cylinders with hat-shaped longitudinal stiffeners and cylinders made of honeycomb sandwich construction. He considered all local stiffener buckling, panel buckling, general buckling and buckling of the shell skin bounded by the longitudinal and circumferential stiffeners, based on classical analyses, as constraints on the design along with a maximum strain constraint; however, his analysis ignored all but the orthotropic terms in the laminate constitutive relations. He employed a commercially available code based on a zero order method to perform the optimization. Aware of the limitations of his analysis, Agarwal checked his optimum designs using BOSOR4⁴⁶. For the ring and stringer configurations he found that the branched shell code calculated buckling loads thirty percent lower than his code's due to considerable distortion of the stringers in the prebuckled state (ring distortion was small). Modifying his code by reducing the torsional stiffness of the stringers solved the problem. In addition to this observation, Agarwal concluded that use of graphite-epoxy composite resulted in designs which were up to fifty percent lighter than comparable aluminum designs, that minimum gage constraints resulted in a substantial weight penalty, and that the honeycomb sandwich cylinder with graphite-epoxy face sheets was the lightest design.

Hansen and Tennyson⁷⁹ presented the results of a series of parametric design studies in which both the axial compression buckling load and imperfection sensitivity of laminated unstiffened and stiffened cylinders were evaluated both theoretically, using analyses similar to those presented by Tennyson, et. al.³⁴ and Booton³⁵, and experi-

mentally. Good correlation between theory and experiment was found in most cases. Their major conclusions were that it was possible to increase the critical buckling load of laminated composite cylinders very significantly through a judicious choice of laminate configuration and, in regards to the results of Card³³ and Tennyson³⁴ noting the increased imperfection sensitivity of optimum configurations, that it was indeed possible to create designs with increased buckling capability without paying too severe a penalty in increased imperfection sensitivity.

2.3.4 Shell Design Based On A Geometrically Nonlinear Analysis

All of the work in the field of optimum design of cylindrical shells subject to buckling constraints cited up to this point has been based on "classical" buckling analyses which are based on the assumption of a membrane prebuckled state of stress. For short cylinders, cylinders with shell wall laminates exhibiting bending-stretching coupling, cylinders loaded with normal pressure, or cylinders exhibiting any combination of these traits, this is a highly questionable practice. The degrading effects of initial geometric imperfections makes the assumption of a membrane prebuckled equilibrium state even more suspect. With access to greater computational power today, more researchers in the area of optimum shell design are basing their methods on analyses which include some degree of geometric nonlinearity in the prebuckled state. Narusberg, et. al.⁸⁰ used a geometrically nonlinear analysis to determine limit point loads in developing optimum designs of symmetrically laminated imperfect cylindrical shells subjected to external hydrostatic pressure loads. Specifying the fiber orientation angles of the various lamina from which the shell was to be constructed, they determined the distribution of lamina thicknesses that resulted in a minimum weight shell using the random search procedure. They also performed the optimization using a classical buckling analysis and compared the results to corresponding optimum designs developed using the nonlinear analysis. The results of this comparison were that the difference in optimum weight of the cylinders based on buckling loads calculated based on an as-

sumed membrane prebuckled state versus those based on limit point loads calculated using a geometrically nonlinear analysis was small (3%); however, the resulting optimum designs were very different. The designs based on the nonlinear analysis tended to exhibit more stable postbuckled paths in the postbuckled state. The work of Narusberg, et. al. was published in the Soviet literature. A good survey of East European literature devoted to optimal design of structures under stability constraints appears in Ref. 81.

Sun and Hansen⁸² based their design studies on the theoretical buckling analysis published by Booton³⁵. They performed an unconstrained maximization of the buckling load on cylinders of fixed weight having lamina fiber orientation angles as design variables. While the analysis could account for axisymmetric imperfections in the form of the classical axisymmetric buckling mode, Sun and Hansen did not include imperfections in the design process since a priori knowledge of a root-mean-squared imperfection amplitude was not available. However, they did calculate postbuckling coefficients in order to assess the imperfection sensitivity of the optimum designs. They employed the two step algorithm described by Sun⁷⁵ in the optimization, using hundreds of runs in the random search, and found that the optimum laminate designs were both unbalanced and unsymmetric. It appeared that such designs tended to exhibit the highest flexural rigidity along the axis of principle compression; however, the designs were suspect since they were based on the theoretical buckling analysis of a perfect cylinder. This suspicion led to a series of experiments on cylinders with measured imperfections that seemed to confirm the higher buckling loads of the optimized cylinders over baseline designs. With the measured imperfections included in the analysis, experimental/theoretical correlation was good, with the experimentally determined buckling loads being within 5 to 15% of the theoretical values depending on the imposed loading. Based on the postbuckling coefficient calculations, Sun and Hansen found that the optimization tended to result in significant changes in the imperfection sensitivity of the final designs with respect to the initial designs.

Very recently Ringertz⁸³ performed the structural optimization of isotropic stiffened shells based on a geometrically nonlinear finite element analysis using a SUMT. He presented two novel approaches to the problem. First, buckling constraints that do not rely on the solution of a nonlinear eigenvalue problem are imposed to insure that the Hessian of the strain energy remains positive definite. Second, instead of solving the nonlinear equilibrium equations directly, the displacements and rotations which describe the deformation are added to the set of design variables and the equilibrium equations are added as a set of equality constraints. Ringertz presents three example problems demonstrating the code's usefulness.

2.4 Summary

Based on a review of past work performed in the area of stiffened and unstiffened cylindrical shell analysis and design, the following observations can be made

1. DMV theory yields reliable estimates of the axisymmetric prebuckled response and buckling loads provided the degree of orthotropy of the layers of the shell laminate is not too severe and the shell is not too long (L/R less than 5) so that a large number (at least 5) of circumferential waves comprise the buckled mode shape. It will be assumed throughout this study that these conditions are satisfied to a reasonable degree. Any results generated that exhibit a substantial deviation from these conditions will be reported with the appropriate caveat.
2. A geometrically nonlinear analysis of the prebuckled shell, including the effects of initial geometric imperfections, is warranted.
3. Accurate mathematical models that account for cross sectional distortion of the stiffeners in the prebuckled equilibrium state should be employed, particularly when optimum design configurations are being sought.
4. Pillowing of the shell skin under pressure results in highly localized regions of high strains near the stiffeners. In-plane compressive loads may exacerbate this effect. Quantification of the stresses and strains in these regions is particularly important in the case of shells made of fiber composite materials due to the brittle nature and low transverse strength exhibited by these materials.
5. The optimal design problem is complicated by the presence of many relative and alternative optima in the design space as well as the occurrence of mode coalescence and mode switching during the design process.

Chapter 3

PROBLEM STATEMENT, ASSUMPTIONS AND GOVERNING EQUATIONS

3.1 Problem Statement

For the ring-stiffened cylinder of Fig. 1.1.1, the problem to be addressed in this study can be stated as follows:

Minimize: Total structural weight

Such that:

1. The buckling load of the structure is larger than the applied load.
2. Stresses remain below material allowable strengths.
3. Design variables remain within imposed limits.

The behavioral constraints (items 1 and 2) are evaluated using a structural analysis based on the following analytical model.

3.2 Analytical Model and Assumptions

The stiffened cylindrical shell of Fig. 1.1.1 is assumed to be clamped at both ends and loaded by an axisymmetric combination of axial compression, torsion, and pressure. In order to simplify the analysis, the behavioral constraints indicated in section 3.1 are evaluated based on analytical models developed under the assumption that all response quantities in the prebuckled equilibrium state are axisymmetric. This greatly simplifies the governing equations and makes the problem more tractable. The cylinder and ring attachment flanges are modeled as thin cylindrical shell segments constructed of layers of material laminated as shown in Fig. 3.2.1. Note that for purposes of calculating theoretical buckling loads of the ring-stiffened cylinder, the ring flange, adhesive bond and attached skin are treated as a single cylindrical shell segment. The ring webs are modeled as thin laminated annular plates, with free inboard edges, made of layers of material monoclinic with respect to the plane of the plate defined in a cylindrical coordinate system as shown in Fig. 3.2.2. Rings in the form of steps in thickness and

inverted T-shaped sections are considered. The cylindrical shell and annular plate segments are joined mathematically using conditions of compatibility of deformation and equilibrium at each junction where segments are connected. A typical cross-section of the ring-stiffened shell appears in Fig. 3.2.3.

Except at the point where the shell skin meets the edge of a ring flange, The mathematical model used in the calculation of the theoretical buckling load (referred to as the "global" model) can also be used to provide reasonable estimates of the stresses and strains in the various structural segments. Modeling the segment formed by the frame attachment flange and attached skin as a single shell segment, and forcing a jump discontinuity in shell material properties at the point where the skin and flange meet does not provide the free edge boundary condition which exists at the end of the ring attachment flange. While it will be assumed here that in-plane (tangential) stresses in the skin in this region can be adequately estimated using the global model, the through-the-thickness normal and transverse shearing stresses occurring there can only be reasonably estimated using a more refined local model. These normal and shear stresses are known to lead to strength failure in the flange/skin interface area. The approach taken here is to apply the stress resultants and stress couples in the skin and ring web from the global model, evaluated where they intersect the ring flange, to a more detailed model that approximates the ring flange / adhesive / attached skin combination as two concentric cylindrical shells connected by a set of equivalent normal and shear springs. This results in having to solve a system of differential equations to determine the response of the flange / skin segment that is more complex than the single differential equation governing the response of the flange/skin shell segment in the global model.

The governing equations are based on the kinematic assumptions of DMV theory for shells and von Kármán theory for plates. Justification for using these theories is provided in Chapter 2. It is tacitly assumed here that the conditions necessary for correct implementation of these theories in both the buckling analyses and the analysis of

the prebuckled equilibrium state do indeed exist. The main assumptions are:

1. Normals to the undeformed reference surface (skin middle surface) remain straight and normal to the deformed middle surface and are inextensional.
2. Transverse normal stress is small compared to other normal stress components and may be neglected in the constitutive equations.
3. The shell (plate) is thin so that the ratio of the shell (plate) thickness to radius is much smaller than 1 ($0 < h/R \ll 1$).
4. Strains are small (of the order ϵ where $0 < \epsilon \ll 1$). Displacements are also small but flexural rotations of shell (plate) elements are moderately large (large enough to warrant consideration of the out-of-plane projections of in-plane forces in the out-of-plane equilibrium of the element but still small enough to justify neglect of changes in geometry in the definition of stress components and in the limits of integration needed for work and energy considerations).
5. The shell exhibits quasi shallow behavior, a basic assumption of DMV theory.
6. Material behavior is linearly elastic.

One significant ramification of these assumptions is that the integrated constitutive equations for the cylindrical shell are of the same form as those for a flat plate.

3.3 Governing Equations

In order to present a single set of governing equations that can be specialized to either a cylindrical shell or an annular plate, equations governing the geometrically nonlinear response of the conical shell segment shown in Fig. 3.3.1 are considered. In Fig. 3.3.1, ξ_1 , ξ_2 and ξ_3 are the meridional (or axial in the case of a cylinder, radial in the case of an annular plate), circumferential and normal coordinates respectively, R is the radius to the origin of the coordinate system, ϕ is the cone angle (0° for the cylindrical shell, 90° for the annular plate), u_1 , u_2 and u_3 are displacements in the ξ_1 , ξ_2 and ξ_3 coordinate directions respectively and $(\vec{k}_1, \vec{k}_2, \vec{k}_3)$ are the unit basis vectors of an inertial coordinate system (z_1, z_2, z_3) . Note that ξ_2/R is the circumferential angle in shell of revolution coordinates. The origin of coordinates of the cylindrical shell is located at the middle surface of the shell. The origin of coordinates of the annular plate is located at the point where the extension of the midplane of the annular plate intersects the middle surface of the cylinder to which it is attached. The initial end of the segment is located at $\xi_1 = \xi_1^i$ and the final end is located at $\xi_1 = \xi_1^{i+1}$. An outline of the major steps involved in the derivation of the governing equations is provided below.

3.3.1 Strain-Displacement Equations

The development of the strain-displacement equations begins with the nonlinear strain tensor, \vec{E} , written in vector notation as

$$\vec{E} = \left(\frac{1}{2} \right) \left[\vec{\nabla} \vec{u} + (\vec{\nabla} \vec{u})^T + (\vec{\nabla} \vec{u})^T \bullet (\vec{\nabla} \vec{u}) \right] \quad (3.3.1.1)$$

where $\vec{\nabla} \vec{u}$ is the gradient of \vec{u} - the vector of displacements - and \vec{E} indicates that E is a second order tensor. Next, a set of local normalized orthogonal basis vectors, \vec{s}_1 , \vec{s}_2 , and \vec{s}_3 can be derived so that the displacement vector, \vec{u} , at any point (ξ_1, ξ_2, ξ_3) (see Fig. 3.3.1) can be written as

$$\vec{u} = u_1 \vec{s}_1(\xi_1, \xi_2, \xi_3) + u_2 \vec{s}_2(\xi_1, \xi_2, \xi_3) + u_3 \vec{s}_3(\xi_1, \xi_2, \xi_3). \quad (3.3.1.2)$$

where the components of \vec{s}_1 , \vec{s}_2 , and \vec{s}_3 are written in terms of the basis vectors, $(\vec{k}_1, \vec{k}_2, \vec{k}_3)$, of the inertial coordinate system, (z_1, z_2, z_3) .

With \vec{u} written as it is in Eq. (3.3.1.2), the principles of vector analysis can be used to derive the following expression for $\vec{\nabla}\vec{u}$.

$$\vec{\nabla}\vec{u} = \begin{bmatrix} \partial u_1/\partial \xi_1 & (R/r_o) \partial u_1/\partial \xi_2 + u_2 \sin \phi / r_o & \partial u_1/\partial \xi_3 \\ \partial u_2/\partial \xi_1 & (R/r_o) \partial u_2/\partial \xi_2 - (u_1 \sin \phi - u_3 \cos \phi) / r_o & \partial u_2/\partial \xi_3 \\ \partial u_3/\partial \xi_1 & (R/r_o) \partial u_3/\partial \xi_2 - u_2 \cos \phi / r_o & \partial u_3/\partial \xi_3 \end{bmatrix} \quad (3.3.1.3)$$

where

$$r_o = R - \xi_1 \sin \phi + \xi_3 \cos \phi \quad (3.3.1.4)$$

Substituting Eqs. (3.3.1.3) and (3.3.1.4) into Eq. (3.3.1.1), using the assumptions listed in section 3.2, and performing the indicated mathematical operations yields the desired set of strain-displacement equations below

$$\epsilon_{11} = \frac{\partial u_1^o}{\partial \xi_1} + \left(\frac{1}{2}\right) \left(\frac{\partial u_3^o}{\partial \xi_1}\right)^2 - \xi_3 \left(\frac{\partial^2 u_3^o}{\partial \xi_1^2}\right) = \epsilon_{11}^o + \xi_3 \kappa_{11} \quad (3.3.1.5)$$

$$\begin{aligned} 2\epsilon_{12} &= \frac{\partial u_2^o}{\partial \xi_1} + \frac{R}{r} \frac{\partial u_1^o}{\partial \xi_2} + \frac{u_2^o \sin \phi}{r} + \frac{R}{r} \frac{\partial u_3^o}{\partial \xi_1} \frac{\partial u_3^o}{\partial \xi_2} \\ &\quad - \xi_3 \left[\frac{2R}{r} \frac{\partial^2 u_3^o}{\partial \xi_1 \partial \xi_2} + \frac{2R \sin \phi}{r^2} \frac{\partial u_3^o}{\partial \xi_2} \right] \\ &= \gamma_{12}^o + \xi_3 \kappa_{12} \end{aligned} \quad (3.3.1.6)$$

$$\begin{aligned} \epsilon_{22} &= \frac{R}{r} \frac{\partial u_2^o}{\partial \xi_2} - \frac{u_1^o \sin \phi - u_3^o \cos \phi}{r} + \frac{1}{2} \left(\frac{R}{r} \frac{\partial u_3^o}{\partial \xi_2} \right)^2 \\ &\quad - \xi_3 \left[\left(\frac{R}{r} \right)^2 \frac{\partial^2 u_3^o}{\partial \xi_2^2} - \frac{\sin \phi}{r} \frac{\partial u_3^o}{\partial \xi_1} \right] \\ &= \epsilon_{22}^o + \xi_3 \kappa_{22} \end{aligned} \quad (3.3.1.7)$$

$$2\epsilon_{13} = 2\epsilon_{23} = \epsilon_{33} = 0 \quad (3.3.1.8)$$

where

$$r = R - \xi_1 \sin \phi, \quad (3.3.1.9)$$

the ϵ_{ij} are strains with respect to the $\xi_i \xi_j$ coordinate directions, the κ_{ij} are curvatures with respect to the $\xi_i \xi_j$ coordinate directions and the superscript ° indicates quantities evaluated at the reference surface of the shell.

3.3.2 Stress-Strain Equations

As was mentioned in section 3.2, a ramification of DMV shallow shell theory is that the integrated stress-strain equations for the shell have the same form as those for a flat laminated plate. A derivation of these equations, based on classical laminated plate theory (CLPT), is straightforward and can be found in the text by Jones⁸⁴. The required equations have the familiar form

$$\begin{Bmatrix} \{N\} \\ \{M\} \end{Bmatrix} = \begin{bmatrix} [A] & [B] \\ [B]^T & [D] \end{bmatrix} \begin{Bmatrix} \{\epsilon^\circ\} \\ \{\kappa\} \end{Bmatrix}. \quad (3.3.2.1)$$

where $\{\epsilon^\circ\}$ is the 3-by-1 vector of middle surface strains, $\{\kappa\}$ is the 3-by-1 vector of curvatures, and, given the 3-by-1 vector of stresses, $\{\sigma\}$,

$$\{N\} = \int_{-h/2}^{h/2} \{\sigma\} d\xi_3 \quad (3.3.2.2)$$

is the 3-by-1 vector of stress resultants,

$$\{M\} = \int_{-h/2}^{h/2} \{\sigma\} \xi_3 d\xi_3 \quad (3.3.2.3)$$

is the 3-by-1 vector of stress couples,

$$\{[A], [B], [D]\} = \sum_{i=1}^{N_{layer}} \int_{\xi_3^i}^{\xi_3^{i+1}} [\bar{Q}] \{1, \xi_3, \xi_3^2\} d\xi_3 \quad (3.3.2.4)$$

are the 3-by-3 membrane, membrane-bending coupling and bending stiffness matrices respectively, N_{layer} is the total number of laminae in the laminate, h is the total laminate thickness, ξ_3^i and ξ_3^{i+1} are the normal coordinates bounding the i^{th} lamina, and $[\bar{Q}]$ is the 3-by-3 transformed reduced stiffness matrix. Within each individual lamina, stresses and strains in the load-oriented or global coordinate system are related by

$$\{\sigma\} = [\bar{Q}] \{\epsilon\}. \quad (3.3.2.5)$$

It is sometimes useful to express Eq. (3.3.2.1) in its semi-inverted form

$$\begin{Bmatrix} \{\epsilon^o\} \\ \{M\} \end{Bmatrix} = \begin{bmatrix} [A^*] & [B^*] \\ [-B^*]^T & [D^*] \end{bmatrix} \begin{Bmatrix} \{N\} \\ \{\kappa\} \end{Bmatrix} \quad (3.3.2.6)$$

where

$$[A^*] = [A]^{-1} \quad (3.3.2.7)$$

$$[B^*] = [A]^{-1} [B] \quad (3.3.2.8)$$

$$[D^*] = [D] - [B]^T [A]^{-1} [B]. \quad (3.3.2.9)$$

3.3.3 Equilibrium Equations and Boundary Conditions

Equilibrium equations can be derived using the principle of virtual work. For a body of total volume V , this principle can be stated as

$$\int_V \sigma_{ij} \delta \epsilon_{ij} dV + \delta P = 0 \quad (3.3.3.1)$$

where σ_{ij} is the stress tensor, $\delta \epsilon_{ij}$ is the first variation of the strain tensor and δP is the virtual work of external forces. Substituting Eqs. (3.3.1.5) through (3.3.1.9) into Eq. (3.3.3.1), using the stress resultants and stress couples defined in Eqs. (3.3.2.2) and (3.3.2.3), performing an integration by parts, and recognizing the arbitrary nature of the first variation of the displacement vector results in the following set of equilibrium equations

$$\frac{\partial N_{11}}{\partial \xi_1} + \frac{R}{r} \frac{\partial N_{12}}{\partial \xi_2} - \frac{(N_{11} - N_{22}) \sin \phi}{r} = 0 \quad (3.3.3.2)$$

$$\frac{\partial N_{12}}{\partial \xi_1} + \frac{R}{r} \frac{\partial N_{22}}{\partial \xi_2} - \frac{2N_{12} \sin \phi}{r} = 0 \quad (3.3.3.3)$$

$$\begin{aligned} & N_{11} \left[\frac{-\sin \phi}{r} \frac{\partial u_3^o}{\partial \xi_1} + \frac{\partial^2 u_3^o}{\partial \xi_1^2} \right] + N_{22} \left[\frac{-\cos \phi}{r} + \left(\frac{R}{r} \right)^2 \frac{\partial^2 u_3^o}{\partial \xi_2^2} \right] + \\ & N_{12} \left[\frac{2R}{r} \frac{\partial^2 u_3^o}{\partial \xi_1 \partial \xi_2} \right] + \frac{\partial N_{11}}{\partial \xi_1} \frac{\partial u_3^o}{\partial \xi_1} + \frac{R}{r} \frac{\partial N_{12}}{\partial \xi_2} \frac{\partial u_3^o}{\partial \xi_1} + \frac{R}{r} \frac{\partial N_{12}}{\partial \xi_1} \frac{\partial u_3^o}{\partial \xi_2} + \\ & \left(\frac{R}{r} \right)^2 \frac{\partial N_{22}}{\partial \xi_2} \frac{\partial u_3^o}{\partial \xi_2} + \frac{\partial^2 M_{11}}{\partial \xi_1^2} + \frac{2R}{r} \frac{\partial^2 M_{12}}{\partial \xi_1 \partial \xi_2} - \frac{2 \sin \phi}{r} \frac{\partial M_{11}}{\partial \xi_1} + \\ & \frac{\sin \phi}{r} \frac{\partial M_{22}}{\partial \xi_1} + \left(\frac{R}{r} \right)^2 \frac{\partial^2 M_{22}}{\partial \xi_2^2} - \frac{2R \sin \phi}{r^2} \frac{\partial M_{12}}{\partial \xi_2} = -p. \end{aligned} \quad (3.3.3.4)$$

where

$$r = R - \xi_1 \sin \phi, \quad (3.3.3.5)$$

the N_{ij} are stress resultants with respect to the $\xi_i \xi_j$ coordinate directions, the M_{ij} are stress couples with respect to the $\xi_i \xi_j$ coordinate directions and p is an applied normal pressure.

The associated boundary conditions at $\xi_1 = \xi_1^i$ and $\xi_1 = \xi_1^{i+1}$ are

$$u_1^o = \text{specified} \quad \text{or} \quad N_{11} \left[1 - \left(\frac{\xi_1}{R} \right) \sin \phi \right] = \text{specified} \quad (3.3.3.6)$$

$$u_2^o = \text{specified} \quad \text{or} \quad N_{12} \left[1 - \left(\frac{\xi_1}{R} \right) \sin \phi \right] = \text{specified} \quad (3.3.3.7)$$

$$u_3^o = \text{specified} \quad \text{or} \quad V_{11} = \text{specified} \quad (3.3.3.8)$$

$$\frac{\partial u_3^o}{\partial \xi_1} = \text{specified} \quad \text{or} \quad -M_{11} \left[1 - \left(\frac{\xi_1}{R} \right) \sin \phi \right] = \text{specified} \quad (3.3.3.9)$$

where

$$\begin{aligned} V_{11} \equiv & \frac{\partial M_{11}}{\partial \xi_1} \left[1 - \left(\frac{\xi_1}{R} \right) \sin \phi \right] + 2 \frac{\partial M_{12}}{\partial \xi_2} + N_{11} \left[1 - \left(\frac{\xi_1}{R} \right) \sin \phi \right] \frac{\partial u_3^o}{\partial \xi_1} \\ & + N_{12} \frac{\partial u_3^o}{\partial \xi_2} + \frac{(M_{22} - M_{11}) \sin \phi}{R} \end{aligned} \quad (3.3.3.10)$$

is the Kirchhoff shear stress resultant.

3.3.4 Compatibility Equations

Use of a pure stress or mixed stress/displacement formulation of the problem requires additional equations to insure that the resulting displacement vector is single valued and continuous. These are referred to as compatibility equations. A thorough derivation of these equations for the geometrically linear case with respect to a rectangular cartesian coordinate system can be found in the text by Frederick and Chang⁸⁵. For the more general case of a geometrically nonlinear problem specified in terms of a curvilinear coordinate system, the derivation of the compatibility equations follows the same steps as does the derivation found in Frederick and Chang with the following modifications. The index notation used by the authors, valid only for the rectangular cartesian coordinate system, must be replaced by vector (or Gibb's) notation - a more general notation which is not dependent on the coordinate system being used. Derivation of the compatibility equations then begins with the expression for the relative displacement vector of two neighboring points, say P and Q ,

$$d\vec{u} = \vec{\nabla}\vec{u} \bullet d\vec{r} \quad (3.3.4.1)$$

where $\vec{\nabla}\vec{u}$ is the gradient of the displacement vector (a second order tensor) and $d\vec{r}$ is the relative position vector connecting points P and Q and \bullet indicates an inner (or dot) product. It is understood that $\vec{\nabla}\vec{u}$ is evaluated at point P . It can be shown that Eq.

(3.3.4.1) can be written as

$$d\vec{u} = (\vec{E} + \vec{W}) \bullet d\vec{r} \quad (3.3.4.2)$$

where \vec{E} is the nonlinear strain tensor given in Eq. (3.3.1.1) and

$$\vec{W} = \left(\frac{1}{2}\right) \left[\vec{\nabla}\vec{u} - (\vec{\nabla}\vec{u})^T - (\vec{\nabla}\vec{u})^T \bullet (\vec{\nabla}\vec{u}) \right] \quad (3.3.4.3)$$

is the nonlinear rotation tensor. Once the proper form of $\vec{\nabla}$ is determined based on the particular coordinate system being used and the techniques of tensor analysis are

applied, derivation of the compatibility equations follows precisely the same steps outlined in detail on pages 100 - 102 of the text by Frederick and Chang. Of the six resulting compatibility equations, upon imposition of the assumptions listed in section 3.2, only one equation remains that is not automatically satisfied. This equation, listed below, is the final equation needed for a complete description of the problem.

$$\begin{aligned}
& - \left(\frac{R}{r} \right)^2 \frac{\partial^2 \epsilon_{11}^o}{\partial \xi_2^2} - \left(\frac{\sin \phi}{r} \right) \frac{\partial \epsilon_{11}^o}{\partial \xi_1} + \left(\frac{2 \sin \phi}{r} \right) \frac{\partial \epsilon_{22}^o}{\partial \xi_1} - \\
& \frac{\partial^2 \epsilon_{22}^o}{\partial \xi_1^2} + \left(\frac{R}{r} \right) \frac{\partial^2 (2\epsilon_{12}^o)}{\partial \xi_1 \partial \xi_2} - \left(\frac{R \sin \phi}{r^2} \right) \frac{\partial (2\epsilon_{12}^o)}{\partial \xi_2} \\
& = \\
& \left(\frac{-\cos \phi}{r} \right) \frac{\partial^2 u_3^o}{\partial \xi_1^2} - \left[\left(\frac{R}{r} \right) \frac{\partial^2 u_3^o}{\partial \xi_1 \partial \xi_2} \right]^2 - \left(\frac{\sin \phi}{r} \right) \frac{\partial u_3^o}{\partial \xi_1} \frac{\partial^2 u_3^o}{\partial \xi_1^2} - \\
& \left(\frac{2 R^2 \sin \phi}{r^3} \right) \frac{\partial u_3^o}{\partial \xi_2} \frac{\partial^2 u_3^o}{\partial \xi_1 \partial \xi_2} - \left(\frac{R^2 \sin^2 \phi}{r^4} \right) \left(\frac{\partial u_3^o}{\partial \xi_2} \right)^2 + \\
& \left(\frac{R}{r} \right)^2 \frac{\partial^2 u_3^o}{\partial \xi_1^2} \frac{\partial^2 u_3^o}{\partial \xi_2^2} \tag{3.3.4.4}
\end{aligned}$$

where

$$r = R - \xi_1 \sin \phi, \tag{3.3.4.5}$$

the ϵ_{ij}^o are middle surface strains with respect to the $\xi_i \xi_j$ coordinate directions and u_3^o is the middle surface displacement in the ξ_3 coordinate direction

Chapter 4
STRUCTURAL ANALYSIS OF THE AXISYMMETRIC
PREBUCKLED EQUILIBRIUM STATE

4.1 Solution To The Equations Governing The Geometrically Nonlinear
Axisymmetric Response Of Cylindrical Shell Segments

The equations governing the response of the prebuckled cylinder can be derived by setting the cone angle, ϕ (see Fig. 3.3.1), to zero and imposing the assumption of an axisymmetric response ($\partial () / \partial \xi_2 = 0$) in Eqs. (3.3.3.2), (3.3.3.3), and (3.3.3.4). The governing equations, in nondimensional form, are

$$\frac{d\bar{N}_X}{dX} = 0 \quad (4.1.1)$$

$$\frac{d\bar{N}_{XY}}{dX} = 0 \quad (4.1.2)$$

$$\frac{d^2\bar{M}_X}{dX^2} - \bar{Z}\bar{N}_Y + \bar{N}_X \frac{d^2\bar{w}^o}{dX^2} + \bar{Z}\bar{p} = 0 \quad (4.1.3)$$

where the following change of variables has been made in order to match the notation used by Tennyson, et. al.³⁴, Booton³⁵ and Sun and Hansen⁸²:

$$X = \bar{\xi}_1 \quad (4.1.4)$$

$$\bar{w}^o = \bar{u}_3^o \quad (4.1.5)$$

$$\bar{N}_X = \bar{N}_{11} \quad (4.1.6)$$

$$\bar{N}_Y = \bar{N}_{22} \quad (4.1.7)$$

$$\bar{N}_{XY} = \bar{N}_{12} \quad (4.1.8)$$

$$\bar{M}_X = \bar{M}_{11} \quad (4.1.9)$$

$$\bar{M}_Y = \bar{M}_{22} \quad (4.1.10)$$

$$\overline{M}_{XY} = \overline{M}_{12}. \quad (4.1.11)$$

The \overline{N}_{ij} are nondimensional stress resultants and the \overline{M}_{ij} are nondimensional stress couples with respect to the $\xi_i \xi_j$ coordinate directions, and $\overline{Z} = L^2/(Rt_s)$ where L is the length of the cylinder, R is the radius to the middle surface of the cylinder wall and t_s is the total thickness of the cylinder. The nondimensional quantities, indicated by $\overline{(\quad)}$, are defined in Table 1. If the wall of the cylindrical shell contains a small axisymmetric imperfection in the form of a stress-free radial displacement, w_o , then Eq. (4.1.3) becomes

$$\frac{d^2 \overline{M}_X}{dX^2} - \overline{Z} \overline{N}_Y + \overline{N}_X \left(\frac{d^2 \overline{w}^o}{dX^2} + \frac{d^2 \overline{w}_o}{dX^2} \right) + \overline{Z} \overline{p} = 0 \quad (4.1.12)$$

where \overline{w}_o is the nondimensional form of w_o defined in Table 1. The associated boundary conditions at the ends of the cylindrical shell segment ($X = \overline{\xi}_1^i$ and $X = \overline{\xi}_1^{i+1}$) from Eqs. (3.3.3.6) through (3.3.3.10), in nondimensional form, are

$$\overline{N}_X = \text{specified} \quad \text{or} \quad \overline{u}_1^o = \text{specified} \quad (4.1.13)$$

$$\overline{N}_{XY} = \text{specified} \quad \text{or} \quad \overline{u}_2^o = \text{specified} \quad (4.1.14)$$

$$\overline{V}_X = \text{specified} \quad \text{or} \quad \overline{w}^o = \text{specified} \quad (4.1.15)$$

$$\overline{M}_X = \text{specified} \quad \text{or} \quad \frac{d\overline{w}^o}{dX} = \text{specified} \quad (4.1.16)$$

where

$$\overline{V}_X \equiv \frac{d\overline{M}_X}{dX} + \overline{N}_X \left(\frac{d\overline{w}^o}{dX} + \frac{d\overline{w}_o}{dX} \right). \quad (4.1.17)$$

From section 3.3.2, using Eqs. (4.1.4) through (4.1.11), the semi-inverted form of the nondimensional constitutive equations for the laminated cylindrical shell wall are

$$\begin{Bmatrix} \overline{\epsilon}_{11}^o \\ \overline{\epsilon}_{22}^o \\ \overline{\gamma}_{12}^o \\ \overline{M}_X \\ \overline{M}_Y \\ \overline{M}_{XY} \end{Bmatrix} = \begin{bmatrix} \overline{A}_{11}^* & \overline{A}_{12}^* & \overline{A}_{16}^* & \overline{B}_{11}^* & \overline{B}_{12}^* & \overline{B}_{16}^* \\ \overline{A}_{12}^* & \overline{A}_{22}^* & \overline{A}_{26}^* & \overline{B}_{21}^* & \overline{B}_{22}^* & \overline{B}_{26}^* \\ \overline{A}_{16}^* & \overline{A}_{26}^* & \overline{A}_{66}^* & \overline{B}_{61}^* & \overline{B}_{62}^* & \overline{B}_{66}^* \\ -\overline{B}_{11}^* & -\overline{B}_{21}^* & -\overline{B}_{61}^* & \overline{D}_{11}^* & \overline{D}_{12}^* & \overline{D}_{16}^* \\ -\overline{B}_{12}^* & -\overline{B}_{22}^* & -\overline{B}_{62}^* & \overline{D}_{12}^* & \overline{D}_{22}^* & \overline{D}_{26}^* \\ -\overline{B}_{16}^* & -\overline{B}_{26}^* & -\overline{B}_{66}^* & \overline{D}_{16}^* & \overline{D}_{26}^* & \overline{D}_{66}^* \end{bmatrix} \begin{Bmatrix} \overline{N}_X \\ \overline{N}_Y \\ \overline{N}_{XY} \\ \overline{\kappa}_{11} \\ 0 \\ 0 \end{Bmatrix} \quad (4.1.18)$$

where

$$\bar{\kappa}_{11} = -\frac{d^2 \bar{w}^o}{dX^2}. \quad (4.1.19)$$

Eqs. (4.1.1) and (4.1.2) can be solved immediately yielding constant \bar{N}_X and \bar{N}_{XY} throughout the shell that are equal to the corresponding applied loads. The axisymmetric, nondimensional form of Eq. (3.3.1.7), the strain-displacement equation for ϵ_{22} , is

$$\bar{\epsilon}^o_{22} = \bar{Z} \bar{w}^o. \quad (4.1.20)$$

Equating the right hand side of Eq. (4.1.20) to the right hand side of the expression for $\bar{\epsilon}^o_{22}$ in Eq. (4.1.18) and solving for \bar{N}_Y yields

$$\bar{N}_Y(X) = b_1 + b_2 \bar{w}^o(X) + b_3 \frac{d^2 \bar{w}^o}{dX^2}(X) \quad (4.1.21)$$

where

$$b_1 = -\left(\frac{\bar{A}_{12}^*}{\bar{A}_{22}^*}\right) \bar{N}_X - \left(\frac{\bar{A}_{26}^*}{\bar{A}_{22}^*}\right) \bar{N}_{XY} \quad (4.1.22)$$

$$b_2 = \left(\frac{\bar{Z}}{\bar{A}_{22}^*}\right) \quad (4.1.23)$$

$$b_3 = \left(\frac{\bar{B}_{21}^*}{\bar{A}_{22}^*}\right). \quad (4.1.24)$$

Since \bar{N}_X and \bar{N}_{XY} are constants, Eq. (4.1.12) is a linear ordinary differential equation in $\bar{w}^o(X)$. The functional form of the initial imperfection \bar{w}_o used in this study is that of the axisymmetric buckled mode shape of an infinitely long anisotropic cylinder subject to axial compression derived by Tennyson, Chan, and Muggeridge³⁴ and used by Booton³⁵ and Sun and Hansen⁸². The form of this mode shape is

$$\bar{w}_o(X) = -\mu \cos \omega X \quad (4.1.25)$$

where

$$\omega = \sqrt{\frac{\bar{Z}}{\bar{A}_{22}^*}}. \quad (4.1.26)$$

If R represents the mean radius to the middle surface of the imperfect cylindrical shell wall, then μ is the root-mean-square of deviations from this mean radius. Substituting Eqs. (4.1.18), (4.1.19), and (4.1.21) through (4.1.26) into Eq. (4.1.12) yields

$$a_1 \frac{d^4 \bar{w}^o}{dX^4} + a_2 \frac{d^2 \bar{w}^o}{dX^2} + a_3 \bar{w}^o = g_1 + \bar{N}_X (\mu \omega^2 \cos \omega X) \quad (4.1.27)$$

where

$$a_1 = \frac{\bar{B}_{21}^2}{\bar{A}_{22}} + \bar{D}_{11} \quad (4.1.28)$$

$$a_2 = 2 \frac{\bar{Z} \bar{B}_{21}}{\bar{A}_{22}} - \bar{N}_X \quad (4.1.29)$$

$$a_3 = \frac{\bar{Z}^2}{\bar{A}_{22}} \quad (4.1.30)$$

$$g_1 = \bar{Z} \left(\bar{p} + \frac{\bar{A}_{12} \bar{N}_X}{\bar{A}_{22}} + \frac{\bar{A}_{26} \bar{N}_{XY}}{\bar{A}_{22}} \right). \quad (4.1.31)$$

Eq. (4.1.27) is a fourth order nonhomogeneous ordinary differential equation with constant coefficients for \bar{w}^o , the normalized radial displacement of the prebuckled cylindrical shell. The particular solution, $\bar{w}_P^o(X)$, is

$$\bar{w}_P^o(X) = \frac{\mu \omega^2 \bar{N}_X}{a_1 \omega^4 - a_2 \omega^2 + a_3} \cos \omega X + \frac{g_1}{a_3}. \quad (4.1.32)$$

The homogeneous solution, $\bar{w}_H^o(X)$, is of the form

$$\bar{w}_H^o(X) = \sum_{j=1}^4 B_j e^{\bar{\lambda}_j X} \quad (4.1.33)$$

where the B_j are constants of integration to be evaluated using the boundary conditions and the $\bar{\lambda}_j$ are the roots of the associated characteristic equation

$$a_1 \bar{\lambda}^4 + a_2 \bar{\lambda}^2 + a_3 = 0. \quad (4.1.34)$$

These roots are

$$\bar{\lambda}_j = \pm \lambda_1 \pm i \lambda_2 \quad (4.1.35)$$

where

$$\lambda_1 = \frac{1}{2} \sqrt{2 \sqrt{\frac{a_3}{a_1}} - \frac{a_2}{a_1}}, \quad (4.1.36)$$

$$\lambda_2 = \frac{1}{2} \sqrt{2 \sqrt{\frac{a_3}{a_1}} + \frac{a_2}{a_1}} \quad (4.1.37)$$

and $i = \sqrt{-1}$. For the case where \overline{N}_X is negative (compressive), Booton³⁵ has shown that if \overline{N}_X is less than the classical axisymmetric buckling (or collapse) load of the shell (the only case to be considered in this study) then

$$\begin{aligned} \overline{w}_H^o(X) = & B_1 e^{\lambda_1 X} \sin(\lambda_2 X) + B_2 e^{-\lambda_1 X} \cos(\lambda_2 X) \\ & + B_3 e^{\lambda_1 X} \cos(\lambda_2 X) + B_4 e^{-\lambda_1 X} \sin(\lambda_2 X) \end{aligned} \quad (4.1.38)$$

The total solution, $\overline{w}^o(X)$, is

$$\overline{w}^o(X) = \overline{w}_H^o(X) + \overline{w}_P^o(X). \quad (4.1.39)$$

4.2 Solution To Equations Governing The Geometrically Linear Axisymmetric Response Of Annular Plate Segments

The equations governing the geometrically nonlinear axisymmetric response of the prebuckled annular plate can be derived by setting the cone angle (ϕ) to ninety degrees and imposing the assumption of an axisymmetric response ($\partial () / \partial \xi_2 = 0$) in Eqs. (3.3.3.2) through (3.3.3.10). The normal pressure, p , is assumed to be zero and the radius, R , is to the origin of the (ξ_1, ξ_2, ξ_3) coordinate system which is located at the middle surface of the cylinder to which the annular plate is attached and not at the outboard edge of the plate. Unfortunately, this does not lead to a set of linear equations which can be solved exactly as it does in the case of the cylindrical shell. To avoid the numerical/iterative analysis necessary to predict the geometrically nonlinear response, it will be assumed that the response can be estimated reasonably accurately using a geometrically linear analysis. Ignoring prebuckling nonlinearities might be acceptable for the ring webs since it is likely that the combination of the radial membrane resultant in the annular plate and flexural rotations, which form the dominant nonlinear terms, would be small considering that the inboard edge of the annular plate is free and that the axial compression and torsional loadings in the shell act normal to the outboard edge of the annular plate. Dropping the nonlinear terms from the axisymmetric form of Eqs. (3.3.3.2) through (3.3.3.4) and nondimensionalizing the result (see Table 1) yields the desired equations shown below.

$$\frac{d\bar{N}_{11}}{d\bar{\xi}_1} - \left(\frac{L}{R}\right) \frac{\bar{N}_{11} - \bar{N}_{22}}{\bar{r}} = 0 \quad (4.2.1)$$

$$\frac{d\bar{N}_{12}}{d\bar{\xi}_1} - \left(\frac{L}{R}\right) \frac{2\bar{N}_{12}}{\bar{r}} = 0 \quad (4.2.2)$$

$$\frac{d^2\bar{M}_{11}}{d\bar{\xi}_1^2} - \frac{2(L/R)}{\bar{r}} \frac{d\bar{M}_{11}}{d\bar{\xi}_1} + \frac{(L/R)}{\bar{r}} \frac{d\bar{M}_{22}}{d\bar{\xi}_1} = 0. \quad (4.2.3)$$

where

$$\bar{r} = \left[1 - \left(\frac{L}{R}\right) \bar{\xi}_1 \right], \quad (4.2.4)$$

L is the length of the cylindrical shell to which the annular plate is attached and \bar{N}_{ij} and \bar{M}_{ij} are nondimensional stress resultants and stress couples, respectively, with respect to the $\xi_i \xi_j$ coordinate directions. The associated boundary conditions at $\bar{\xi}_1 = \xi_1^i/L$ and $\bar{\xi}_1 = \xi_1^{i+1}/L$ (see Fig. 3.3.1) from the geometrically linear, axisymmetric, nondimensional form of Eqs. (3.3.3.6) through (3.3.3.10) are

$$\bar{N}_{11}\bar{r} = \text{specified} \quad \text{or} \quad \bar{u}_1^o = \text{specified} \quad (4.2.5)$$

$$\bar{N}_{12}\bar{r} = \text{specified} \quad \text{or} \quad \bar{u}_2^o = \text{specified} \quad (4.2.6)$$

$$\bar{V}_{11}\bar{r} = \text{specified} \quad \text{or} \quad \bar{u}_3^o = \text{specified} \quad (4.2.7)$$

$$\bar{M}_{11}\bar{r} = \text{specified} \quad \text{or} \quad \frac{d\bar{u}_3^o}{d\bar{\xi}_1} = \text{specified} \quad (4.2.8)$$

where \bar{u}_i^o is a nondimensional midplane displacement in the ξ_i coordinate direction, \bar{r} is defined in Eq. (4.2.4) and

$$\bar{V}_{11} \equiv \frac{d\bar{M}_{11}}{d\bar{\xi}_1} + \left(\frac{L}{R}\right) \frac{\bar{M}_{22} - \bar{M}_{11}}{\bar{r}}. \quad (4.2.9)$$

is the nondimensional Kirchhoff shear stress resultant. The equation governing in-plane strain compatibility, from the geometrically linear, axisymmetric, nondimensional form of Eq. (3.3.4.4), is

$$-\frac{(L/R)}{\bar{r}} \frac{d\bar{\epsilon}_{11}^o}{d\bar{\xi}_1} + \frac{2(L/R)}{\bar{r}} \frac{d\bar{\epsilon}_{22}^o}{d\bar{\xi}_1} - \frac{d^2\bar{\epsilon}_{22}^o}{d\bar{\xi}_1^2} = 0. \quad (4.2.10)$$

where the $\bar{\epsilon}_{ij}^o$ are nondimensional midplane strains with respect to the ij coordinate directions and \bar{r} is defined in Eq. (4.2.4).

Solutions to the equations governing the axisymmetric response of annular plates made of polar orthotropic material (e.g. a fiber composite laminate with fibers running radially and circumferentially) have been published by Lekhnitskii⁸⁶ and Bryant⁸⁷. Padovan⁸⁸ presented solutions to the linear equations governing the bending of such plates subject to generally asymmetric loads; however, it can be shown that the axisymmetric problem admits exact solutions regardless of the stacking sequence of the plate. This can be shown as follows.

The semi-inverted form of the laminate constitutive equations for the annular plate are presented in section 3.3.2. Referring to Table 1, the constitutive equations in nondimensional form are

$$\begin{Bmatrix} \bar{\epsilon}_{11}^o \\ \bar{\epsilon}_{22}^o \\ \bar{\gamma}_{12}^o \\ \bar{M}_{11} \\ \bar{M}_{22} \\ \bar{M}_{12} \end{Bmatrix} = \begin{bmatrix} \bar{A}_{11} & \bar{A}_{12} & \bar{A}_{16} & \bar{B}_{11} & \bar{B}_{12} & \bar{B}_{16} \\ \bar{A}_{12} & \bar{A}_{22} & \bar{A}_{26} & \bar{B}_{21} & \bar{B}_{22} & \bar{B}_{26} \\ \bar{A}_{16} & \bar{A}_{26} & \bar{A}_{66} & \bar{B}_{61} & \bar{B}_{62} & \bar{B}_{66} \\ -\bar{B}_{11} & -\bar{B}_{21} & -\bar{B}_{61} & \bar{D}_{11} & \bar{D}_{12} & \bar{D}_{16} \\ -\bar{B}_{12} & -\bar{B}_{22} & -\bar{B}_{62} & \bar{D}_{12} & \bar{D}_{22} & \bar{D}_{26} \\ -\bar{B}_{16} & -\bar{B}_{26} & -\bar{B}_{66} & \bar{D}_{16} & \bar{D}_{26} & \bar{D}_{66} \end{bmatrix} \begin{Bmatrix} \bar{N}_{11} \\ \bar{N}_{22} \\ \bar{N}_{12} \\ \bar{\kappa}_{11} \\ \bar{\kappa}_{22} \\ 0 \end{Bmatrix} \quad (4.2.11)$$

where, from the axisymmetric, nondimensional form of Eqs. (3.3.1.5) and (3.3.1.7)

$$\bar{\kappa}_{11} = -\frac{d^2 \bar{u}_3^o}{d\bar{\xi}_1^2} \quad (4.2.12)$$

$$\bar{\kappa}_{22} = -\frac{(L/R)}{\bar{r}} \frac{d\bar{u}_3^o}{d\bar{\xi}_1}. \quad (4.2.13)$$

It can be shown by direct substitution that the solution to Eq. (4.2.2) is

$$\bar{N}_{12} = \frac{A}{\bar{r}^2} \quad (4.2.14)$$

where A is a constant of integration which depends on the imposed boundary conditions. The annular plates considered in this study are assumed to have traction-free inboard edges; hence, at this edge

$$\bar{N}_{12} = 0. \quad (4.2.15)$$

Therefore,

$$A = 0, \quad \text{and thus} \quad (4.2.16)$$

$$\bar{N}_{12}(\bar{\xi}_1) = 0. \quad (4.2.17)$$

Rewriting Eq. (4.2.3), the out-of-plane equilibrium equation, can be written as

$$\frac{d^2 (\bar{r} \bar{M}_{11})}{d\bar{r}^2} - \frac{d\bar{M}_{22}}{d\bar{r}} = 0. \quad (4.2.18)$$

where

$$-\left(\frac{L}{R}\right) \frac{d(\cdot)}{d\bar{r}} = \frac{d(\cdot)}{d\xi_1} \quad (4.2.19)$$

This equation can be integrated once to yield

$$\frac{d(\bar{r}\bar{M}_{11})}{d\bar{r}} - \bar{M}_{22} = \bar{r} \frac{d\bar{M}_{11}}{d\xi_1} + \left(\frac{L}{R}\right) (\bar{M}_{22} - \bar{M}_{11}) = \bar{V}_{11}\bar{r} = c_1 \quad (4.2.20)$$

where c_1 is a constant. Since the inboard edge of the annular plate is assumed to be traction-free, $\bar{V}_{11}\bar{r} = 0$ at this edge. Thus $c_1 = 0$ and

$$\frac{d(\bar{r}\bar{M}_{11})}{d\bar{r}} - \bar{M}_{22} = 0. \quad (4.2.21)$$

Using Eq. (4.2.19), Eq. (4.2.1) becomes

$$\frac{d\bar{N}_{11}}{d\bar{r}} - \frac{(\bar{N}_{11} - \bar{N}_{22})}{\bar{r}} = 0. \quad (4.2.22)$$

Eq. (4.2.22) is satisfied exactly by the stress function $\chi(\bar{r})$ defined such that

$$\bar{N}_{11} = \frac{\chi}{\bar{r}} \quad (4.2.23)$$

$$\bar{N}_{22} = \frac{d\chi}{d\bar{r}}. \quad (4.2.24)$$

Use of the stress function χ requires satisfaction of the in-plane strain compatibility equation - Eq. (4.2.10). Using Eq. (4.2.19) and integrating once with respect to \bar{r} , this equation becomes

$$(\bar{\epsilon}^o_{11} - \bar{\epsilon}^o_{22}) - \bar{r} \frac{d\bar{\epsilon}^o_{22}}{d\bar{r}} = c_2 \quad (4.2.25)$$

where c_2 is a constant allowing for a uniform prestraining of the structure. Ignoring any such prestraining results in $c_2 = 0$ and

$$(\bar{\epsilon}^o_{11} - \bar{\epsilon}^o_{22}) - \bar{r} \frac{d\bar{\epsilon}^o_{22}}{d\bar{r}} = 0. \quad (4.2.26)$$

Eqs. (4.2.21) and (4.2.26) can be solved using Eqs. (4.2.11) through (4.2.13). First, applying Eq. (4.2.19) to Eqs. (4.2.12) and (4.2.13) gives

$$\bar{\kappa}_{11} = -\left(\frac{L}{R}\right)^2 \frac{d\Omega}{d\bar{r}} \quad (4.2.27)$$

$$\bar{\kappa}_{22} = - \left(\frac{L}{R} \right)^2 \frac{\Omega}{\bar{r}} \quad (4.2.28)$$

where

$$\Omega = \frac{d\bar{u}_3^o}{d\bar{r}}. \quad (4.2.29)$$

Substituting Eqs. (4.2.23), (4.2.24) and (4.2.27) through (4.2.29) into Eqs. (4.2.11) then substituting Eqs. (4.2.11) into Eqs. (4.2.21) and (4.2.26) and collecting terms results in the governing equations for the midplane flexural rotation Ω and the stress function χ of the annular plate

$$\gamma_1 \frac{d^2 \Omega}{d\bar{r}^2} + \frac{\gamma_2}{\bar{r}} \frac{d\Omega}{d\bar{r}} - \frac{\gamma_3}{\bar{r}^2} \Omega - \gamma_4 \frac{d^2 \chi}{d\bar{r}^2} - \frac{\gamma_4}{\bar{r}} \frac{d\chi}{d\bar{r}} + \frac{\gamma_5}{\bar{r}^2} \chi = 0. \quad (4.2.30)$$

$$\gamma_6 \frac{d^2 \Omega}{d\bar{r}^2} + \frac{\gamma_6}{\bar{r}} \frac{d\Omega}{d\bar{r}} - \frac{\gamma_7}{\bar{r}^2} \Omega + \gamma_8 \frac{d^2 \chi}{d\bar{r}^2} + \frac{\gamma_9}{\bar{r}} \frac{d\chi}{d\bar{r}} - \frac{\gamma_{10}}{\bar{r}^2} \chi = 0. \quad (4.2.31)$$

where

$$\gamma_1 = \bar{B}_{21}^* \left(\frac{L}{R} \right)^2 \quad (4.2.32)$$

$$\gamma_2 = (\bar{B}_{22}^* + \bar{B}_{21}^* - \bar{B}_{11}^*) \left(\frac{L}{R} \right)^2 \quad (4.2.33)$$

$$\gamma_3 = \bar{B}_{12}^* \left(\frac{L}{R} \right)^2 \quad (4.2.34)$$

$$\gamma_4 = \bar{A}_{22}^* \quad (4.2.35)$$

$$\gamma_5 = \bar{A}_{11}^* \quad (4.2.36)$$

$$\gamma_6 = \bar{D}_{11}^* \left(\frac{L}{R} \right)^2 \quad (4.2.37)$$

$$\gamma_7 = \bar{D}_{22}^* \left(\frac{L}{R} \right)^2 \quad (4.2.38)$$

$$\gamma_8 = \bar{B}_{21}^* \quad (4.2.39)$$

$$\gamma_9 = (\bar{B}_{11}^* + \bar{B}_{21}^* - \bar{B}_{22}^*) \quad (4.2.40)$$

$$\gamma_{10} = \bar{B}_{12}^*. \quad (4.2.41)$$

The governing equations (Eqs. (4.2.30) and (4.2.31)) are equidimensional in \bar{r} ; hence, they can be made autonomous by using the change of variables

$$s = \ln \bar{r}. \quad (4.2.42)$$

This change of variables transforms Eqs. (4.2.30) and (4.2.31) into two simultaneous linear ordinary differential equations with constant coefficients

$$L_1(\Omega) + L_2(\chi) = 0 \quad (4.2.43)$$

$$L_3(\Omega) + L_4(\chi) = 0 \quad (4.2.44)$$

where the L_i are the linear, constant-coefficient, second order operators

$$L_1 = \gamma_1 \frac{d^2(\cdot)}{ds^2} + (\gamma_2 - \gamma_1) \frac{d(\cdot)}{ds} - \gamma_3(\cdot) \quad (4.2.45)$$

$$L_2 = -\gamma_4 \frac{d^2(\cdot)}{ds^2} + \gamma_5(\cdot) \quad (4.2.46)$$

$$L_3 = \gamma_6 \frac{d^2(\cdot)}{ds^2} - \gamma_7(\cdot) \quad (4.2.47)$$

$$L_4 = \gamma_8 \frac{d^2(\cdot)}{ds^2} + (\gamma_9 - \gamma_8) \frac{d(\cdot)}{ds} - \gamma_{10}(\cdot) \quad (4.2.48)$$

The operators L_1 and L_4 are nonzero when material coupling of bending and extension exists, as is the case when the annular plate is laminated unsymmetrically with respect to its reference surface (midplane). For symmetric laminates, Eqs.(4.2.43) and (4.2.44) uncouple since $[\bar{B}^*] = 0$ so that

$$\gamma_4 \frac{d^2 \chi}{ds^2} - \gamma_5 \chi = 0 \quad (4.2.49)$$

$$\gamma_6 \frac{d^2 \Omega}{ds^2} - \gamma_7 \Omega = 0. \quad (4.2.50)$$

The solutions to these equations are

$$\chi(s) = C_1 e^{\alpha_1 s} + C_2 e^{-\alpha_1 s} \quad (4.2.51)$$

$$\Omega(s) = C_3 e^{\alpha_1 s} + C_4 e^{-\alpha_2 s} \quad (4.2.52)$$

where the C_i are constants of integration to be evaluated using the imposed boundary conditions and

$$\alpha_1 = \sqrt{\frac{\gamma_5}{\gamma_4}} = \sqrt{\frac{\overline{A}_{11}}{\overline{A}_{22}}} \quad (4.2.53)$$

$$\alpha_2 = \sqrt{\frac{\gamma_7}{\gamma_6}} = \sqrt{\frac{\overline{D}_{22}}{\overline{D}_{11}}} \quad (4.2.54)$$

Since the radicands are always positive, α_1 and α_2 are always real; hence, Eqs. (4. 2. 51) through (4.2.54) represent all the possible solutions to Eqs. (4.2.49) and (4.2.50).

The special case of a symmetric laminate is typically the most practical; however, exact solutions to the more general problem of an annular plate made of an unsymmetric laminate can also be found. When Eqs. (4.2.43) and (4.2.44) remain coupled, they can be solved by the method of elimination (see Boyce and Diprima⁸⁹). When L_2 and L_4 are nonzero operators, application of this method to these equations results in the single ordinary differential equation for Ω

$$L_4 [L_1 (\Omega)] - L_2 [L_3 (\Omega)] = 0 \quad (4.2.55)$$

Note that if $[B^*] = 0$, L_2 and L_4 are both zero and Eq. (4.2.55) becomes $0 = 0$, an identity. Assuming $[B^*] \neq 0$, expanding Eq. (4.2.55), and collecting terms produces

$$\rho_1 \frac{d^4 \Omega}{ds^4} + \rho_3 \frac{d^2 \Omega}{ds^2} + \rho_5 \Omega = 0 \quad (4.2.56)$$

where

$$\rho_1 = \left[(\overline{B}_{21}^*)^2 + \overline{A}_{22} \overline{D}_{11} \right] \left(\frac{L}{R} \right)^2 \quad (4.2.57)$$

$$\rho_3 = - \left[(\overline{B}_{11}^* - \overline{B}_{22}^*)^2 + 2\overline{B}_{12}^* \overline{B}_{21}^* + \overline{A}_{22} \overline{D}_{22} + \overline{A}_{11} \overline{D}_{11} \right] \left(\frac{L}{R} \right)^2 \quad (4.2.58)$$

$$\rho_5 = \left[(\overline{B}_{12}^*)^2 + \overline{A}_{11} \overline{D}_{22} \right] \left(\frac{L}{R} \right)^2 \quad (4.2.59)$$

Eq. (4.2.56) is a fourth order homogeneous ordinary differential equation with constant coefficients for the normalized flexural rotation, Ω , of the prebuckled annular plate. As was the case for the cylindrical shell segment, the form of the solution to Eq. (4.2.56) is

$$\Omega(s) = \sum_{j=1}^4 C_j e^{\bar{\lambda}_j s} \quad (4.2.60)$$

where the C_j are constants of integration to be evaluated using the remaining boundary conditions (Eqs. (4.2.5) and (4.2.8)) and the $\bar{\lambda}_j$ are the roots of the associated characteristic equation

$$\rho_1 \bar{\lambda}^4 + \rho_3 \bar{\lambda}^2 + \rho_5 = 0. \quad (4.2.61)$$

the roots of this equation are

$$\bar{\lambda}_j = \pm \lambda_1 \pm i \lambda_2 \quad (4.2.62)$$

where $i = \sqrt{-1}$

$$\lambda_1 = \frac{1}{2} \sqrt{2 \sqrt{\frac{\rho_5}{\rho_1}} - \frac{\rho_3}{\rho_1}} \quad (4.2.63)$$

$$\lambda_2 = \frac{1}{2} \sqrt{2 \sqrt{\frac{\rho_5}{\rho_1}} + \frac{\rho_3}{\rho_1}}. \quad (4.2.64)$$

χ can now be determined using either Eq. (4.2.43) or Eq. (4.2.44). From Eq. (4. 2. 43)

$$L_2(\chi) = -L_1(\Omega). \quad (4.2.65)$$

This is a second order nonhomogeneous ordinary differential equation with constant coefficients. The particular solution can be found using the method of undetermined coefficients and Eq. (4.2.60) - the solution for Ω . The homogeneous solution produces two more extraneous constants of integration; however, by considering equation (4.2.44), it can be shown that unless bending-stretching coupling is absent (another solution altogether) these constants must be zero. This completes the solution of the problem. The stress resultants can now be found using Eqs. (4.2.23) and Eq. (4.2.24);

the normal displacement, \bar{u}_3^o , can be found by integrating the expression for the rotation, Ω , once - the constant of integration representing rigid body normal displacement (if any) of the plate. An expression for the in-plane radial displacement, \bar{u}_1^o , can be found using the solutions for Ω and χ , the laminate constitutive relations (Eqs. (4.2.11)), and the strain-displacement equation

$$\bar{\epsilon}_{22}^o = -\frac{\bar{Z}\bar{u}_1^o}{\bar{r}}. \quad (4.2.66)$$

4.3 Determination of Constants of Integration

In sections 4.1 and 4.2, the particular and homogeneous solutions to the differential equations governing the prebuckling response of cylindrical shell and annular plate segments were presented. It remains to determine the constants of integration associated with the homogeneous solutions of the governing equations. Each of the shell segments, whether they are cylinder or annular plate segments, have four constants of integration associated with the solution to that segment's governing differential equation(s); thus, if there are a total of N shell branches, a total of $4N$ equations is needed to determine the required constants of integration. Determination of these constants is related to the boundary conditions which have yet to be imposed. The first four necessary equations are those associated with the clamped boundary conditions at the ends of the cylindrical shell

$$\bar{w}^o = \frac{d\bar{w}^o}{dX} = 0 \quad \text{at} \quad X = \pm \frac{1}{2}. \quad (4.3.1)$$

The next $2m$ equations, where m is the number of ring webs present in the structure, reflect the assumption that the inboard edges of these webs are traction-free. At these edges, therefore

$$\bar{N}_{11}^l = \bar{M}_{11}^l = 0 \quad l = 1, 2, \dots, m. \quad (4.3.2)$$

The remaining necessary equations are related to deformation compatibility and equilibrium at junctions where shell branches are connected. The most general situation is depicted in Fig. 4.3.1, where an annular plate segment intersects the cylindrical shell. Deformation compatibility and equilibrium enforcement at the point P indicated in the figure result in the following six equations:

$$u_3^{i+1} - u_3^i = 0 \quad (4.3.3)$$

$$u_3^{i+1} + u_1^{web} = 0 \quad (4.3.4)$$

$$\frac{du_3^{i+1}}{d\xi_1^{cyl}} - \frac{du_3^i}{d\xi_1^{cyl}} = 0 \quad (4.3.5)$$

$$\frac{du_3^{i+1}}{d\xi_1^{cyl}} - \frac{du_3^{web}}{d\xi_1^{web}} = 0 \quad (4.3.6)$$

$$M_{11}^{i+1} - M_{11}^i + M_{11}^{web} = 0 \quad (4.3.7)$$

$$V_1^{i+1} - V_1^i - N_{11}^{web} = 0 \quad (4.3.8)$$

where i and $i + 1$ identify the two cylindrical shell segments that meet where the ring web is connected to the shell and web identifies quantities related to the ring web (annular plate) evaluated at the outboard edge of the web. At first, it appears that the additional equilibrium equation $N_{11}^{i+1} - N_{11}^i + V_{11}^{web} = 0$ and the additional deformation compatibility equations $u_1^{i+1} - u_1^i = 0$ and $u_1^{i+1} - u_3^{web} = 0$ are also needed. However, since the inboard edges of the ring webs are assumed to be traction-free, the assumption of an axisymmetric prebuckling response and equilibrium of the ring web in the ξ_3 coordinate direction dictates that $V_{11}^{web} = 0$. Hence, the attachment of the ring webs to the cylinder wall does not affect the constant N_{11} in the cylinder wall - it remains equal to the applied axial load in each cylindrical shell segment. The additional deformation compatibility equations, $u_1^{i+1} - u_1^i = 0$ and $u_1^{i+1} - u_3^{web} = 0$, would be needed only if the distribution of u_1 in the cylinder wall was required. However, since the prebuckling stress state in the ring-stiffened cylinder can be completely determined without calculating u_1 , this calculation is not made in the present study.

Using Table 1, Eqs. (4.3.3) through (4.3.8) in nondimensional form become

$$\bar{u}_3^{i+1} - \bar{u}_3^i = 0 \quad (4.3.9)$$

$$\bar{u}_3^{i+1} + \bar{u}_1^{web} = 0 \quad (4.3.10)$$

$$\frac{d\bar{u}_3^{i+1}}{d\xi_1^{cyl}} - \frac{d\bar{u}_3^i}{d\xi_1^{cyl}} = 0 \quad (4.3.11)$$

$$\frac{d\bar{u}_3^{i+1}}{d\xi_1^{cyl}} - \frac{d\bar{u}_3^{web}}{d\xi_1^{web}} = 0 \quad (4.3.12)$$

$$\overline{M}_{11}^{i+1} - \overline{M}_{11}^i + \overline{M}_{11}^{web} = 0 \quad (4.3.13)$$

$$\overline{V}_{11}^{i+1} - \overline{V}_{11}^i - \frac{L}{t_s} \overline{N}_{11}^{web} = 0. \quad (4.3.14)$$

For the case where no ring web is present but the cylinder skin experiences a sudden thickness change, the following four equations (in nondimensional form) are needed to enforce deformation compatibility and equilibrium at the point where the two cylindrical shell segments are joined

$$\overline{u}_3^{i+1} - \overline{u}_3^i = 0 \quad (4.3.15)$$

$$\frac{d\overline{u}_3^{i+1}}{d\overline{\xi}_1^{cyl}} - \frac{d\overline{u}_3^i}{d\overline{\xi}_1^{cyl}} = 0 \quad (4.3.16)$$

$$\overline{M}_{11}^{i+1} - \overline{M}_{11}^i = 0 \quad (4.3.17)$$

$$\overline{V}_{11}^{i+1} - \overline{V}_{11}^i = 0. \quad (4.3.18)$$

Should the ring web itself experience a sudden thickness change, the following four equations (in nondimensional form) are needed to enforce deformation compatibility and equilibrium at the point where the two annular plate segments, web and $web + 1$, are joined

$$\overline{u}_1^{web+1} - \overline{u}_1^{web} = 0 \quad (4.3.19)$$

$$\frac{d\overline{u}_3^{web+1}}{d\overline{\xi}_1^{web}} - \frac{d\overline{u}_3^{web}}{d\overline{\xi}_1^{web}} = 0 \quad (4.3.20)$$

$$\overline{M}_{11}^{web+1} - \overline{M}_{11}^{web} = 0 \quad (4.3.21)$$

$$\overline{N}_{11}^{web+1} - \overline{N}_{11}^{web} = 0. \quad (4.3.22)$$

As noted earlier, the inboard edges of the ring webs are assumed to be traction-free; hence, the assumption of an axisymmetric prebuckling response and equilibrium of the ring web in the ξ_3 coordinate direction dictates that $V_{11}^{web} = 0$ in each web segment, making an additional set of equilibrium equations for the Kirchhoff shears in the various segments unnecessary. The additional deformation compatibility equation, $u_3^{web+1} - u_3^{web} = 0$ would be needed only if the distributions of u_3 in the ring

webs were required. However, since the prebuckling stress state can be completely determined without calculating u_3 in the ring webs, this calculation is not made in the present study.

Eqs. (4.3.1) through (4.3.22) can be used to completely determine all of the constants of integration arising from the exact solutions to the governing differential equations of each shell branch. Using these exact solutions evaluated at the boundaries and at points where separate segments are connected in Eqs. (4.3.1) through (4.3.22), as required, results in a system of linear algebraic equations of the form

$$[KK]\{C\} = \{FF\} \quad (4.3.23)$$

where $[KK]$ contains terms from the homogeneous solutions to the governing equations of the various shell branches evaluated at boundaries and where the branches are connected, $\{FF\}$ contains terms from the nonhomogeneous solutions to the governing equations and $\{C\}$ is the vector containing the constants of integration of the various shell branches. It was discovered that using homogeneous solutions to Eq. (4.1.27) written in terms of hyperbolic sines and cosines results in a singular $[KK]$ matrix for cylinders with length-to-radius (L/R) ratios greater than about 2. The matrix $[KK]$ becomes singular because for large arguments the hyperbolic sine and cosine functions become numerically equal causing a linear dependence among the four terms of the homogeneous solution to the governing equation. This difficulty can be overcome by writing the solution in the form of exponentially modulated harmonic functions, as shown in Eq. (4.1.38).

4.4 Stress Analysis at the Ring Flange/Cylinder Wall Interface

The solutions to the governing equations of sections 4.1 through 4.3 can be used to calculate the stresses at any point in the ring-stiffened cylindrical shell. For the cylindrical shell segments, calculation of the in-plane axial and circumferential stresses is straightforward and is outlined in section A.1 of Appendix A. While the interlaminar stresses are ignored in the development of the shell analysis, these stresses are not zero. As shown by, for example, Boitnott⁵⁴, the interlaminar stresses may be calculated by substituting the tangential stresses calculated using shell theory into the three-dimensional elasticity equations and solving for the interlaminar stresses by integrating the equations with respect to the thickness coordinate, layer by layer through the entire thickness of the laminate, then imposing stress continuity at each layer interface and surface traction boundary conditions at one surface of the laminate. Details of this development can be found in section A.2 of Appendix A.

As mentioned in section 3.2, high through-the-thickness normal and transverse shear stresses which have been demonstrated to exist in the region adjacent to the point where the shell skin first meets a frame flange cannot be adequately estimated using the technique outlined in section A.2 of Appendix A. Integration of the three-dimensional elasticity equations using the in-plane stress resultants from the two-dimensional theory does not reflect the existence of a free edge in the ring flange. The result of the neglect of this free edge can be seen immediately in Eqs. (A.1.8) through (A.1.10) of Appendix A - the expressions for the tangential stresses. Note that each resulting stress varies linearly throughout the entire thickness of the laminate. At the point where a ring flange steps down to meet the cylindrical shell skin this linearly varying stress distribution is not possible since the edge of the frame flange at this point is traction-free.

Another reason that the stress analysis of Appendix A is deficient in the flange/skin region is that by merely treating the adhesive layer as a "soft" ply in CLT theory, it is assumed that the through-the-thickness transverse shear and normal stresses in this

layer are negligibly small compared to the in-plane stresses (plane stress assumption). In their widely recognized paper on the analysis of adhesively-bonded single-shear lap joints, Goland and Reissner⁹⁰ indicate that the neglect of the in-plane stresses in comparison to the through-the-thickness transverse shear and normal stresses is actually more representative of the load transfer mechanism in an adhesive layer that is much thinner than the adherends and that has a much lower Young's modulus than the adherends. Goland and Reissner offered two rational formulations, one applicable to the analysis of single shear lap joints made of thin metallic adherends, the other applicable to the analysis of single-shear lap joints made of thick wood or plastic adherends. The former formulation, applicable to most thin-walled aerospace structures, relies on the following basic assumptions

1. Through-the-thickness normal and transverse shear stresses in the *adherends* can be neglected in comparison to in-plane stresses
2. In-plane stresses in the *adhesive* can be neglected in comparison to the through-the-thickness normal and transverse shear stresses.
3. The through-the-thickness normal and transverse shear stresses in the adhesive do not vary through the thickness of the adhesive.

Since Goland and Reissner's paper was first published in 1944, these basic assumptions have formed the basis of nearly every study in which a practical working estimate of the stresses in the joints of secondarily bonded thin-walled structures is required. For example, the relatively recent work of Wang and Biggers⁵⁰ on skin/stiffener interface stresses in bonded, stiffened, flat panels relies heavily on these assumptions. Goland and Reissner's assumptions have also been used in the study of tubular lap joints in isotropic cylinders by Lubkin and Reissner⁹¹, Terekhova and Skoryi⁹², and Adams and Peppiatt⁹³, and in the study of tubular lap joints in laminated fiber composite cylinders by Updike and Yuceoglu⁹⁴ and Chon⁹⁵. These studies quantified the importance of accounting for curvature of the adherends and nonlinear material behavior of the adhesive in the theoretical analysis. Hart-Smith⁹⁶ identified the neglect of nonlinear adhesive

material behavior as a serious shortcoming of Goland and Reissner's theory in his thorough study of single-shear lap joints made of both metal and laminated fiber composite adherends.

It is assumed in the present study that the rings are secondarily bonded along their flanges to the shell skin using a *ductile* (see Hart-Smith⁹⁶) adhesive. To obtain estimates of the stresses in the adhesive layer, an analysis is proposed incorporating the Goland and Reissner assumptions and using an approach similar to that of Wang and Biggers⁵⁰. Whereas in sections 4.1-4.3 the flange-adhesive-attached skin combination was treated as a single shell segment characterized by a single set of constitutive equations, the segment is now treated as two short cylindrical segments connected along an outer surface by a ductile adhesive as shown in Fig. 4.4.1. In Fig. 4.4.1, the superscripts w , f , B , and s are used to indicate quantities related to the ring web, ring flange, adhesive bond and attached skin respectively. N_{ij} and M_{ij} are stress resultants and stress couples related to the $\xi_i\xi_j$ coordinate directions of the various shell segments, σ_{33} is the normal stress (referred to as "peel" stress if this stress is tensile) in the adhesive and τ_{13} and τ_{23} are the adhesive transverse shear stresses. The thickness of the adhesive layer is h and it is assumed that the adhesive is applied over the entire ring flange length L_f . Note from Fig. 4.4.1 that $\xi_1^s = \xi_1^b = \xi_1^f$ and $\xi_2^s = \xi_2^b = \xi_2^f$ so that the superscripts can be dropped from these quantities. DMV theory is again used to determine the response of the flange segment and attached skin; furthermore, the Goland and Reissner assumptions are considered valid. Since this analysis is only to be used to estimate stresses in the prebuckled equilibrium configuration, the axisymmetric form of the governing equations is applicable. The equilibrium equations governing the axisymmetric response of the ring flange are

$$\frac{dN_{11}^f}{d\xi_1} + \tau_{13} = 0 \quad (4.4.1)$$

$$\frac{dN_{12}^f}{d\xi_1} + \tau_{23} = 0 \quad (4.4.2)$$

$$\frac{d^2 M_{11}^f}{d\xi_1^2} - \frac{N_{22}^f}{R_f} + \frac{dN_{11}^f}{d\xi_1} \frac{du_3^{of}}{d\xi_1} + N_{11}^f \frac{d^2 u_3^{of}}{d\xi_1^2} + \sigma_{33} + \frac{t_f}{2} \frac{d\tau_{13}}{d\xi_1} = -p \quad (4.4.3)$$

The equilibrium equations governing the axisymmetric response of the skin attached to the ring flange are

$$\frac{dN_{11}^s}{d\xi_1} - \tau_{13} = 0 \quad (4.4.4)$$

$$\frac{dN_{12}^s}{d\xi_1} - \tau_{23} = 0 \quad (4.4.5)$$

$$\frac{d^2 M_{11}^s}{d\xi_1^2} - \frac{N_{22}^s}{R_s} + \frac{dN_{11}^s}{d\xi_1} \frac{du_3^{os}}{d\xi_1} + N_{11}^s \frac{d^2 u_3^{os}}{d\xi_1^2} - \sigma_{33} - \frac{t_s}{2} \frac{d\tau_{13}}{d\xi_1} = 0 \quad (4.4.6)$$

where R_f is the radius to the middle surface of the ring flange, R_s is the radius to the middle surface of the cylinder skin, t_f is the total ring flange thickness, and t_s is the total cylinder skin thickness. Eqs. (4.4.1) through (4.4.6) can be derived by setting $\phi = 0$ and $\partial(\cdot)/\partial\xi_2 = 0$ (see Fig. 3.3.1) in Eqs. (3.3.3.2) through (3.3.3.5) and accounting for the surface tractions σ_{33} , τ_{13} and τ_{23} arising due to the presence of the adhesive layer. Since these stresses are assumed to be constant through the entire thickness, h , of the adhesive, they act on both the outboard surface of the ring flange segment and on the inboard surface of the attached skin segment at the same value of ξ_1 . Since it is assumed that t_f and t_s are small, the term $(t_f/2)(d\tau_{13}/d\xi_1)$ in Eq. (4.4.3) and the term $(t_s/2)(d\tau_{13}/d\xi_1)$ in Eq. (4.4.6) are neglected. The effects of geometric imperfections are ignored in this theoretical analysis; furthermore, like in the analysis of Wang and Biggers⁵⁰, the strain-displacement equations for the adhesive are based on geometrically linear theory while the strain-displacement equations related to the ring flange and attached skin are based on geometrically nonlinear theory. The resulting geometrically nonlinear equilibrium equations that characterize the response of the ring flange and attached skin, Eqs. (4.4.1) through (4.4.6), are then linearized in the following way. Consider Eqs. (4.4.1) and (4.4.4). If $\tau_{13} = 0$ then N_{11}^f and N_{11}^s would both be constant and equal to the axial load applied to the segment boundary. If $\tau_{13} \neq 0$ then assume that N_{11}^f and N_{11}^s can be written as $N_{11}^{f(o)} + N_{11}^{f(1)}(\xi_1)$ and $N_{11}^{s(o)} + N_{11}^{s(1)}(\xi_1)$ respectively where $N_{11}^{f(o)}$ and $N_{11}^{s(o)}$ are constant and equal

to the N_{11} applied at the boundaries of the short cylindrical segments and the terms $N_{11}^{f(1)}(\xi_1)$ and $N_{11}^{s(1)}(\xi_1)$ represent additions to these constant stress resultants resulting from the $\tau_{13}(\xi_1)$ that arises due to the presence of the adhesive. While the products of $N_{11}^{f(o)}$ and $N_{11}^{s(o)}$ and the local flexural rotations of the adherends are retained in the analysis, the products of these rotations and $N_{11}^{f(1)}(\xi_1)$ and $N_{11}^{s(1)}(\xi_1)$ are assumed to be small and are neglected. $N_{11}^{f(o)}$ is zero and $N_{11}^{s(o)}$ is equal to the axial compressive load applied to the cylinder. Since N_{11}^f and N_{11}^s are assumed constant, Eqs. (4.4.1) through (4.4.6) now form a system of linear ordinary differential equations with constant coefficients. The adhesive is assumed to be isotropic and homogeneous. The linear strain-displacement equations in the adhesive, consistent with DMV shell theory are

$$\epsilon_{33} = \frac{\partial u_3^B}{\partial \xi_3^B} \quad (4.4.7)$$

$$\gamma_{23} = \frac{\partial u_3^B}{\partial \xi_2^B} + \frac{\partial u_2^B}{\partial \xi_3^B} \quad (4.4.8)$$

$$\gamma_{13} = \frac{\partial u_3^B}{\partial \xi_1^B} + \frac{\partial u_1^B}{\partial \xi_3^B} \quad (4.4.9)$$

where ϵ_{33} is the adhesive normal strain (or "peel" strain if the strain is tensile), the γ_{ij} are adhesive transverse shear strains with respect to the ij coordinate directions and the u_i^B are adhesive displacements in the ξ_i^B coordinate directions. Based on linear isotropic elasticity, the stress-strain equations within the adhesive, neglecting the tangential stresses, are

$$\epsilon_{33} = \frac{\sigma_{33}}{E_B} \quad (4.4.10)$$

$$\gamma_{23} = \frac{\tau_{23}}{G_B} \quad (4.4.11)$$

$$\gamma_{13} = \frac{\tau_{13}}{G_B} \quad (4.4.12)$$

where E_B is the Young's modulus and G_B is the shear modulus of the adhesive. In joints with laminated fiber composite adherends, Hart-Smith⁹⁶ recommends replacing

E_B with an “effective peel modulus” to account for the low transverse Young’s moduli of the adherends not present in metallic structures. This recommended “effective peel modulus”, E_P , is given by

$$\frac{1}{E_P} = \frac{1}{E_B} + \frac{6}{E_2} \quad (4.4.13)$$

where E_2 is the transverse Young’s modulus of a single lamina of the adherends.

After imposing the assumption of an axisymmetric response ($(\partial(\cdot)/\partial\xi_2) = 0$), Eqs. (4.4.7) through (4.4.12) can be used to solve for the adhesive displacements in terms of the adhesive stresses. Using boundary conditions at the outboard surface of the ring flange and the inboard surface of the cylinder skin, the expressions for the adhesive displacements can be re-written as equations that relate the middle surface displacements in the ring flange to those of the attached cylinder skin, effectively eliminating the adhesive displacements from the problem. These equations are

$$u_3^{\circ f} = \frac{-h\sigma_{33}}{E_P} + u_3^{\circ s} \quad (4.4.14)$$

$$u_2^{\circ f} = \frac{-h\tau_{23}}{G_B} + u_2^{\circ s} \quad (4.4.15)$$

$$u_1^{\circ f} = \frac{-h\tau_{13}}{G_B} - \left[\frac{t_f h}{2E_P} + \frac{h^2}{2E_P} \right] \frac{d\sigma_{33}}{d\xi_1} - \left(\frac{-t_f}{2} - \frac{t_s}{2} - h \right) \frac{du_3^{\circ s}}{d\xi_1} + u_1^{\circ s}. \quad (4.4.16)$$

In these equations, the $u_i^{\circ s}$ are middle surface displacements of the cylinder skin in the ξ_i^s coordinate directions, $u_i^{\circ f}$ are middle surface displacements of the ring flange in the ξ_i^f coordinate directions, t_s is the total cylinder skin thickness and t_f is the total ring flange thickness. Solving for the adhesive stresses in Eqs. (4.4.14) through (4.4.16) yields

$$\sigma_{33} = \frac{E_P}{h}(u_3^{\circ s} - u_3^{\circ f}) \quad (4.4.17)$$

$$\tau_{23} = \frac{G_B}{h}(u_2^{\circ s} - u_2^{\circ f}) \quad (4.4.18)$$

$$\tau_{13} = \frac{G_B}{h} \left[(u_1^{\circ s} - u_1^{\circ f}) + \left(\frac{t_f}{2} + \frac{h}{2} \right) \frac{du_3^{\circ f}}{d\xi_1} + \left(\frac{t_s}{2} + \frac{h}{2} \right) \frac{du_3^{\circ s}}{d\xi_1} \right] \quad (4.4.19)$$

Substituting Eqs. (4.4.17) through (4.4.19) into Eqs. (4.4.1) through (4.4.6) and non-dimensionalizing the resulting set of equations using Table 1 gives

$$\frac{d\bar{N}_{11}^f}{d\bar{\xi}_1} + \bar{\tau}_{13} = 0 \quad (4.4.20)$$

$$\frac{d\bar{N}_{12}^f}{d\bar{\xi}_1} + \bar{\tau}_{23} = 0 \quad (4.4.21)$$

$$\frac{d^2\bar{M}_{11}^f}{d\bar{\xi}_1^2} - \left(\frac{L^2}{R_f t_s}\right) \bar{N}_{22}^f + \bar{\sigma}_{33} = -\bar{Z}\bar{p} \quad (4.4.22)$$

$$\frac{d\bar{N}_{11}^s}{d\bar{\xi}_1} - \bar{\tau}_{13} = 0 \quad (4.4.23)$$

$$\frac{d\bar{N}_{12}^s}{d\bar{\xi}_1} - \bar{\tau}_{23} = 0 \quad (4.4.24)$$

$$\frac{d^2\bar{M}_{11}^s}{d\bar{\xi}_1^2} - \left(\frac{L^2}{R_s t_s}\right) \bar{N}_{22}^s + \hat{N}_{11} \frac{d^2\bar{u}_3^{os}}{d\bar{\xi}_1^2} - \bar{\sigma}_{33} = 0 \quad (4.4.25)$$

where

$$\bar{\tau}_{13} = \bar{C}_{13}^B(\bar{u}_1^{of} - \bar{u}_1^{os}) + \bar{K}_{Bf} \frac{d\bar{u}_3^{of}}{d\bar{\xi}_1} + \bar{K}_{Bs} \frac{d\bar{u}_3^{os}}{d\bar{\xi}_1} \quad (4.4.26)$$

$$\bar{\tau}_{23} = \bar{C}_{13}^B(\bar{u}_2^{of} - \bar{u}_2^{os}) \quad (4.4.27)$$

$$\bar{\sigma}_{33} = \bar{C}_{33}^B(\bar{u}_3^{of} - \bar{u}_3^{os}) \quad (4.4.28)$$

$$\bar{C}_{13}^B = \frac{-L^3 G_B t_s}{D_{11}^s h} \quad (4.4.29)$$

$$\bar{C}_{33}^B = \frac{-L^4 E_P}{D_{11}^s h} \quad (4.4.30)$$

$$\bar{K}_{Bf} = \bar{C}_{13}^B \left(\frac{-t_f}{2L} - \frac{h}{2L} \right) \quad (4.4.31)$$

$$\bar{K}_{Bs} = \bar{C}_{13}^B \left(-\frac{t_s}{2L} - \frac{h}{2L} \right), \quad (4.4.32)$$

$\bar{()}$ indicates that $()$ is a nondimensional quantity, D_{11}^s is the axial bending stiffness of the cylinder skin, L is the total cylinder length, R_f is the radius to the middle surface

of the ring flange, R_s is the radius to the middle surface of the cylinder wall, and \widehat{N}_{11} is the nondimensional axial compressive load applied to the shell, which is constant.

The nondimensional stress-strain equations for the ring flange and attached cylinder skin are (see section 3.3.2 and Table 1)

$$\begin{Bmatrix} \overline{N}_{11} \\ \overline{N}_{22} \\ \overline{N}_{12} \\ \overline{M}_{11} \\ \overline{M}_{22} \\ \overline{M}_{12} \end{Bmatrix}^{s(f)} = \begin{bmatrix} \overline{A}_{11} & \overline{A}_{12} & \overline{A}_{16} & \overline{B}_{11} & \overline{B}_{12} & \overline{B}_{16} \\ \overline{A}_{12} & \overline{A}_{22} & \overline{A}_{26} & \overline{B}_{21} & \overline{B}_{22} & \overline{B}_{26} \\ \overline{A}_{16} & \overline{A}_{26} & \overline{A}_{66} & \overline{B}_{61} & \overline{B}_{62} & \overline{B}_{66} \\ \overline{B}_{11} & \overline{B}_{21} & \overline{B}_{61} & \overline{D}_{11} & \overline{D}_{12} & \overline{D}_{16} \\ \overline{B}_{12} & \overline{B}_{22} & \overline{B}_{62} & \overline{D}_{12} & \overline{D}_{22} & \overline{D}_{26} \\ \overline{B}_{16} & \overline{B}_{26} & \overline{B}_{66} & \overline{D}_{16} & \overline{D}_{26} & \overline{D}_{66} \end{bmatrix}^{s(f)} \begin{Bmatrix} \overline{\epsilon}_{11}^o \\ \overline{\epsilon}_{22}^o \\ \overline{\gamma}_{12}^o \\ \overline{\kappa}_{11} \\ 0 \\ 0 \end{Bmatrix}^{s(f)} \quad (4.4.33)$$

where

$$\overline{\epsilon}_{11}^{os(f)} = \left(\frac{L}{t_s} \right) \frac{d\overline{u}_1^{os(f)}}{d\overline{\xi}_1} \quad (4.4.34)$$

$$\overline{\epsilon}_{22}^{os(f)} = \left(\frac{L^2}{R_s(f)t_s} \right) \overline{u}_3^{os(f)} \quad (4.4.35)$$

$$\overline{\gamma}_{12}^{os(f)} = \left(\frac{L}{t_s} \right) \frac{d\overline{u}_2^{os(f)}}{d\overline{\xi}_1} \quad (4.4.36)$$

$$\overline{\kappa}_{11}^{os(f)} = -\frac{d^2\overline{u}_3^{os(f)}}{d\overline{\xi}_1^2}. \quad (4.4.37)$$

Substitution of Eqs. (4.4.33) into Eqs. (4.4.20) through (4.4.25) results in

$$\begin{aligned} & \overline{A}_{11}^f \left(\frac{L}{t_s} \right) \frac{d^2\overline{u}_1^{of}}{d\overline{\xi}_1^2} + \overline{A}_{16}^f \left(\frac{L}{t_s} \right) \frac{d^2\overline{u}_2^{of}}{d\overline{\xi}_1^2} + \overline{A}_{12}^f \left(\frac{L^2}{R_f t_s} \right) \frac{d\overline{u}_3^{of}}{d\overline{\xi}_1} \\ & - \overline{B}_{11}^f \frac{d^3\overline{u}_3^{of}}{d\overline{\xi}_1^3} + \overline{K}_{Bf} \frac{d\overline{u}_3^{of}}{d\overline{\xi}_1} + \overline{K}_{Bs} \frac{d\overline{u}_3^{os}}{d\overline{\xi}_1} + \overline{C}_{13}^B \overline{u}_1^{of} - \overline{C}_{13}^B \overline{u}_1^{os} \\ & = 0 \end{aligned} \quad (4.4.38)$$

$$\begin{aligned} & \overline{A}_{16}^f \left(\frac{L}{t_s} \right) \frac{d^2\overline{u}_1^{of}}{d\overline{\xi}_1^2} + \overline{A}_{66}^f \left(\frac{L}{t_s} \right) \frac{d^2\overline{u}_2^{of}}{d\overline{\xi}_1^2} + \overline{A}_{26}^f \left(\frac{L^2}{R_f t_s} \right) \frac{d\overline{u}_3^{of}}{d\overline{\xi}_1} \\ & - \overline{B}_{61}^f \frac{d^3\overline{u}_3^{of}}{d\overline{\xi}_1^3} + \overline{C}_{13}^B \overline{u}_2^{of} - \overline{C}_{13}^B \overline{u}_2^{os} \\ & = 0 \end{aligned} \quad (4.4.39)$$

$$\begin{aligned}
& \bar{B}_{11}^f \left(\frac{L}{t_s} \right) \frac{d^3 \bar{u}_1^{\circ f}}{d\bar{\xi}_1^3} + \bar{B}_{16}^f \left(\frac{L}{t_s} \right) \frac{d^3 \bar{u}_2^{\circ f}}{d\bar{\xi}_1^3} + \bar{B}_{12}^f \left(\frac{L^2}{R_f t_s} \right) \frac{d^2 \bar{u}_3^{\circ f}}{d\bar{\xi}_1^2} \\
& - \bar{A}_{12}^f \left(\frac{L^3}{R_f t_s^2} \right) \frac{d\bar{u}_1^{\circ f}}{d\bar{\xi}_1} - \bar{A}_{26}^f \left(\frac{L^3}{R_f t_s^2} \right) \frac{d\bar{u}_2^{\circ f}}{d\bar{\xi}_1} - \bar{A}_{22}^f \left(\frac{L^2}{R_f t_s} \right)^2 \bar{u}_3^{\circ f} \\
& + \bar{B}_{21}^f \frac{L^2}{R_f t_s} \frac{d^2 \bar{u}_3^{\circ f}}{d\bar{\xi}_1^2} - \bar{D}_{11}^f \frac{d^4 \bar{u}_3^{\circ f}}{d\bar{\xi}_1^4} + \bar{C}_{33}^B \bar{u}_3^{\circ f} - \bar{C}_{33}^B \bar{u}_3^{\circ s} \\
& = -\bar{Z}\bar{p}
\end{aligned} \tag{4.4.40}$$

$$\begin{aligned}
& \bar{A}_{11}^s \left(\frac{L}{t_s} \right) \frac{d^2 \bar{u}_1^{\circ s}}{d\bar{\xi}_1^2} + \bar{A}_{16}^s \left(\frac{L}{t_s} \right) \frac{d^2 \bar{u}_2^{\circ s}}{d\bar{\xi}_1^2} + \bar{A}_{12}^s \left(\frac{L^2}{R_s t_s} \right) \frac{d\bar{u}_3^{\circ s}}{d\bar{\xi}_1} \\
& - \bar{B}_{11}^s \frac{d^3 \bar{u}_3^{\circ s}}{d\bar{\xi}_1^3} - \bar{K}_{Bf} \frac{d\bar{u}_3^{\circ f}}{d\bar{\xi}_1} - \bar{K}_{Bs} \frac{d\bar{u}_3^{\circ s}}{d\bar{\xi}_1} - \bar{C}_{13}^B \bar{u}_1^{\circ f} + \bar{C}_{13}^B \bar{u}_1^{\circ s} \\
& = 0
\end{aligned} \tag{4.4.41}$$

$$\begin{aligned}
& \bar{A}_{16}^s \left(\frac{L}{t_s} \right) \frac{d^2 \bar{u}_1^{\circ s}}{d\bar{\xi}_1^2} + \bar{A}_{66}^s \left(\frac{L}{t_s} \right) \frac{d^2 \bar{u}_2^{\circ s}}{d\bar{\xi}_1^2} + \bar{A}_{26}^s \left(\frac{L^2}{R_s t_s} \right) \frac{d\bar{u}_3^{\circ s}}{d\bar{\xi}_1} \\
& - \bar{B}_{61}^s \frac{d^3 \bar{u}_3^{\circ s}}{d\bar{\xi}_1^3} - \bar{C}_{13}^B \bar{u}_2^{\circ f} + \bar{C}_{13}^B \bar{u}_2^{\circ s} \\
& = 0
\end{aligned} \tag{4.4.42}$$

$$\begin{aligned}
& \bar{B}_{11}^s \left(\frac{L}{t_s} \right) \frac{d^3 \bar{u}_1^{\circ s}}{d\bar{\xi}_1^3} + \bar{B}_{16}^s \left(\frac{L}{t_s} \right) \frac{d^3 \bar{u}_2^{\circ s}}{d\bar{\xi}_1^3} + \bar{B}_{12}^s \left(\frac{L^2}{R_s t_s} \right) \frac{d^2 \bar{u}_3^{\circ s}}{d\bar{\xi}_1^2} \\
& - \bar{A}_{12}^s \left(\frac{L^3}{R_s t_s^2} \right) \frac{d\bar{u}_1^{\circ s}}{d\bar{\xi}_1} - \bar{A}_{26}^s \left(\frac{L^3}{R_s t_s^2} \right) \frac{d\bar{u}_2^{\circ s}}{d\bar{\xi}_1} - \bar{A}_{22}^s \left(\frac{L^2}{R_s t_s} \right)^2 \bar{u}_3^{\circ s} \\
& + \bar{B}_{21}^s \frac{L^2}{R_s t_s} \frac{d^2 \bar{u}_3^{\circ s}}{d\bar{\xi}_1^2} - \bar{D}_{11}^s \frac{d^4 \bar{u}_3^{\circ s}}{d\bar{\xi}_1^4} + \hat{N}_{11} \frac{d^2 \bar{u}_3^{\circ s}}{d\bar{\xi}_1^2} - \bar{C}_{33}^B \bar{u}_3^{\circ f} + \bar{C}_{33}^B \bar{u}_3^{\circ s} \\
& = 0
\end{aligned} \tag{4.4.43}$$

Eqs. (4.4.38) through (4.4.43) form a system of coupled, nonhomogeneous ordinary differential equations with constant coefficients. As shown in Appendix B, the equations governing the response of a flange segment and the attached skin can be

written as a nonhomogeneous, constant-coefficient system of 16 first order differential equations of the form

$$\{U'\} = [B]\{U\} + \{F\} \quad (4.4.44)$$

where the 16-by-1 vector $\{U\}$ contains flange and skin nondimensional displacements and their derivatives up to order three (see Eq. (B.17) in Appendix B) and

$$\{U'\} = \frac{d}{d\bar{\xi}_1} \{U\}. \quad (4.4.45)$$

Assuming the solution to the homogeneous problem is of the form

$$\{U\} = \{C\} e^{r\bar{\xi}_1} \quad (4.4.46)$$

the total solution is

$$\{U(\bar{\xi}_1)\} = [\Phi(\bar{\xi}_1)]\{C\} + \{U_P(\bar{\xi}_1)\} \quad (4.4.47)$$

where $[\Phi(\bar{\xi}_1)]$ is a 16-by-16 fundamental matrix whose columns are made up of the 16 linearly independent solutions to the homogeneous problem (see Boyce and Dipri-⁸⁹ma).

The particular solution, $\{U_P\}$, can be found using the method of undetermined coefficients. Since the only nonzero entry in the vector $\{F\}$ is F_8 and it is a constant (see Eq. (B.19) in Appendix B), then a spatially uniform particular solution is suggested. Let u_1^{ofP} , u_2^{ofP} , u_3^{ofP} , u_1^{osP} , u_2^{osP} , and u_3^{osP} represent the nonzero, but constant, elements of the particular solution. It can be shown by direct substitution that

$$\begin{pmatrix} u_1^{ofP} \\ u_2^{ofP} \\ u_3^{ofP} \\ u_1^{osP} \\ u_2^{osP} \\ u_3^{osP} \end{pmatrix} = \begin{pmatrix} 0 \\ 0 \\ P_1 \\ 0 \\ 0 \\ P_2 \end{pmatrix} \quad (4.4.48)$$

where

$$P_1 = -\frac{e3_3^* \bar{p} \bar{Z}}{e3_3^* e3_3^f - e3_7^* e3_7^f} \quad (4.4.49)$$

$$P_2 = \frac{e_{37}^s \bar{p} \bar{Z}}{e_{33}^s e_{33}^f - e_{37}^s e_{37}^f} \quad (4.4.50)$$

\bar{p} is the nondimensional applied pressure, $\bar{Z} = L^2/(R_s t_s)$ and $e_{33}^s, e_{33}^f, e_{37}^s$, and e_{37}^f are defined in Eqs. (B.15) and (B.16) of Appendix B.

Determining the form of $[\Phi]$ involves finding the eigenvalues of the coefficient matrix $[B]$. When all of these eigenvalues are distinct, determining a set of linearly independent solutions to the homogeneous form of Eq. (4.4.44) is straightforward; however, if several eigenvalues are repeated, finding a linearly independent set of solutions becomes much more difficult. It was discovered that $[B]$ possesses repeated eigenvalues of unknown multiplicity; hence, a numerical method known as the multi-segment technique, successfully employed by Kalnins⁹⁷ in the linear static analysis of shells of revolution, has been chosen to solve the homogeneous problem. In the multi-segment technique, the domain is artificially divided into additional segments (referred to as multi-segments in the present study to distinguish them from physical structural segments) in order to ensure that a loss of accuracy, due to the exponential growth of the solutions to the homogeneous form of Eq. (4.4.44), does not occur during the numerical integration of the homogeneous form of Eq. (4.4.44) over a domain that is too long. The form of the total solution in *each multi-segment* is still the same as Eq. (4.4.47). However, in this case $\{C\}$ is a 16-by-1 vector of $\{U\}$ evaluated at the initial end of a multisegment, say multisegment number ms . For clarity, this vector of constants will be referred to as $\{u_I\}^{ms}$.

In order to determine the $\{u_I\}^{ms}$ in the various multisegments, boundary conditions must be imposed at the ends of the flanges, at the ends of the attached skin, at the junction where the ring web is connected to the ring flange, and at the ends of the various multisegments. Stress resultants and stress couples from the shell analysis described in sections 4.1 through 4.3 are used as loads applied to the joint. This is the same approach as that originally used by Goland and Reissner and has been criticized by Hart-Smith⁹⁶. However, since the stresses calculated by Hart-Smith using his more

consistent analysis are generally lower (and therefore less conservative with respect to design) than those calculated using the Goland and Reissner approach, the latter approach will be used in the present study. Conditions at the point where the frame web intersects the frame flange assuring continuity of displacements and flexural rotations are also needed. Finally, continuity of all response quantities at segment boundaries remote from the flange edges and the web intersection must be enforced. Mathematically these conditions can be stated as, at $\xi_1 = \xi_1^i$ (see Fig. 4.4.1)

$$\overline{M}_{11}^{s_i} = \widehat{M}_{11} \quad (4.4.51)$$

$$\overline{V}_{11}^{s_i} = \widehat{V}_{11} \quad (4.4.52)$$

$$\overline{N}_{11}^{s_i} = \widehat{N}_{11} \quad (4.4.53)$$

$$\overline{N}_{12}^{s_i} = \widehat{N}_{12} \quad (4.4.54)$$

$$\overline{M}_{11}^{f_i} = 0 \quad (4.4.55)$$

$$\overline{V}_{11}^{f_i} = 0 \quad (4.4.56)$$

$$\overline{N}_{11}^{f_i} = 0 \quad (4.4.57)$$

$$\overline{N}_{12}^{f_i} = 0. \quad (4.4.58)$$

where superscript f_i indicates quantities related to the first flange segment evaluated at $\xi_1 = \xi_1^i$, superscript s_i indicates quantities related to the first attached skin segment evaluated at $\xi_1 = \xi_1^i$ and \widehat{M}_{11} , \widehat{V}_{11} , \widehat{N}_{11} , and \widehat{N}_{12} are the nondimensional axial stress couple, Kirchhoff shear stress resultant, axial stress resultant and tangential shear stress resultant at $\xi_1 = \xi_1^i$ from the analysis of sections 4.1 through 4.3. Note that similar conditions exist at $\xi_1 = \xi_1^{i+2}$ (see Fig. 4.4.1). At $\xi_1 = \xi_1^{i+1}$, where the ring web intersects the ring flange

$$\overline{u}_3^{of_{i+1}} - \overline{u}_3^{of_i} = 0 \quad (4.4.59)$$

$$\overline{u}_3^{of_{i+1}} + \overline{u}_1^{ow} = 0 \quad (4.4.60)$$

$$\frac{d\bar{u}_3^{\circ f_{i+1}}}{d\bar{\xi}_1} - \frac{d\bar{u}_3^{\circ f_i}}{d\bar{\xi}_1} = 0 \quad (4.4.61)$$

$$\frac{d\bar{u}_3^{\circ f_{i+1}}}{d\bar{\xi}_1} - \frac{d\bar{u}_3^{\circ w}}{d\bar{\xi}_1} = 0 \quad (4.4.62)$$

$$\bar{u}_1^{\circ f_{i+1}} - \bar{u}_1^{\circ f_i} = 0 \quad (4.4.63)$$

$$\bar{u}_2^{\circ f_{i+1}} - \bar{u}_2^{\circ f_i} = 0 \quad (4.4.64)$$

$$\bar{M}_{11}^{f_{i+1}} - \bar{M}_{11}^{f_i} + \bar{M}_{11}^w = 0 \quad (4.4.65)$$

$$\bar{V}_{11}^{f_{i+1}} - \bar{V}_{11}^{f_i} - \left(\frac{L}{t_s}\right) \bar{N}_{11}^w = 0 \quad (4.4.66)$$

$$\bar{N}_{11}^{f_{i+1}} - \bar{N}_{11}^{f_i} = 0 \quad (4.4.67)$$

$$\bar{N}_{22}^{f_{i+1}} - \bar{N}_{22}^{f_i} = 0 \quad (4.4.68)$$

where superscript f_{i+1} indicates quantities related to the ring flange segment $i + 1$ in Fig. 4.4.1 evaluated at $\xi_1 = \xi_1^{i+1}$, and superscript w indicates quantities related to the ring web. \hat{N}_{11}^w and \hat{M}_{11}^w are the stress resultant and stress couple at the outboard edge of the web which are calculated based on the analysis of section 5.3. Note that similar boundary conditions are not required for the attached skin beneath the ring web since it is assumed that the web is connected to the ring flange only. Finally, at segment boundaries remote from the frame web and frame flange edges

$$\{u_F\}^{ms_i} + \{u_P\}^{ms_i} = \{u_I\}^{ms_{i+1}} + \{u_P\}^{ms_{i+1}} \quad (4.4.69)$$

where $\{u_F\}^{ms_i}$ represents $\{U\}$ evaluated at the end of multisegment ms_i , $\{u_I\}^{ms_{i+1}}$ represents $\{U\}$ evaluated at the beginning of the next adjacent multisegment ms_{i+1} and $\{u_P\}^{ms_i}$ and $\{u_P\}^{ms_{i+1}}$ represent the (constant) $\{U_P\}$ associated with multisegments ms_i and ms_{i+1} respectively. Assuming the domain is divided into a total of m multisegments, all of these boundary conditions can be written as a system of linear algebraic equations of the form

$$[b] \begin{Bmatrix} \{u_I^1\} \\ \vdots \\ \{u_I^m\} \end{Bmatrix} = \{f\}. \quad (4.4.70)$$

where $[b]$ contains terms associated with the $[\Phi]$ matrix of the various multisegments evaluated at the ends of these multisegments and $\{f\}$ contains terms associated with the applied loads and the particular solutions, $\{U_P\}$, of the various multisegments.

Hence,

$$\begin{Bmatrix} \{u_I^1\} \\ \vdots \\ \{u_I^m\} \end{Bmatrix} = [b]^{-1} \{f\}. \quad (4.4.71)$$

thus completing the solution of the problem. Note that the size of the $[b]$ matrix is $24+16m$ where m is the total number of multisegments. The adhesive stresses can then be calculated using Eqs. (4.4.17) through (4.4.19).

As stated earlier, some consideration of nonlinear material behavior of the adhesive is necessary in order to develop meaningful estimates of adhesive stresses. As noted by Hart-Smith⁹⁶, a typical ductile adhesive used in structural bonding exhibits significant nonlinear material behavior at stresses above 6000 psi. If this stress is a σ_{33} "peel" stress, failure due to delamination of the composite adherends would occur in a typical graphite/epoxy fiber composite laminate. This is the most typical failure mode for single-shear joints with laminated fiber composite adherends observed by Hart-Smith in the laboratory. Hence, assuming interlaminar normal stresses in the as-designed joint must remain below this 6000 psi threshold, Hart-Smith recognized that use of a linear relation between peel stress and peel strain (Eq. (4.4.10)) was adequate. Since the interlaminar shear strengths of most composite laminates tend to be significantly higher than 6000 psi, Hart-Smith chose to use an elastic-perfectly plastic adhesive model to relate transverse shear stresses to transverse shear strains.

Use of an elastic-perfectly plastic adhesive model is beyond the scope of this study. Instead, a simpler, more approximate approach will be taken. A "knockdown" factor will be applied to the transverse shear stresses of Eqs. (4.4.18) and (4.4.19) to

account for the shear stress relief afforded by nonlinear material behavior in the adhesive . An approach used by Corvelli⁹⁸, which yielded good correlation with experimental results, involves reducing the shear stress concentration factor in single-shear lap joints, calculated using a linear elastic analysis, by the ratio of the adhesive secant shear modulus to its initial tangent modulus. The stress concentration factor, K , is the ratio of the peak shear stress occurring at a joint edge to the nominal shear stress calculated by dividing the shear load applied to the joint by the bond area. Corvelli reduced K_e , the stress concentration factor calculated using a linear elastic analysis, to K_p , the estimated stress concentration factor accounting for adhesive plasticity using the relation

$$K_p = 1 + (K_e - 1) \frac{G_{sec}}{G_{tan}}. \quad (4.4.72)$$

where G_{sec} is the adhesive secant shear modulus and G_{tan} is the initial tangent shear modulus. In the case under consideration here, the nominal shear stress is very small since, unlike the case of a single-shear lap joint, the ring flange/cylinder skin joint considered in the present study transmits a very small net shearing force. Recognizing that the nominal shear stresses in Eq. (4.4.72) are small, the peak "elastic" and "plastic" adhesive shear stresses are related by a simple "knockdown" factor. This "knockdown" factor for the transverse shear stresses of the present study is G_{sec}/G_{tan} . Corvelli used 0.29 for this ratio. This value will also be used in the present study.

Chapter 5

BUCKLING ANALYSIS

5.1 Solution Methods

The buckling problem generally involves the solution of a set of linear, homogeneous partial differential equations and the satisfaction of a set of homogeneous boundary conditions. For example, the homogeneous equations derived by Booton³⁵, Eqs. (2.85) and (2.86) of Ref. 35, are the stability equations for imperfect, anisotropic cylindrical shells subject to combined loads. For the cylindrical shell and annular plate structures considered in this study the solutions to the partial differential equations must be periodic with respect to the circumferential coordinate ξ_2 ; hence, these partial differential equations can be reduced to a set of ordinary differential equations using the Fourier series. If for a specified load (assumed here to be characterized by a single parameter λ as will be described later in section 5.5) $F(\xi_1, \xi_2; \lambda)$ represents a typical solution to the stability equations, then F can be written in the form

$$F(\xi_1, \xi_2; \lambda) = \sum_{n=0}^{\infty} [f_1(\xi_1; \lambda) \sin \frac{n\xi_2}{R} + f_2(\xi_1; \lambda) \cos \frac{n\xi_2}{R}] \quad (5.1.1)$$

where ξ_1 is the axial coordinate of the cylindrical shell or the radial coordinate of the annular plate, ξ_2 is the circumferential coordinate, and R is the radius to the origin of the (ξ_1, ξ_2, ξ_3) coordinate system (the middle surface of the ring-stiffened cylindrical shell). Since stability equations are linear and homogeneous, then each term of Eq. (5.1.1) must satisfy these equations individually; hence, for a specified number of circumferential waves, $n_i \in \{n_1, n_2, \dots, n_t\}$, where t is the total number of different values of n considered in the analysis, the solution F can be written for each n_i

$$F(n_i; \xi_1, \xi_2; \lambda) = f_1(\xi_1; \lambda) \sin \frac{n_i \xi_2}{R} + f_2(\xi_1; \lambda) \cos \frac{n_i \xi_2}{R}. \quad (5.1.2)$$

Substitution of Eq. (5.1.2) into stability equations (such as Eqs. (2.85) and (2.86) of Ref. 35) eliminates the ξ_2 dependence of the problem and reduces the buckling problem to the solution of a set of ordinary differential equations in ξ_1 (see Eqs. (2.101)

through (2.104) of Ref. 35). Upon integration of these ordinary differential equations, a set of boundary conditions must be satisfied to determine the constants of integration. Since these boundary conditions are homogeneous, Eq. (5.1.2) is the only term from the original Fourier series (Eq. (5.1.1)) needed for a complete solution of the buckling problem. Satisfaction of the boundary conditions leads to an algebraic eigenvalue problem of the form

$$[B(n; \lambda)] \{C\} = 0 \quad (5.1.3)$$

where $[B(n; \lambda)]$ contains the solutions to the stability equations evaluated at boundary points, n_i is a specified circumferential wave number, λ is a parameter related to the imposed loads and $\{C\}$ is a vector of constants. If the order of $[B]$ is M-by-M then M discrete values of λ and corresponding vectors $\{C\}$ exist that result in a nontrivial solution of Eq. (5.1.3). For the specified value of n_i , the lowest value of λ (defined here as λ_n) is the critical load associated with that specified value of n_i and $\{C\}$ can be used along with Eq. (5.1.2) to determine the mode shape associated with λ_n . The buckling load (λ_{cr}) of the structure is then

$$\lambda_{cr} = \min(\lambda_n) \quad n = 0, 1, 2, \dots, n_t \quad (5.1.4)$$

and the mode shape associated with $\min(\lambda_n)$ is the buckled mode shape of the structure. If n_{cr} is the circumferential wave number associated with λ_{cr} , then this mode shape is

$$F(n_{cr}; \xi_1, \xi_2; \lambda_{cr}) = f_1(\xi_1; \lambda_{cr}) \sin \frac{n_{cr} \xi_2}{R} + f_2(\xi_1; \lambda_{cr}) \cos \frac{n_{cr} \xi_2}{R}. \quad (5.1.5)$$

For both the cylindrical shell and the annular plate, the stress resultants of the pre-buckled equilibrium configuration vary with the coordinate ξ_1 ; hence, the equations governing the stability of this equilibrium configuration have variable coefficients, making it very difficult to solve these equations in closed form. Hence, a numerical method must be chosen to solve the buckling problem. Many numerical techniques

exist that can be used to integrate the ordinary differential equations which characterize the buckling problem for a shell of revolution. One of the earliest methods used was finite differences (see, for example, Budiansky and Radkowski⁹⁹). Since the set of ordinary differential equations, generally of order four or higher, can be written as a system of first order equations, attempts were made to apply a forward integration technique such as Runge-Kutta integration or one of the predictor-corrector methods to solve this first order system. It was thought that such an analysis would be more efficient since it would alleviate the high computer storage requirements associated with the method of finite differences. Unfortunately, it was discovered that loss of numerical accuracy attributed to the exponential growth of the solutions to the first order system of equations limited the distance over which a forward integration could be performed. Kalnins⁹⁷ and Cohen^{100,101} solved the problem by breaking up the domain of integration into segments and restarting the forward integration procedure at the beginning of each segment. This numerical method is known as the "Multi-segment Technique" or "Parallel Shooting". Booton³⁵ used this method to determine theoretical buckling loads of imperfect, anisotropic cylindrical shells subject to combined loads. A technique known as the "field method", developed by Jordan and Shelley¹⁰², where the governing equations are reconfigured in order to eliminate the unbounded growth of the solutions to these equations, was successfully used by Cohen^{103,104} to solve highly complex branched shell problems without having to discretize the domain of integration of the governing equations, resulting in increased computational speed and significant savings in computer storage.

No matter which method is chosen to integrate the stability equations, the solution of an algebraic eigenvalue problem like Eq. (5.1.3) for λ_n generally accounts for the greatest expenditure of computer processing time, thus driving the efficiency of the entire algorithm. In general, for a specified value of the circumferential wave number, n_i , λ_n can be found from the following nonlinear equation

$$\det[B(n_i; \lambda)] = 0 \quad (5.1.6)$$

where $\det[B(n; \lambda)]$ is the determinant of the $[B(n; \lambda)]$ matrix in Eq. (5.1.3). In the classical buckling analyses of plates and shells, the prebuckling problem is solved using the techniques of linear structural analysis so that $[B(n; \lambda)]$ is a linear function of the load, represented by λ ; hence, Eq. (5.1.3) can be written as

$$\{[B_1(n)] + \lambda[B_2(n)]\}\{C\} = \{0\} \quad (5.1.7)$$

yielding a linear algebraic eigenvalue problem for the λ and their associated $\{C\}$. If, on the other hand, $[B(n; \lambda)]$ is a *nonlinear* function of λ , as is the case in this study, solution of Eq. (5.1.3) becomes more complicated. One popular method, known as determinant plotting, simply evaluates Eq. (5.1.6) for values of λ increasing incrementally from some initial value which is known to be less than λ_n until a change in the sign of the determinant is observed indicating that the determinant has passed through zero. Booton³⁵ used a generalized Gaussian elimination technique, sometimes referred to as "Potter's method"¹⁰⁵, involving submatrices of $[B(n; \lambda)]$ to reduce the search to one of finding zeros of the determinant of a much smaller submatrix known to possess all the zeros of the determinant of the original matrix $[B(n; \lambda)]$. This eliminated the numerical overflow or underflow problems associated with calculating the determinants of large order matrices. While the determinant plotting technique is very straightforward to implement, it is not suited for implementation into an automated search algorithm for λ_n . It was observed during the development of the theoretical analysis of this study that while $\det[B(n; \lambda)]$ does reach zero when $\lambda = \lambda_n$, the determinant *does not change sign* when the $\lambda > \lambda_n$. As was confirmed using the STAGS¹⁰⁶ finite element program, all of the values of λ leading to nontrivial solutions of Eq. (5.1.3) have two different mode shapes associated with them. In other words, all the eigenvalues of Eq. (5.1.3) are repeated once. This means that as λ is incremented past a critical value (a value resulting in a zero $\det[B(n; \lambda)]$), two critical values of λ are actually passed resulting in two simultaneous sign changes of the determinant for a net change of zero. Without a sign change in the determinant, an automated search for λ_n is very difficult. Upon plotting the two mode shapes associated with the repeated eigenvalues, it was

observed that the only difference between the two was a phase shift in the circumferential wave pattern. This could be caused by the fact that, in addition to Eq. (5.1.2), another possible solution to the stability equations is

$$F(n; \xi_1, \xi_2; \lambda) = f_2(\xi_1; \lambda) \sin \frac{n\xi_2}{R} + f_1(\xi_1; \lambda) \cos \frac{n\xi_2}{R}. \quad (5.1.8)$$

While it was not confirmed that this is indeed the reason for the repeated eigenvalues, it would produce two mode shapes that differ only by a phase shift. Booton's analysis does not suffer from the problem of these repeated eigenvalues because, by taking advantage of symmetry to reduce the domain of integration across the length of the shell by half, he eliminated Eq. (5.1.8) as a possible solution. The fact that values of λ leading to a zero determinant of $[B(n; \lambda)]$ tend to be very closely spaced forced Booton to use very small increments in λ to avoid passing two neighboring eigenvalues. Without a good initial estimate of λ_n , the determinant plotting method in this case could be computationally expensive.

As an alternative to determinant plotting, another technique proposed for the solution of Eq. (5.1.6) for critical values of λ is Newton's method. Application of Newton's method is hampered, however, by the behavior of the function $\det[B(n; \lambda)]$. As described in the paper by Blum and Fulton¹⁰⁷, as λ approaches a critical value, $\det[B(n; \lambda)]$ is not a monotonically decreasing function. Instead, $\det[B(n; \lambda)]$ behaves more like a step function in the vicinity of a critical value of λ ; hence, unless a very good initial estimate of the desired critical value is available ("very good" in this case being an initial value of λ within five percent of a critical value or less), it is highly likely that Newton's method will converge to an eigenvalue that is greater than λ_n if the method converges at all, rendering the method unreliable. Keller¹⁰⁸ presents ways of deriving functions which are smoother and more well-behaved than $\det[B(n; \lambda)]$ that have all the same zeros as $\det[B(n; \lambda)]$. These methods were also evaluated during the course of this study. While the functions proposed by Keller were more well-behaved than $\det[B(n; \lambda)]$, the close spacing of the critical values of λ which is a

characteristic of shell buckling problems still made it too likely that application of Newton's method would result in convergence to an eigenvalue, λ , greater than λ_n .

For the case where $[B(n; \lambda)]$ is a nonlinear function of λ , greater success has been achieved by applying Newton's method to Eq. (5.1.3) rather than Eq. (5.1.6). If λ^i represents an estimate of λ_n such that $\lambda^i < \lambda_n$, then a better estimate, λ^{i+1} can be found by solving the linear eigenvalue problem (see Eq. (3) of Ref. 109)

$$\{[B(n; \lambda^i)] + \Delta\lambda^i [\dot{B}(n; \lambda^i)]\}\{C\} = \{0\} \quad (5.1.9)$$

for the correction term $\Delta\lambda^i$, which is the smallest eigenvalue of Eq. (5.1.9), where $[\dot{B}(n; \lambda^i)]$ is the first derivative of $[B(n; \lambda^i)]$ with respect to λ . An improved estimate of λ_n (λ^{i+1}) is found by

$$\lambda^{i+1} = \lambda^i + r\Delta\lambda^i \quad (5.1.10)$$

where $0 \leq r \leq 1$ to insure that $\lambda^i < \lambda_n$ after each iteration (see Sun¹¹⁰). Iterations continue until λ^{i+1} is sufficiently close to λ^i to assume convergence has been achieved.

In order for the technique of solving the nonlinear buckling eigenvalue problem as a series of linear eigenvalue problems to be efficient, Eq. (5.1.9) must be solved very rapidly. A number of computer programs are available to do this. The most numerous and efficient programs have been written to solve linear eigenvalue problems such as Eq. (5.1.9) where both $[B(n; \lambda^i)]$ and $[\dot{B}(n; \lambda^i)]$ are symmetric matrices and one of them is positive definite so that all of the eigenvalues, $\Delta\lambda$, are real numbers. When neither $[B(n; \lambda^i)]$ nor $[\dot{B}(n; \lambda^i)]$ is positive definite and/or one of the matrices is not symmetric, then *complex* values of $\Delta\lambda$ may exist (see Meirovitch¹¹¹) requiring a more general (and time-consuming) algorithm to solve the eigenvalue problem. It was observed during the course of this study that such complex values of $\Delta\lambda$ occurred when the buckling problem was posed using the mixed stress/displacement formulation employed by Booton³⁵ and Sun¹¹⁰. These complex values of $\Delta\lambda$ do not have a clear physical meaning. Posing the buckling problem using a pure displacement formulation yields symmetric matrices for both $[B(n; \lambda^i)]$ and $[\dot{B}(n; \lambda^i)]$ of Eq. (5.1.9).

If λ^i is chosen so that $\lambda^i < \lambda_n$, then $[B(n; \lambda^i)]$ being positive definite eliminates the possibility of complex values of $\Delta\lambda$. During the present study, it was concluded that the loss of efficiency in solving Eq. (5.1.9) caused by the existence of complex values of $\Delta\lambda$ eclipsed the gains in efficiency realized by reducing the number of primary unknowns from three to two using the mixed stress/displacement formulation. Hence, a pure displacement formulation, for which a well-documented stability theory related to the second variation of the total potential energy exists, was chosen for the present study.

Along with the pure displacement formulation of the buckling problem, the numerical technique chosen to solve this problem in the present study is the finite element method. The finite element method was chosen since a limited amount of computer storage was not a critical issue and the method can be formulated directly from variational principles without the need for an explicit derivation of the stability equations. What follows in section 5.2 is the derivation of the finite element model of the second variation of the total potential energy for a cylindrical shell element. The derivation of the finite element model of the second variation of the total potential energy for the annular plate element appears in section 5.3. Assembly of the elemental finite element models into the global finite element model for the ring-stiffened cylinder is outlined in section 5.4, and the application of Trefftz criterion which yields the nonlinear buckling eigenvalue problem is outlined in section 5.5.

5.2 Finite Element Model of The Second Variation Of The Total Potential Energy of a Laminated Cylindrical Shell

The total potential energy of a thin, imperfect cylindrical shell element subject to combined loads is

$$\Pi = \frac{1}{2} \int_{\xi_1} \int_{\xi_2} \int_{\xi_3} \{\sigma\}^T \{\epsilon - \epsilon^P\} d\xi_3 d\xi_2 d\xi_1 + \Pi_{load} \quad (5.2.1)$$

where

$$\{\sigma\} = \begin{Bmatrix} \sigma_{11} \\ \sigma_{22} \\ \tau_{12} \end{Bmatrix} \quad (5.2.2)$$

and

$$\{\epsilon - \epsilon^P\} = \begin{Bmatrix} \epsilon_{11} - \epsilon_{11}^P \\ \epsilon_{22} - \epsilon_{22}^P \\ \gamma_{12} - \gamma_{12}^P \end{Bmatrix} \quad (5.2.3)$$

where σ_{ij} is a stress with respect to the $\xi_i \xi_j$ *load oriented* or *global* coordinate direction (not to be confused with the *material* or *local* coordinate direction), ϵ_{ij} is a total strain with respect to the $\xi_i \xi_j$ coordinate direction, Π_{load} is the potential energy of the interactive loads between elements and any externally applied loads and ϵ_{ij}^P is an initial strain with respect to the $\xi_i \xi_j$ coordinate direction arising from the initial geometric imperfection. It is assumed that the unloaded, imperfect cylinder is stress-free; furthermore, the imperfection is assumed to be in the form of an axisymmetric radial displacement, w_o , where

$$w_o = w_o(\xi_1) \quad (5.2.4)$$

and the nondimensional functional form of w_o is given in Eq. (4.1.25). Setting the cone angle ϕ equal to zero (see Fig. 3.3.1) in Eqs. (3.3.1.5) through (3.3.1.9), the strain-displacement relations from DMV theory are

$$\epsilon_{11} = \epsilon_{11}^o(\xi_1, \xi_2) + \xi_3 \kappa_{11}(\xi_1, \xi_2) \quad (5.2.5)$$

$$\epsilon_{22} = \epsilon_{22}^o(\xi_1, \xi_2) + \xi_3 \kappa_{22}(\xi_1, \xi_2) \quad (5.2.6)$$

$$\gamma_{12} = \gamma_{12}^{\circ}(\xi_1, \xi_2) + \xi_3 \kappa_{12}(\xi_1, \xi_2) \quad (5.2.7)$$

where

$$\epsilon_{11}^{\circ} = \frac{\partial u_1^{\circ}}{\partial \xi_1} + \frac{1}{2} \left(\frac{\partial u_3^{\circ}}{\partial \xi_1} \right)^2 \quad (5.2.8)$$

$$\epsilon_{22}^{\circ} = \frac{\partial u_2^{\circ}}{\partial \xi_2} + \frac{u_3^{\circ}}{R} + \frac{1}{2} \left(\frac{\partial u_3^{\circ}}{\partial \xi_2} \right)^2 \quad (5.2.9)$$

$$\gamma_{12}^{\circ} = \frac{\partial u_1^{\circ}}{\partial \xi_2} + \frac{\partial u_2^{\circ}}{\partial \xi_1} + \frac{\partial u_3^{\circ}}{\partial \xi_1} \frac{\partial u_3^{\circ}}{\partial \xi_2} \quad (5.2.10)$$

$$\kappa_{11} = -\frac{\partial^2 u_3^{\circ}}{\partial \xi_1^2} \quad (5.2.11)$$

$$\kappa_{22} = -\frac{\partial^2 u_3^{\circ}}{\partial \xi_2^2} \quad (5.2.12)$$

$$\kappa_{12} = -2 \frac{\partial^2 u_3^{\circ}}{\partial \xi_1 \partial \xi_2}. \quad (5.2.13)$$

and all of the terms in Eqs. (5.2.5) through (5.2.13) have been defined in section

3.3.1. The initial strains due to the geometric imperfection can be found by setting

$u_3^{\circ} = w_0$ and $u_1^{\circ} = u_2^{\circ} = 0$ in Eqs. (5.2.8) through (5.2.13), yielding

$$\epsilon_{11}^P = \epsilon_{11}^{\circ P} + \xi_3 \kappa_{11}^P \quad (5.2.14)$$

$$\epsilon_{22}^P = \epsilon_{22}^{\circ P} + \xi_3 \kappa_{22}^P \quad (5.2.15)$$

$$\epsilon_{12}^P = \gamma_{12}^{\circ P} + \xi_3 \kappa_{12}^P \quad (5.2.16)$$

where

$$\epsilon_{11}^{\circ P} = \frac{1}{2} \left(\frac{\partial w_0}{\partial \xi_1} \right)^2 \quad (5.2.17)$$

$$\epsilon_{22}^{\circ P} = \frac{w_0}{R} \quad (5.2.18)$$

$$\gamma_{12}^{\circ P} = 0 \quad (5.2.19)$$

$$\kappa_{11}^P = -\frac{\partial^2 w_0}{\partial \xi_1^2} \quad (5.2.20)$$

$$\kappa_{22}^P = 0 \quad (5.2.21)$$

$$\kappa_{12}^P = 0 \quad (5.2.22)$$

The displacement u_3° in Eqs. (5.2.8) through (5.2.13) is the radial displacement of the middle surface of the perfect cylinder. Replacing u_3° in these equations with $u_3^\circ + w_o$ so that u_3° now represents the radial displacement of the middle surface of the imperfect cylinder, then substituting Eqs. (5.2.5) through (5.2.22) into Eq. (5.2.1) gives

$$\Pi = \frac{1}{2} \int_{\xi_1} \int_{\xi_2} \int_{\xi_3} \{\sigma\}^T \{ \{\tilde{\epsilon}^\circ\} + \xi_3 \{\hat{\kappa}\} \} d\xi_3 d\xi_2 d\xi_1 + \Pi_{load} \quad (5.2.23)$$

where

$$\{\tilde{\epsilon}^\circ\} = \begin{Bmatrix} \tilde{\epsilon}_{11}^\circ \\ \tilde{\epsilon}_{22}^\circ \\ \tilde{\gamma}_{12}^\circ \end{Bmatrix} \quad (5.2.24)$$

$$\{\hat{\kappa}\} = \begin{Bmatrix} \hat{\kappa}_{11} \\ \hat{\kappa}_{22} \\ \hat{\kappa}_{12} \end{Bmatrix} \quad (5.2.25)$$

$$\tilde{\epsilon}_{11}^\circ = \frac{\partial u_1^\circ}{\partial \xi_1} + \frac{1}{2} \left(\frac{\partial u_3^\circ}{\partial \xi_1} \right)^2 + \frac{\partial u_3^\circ}{\partial \xi_1} \frac{\partial w_o}{\partial \xi_1} \quad (5.2.26)$$

$$\tilde{\epsilon}_{22}^\circ = \epsilon_{22}^\circ = \frac{\partial u_2^\circ}{\partial \xi_2} + \frac{u_3^\circ}{R} + \frac{1}{2} \left(\frac{\partial u_3^\circ}{\partial \xi_2} \right)^2 \quad (5.2.27)$$

$$\tilde{\gamma}_{12}^\circ = \frac{\partial u_1^\circ}{\partial \xi_2} + \frac{\partial u_2^\circ}{\partial \xi_1} + \frac{\partial u_3^\circ}{\partial \xi_1} \frac{\partial u_3^\circ}{\partial \xi_2} + \frac{\partial w_o}{\partial \xi_1} \frac{\partial u_3^\circ}{\partial \xi_2} \quad (5.2.28)$$

$$\hat{\kappa}_{11} = \kappa_{11} = -\frac{\partial^2 u_3^\circ}{\partial \xi_1^2} \quad (5.2.29)$$

$$\hat{\kappa}_{22} = \kappa_{22} = -\frac{\partial^2 u_3^\circ}{\partial \xi_2^2} \quad (5.2.30)$$

$$\hat{\kappa}_{12} = \kappa_{12} = -2 \frac{\partial^2 u_3^\circ}{\partial \xi_1 \partial \xi_2} \quad (5.2.31)$$

and the $\tilde{\epsilon}_{ij}^\circ$ and $\hat{\kappa}_{ij}$ are shell middle surface mechanical strains and curvatures with respect to the $\xi_i \xi_j$ coordinate directions, which are zero in the unloaded structure. Integrating Eq. (5.2.23) with respect to ξ_3 yields

$$\Pi = \frac{1}{2} \int_{\xi_1} \int_{\xi_2} \{ \{N\}^T \{\tilde{\epsilon}^\circ\} + \{M\}^T \{\hat{\kappa}\} \} d\xi_2 d\xi_1 + \Pi_{load} \quad (5.2.32)$$

where, as in Eqs. (3.3.2.2) and (3.3.2.3)

$$\{N\} = \begin{Bmatrix} N_{11} \\ N_{22} \\ N_{12} \end{Bmatrix} = \int_{\xi_3} \begin{Bmatrix} \sigma_{11} \\ \sigma_{22} \\ \tau_{12} \end{Bmatrix} d\xi_3 \quad (5.2.33)$$

and

$$\{M\} = \begin{Bmatrix} M_{11} \\ M_{22} \\ M_{12} \end{Bmatrix} = \int_{\xi_3} \xi_3 \begin{Bmatrix} \sigma_{11} \\ \sigma_{22} \\ \tau_{12} \end{Bmatrix} d\xi_3 \quad (5.2.34)$$

are stress resultants and stress couples and the superscript T indicates the transpose of a matrix or vector. Eq. (5.2.32), written in nondimensional form becomes

$$\bar{\Pi} = \frac{1}{2} \int_{\bar{\xi}_1} \int_{\bar{\xi}_2} \{ \{\bar{N}\}^T \{\bar{\epsilon}^\circ\} + \{\bar{M}\}^T \{\bar{\kappa}\} \} d\bar{\xi}_2 d\bar{\xi}_1 + \bar{\Pi}_{load}. \quad (5.2.35)$$

where the overlined quantities are nondimensional quantities that are defined in Table 1. Also defined in Table 1 are the nondimensional membrane stiffnesses \bar{A}_{nm} , the nondimensional membrane-bending coupling stiffnesses \bar{B}_{nm} and the nondimensional bending stiffnesses \bar{D}_{nm} used in the nondimensional form of the stress-strain equations (Eq. (3.3.2.1)) given by

$$\begin{Bmatrix} \bar{N}_{11} \\ \bar{N}_{22} \\ \bar{N}_{12} \\ \bar{M}_{11} \\ \bar{M}_{22} \\ \bar{M}_{12} \end{Bmatrix} = \begin{bmatrix} \bar{A}_{11} & \bar{A}_{12} & \bar{A}_{16} & \bar{B}_{11} & \bar{B}_{12} & \bar{B}_{16} \\ \bar{A}_{12} & \bar{A}_{22} & \bar{A}_{26} & \bar{B}_{21} & \bar{B}_{22} & \bar{B}_{26} \\ \bar{A}_{16} & \bar{A}_{26} & \bar{A}_{66} & \bar{B}_{61} & \bar{B}_{62} & \bar{B}_{66} \\ \bar{B}_{11} & \bar{B}_{21} & \bar{B}_{61} & \bar{D}_{11} & \bar{D}_{12} & \bar{D}_{16} \\ \bar{B}_{12} & \bar{B}_{22} & \bar{B}_{62} & \bar{D}_{12} & \bar{D}_{22} & \bar{D}_{26} \\ \bar{B}_{16} & \bar{B}_{26} & \bar{B}_{66} & \bar{D}_{16} & \bar{D}_{26} & \bar{D}_{66} \end{bmatrix} \begin{Bmatrix} \bar{\epsilon}_{11}^\circ \\ \bar{\epsilon}_{22}^\circ \\ \bar{\gamma}_{12}^\circ \\ \bar{\kappa}_{11} \\ \bar{\kappa}_{22} \\ \bar{\kappa}_{12} \end{Bmatrix} \equiv [c] \begin{Bmatrix} \bar{\epsilon}_{11}^\circ \\ \bar{\epsilon}_{22}^\circ \\ \bar{\gamma}_{12}^\circ \\ \bar{\kappa}_{11} \\ \bar{\kappa}_{22} \\ \bar{\kappa}_{12} \end{Bmatrix}. \quad (5.2.36)$$

The prebuckled equilibrium configuration can be determined by setting the first variation of the total potential energy equal to zero. This leads to

$$\delta \bar{\Pi} = \int_{\bar{\xi}_1} \int_{\bar{\xi}_2} \{ \{\bar{N}\}^T \{\delta \bar{\epsilon}^\circ\} + \{\bar{M}\}^T \{\delta \bar{\kappa}\} \} d\bar{\xi}_2 d\bar{\xi}_1 + \delta \bar{\Pi}_{load} = 0 \quad (5.2.37)$$

where δ is the variational operator. The equilibrium configuration resulting from Eq. (5.2.37) is stable if the second variation of the total potential energy is positive for all

kinematically admissible displacement fields. The second variation can be written (in nondimensional form) as

$$\delta^2 \Pi = \int_{\bar{\xi}_1} \int_{\bar{\xi}_2} \{ \{\bar{N}'\}^T \{\delta \hat{\epsilon}^\circ\} + \{\bar{M}'\}^T \{\delta \hat{\kappa}\} + \{\bar{N}\}^T \{\delta^2 \hat{\epsilon}^\circ\} + \{\bar{M}\}^T \{\delta^2 \hat{\kappa}\} \} d\bar{\xi}_2 d\bar{\xi}_1 + \delta^2 \Pi_{load} \quad (5.2.38)$$

where $\{\bar{N}'\}$ and $\{\bar{M}'\}$ are buckling stress resultants and stress couples given by

$$\begin{Bmatrix} \bar{N}'_{11} \\ \bar{N}'_{22} \\ \bar{N}'_{12} \\ \bar{M}'_{11} \\ \bar{M}'_{22} \\ \bar{M}'_{12} \end{Bmatrix} = \begin{bmatrix} \bar{A}_{11} & \bar{A}_{12} & \bar{A}_{16} & \bar{B}_{11} & \bar{B}_{12} & \bar{B}_{16} \\ \bar{A}_{12} & \bar{A}_{22} & \bar{A}_{26} & \bar{B}_{21} & \bar{B}_{22} & \bar{B}_{26} \\ \bar{A}_{16} & \bar{A}_{26} & \bar{A}_{66} & \bar{B}_{61} & \bar{B}_{62} & \bar{B}_{66} \\ \bar{B}_{11} & \bar{B}_{21} & \bar{B}_{61} & \bar{D}_{11} & \bar{D}_{12} & \bar{D}_{16} \\ \bar{B}_{12} & \bar{B}_{22} & \bar{B}_{62} & \bar{D}_{12} & \bar{D}_{22} & \bar{D}_{26} \\ \bar{B}_{16} & \bar{B}_{26} & \bar{B}_{66} & \bar{D}_{16} & \bar{D}_{26} & \bar{D}_{66} \end{bmatrix} \begin{Bmatrix} \delta \hat{\epsilon}_{11}^\circ \\ \delta \hat{\epsilon}_{22}^\circ \\ \delta \hat{\gamma}_{12}^\circ \\ \delta \hat{\kappa}_{11} \\ \delta \hat{\kappa}_{22} \\ \delta \hat{\kappa}_{12} \end{Bmatrix} \equiv [c] \begin{Bmatrix} \delta \hat{\epsilon}_{11}^\circ \\ \delta \hat{\epsilon}_{22}^\circ \\ \delta \hat{\gamma}_{12}^\circ \\ \delta \hat{\kappa}_{11} \\ \delta \hat{\kappa}_{22} \\ \delta \hat{\kappa}_{12} \end{Bmatrix} \quad (5.2.39)$$

Taking two variations of the strain-displacement equations (Eqs. (5.2.26) through (5.2.31), substituting the resulting expressions into Eq. (5.2.38), and simplifying $\delta^2 \Pi$ using Eq. (5.2.37) results in

$$\begin{aligned} \delta^2 \Pi = & \int_{\bar{\xi}_1} \int_{\bar{\xi}_2} \left\{ \begin{Bmatrix} \bar{N}'_{11} \\ \bar{N}'_{22} \\ \bar{N}'_{12} \end{Bmatrix}^T \begin{Bmatrix} (\partial \bar{u}_1' / \partial \bar{\xi}_1) \\ (\partial \bar{u}_2' / \partial \bar{\xi}_2) + \bar{Z} \bar{u}_3' \\ (\partial \bar{u}_1' / \partial \bar{\xi}_2) + (\partial \bar{u}_2' / \partial \bar{\xi}_1) \end{Bmatrix} \right\} d\bar{\xi}_2 d\bar{\xi}_1 \\ & + \int_{\bar{\xi}_1} \int_{\bar{\xi}_2} \left\{ \begin{Bmatrix} \bar{M}'_{11} \\ \bar{M}'_{22} \\ \bar{M}'_{12} \end{Bmatrix}^T \begin{Bmatrix} -(\partial^2 \bar{u}_3' / \partial \bar{\xi}_1^2) \\ -(\partial^2 \bar{u}_3' / \partial \bar{\xi}_2^2) \\ -2(\partial^2 \bar{u}_3' / \partial \bar{\xi}_1 \partial \bar{\xi}_2) \end{Bmatrix} \right\} d\bar{\xi}_2 d\bar{\xi}_1 \end{aligned}$$

$$\begin{aligned}
& + \int_{\bar{\xi}_1} \int_{\bar{\xi}_2} \left\{ \begin{pmatrix} \bar{N}'_{11} \\ \bar{N}'_{22} \\ \bar{N}'_{12} \end{pmatrix}^T \begin{pmatrix} [d\bar{u}_3'/d\bar{\xi}_1 + d\bar{w}_o/d\bar{\xi}_1] (\partial\bar{u}_3'/\partial\bar{\xi}_1) \\ 0 \\ [d\bar{u}_3'/d\bar{\xi}_1 + d\bar{w}_o/d\bar{\xi}_1] (\partial\bar{u}_3'/\partial\bar{\xi}_2) \end{pmatrix} \right\} d\bar{\xi}_2 d\bar{\xi}_1 \\
& + \int_{\bar{\xi}_1} \int_{\bar{\xi}_2} \left\{ \begin{pmatrix} \bar{N}_{11} \\ \bar{N}_{22} \\ \bar{N}_{12} \end{pmatrix}^T \begin{pmatrix} (\partial\bar{u}_3'/\partial\bar{\xi}_1)(\partial\bar{u}_3'/\partial\bar{\xi}_1) \\ (\partial\bar{u}_3'/\partial\bar{\xi}_2)(\partial\bar{u}_3'/\partial\bar{\xi}_2) \\ 2(\partial\bar{u}_3'/\partial\bar{\xi}_1)(\partial\bar{u}_3'/\partial\bar{\xi}_2) \end{pmatrix} \right\} d\bar{\xi}_2 d\bar{\xi}_1 \\
& + \delta^2 \bar{\Pi}_{load} \tag{5.2.40}
\end{aligned}$$

where $()'$ indicates that $()$ is a buckling quantity and unprimed quantities are determined from the prebuckling equilibrium configuration. Any derivatives of a prebuckling quantity with respect to ξ_2 have been dropped due to the assumed axisymmetric response of the prebuckled equilibrium configuration. As mentioned in section 5.1, due to the periodic geometry of the cylindrical shell, the nondimensional middle surface buckling displacements \bar{u}_1' , \bar{u}_2' and \bar{u}_3' and the nondimensional buckling stress resultants and stress couples \bar{N}'_{11} , \bar{N}'_{22} , \bar{N}'_{12} , \bar{M}'_{11} , \bar{M}'_{22} and \bar{M}'_{12} can be written in terms of a Fourier series in the circumferential coordinate, ξ_2 . In other words

$$\begin{pmatrix} \bar{u}_1' \\ \bar{u}_2' \\ \bar{u}_3' \end{pmatrix} = \begin{pmatrix} \bar{U}_1(\bar{\xi}_1) \\ \bar{V}_1(\bar{\xi}_1) \\ \bar{W}_1(\bar{\xi}_1) \end{pmatrix} \sin \beta \bar{\xi}_2 + \begin{pmatrix} \bar{U}_2(\bar{\xi}_1) \\ \bar{V}_2(\bar{\xi}_1) \\ \bar{W}_2(\bar{\xi}_1) \end{pmatrix} \cos \beta \bar{\xi}_2 \tag{5.2.41}$$

$$\begin{Bmatrix} \overline{N}'_{11} \\ \overline{N}'_{22} \\ \overline{N}'_{12} \end{Bmatrix} = \begin{Bmatrix} \overline{NX}_1(\bar{\xi}_1) \\ \overline{NY}_1(\bar{\xi}_1) \\ \overline{NXY}_1(\bar{\xi}_1) \end{Bmatrix} \sin \beta \bar{\xi}_2 + \begin{Bmatrix} \overline{NX}_2(\bar{\xi}_1) \\ \overline{NY}_2(\bar{\xi}_1) \\ \overline{NXY}_2(\bar{\xi}_1) \end{Bmatrix} \cos \beta \bar{\xi}_2 \quad (5.2.42)$$

$$\begin{Bmatrix} \overline{M}'_{11} \\ \overline{M}'_{22} \\ \overline{M}'_{12} \end{Bmatrix} = \begin{Bmatrix} \overline{MX}_1(\bar{\xi}_1) \\ \overline{MY}_1(\bar{\xi}_1) \\ \overline{MXY}_1(\bar{\xi}_1) \end{Bmatrix} \sin \beta \bar{\xi}_2 + \begin{Bmatrix} \overline{MX}_2(\bar{\xi}_1) \\ \overline{MY}_2(\bar{\xi}_1) \\ \overline{MXY}_2(\bar{\xi}_1) \end{Bmatrix} \cos \beta \bar{\xi}_2 \quad (5.2.43)$$

where

$$\beta = \frac{nL}{R} \quad (5.2.44)$$

n is a circumferential wave number, L is the length and R is the middle surface radius of the cylinder. Substituting Eqs. (5.2.41) through (5.2.43) into Eq. (5.2.40) and performing the integration with respect to the nondimensional circumferential coordinate, $\bar{\xi}_2$, results in

$$\begin{aligned} \delta^2 \overline{\Pi} = & \frac{\pi R}{L} \int_{\bar{\xi}_1} \left\{ \begin{Bmatrix} \{f1\} \\ \{f2\} \end{Bmatrix}^T \begin{Bmatrix} \{ek1\} \\ \{ek2\} \end{Bmatrix} + \begin{Bmatrix} \{f1\} \\ \{f2\} \end{Bmatrix}^T \begin{Bmatrix} \{el1\} \\ \{el2\} \end{Bmatrix} \right\} d\bar{\xi}_1 \\ & + \frac{\pi R}{L} \int_{\bar{\xi}_1} \left\{ \overline{N}_{11} \left(\frac{d\overline{W}_1}{d\bar{\xi}_1} \frac{d\overline{W}_1}{d\bar{\xi}_1} + \frac{d\overline{W}_2}{d\bar{\xi}_1} \frac{d\overline{W}_2}{d\bar{\xi}_1} \right) + \overline{N}_{22} \beta^2 (\overline{W}_1 \overline{W}_1 + \overline{W}_2 \overline{W}_2) \right\} d\bar{\xi}_1 \\ & + \frac{\pi R}{L} \int_{\bar{\xi}_1} \left\{ 2\overline{N}_{12} \left(\frac{d\overline{W}_2}{d\bar{\xi}_1} \overline{W}_1 - \frac{d\overline{W}_1}{d\bar{\xi}_1} \overline{W}_2 \right) \right\} d\bar{\xi}_1 + \delta^2 \overline{\Pi}_{load} \end{aligned} \quad (5.2.45)$$

where

$$\begin{aligned}
ek1_1 &= \frac{d\bar{U}_1}{d\xi_1} & el1_1 &= \left[\frac{d\bar{u}_a}{d\xi_1} + \frac{d\bar{w}_a}{d\xi_1} \right] \frac{d\bar{W}_1}{d\xi_1} \\
ek1_2 &= -\beta\bar{V}_2 + \bar{Z}\bar{W}_1 & el1_2 &= 0 \\
ek1_3 &= -\beta\bar{U}_2 + \frac{d\bar{V}_1}{d\xi_1} & el1_3 &= -\left[\frac{d\bar{u}_a}{d\xi_1} + \frac{d\bar{w}_a}{d\xi_1} \right] \frac{d\bar{W}_1}{d\xi_1} \beta\bar{W}_2 \\
ek1_4 &= \frac{-d^2\bar{W}_1}{d\xi_1^2} & el1_4 &= 0 \\
ek1_5 &= \beta^2\bar{W}_1 & el1_5 &= 0 \\
ek1_6 &= 2\beta\frac{d\bar{W}_2}{d\xi_1} & el1_6 &= 0 \\
ek2_1 &= \frac{d\bar{U}_2}{d\xi_1} & el2_1 &= \left[\frac{d\bar{u}_a}{d\xi_1} + \frac{d\bar{w}_a}{d\xi_1} \right] \frac{d\bar{W}_2}{d\xi_1} \\
ek2_2 &= \beta\bar{V}_1 + \bar{Z}\bar{W}_2 & el2_2 &= 0 \\
ek2_3 &= \beta\bar{U}_1 + \frac{d\bar{V}_2}{d\xi_1} & el2_3 &= -\left[\frac{d\bar{u}_a}{d\xi_1} + \frac{d\bar{w}_a}{d\xi_1} \right] \beta\bar{W}_1 \\
ek2_4 &= \frac{-d^2\bar{W}_2}{d\xi_1^2} & el2_4 &= 0 \\
ek2_5 &= \beta^2\bar{W}_2 & el2_5 &= 0 \\
ek2_6 &= -2\beta\frac{d\bar{W}_1}{d\xi_1} & el2_6 &= 0.
\end{aligned} \tag{5.2.46}$$

$$\begin{aligned}
f1_1 &= \bar{N}\bar{X}_1 & f2_1 &= \bar{N}\bar{X}_2 \\
f1_2 &= \bar{N}\bar{Y}_1 & f2_2 &= \bar{N}\bar{Y}_2 \\
f1_3 &= \bar{N}\bar{X}\bar{Y}_1 & f2_3 &= \bar{N}\bar{X}\bar{Y}_2 \\
f1_4 &= \bar{M}\bar{X}_1 & f2_4 &= \bar{M}\bar{X}_2 \\
f1_5 &= \bar{M}\bar{Y}_1 & f2_5 &= \bar{M}\bar{Y}_2 \\
f1_6 &= \bar{M}\bar{X}\bar{Y}_1 & f2_6 &= \bar{M}\bar{X}\bar{Y}_2
\end{aligned} \tag{5.2.47}$$

and $ek1_i$, $ek1_2$, $el1_i$, $el2_i$, $f1_i$ and $f2_i$ are the i th row elements of $\{ek1\}$, $\{ek2\}$, $\{el1\}$, $\{el2\}$, $\{f1\}$ and $\{f2\}$ respectively. By substituting Eqs. (5.2.41) through (5.2.43) into Eq. (5.2.39), it can be shown that

$$\begin{Bmatrix} \{f1\} \\ \{f2\} \end{Bmatrix}^T = \begin{Bmatrix} \{ek1\} \\ \{ek2\} \end{Bmatrix}^T \begin{bmatrix} [\mathbf{c}] & [0] \\ [0] & [\mathbf{c}] \end{bmatrix}^T + \begin{Bmatrix} \{el1\} \\ \{el2\} \end{Bmatrix}^T \begin{bmatrix} [\mathbf{c}] & [0] \\ [0] & [\mathbf{c}] \end{bmatrix}^T. \tag{5.2.48}$$

For a single finite element (see Fig. 5.2.1), the buckling displacements $\bar{U}_1, \bar{U}_2, \bar{V}_1, \bar{V}_2, \bar{W}_1$ and \bar{W}_2 are written as

$$\begin{aligned}\bar{U}_1(\bar{\xi}_1) &= \{U1\}^T \{\Phi_1(\bar{\xi}_1)\} & \bar{V}_2(\bar{\xi}_1) &= \{V2\}^T \{\Psi_2(\bar{\xi}_1)\} \\ \bar{U}_2(\bar{\xi}_1) &= \{U2\}^T \{\Phi_2(\bar{\xi}_1)\} & \bar{W}_1(\bar{\xi}_1) &= \{W1\}^T \{\Omega_1(\bar{\xi}_1)\} \\ \bar{V}_1(\bar{\xi}_1) &= \{V1\}^T \{\Psi_1(\bar{\xi}_1)\} & \bar{W}_2(\bar{\xi}_1) &= \{W2\}^T \{\Omega_2(\bar{\xi}_1)\}\end{aligned}\quad (5.2.49)$$

where $\{\Phi_1(\bar{\xi}_1)\}, \{\Phi_2(\bar{\xi}_1)\}, \{\Psi_1(\bar{\xi}_1)\}, \{\Psi_2(\bar{\xi}_1)\}, \{\Omega_1(\bar{\xi}_1)\}$, and $\{\Omega_2(\bar{\xi}_1)\}$ are vectors of polynomials whose dimensions depend on the type of interpolation employed and $\{U1\}, \{U2\}, \{V1\}, \{V2\}, \{W1\}$ and $\{W2\}$ are vectors of nodal buckling displacements and rotations. The domain of $\bar{\xi}_1$ in this case is understood to be from $\bar{\xi}_1^e$ to $\bar{\xi}_1^{e+1}$. $\{\Omega_1(\bar{\xi}_1)\}$, and $\{\Omega_2(\bar{\xi}_1)\}$ are Hermite polynomial interpolation functions of order three and $\{\Phi_1(\bar{\xi}_1)\}, \{\Phi_2(\bar{\xi}_1)\}, \{\Psi_1(\bar{\xi}_1)\}$ and $\{\Psi_2(\bar{\xi}_1)\}$ are Lagrange polynomial interpolation functions of at least order one. Substituting Eqs. (5.2.48) and (5.2.49) into Eq. (5.2.45), the second variation of the nondimensional total potential energy for a single cylindrical shell element and a single specified circumferential wave number, n , can be written in terms of a stiffness matrix, $[K^e(n)]$, which is not a function of the applied loads, and a geometric stiffness matrix, $[K_G^e(n; \lambda)]$ which is a function of the applied loads indicated by the load parameter λ . The matrices $[K^e(n)]$ and $[K_G^e(n; \lambda)]$ along with the finite element model of the second variation of the nondimensional total potential energy appear in Appendix C.

5.3 Finite Element Model of The Second Variation Of The Total Potential Energy of a Laminated Annular Plate

The development of the finite element model for the second variation of the total potential energy for the laminated annular plate follows the same steps as the development of the model for the cylindrical shell; however, initial geometric imperfections in the annular plate are ignored. The total potential energy for the perfect annular plate element is

$$\Pi = \frac{1}{2} \int_{\xi_1} \int_{\xi_2} \int_{\xi_3} \{\sigma\}^T \{\epsilon\} \left(1 - \frac{\xi_1}{R}\right) d\xi_3 d\xi_2 d\xi_1 + \Pi_{load} \quad (5.3.1)$$

where

$$\{\sigma\} = \begin{Bmatrix} \sigma_{11} \\ \sigma_{22} \\ \tau_{12} \end{Bmatrix} \quad (5.3.2)$$

and

$$\{\epsilon\} = \begin{Bmatrix} \epsilon_{11} \\ \epsilon_{22} \\ \gamma_{12} \end{Bmatrix} \quad (5.3.3)$$

where σ_{ij} is a stress with respect to the $\xi_i \xi_j$ coordinate direction, ϵ_{ij} is a strain with respect to the $\xi_i \xi_j$ coordinate direction and Π_{load} is the potential energy of the interactive loads between elements and externally applied loads. Setting the cone angle ϕ equal to ninety degrees (see Fig. 3.3.1) in Eqs. (3.3.1.5) through (3.3.1.9), the strain-displacement relations are

$$\epsilon_{11} = \epsilon_{11}^o(\xi_1, \xi_2) + \xi_3 \kappa_{11}(\xi_1, \xi_2) \quad (5.3.4)$$

$$\epsilon_{22} = \epsilon_{22}^o(\xi_1, \xi_2) + \xi_3 \kappa_{22}(\xi_1, \xi_2) \quad (5.3.5)$$

$$\gamma_{12} = \gamma_{12}^o(\xi_1, \xi_2) + \xi_3 \kappa_{12}(\xi_1, \xi_2) \quad (5.3.6)$$

where

$$\epsilon_{11}^o = \frac{\partial u_1^o}{\partial \xi_1} + \frac{1}{2} \left(\frac{\partial u_3^o}{\partial \xi_1} \right)^2 \quad (5.3.7)$$

$$\epsilon_{22}^{\circ} = \frac{R}{R-\xi_1} \frac{\partial u_2^{\circ}}{\partial \xi_2} - \frac{u_1^{\circ}}{R-\xi_1} + \frac{1}{2} \left[\left(\frac{R}{R-\xi_1} \right) \frac{\partial u_3^{\circ}}{\partial \xi_2} \right]^2 + \left\{ \frac{1}{2} \left[\left(\frac{R}{R-\xi_1} \right) \frac{\partial u_1^{\circ}}{\partial \xi_2} + \frac{u_2^{\circ}}{R-\xi_1} \right]^2 \right\} \quad (5.3.8)$$

$$\gamma_{12}^{\circ} = \frac{R}{R-\xi_1} \frac{\partial u_1^{\circ}}{\partial \xi_2} + \frac{\partial u_2^{\circ}}{\partial \xi_1} + \frac{u_2^{\circ}}{R-\xi_1} + \frac{R}{R-\xi_1} \frac{\partial u_3^{\circ}}{\partial \xi_1} \frac{\partial u_3^{\circ}}{\partial \xi_2} \quad (5.3.9)$$

$$\kappa_{11} = -\frac{\partial^2 u_3^{\circ}}{\partial \xi_1^2} \quad (5.3.10)$$

$$\kappa_{22} = -\left(\frac{R}{R-\xi_1} \right)^2 \frac{\partial^2 u_3^{\circ}}{\partial \xi_2^2} + \frac{1}{R-\xi_1} \frac{\partial u_3^{\circ}}{\partial \xi_1} \quad (5.3.11)$$

$$\kappa_{12} = -\frac{2R}{R-\xi_1} \frac{\partial^2 u_3^{\circ}}{\partial \xi_1 \partial \xi_2} - \frac{2R}{(R-\xi_1)^2} \frac{\partial u_3^{\circ}}{\partial \xi_2} \quad (5.3.12)$$

and all of the terms in Eqs. (5.3.4) through (5.3.12) have been defined in section 3.3.1. Note that an extra nonlinear term (in $\{ \}$) has been added in Eq. (5.3.8). This is necessary in order to represent a buckled mode shape of the annular plate dominated by in-plane buckling displacements rather than normal buckling displacements. Such a situation would arise if the radial depth of the plate was so small that the structure buckled like a curved beam rather than a flat plate. Substituting Eqs. (5.3.4) through (5.3.12) into Eq. (5.3.1) and integrating with respect to ξ_3 gives

$$\Pi = \frac{1}{2} \int_{\xi_1} \int_{\xi_2} \{ \{N\}^T \{\epsilon^{\circ}\} + \{M\}^T \{\kappa^{\circ}\} \} (1 - \frac{\xi_1}{R}) d\xi_2 d\xi_1 + \Pi_{load} \quad (5.3.13)$$

where, as in Eqs. (3.3.2.2) and (3.3.2.3),

$$\{N\} = \left\{ \begin{matrix} N_{11} \\ N_{22} \\ N_{12} \end{matrix} \right\} = \int_{\xi_3} \left\{ \begin{matrix} \sigma_{11} \\ \sigma_{22} \\ \tau_{12} \end{matrix} \right\} d\xi_3 \quad (5.3.14)$$

and

$$\{M\} = \left\{ \begin{matrix} M_{11} \\ M_{22} \\ M_{12} \end{matrix} \right\} = \int_{\xi_3} \xi_3 \left\{ \begin{matrix} \sigma_{11} \\ \sigma_{22} \\ \tau_{12} \end{matrix} \right\} d\xi_3 \quad (5.3.15)$$

are stress resultants and stress couples and the superscript T indicates the transpose of a matrix or vector. Eq. (5.3.13) written in nondimensional form (see Table 1) is

$$\bar{\Pi} = \frac{1}{2} \int_{\bar{\xi}_1} \int_{\bar{\xi}_2} \{ \{\bar{N}\}^T \{\bar{\epsilon}^\circ\} + \{\bar{M}\}^T \{\bar{\kappa}^\circ\} \} (1 - \frac{L}{R} \bar{\xi}_1) d\bar{\xi}_2 d\bar{\xi}_1 + \bar{\Pi}_{load} \quad (5.3.16)$$

where $\bar{(\quad)}$ indicates that (\quad) is a nondimensional quantity defined in Table 1. Also defined in Table 1 are the nondimensional membrane stiffnesses \bar{A}_{nm} , the nondimensional membrane-bending coupling stiffnesses \bar{B}_{nm} and the nondimensional bending stiffnesses \bar{D}_{nm} used in the nondimensional form of the stress-strain equations (Eq. (3.3.2.1)) given by

$$\begin{Bmatrix} \bar{N}_{11} \\ \bar{N}_{22} \\ \bar{N}_{12} \\ \bar{M}_{11} \\ \bar{M}_{22} \\ \bar{M}_{12} \end{Bmatrix} = \begin{bmatrix} \bar{A}_{11} & \bar{A}_{12} & \bar{A}_{16} & \bar{B}_{11} & \bar{B}_{12} & \bar{B}_{16} \\ \bar{A}_{12} & \bar{A}_{22} & \bar{A}_{26} & \bar{B}_{21} & \bar{B}_{22} & \bar{B}_{26} \\ \bar{A}_{16} & \bar{A}_{26} & \bar{A}_{66} & \bar{B}_{61} & \bar{B}_{62} & \bar{B}_{66} \\ \bar{B}_{11} & \bar{B}_{21} & \bar{B}_{61} & \bar{D}_{11} & \bar{D}_{12} & \bar{D}_{16} \\ \bar{B}_{12} & \bar{B}_{22} & \bar{B}_{62} & \bar{D}_{12} & \bar{D}_{22} & \bar{D}_{26} \\ \bar{B}_{16} & \bar{B}_{26} & \bar{B}_{66} & \bar{D}_{16} & \bar{D}_{26} & \bar{D}_{66} \end{bmatrix} \begin{Bmatrix} \bar{\epsilon}_{11}^\circ \\ \bar{\epsilon}_{22}^\circ \\ \bar{\epsilon}_{12}^\circ \\ \bar{\kappa}_{11}^\circ \\ \bar{\kappa}_{22}^\circ \\ \bar{\kappa}_{12}^\circ \end{Bmatrix} \equiv [c] \begin{Bmatrix} \bar{\epsilon}_{11}^\circ \\ \bar{\epsilon}_{22}^\circ \\ \bar{\epsilon}_{12}^\circ \\ \bar{\kappa}_{11}^\circ \\ \bar{\kappa}_{22}^\circ \\ \bar{\kappa}_{12}^\circ \end{Bmatrix}. \quad (5.3.17)$$

Note that since the individual lamina of the plate are assumed to be monoclinic with respect to the midplane of the plate defined in a cylindrical coordinate system rather than a cartesian coordinate system the stiffnesses are constants with respect to $(\bar{\xi}_1, \bar{\xi}_2)$. Following the same procedure outlined in section 5.2, the second variation of the total potential energy written in nondimensional form is

$$\delta^2 \bar{\Pi} = \int_{\bar{\xi}_1} \int_{\bar{\xi}_2} \{ \{\bar{N}'\}^T \{\delta \bar{\epsilon}^\circ\} + \{\bar{M}'\}^T \{\delta \bar{\kappa}^\circ\} + \{\bar{N}\}^T \{\delta^2 \bar{\epsilon}^\circ\} + \{\bar{M}\}^T \{\delta^2 \bar{\kappa}^\circ\} \} (1 - \frac{L}{R} \bar{\xi}_1) d\bar{\xi}_2 d\bar{\xi}_1 + \delta^2 \bar{\Pi}_{load} \quad (5.3.18)$$

where $\{\bar{N}'\}$ and $\{\bar{M}'\}$ are nondimensional buckling stress resultants and stress couples

given by

$$\begin{Bmatrix} \bar{N}'_{11} \\ \bar{N}'_{22} \\ \bar{N}'_{12} \\ \bar{M}'_{11} \\ \bar{M}'_{22} \\ \bar{M}'_{12} \end{Bmatrix} = \begin{bmatrix} \bar{A}_{11} & \bar{A}_{12} & \bar{A}_{16} & \bar{B}_{11} & \bar{B}_{12} & \bar{B}_{16} \\ \bar{A}_{12} & \bar{A}_{22} & \bar{A}_{26} & \bar{B}_{21} & \bar{B}_{22} & \bar{B}_{26} \\ \bar{A}_{16} & \bar{A}_{26} & \bar{A}_{66} & \bar{B}_{61} & \bar{B}_{62} & \bar{B}_{66} \\ \bar{B}_{11} & \bar{B}_{21} & \bar{B}_{61} & \bar{D}_{11} & \bar{D}_{12} & \bar{D}_{16} \\ \bar{B}_{12} & \bar{B}_{22} & \bar{B}_{62} & \bar{D}_{12} & \bar{D}_{22} & \bar{D}_{26} \\ \bar{B}_{16} & \bar{B}_{26} & \bar{B}_{66} & \bar{D}_{16} & \bar{D}_{26} & \bar{D}_{66} \end{bmatrix} \begin{Bmatrix} \delta \hat{\epsilon}_{11}^\infty \\ \delta \hat{\epsilon}_{22}^\infty \\ \delta \hat{\gamma}_{12}^\infty \\ \delta \hat{\kappa}_{11}^\infty \\ \delta \hat{\kappa}_{22}^\infty \\ \delta \hat{\kappa}_{12}^\infty \end{Bmatrix} \equiv [c] \begin{Bmatrix} \delta \hat{\epsilon}_{11}^\infty \\ \delta \hat{\epsilon}_{22}^\infty \\ \delta \hat{\gamma}_{12}^\infty \\ \delta \hat{\kappa}_{11}^\infty \\ \delta \hat{\kappa}_{22}^\infty \\ \delta \hat{\kappa}_{12}^\infty \end{Bmatrix}. \quad (5.3.19)$$

The second variation of the nondimensional total potential energy analogous to Eq. (5.2.45) for the cylindrical shell is obtained as follows: take two variations of the strain-displacement equations (Eqs. (5.3.7) through (5.3.12) and substitute the resulting expressions into Eq. (5.3.19). Then substitute for the nondimensional midplane buckling displacements \bar{u}_1' , \bar{u}_2' and \bar{u}_3' and the nondimensional buckling stress resultants and stress couples \bar{N}'_{11} , \bar{N}'_{22} , \bar{N}'_{12} , \bar{M}'_{11} , \bar{M}'_{22} and \bar{M}'_{12} the following Fourier series representation

$$\begin{Bmatrix} \bar{u}_1' \\ \bar{u}_2' \\ \bar{u}_3' \end{Bmatrix} = \begin{Bmatrix} \bar{UW}_1(\bar{\xi}_1) \\ \bar{VW}_1(\bar{\xi}_1) \\ \bar{WW}_1(\bar{\xi}_1) \end{Bmatrix} \sin \beta \bar{\xi}_2 + \begin{Bmatrix} \bar{UW}_2(\bar{\xi}_1) \\ \bar{VW}_2(\bar{\xi}_1) \\ \bar{WW}_2(\bar{\xi}_1) \end{Bmatrix} \cos \beta \bar{\xi}_2 \quad (5.3.20)$$

$$\begin{Bmatrix} \bar{N}'_{11} \\ \bar{N}'_{22} \\ \bar{N}'_{12} \end{Bmatrix} = \begin{Bmatrix} \bar{NWX}_1(\bar{\xi}_1) \\ \bar{NWX}_2(\bar{\xi}_1) \\ \bar{NWX}_3(\bar{\xi}_1) \end{Bmatrix} \sin \beta \bar{\xi}_2 + \begin{Bmatrix} \bar{NWX}_4(\bar{\xi}_1) \\ \bar{NWX}_5(\bar{\xi}_1) \\ \bar{NWX}_6(\bar{\xi}_1) \end{Bmatrix} \cos \beta \bar{\xi}_2 \quad (5.3.21)$$

$$\begin{Bmatrix} \overline{M}'_{11} \\ \overline{M}'_{22} \\ \overline{M}'_{12} \end{Bmatrix} = \begin{Bmatrix} \overline{MWX}_1(\bar{\xi}_1) \\ \overline{MWY}_1(\bar{\xi}_1) \\ \overline{MWXY}_1(\bar{\xi}_1) \end{Bmatrix} \sin \beta \bar{\xi}_2 + \begin{Bmatrix} \overline{MWX}_2(\bar{\xi}_1) \\ \overline{MWY}_2(\bar{\xi}_1) \\ \overline{MWXY}_2(\bar{\xi}_1) \end{Bmatrix} \cos \beta \bar{\xi}_2 \quad (5.3.22)$$

with

$$\beta = \frac{nL}{R} \quad (5.3.23)$$

where n is a circumferential wave number, L is the length and R is the middle surface radius of the cylinder to which the annular plate is attached (see Fig 3.3.1)).

For a single finite element (see Fig. 5.3.1), the buckling displacements \overline{UW}_1 , \overline{UW}_2 , \overline{VW}_1 , \overline{VW}_2 , \overline{WW}_1 , and \overline{WW}_2 are written as

$$\begin{aligned} \overline{UW}_1(\bar{\xi}_1) &= \{UW1\}^T \{\Phi_1(\bar{\xi}_1)\} & \overline{VW}_2(\bar{\xi}_1) &= \{VW2\}^T \{\Psi_2(\bar{\xi}_1)\} \\ \overline{UW}_2(\bar{\xi}_1) &= \{UW2\}^T \{\Phi_2(\bar{\xi}_1)\} & \overline{WW}_1(\bar{\xi}_1) &= \{WW1\}^T \{\Omega_1(\bar{\xi}_1)\} \\ \overline{VW}_1(\bar{\xi}_1) &= \{VW1\}^T \{\Psi_1(\bar{\xi}_1)\} & \overline{WW}_2(\bar{\xi}_1) &= \{WW2\}^T \{\Omega_2(\bar{\xi}_1)\} \end{aligned} \quad (5.3.24)$$

where $\{\Phi_1(\bar{\xi}_1)\}$, $\{\Phi_2(\bar{\xi}_1)\}$, $\{\Psi_1(\bar{\xi}_1)\}$, $\{\Psi_2(\bar{\xi}_1)\}$, $\{\Omega_1(\bar{\xi}_1)\}$, and $\{\Omega_2(\bar{\xi}_1)\}$ are vectors of the same polynomials used in Eq. (5.2.49) and $\{UW1\}$, $\{UW2\}$, $\{VW1\}$, $\{VW2\}$, $\{WW1\}$ and $\{WW2\}$ are vectors of nodal buckling displacements and rotations. The domain of $\bar{\xi}_1$ in this case is understood to be from $\bar{\xi}_1^e$ to $\bar{\xi}_1^{e+1}$. As was the case for the cylindrical shell, the second variation of the nondimensional total potential energy for a single annular plate element and a single specified circumferential wave number, n , can be written in terms of a stiffness matrix, $[K^e(n)]$, which is not a function of the applied loads, and a geometric stiffness matrix, $[K_G^e(n; \lambda)]$ which is a function applied loads indicated by the load parameter λ . The matrices $[K^e(n)]$ and $[K_G^e(n; \lambda)]$ along with the finite element model of the second variation of the nondimensional total potential energy appear in Appendix D.

5.4 Finite Element Model of the Second Variation Of The

Total Potential Energy of the Ring-Stiffened Cylinder :

Assembly of Global Stiffness and Geometric Stiffness Matrices

The finite element model of the second variation of the nondimensional total potential energy ($\bar{\Pi}$) of the ring-stiffened cylindrical shell for a specified value of the circumferential wave number, n , is formed by adding together the contributions to $\bar{\Pi}$ from each individual finite element, $\bar{\Pi}^e$. Using Eqs. (C.1) from Appendix C and (D.1) from Appendix D, This sum can be expressed as

$$\begin{aligned}\delta^2 \bar{\Pi}(n; \lambda) &= \sum_{e=1}^N (\delta^2 \bar{\Pi}^e(n; \lambda) + \delta^2 \bar{\Pi}_{load}^e) \\ &= \sum_{e=1}^N \left(\frac{\pi R}{L} \{W^e\}^T [K^e(n)] \{W^e\} \right. \\ &\quad \left. + \frac{\pi R}{L} \{W^e\}^T [K_G^e(n; \lambda)] \{W^e\} + \delta^2 \bar{\Pi}_{load}^e \right).\end{aligned}\quad (5.4.1)$$

where $[K^e(n)]$ is an elemental stiffness matrix and $[K_G^e(n; \lambda)]$ is an elemental geometric stiffness matrix, N is the total number of finite elements in the ring-stiffened cylinder and $\delta^2 \bar{\Pi}_{load}^e$ contains terms associated with the boundary conditions at the ends of each element. Compatibility of the nodal buckling displacements and equilibrium of the corresponding nodal buckling forces and nodal buckling moments at node points where elements are joined are enforced by assembly of the element stiffness and geometric stiffness matrices into the corresponding global (or structural) stiffness and geometric stiffness matrices (see Reddy¹⁰⁹). This assembly, along with the imposition of the boundary conditions at the ends of the cylinder and the inboard edges of the attached ring webs, results in the vanishing of the term $\sum_{e=1}^N \delta^2 \bar{\Pi}_{load}^e$ in Eq. (5.4.1). In order to minimize the bandwidth of the resulting structural matrices, the element matrices are first reorganized so that the nodal buckling displacements and rotations ($\{W^e\}$), for the cylinder elements (see section 5.2) can be written as

$$\{W^e\}^T \equiv \{U1^e \quad V1^e \quad W1^e \quad R1^e \quad U2^e \quad V2^e \quad W2^e \quad R2^e \quad \{U1^m\} \quad \{V1^m\} \quad \{U2^m\} \quad \{V2^m\} \quad U1^{e+1} \quad V1^{e+1} \quad W1^{e+1} \quad R1^{e+1} \quad U2^{e+1} \quad V2^{e+1} \quad W2^{e+1} \quad R2^{e+1}\}^T \quad (5.4.2)$$

and the nodal buckling displacements and rotations for the annular plate elements (see section 5.3) can be written as

$$\{W^e\}^T \equiv \{UW1^e \quad VW1^e \quad WW1^e \quad RW1^e \quad UW2^e \quad VW2^e \quad WW2^e \quad RW2^e \quad \{UW1^m\} \quad \{VW1^m\} \quad \{UW2^m\} \quad \{VW2^m\} \quad UW1^{e+1} \quad VW1^{e+1} \quad WW1^{e+1} \quad RW1^{e+1} \quad UW2^{e+1} \quad VW2^{e+1} \quad WW2^{e+1} \quad RW2^{e+1}\}^T \quad (5.4.3)$$

where the superscript e indicates quantities at initial nodes of the element, $e + 1$ indicates quantities at the final node of the element, m indicates quantities at midlength nodes of the element used for Lagrange quadratic or cubic interpolation of the tangential (or in-plane) buckling displacements and if

$$\bar{R}_1 = \frac{-d\bar{W}_1(\bar{\xi}_1)}{d\bar{\xi}_1} \quad \text{and} \quad \bar{R}_2 = \frac{-d\bar{W}_2(\bar{\xi}_1)}{d\bar{\xi}_1} \quad (5.4.4)$$

are nondimensional buckling flexural rotations in the cylinder (see Eq. (5.2.41)) and

$$\overline{RW}_1 = \frac{-d\overline{WW}_1(\bar{\xi}_1)}{d\bar{\xi}_1} \quad \text{and} \quad \overline{RW}_2 = \frac{-d\overline{WW}_2(\bar{\xi}_1)}{d\bar{\xi}_1} \quad (5.4.5)$$

are nondimensional buckling flexural rotations in the ring web (see Eq. (5.3.20)) then $R1^e$ and $R2^e$ are nodal flexural rotations in a cylinder element used in the Hermite cubic polynomial interpolation of $\bar{W}_1(\bar{\xi}_1)$ and $\bar{W}_2(\bar{\xi}_1)$ respectively and $RW1^e$ and $RW2^e$ are nodal flexural rotations in an annular plate element used in the Hermite cubic polynomial interpolation of $\overline{WW}_1(\bar{\xi}_1)$ and $\overline{WW}_2(\bar{\xi}_1)$ respectively (see Eqs. (5.2.49) and (5.3.24)). For both cylinder and annular plate elements, nodal buckling

force and moment quantities, $\{F^e\}$, are related to nodal buckling displacements and rotations, $\{W^e\}$, by the expression

$$\{F^e\} = [[K^e] + [K_G^e]]\{W^e\}. \quad (5.4.6)$$

where, for the cylinder element (see Fig. (5.2.1)),

$$\begin{aligned} \{F^e\}^T \equiv & \{P1^e \quad S1^e \quad Q1^e \quad M1^e \quad P2^e \quad S2^e \quad Q2^e \\ & M2^e \quad \{P1^m\} \quad \{S1^m\} \quad \{P2^m\} \quad \{S2^m\} \quad P1^{e+1} \quad S1^{e+1} \\ & Q1^{e+1} \quad M1^{e+1} \quad P2^{e+1} \quad S2^{e+1} \quad Q2^{e+1} \quad M2^{e+1}\}^T \end{aligned} \quad (5.4.7)$$

and for the annular plate element (see Fig. (5.3.1)),

$$\begin{aligned} \{F^e\}^T \equiv & \{PW1^e \quad SW1^e \quad QW1^e \quad MW1^e \quad PW2^e \quad SW2^e \quad QW2^e \\ & MW2^e \quad \{PW1^m\} \quad \{SW1^m\} \quad \{PW2^m\} \quad \{SW2^m\} \quad PW1^{e+1} \\ & SW1^{e+1} \quad QW1^{e+1} \quad MW1^{e+1} \quad PW2^{e+1} \quad SW2^{e+1} \\ & QW2^{e+1} \quad MW2^{e+1}\}^T \end{aligned} \quad (5.4.8)$$

Fig. 5.4.1 shows a typical ring web intersecting the cylindrical shell. It is assumed that the outboard edge of the web is connected to the middle surface of the cylindrical shell by a small rigid link of length ecc representing the small offset created by the thickness of the ring flange and the small fillet radius where this flange connects to the web. In order to assemble the element matrices of the two cylindrical shell elements joined at points P_c in Fig. 5.4.1 with the annular plate element having its initial end at point P_w in Fig. 5.4.1, compatibility of the nodal buckling displacements and rotations and equilibrium of the nodal buckling forces and moments at P_c must account for the eccentricity of P_c from P_w , (ecc). Since the offset, ecc , is a rigid link, buckling displacements, rotations, forces, and moments at P_w can be written in terms of buckling displacements, rotations, forces, and moments at P_c if the proper transformations are applied to the quantities at P_c that account for ecc and the different local coordinate systems used for the cylindrical shell elements and the annular plate elements.

Transformation of the nondimensional buckling displacements and flexural rotations at the outboard edge of the annular plate, written in terms of the annular plate local coordinate system, into the corresponding set of nondimensional buckling displacements and rotations at the middle surface of the cylindrical shell, written in terms of the local cylindrical shell coordinate system, is achieved by using

$$(\bar{u}_1')_{web} = - \left(\frac{L}{t_s} \right) (\bar{u}_3')_{cyl} \quad (5.4.9)$$

$$(\bar{u}_2')_{web} = (\bar{u}_1')_{cyl} + \left(\frac{L}{t_s} \right) \bar{e}\bar{c}\bar{c} ((\partial \bar{u}_3' / \partial \bar{\xi}_2))_{cyl} \quad (5.4.10)$$

$$(\bar{u}_3')_{web} = \left(\frac{t_s}{L} \right) (\bar{u}_1')_{cyl} + \bar{e}\bar{c}\bar{c} ((\partial \bar{u}_3' / \partial \bar{\xi}_1))_{cyl} \quad (5.4.11)$$

$$((\partial \bar{u}_3' / \partial \bar{\xi}_1))_{web} = ((\partial \bar{u}_3' / \partial \bar{\xi}_1))_{cyl} \quad (5.4.12)$$

where L is the length of the cylinder and t_s is the total thickness of the cylindrical shell (not including ring flanges). The subscript *web* indicates buckling quantities at the outboard edge of the annular plate written in the annular plate midplane coordinate system and the subscript *cyl* indicates the corresponding buckling quantities at the middle surface of the cylindrical shell written in the cylinder middle surface coordinate system. Quantities with overbars indicate nondimensionalized quantities defined in Table 1. Substituting Eq. (5.3.20) through (5.3.22) into Eqs. (5.4.9) through (5.4.12) and equating quantities multiplying $\sin \beta \bar{\xi}_2$ and $\cos \beta \bar{\xi}_2$ results in

$$\begin{Bmatrix} \overline{UW}_1^{web}(\bar{\xi}_1) \\ \overline{VW}_1^{web}(\bar{\xi}_1) \\ \overline{WW}_1^{web}(\bar{\xi}_1) \\ \overline{RW}_1^{web}(\bar{\xi}_1) \\ \overline{UW}_2^{web}(\bar{\xi}_1) \\ \overline{VW}_2^{web}(\bar{\xi}_1) \\ \overline{WW}_2^{web}(\bar{\xi}_1) \\ \overline{RW}_2^{web}(\bar{\xi}_1) \end{Bmatrix} = [T_1] \begin{Bmatrix} \overline{UW}_1^{cyl}(\bar{\xi}_1) \\ \overline{VW}_1^{cyl}(\bar{\xi}_1) \\ \overline{WW}_1^{cyl}(\bar{\xi}_1) \\ \overline{RW}_1^{cyl}(\bar{\xi}_1) \\ \overline{UW}_2^{cyl}(\bar{\xi}_1) \\ \overline{VW}_2^{cyl}(\bar{\xi}_1) \\ \overline{WW}_2^{cyl}(\bar{\xi}_1) \\ \overline{RW}_2^{cyl}(\bar{\xi}_1) \end{Bmatrix} \quad (5.4.13)$$

where

$$[T_1] = \begin{bmatrix} 0 & 0 & -L/t_s & 0 & 0 & 0 & 0 & 0 \\ 0 & 1 & 0 & 0 & 0 & 0 & -L\bar{e}\bar{c}\bar{c}\beta/t_s & 0 \\ t_s/L & 0 & 0 & -\bar{e}\bar{c}\bar{c} & 0 & 0 & 0 & 0 \\ 0 & 0 & 0 & 1 & 0 & 0 & 0 & 0 \\ 0 & 0 & 0 & 0 & 0 & 0 & -L/t_s & 0 \\ 0 & 0 & L\bar{e}\bar{c}\bar{c}\beta/t_s & 0 & 0 & 1 & 0 & 0 \\ 0 & 0 & 0 & 0 & t_s/L & 0 & 0 & -\bar{e}\bar{c}\bar{c} \\ 0 & 0 & 0 & 0 & 0 & 0 & 0 & 1 \end{bmatrix} \quad (5.4.14)$$

and $\bar{R}\bar{W}_1$ and $\bar{R}\bar{W}_2$ are defined in Eq. (5.4.5). Substituting the finite element model for the annular plate buckling displacements (Eqs. (5.3.24)) into Eq. (5.4.13) and organizing the nondimensional nodal buckling displacements and rotations as shown in Eq. (5.4.3), the transformation of the nondimensional nodal buckling displacements and rotations for the annular plate finite element to nondimensional nodal buckling displacements and rotations at the middle surface of the cylindrical shell in the cylindrical shell coordinate system is accomplished using Eq. (5.4.15) below.

$$\{W^e\}^{web} = [T] \{W^e\}^{cyl} \quad (5.4.15)$$

Note that only quantities at the most outboard node of this annular plate element need to be transformed, In Eq. (5.4.15) *web* indicates nodal quantities at the most outboard node of the annular plate element in the annular plate coordinate system, *cyl* indicates nodal quantities at the point of intersection in the middle surface of the cylindrical shell in the cylindrical shell coordinate system and

$$[T] = \begin{bmatrix} [T_1] & [0] & [0] \\ [0] & [I] & [0] \\ [0] & [0] & [I] \end{bmatrix} \quad (5.4.16)$$

where $[T_1]$ is given in Eq. (5.4.16) and $[I]$ is an identity matrix. It can be shown that the nondimensional nodal buckling forces and moments, $\{F^e\}$, from Eq. (5.4.8), at the outboard node of the annular plate element can be transformed to corresponding nodal quantities at the point of intersection in the middle surface of the cylindrical shell by

$$\{F^e\}^{cyl} = [T]^T \{F^e\}^{web} \quad (5.4.17)$$

where $[T]^T$ is the transpose of the matrix defined in Eq. (5.4.16). Using Eqs. (5.4.15) and (5.4.17) it can be shown that, for the annular plate element, $[T]^T[K^e][T]$ is the transformed element stiffness matrix and $[T]^T[K_G^e][T]$ is the transformed element geometric stiffness matrix which can now be assembled into their respective global or structural matrices.

Once all of the necessary transformations have been made and the structural matrices are assembled, boundary conditions at the ends of the cylinder and at the inboard edges of the ring webs must be imposed. The cylinder ends are assumed to be clamped while the inboard edges of the annular plates are assumed to be free. For the cylinder, this may be stated mathematically as

$$(\partial \bar{u}_1' / \partial \bar{\xi}_2) = (\partial \bar{u}_2' / \partial \bar{\xi}_2) = \bar{u}_3 = (\partial \bar{u}_3' / \partial \bar{\xi}_1) = 0 \quad \text{at} \quad \bar{\xi}_1 = \pm \frac{1}{2}. \quad (5.4.18)$$

Substituting Eq. (5.2.41) and Eqs. (5.2.49) into Eq. (5.4.18) results in

$$U1^i = U2^i = V1^i = V2^i = W1^i = W2^i = R1^i = R2^i = 0 \quad (5.4.19)$$

and

$$U1^f = U2^f = V1^f = V2^f = W1^f = W2^f = R1^f = R2^f = 0 \quad (5.4.20)$$

where the superscript i indicates quantities at the initial node of the first cylinder element and the superscript f indicates quantities at the final node of the last cylinder element. The free edge boundary conditions at the inboard edges of the ring webs are

$$\bar{N}_{11} = \bar{N}_{12} = \bar{V}_{11} = \bar{M}_{11} = 0 \quad \text{at} \quad \bar{\xi}_1 = \frac{H_w}{L} \quad (5.4.21)$$

where \bar{N}_{11} is the nondimensional buckling radial stress resultant, \bar{N}_{12} is the nondimensional buckling in-plane shear stress resultant, \bar{V}_{11} is the nondimensional buckling Kirchhoff shear stress resultant, \bar{M}_{11} is the nondimensional radial stress couple, H_w is the radial depth of the web, and L is the length of the cylindrical shell. Following the same procedure used to develop Eqs. (5.4.19) and (5.4.20), the boundary conditions

at the inboard edges of the ring webs in terms of nodal buckling forces and moments defined in Eq. (5.4.8) are

$$PW_1^f = PW_2^f = SW_1^f = SW_2^f = QW_1^f = QW_2^f = MW_1^f = MW_2^f = 0 \quad (5.4.22)$$

where here the superscript f refers to quantities at the final node of the most inboard annular plate finite element of a ring web.

Assembly of the element matrices and imposition of the homogeneous boundary conditions of Eqs. (5.4.19), (5.4.20) and (5.4.22) results in the final form of the finite element model for the second variation of the nondimensional total potential energy for the ring-stiffened cylindrical shell given a specific value of the circumferential wave number, n , and the load, λ

$$\delta^2 \bar{\Pi}(n; \lambda) = \frac{\pi R}{L} \{W\}^T ([K(n)] + [K_G(n; \lambda)]) \{W\} \quad (5.4.23)$$

where $[K(n)]$ is the global or structural stiffness matrix, $[K_G(n; \lambda)]$ is the global or structural geometric stiffness matrix and $\{W\}$ is the global vector of nodal buckling displacements and rotations.

5.5 Formulation of the Nonlinear Buckling Eigenvalue Problem

Stability of the prebuckled equilibrium configuration is guaranteed if $([K(n)] + [K_G(n; \lambda)])$ in Eq. (5.4.22) is positive definite. The loading which results in a critical situation - where $([K(n)] + [K_G(n; \lambda)])$ first becomes positive semi-definite - can be determined through the application of Trefftz's criterion

$$\delta(\delta^2 \bar{\Pi}(n; \lambda)) = 0. \quad (5.5.1)$$

Substituting Eq. (5.4.22) into Eq. (5.5.1) results in

$$([K(n)] + [K_G(n; \lambda)])\{W\} = 0. \quad (5.5.2)$$

The global geometric stiffness matrix, $[K_G(n; \lambda)]$, is a nonlinear function of the applied load; hence, Eq. (5.5.2) is a nonlinear algebraic eigenvalue problem. Nontrivial solutions of this problem determine critical loads and associated mode shapes for the specified value of the circumferential wave number, n . Given some initial loading P° (axial compression), T° (torsion) and p° (lateral pressure), it is assumed that the structure is loaded to buckling so that P° and T° retain their original proportion and p° remains constant. In other words, the combined loading is defined by the constant pressure, p° , and the load parameter λ where

$$\lambda = P/P^\circ = T/T^\circ \quad (5.5.3)$$

Newton's method is applied to Eq. (5.5.2) (see Eq. (3) of Ref. 106) necessitating solution of a sequence of linear algebraic eigenvalue problems of the form

$$([K(n) + K_G(n; \lambda^i)] + \Delta\lambda[\dot{K}_G(n; \lambda^i)])\{W\} = \{0\} \quad (5.5.4)$$

where $\dot{(\)}$ indicates differentiation with respect to λ . $\Delta\lambda$ is a correction to λ^i , the current estimate of λ_n (see section 5.1), which approaches zero as λ approaches λ_n .

In order to insure that $\lambda^i < \lambda_n$ after each iteration, only a fraction of $\Delta\lambda$ should be added. In other words

$$\lambda^{i+1} = \lambda^i + r\Delta\lambda \quad (5.5.5)$$

where $0 < r < 1$ (see Sun¹⁰⁷). It has been observed that $r = 0.5$ is usually adequate to insure that λ^{i+1} does not exceed λ_n . When λ^{i+1} is close to λ^i to within a specified tolerance, the iterations stop. At this point $\lambda^i = \lambda_n$ and the $\{W\}$ found from the last solution of Eq. (5.5.4) along with Eqs. (5.2.41) and (5.3.20) define the related mode shape. The smallest λ_n , along with its corresponding mode shape, found over all values of n is the buckling load and buckled mode shape of the ring-stiffened cylinder.

Chapter 6

OPTIMAL DESIGN ALGORITHM

6.1 Introduction

One objective of the present study is to design minimum weight (denoted by F) generally anisotropic ring-stiffened cylinders loaded by combined axial compression, torsion, and internal pressure. The cylinders are characterized by a set of design variables X_i ($i = 1, 2, \dots, n_{dv}$ where n_{dv} is the total number of design variables) that define the geometry and the laminate properties of the shell. The design is subject to a set of constraints to insure that the structure does not buckle under the imposed loads, g_j^b , $j = 1, 2, \dots, n_{gb}$, where n_{gb} is the total number of buckling constraints (several buckling constraints on both the minimum buckling load and the buckling loads associated with higher modes may be necessary in order to account for the possible occurrence of mode coalescence and mode switching), and that the prebuckling stresses at selected locations in the structure do not exceed their allowable limits. The stress constraints are represented by g_k^s , $k = 1, 2, \dots, n_{gs}$, where n_{gs} is the total number of stress constraints. A set of lower bounds X_i^l and upper bounds X_i^u on the design variables are also specified. Mathematically the optimal design problem is stated as

$$\begin{aligned}
 &\text{minimize} && F(X_i) \quad i = 1, 2, \dots, n_{dv} \\
 &\text{subject to} && g_j^b \geq 0 \quad j = 1, 2, \dots, n_{gb} \\
 &&& g_k^s \geq 0 \quad k = 1, 2, \dots, n_{gs} \\
 &&& X_i - X_i^l \geq 0 \\
 &&& X_i^u - X_i \geq 0
 \end{aligned} \tag{6.1.1}$$

In the present study, both the objective function, F , and the behavioral constraints g_j^b and g_k^s of Eq. (6.1.1) are generally nonlinear functions of the design variables, X_i ; hence, Eq. (6.1.1) is a nonlinear mathematical programming (MP) problem that needs

to be solved using the methods mentioned in section 1.3.3. Use is made of both an indirect MP technique, described in section 6.2, and a direct MP technique, described in section 6.3, in the present study. In section 6.4, the various design variables used in the present study are discussed. Sections 6.5 and 6.6 contain a formulation of the stress and buckling constraints respectively. Section 6.7 contains a brief outline of the sensitivity analysis. A discussion of the criteria used to establish optimality of a candidate design is presented in section 6.8.

6.2 Quadratic Extended Interior Penalty Function Method

The indirect mathematical programming technique used in the present study is the sequential unconstrained minimization technique based on the quadratic extended interior penalty function¹¹³. The method is implemented in the NEWSUMT-A¹¹⁴ computer program, used in the present study, that internally converts Eq. (6.1.1) to a sequence of unconstrained minimization problems that have the form

$$\Phi(\vec{X}, r_p) = F(\vec{X}) + r_p \left[\sum_{j=1}^{n_{gb}} p(g_j^b) + \sum_{k=1}^{n_{gs}} p(g_k^s) + \sum_{i=1}^{n_{dv}} p(X_i - X_i^l) + \sum_{i=1}^{n_{dv}} p(X_i^u - X_i) \right] \quad (6.2.1)$$

where Φ is the pseudo-objective function, r_p is the penalty parameter, and $p(g)$ is a penalty function associated with constraint g which has the form

$$p(g) = \begin{cases} \frac{1}{g}, & \text{if } g > g_o; \\ \frac{1}{g_o} \left[\left(\frac{g}{g_o} \right)^2 - 3 \left(\frac{g}{g_o} \right) + 3 \right], & \text{if } g \leq g_o. \end{cases} \quad (6.2.2)$$

where g_o is a user-specified transition parameter. Note that when $g > g_o$ the method is essentially the interior penalty function SUMT¹¹⁵. The quadratic extension is added for $g \leq g_o$ in order to allow for constraint violations which may occur during the optimization process. The quadratic extension also has continuous second derivatives at g_o which is desirable if second order methods (Newton's method, for example) are used to solve the unconstrained minimization problem. To determine the optimum design, Eq. (6.2.1) is solved repeatedly by decreasing values of r_p until some specified convergence criterion is met (see section 6.8). Since, for each specified value of r_p , Eq. (6.2.1) is a nonlinear function of the design variables, \vec{X} , this unconstrained minimization problem must be solved iteratively. At the beginning of each new iteration from the design, \vec{X}^q , a move, $\alpha \vec{S}$, within the design space that reduces Φ must be determined in order to generate an improved (lower weight) design, \vec{X}^{q+1} . In other words,

improved designs are generated at each iteration where

$$\vec{X}^{q+1} = \vec{X}^q + \alpha \vec{S} \quad (6.2.3)$$

Many methods exist to determine the search direction \vec{S} . NEWSUMT-A employs Newton's method with approximate second derivatives of the objective function and constraints with respect to the design variables. As shown in Ref. 113, these approximate second derivatives are formed using only the first derivatives of the objective function and constraints with respect to the design variables. Use of Newton's method with approximate second derivatives to determine \vec{S} and solve Eq. (6.2.1) is desirable since the method has the efficient convergence characteristics of a second order method but does not require the computationally expensive calculation of second derivatives. Once \vec{S} is determined, Eq. (6.2.3) is substituted into Eq. (6.2.1) leaving the following one-dimensional unconstrained minimization problem

$$\text{minimize} \quad \Phi(\alpha). \quad (6.2.4)$$

Eq. (6.2.4) is then solved for the optimum step size α^* . In NEWSUMT-A this is done using the Golden Section Search algorithm (see Chapter 4 of Ref. 9). Knowing α^* and \vec{S} , at each iteration the improved design is then

$$\vec{X}^{q+1} = \vec{X}^q + \alpha^* \vec{S}. \quad (6.2.5)$$

For the specified value of r_p , iterations continue until no further reduction in Φ , the pseudo-objective function, is possible. The penalty parameter is then reduced and another unconstrained minimization is performed. This process continues until final convergence is achieved.

6.3 Method of Feasible Directions

Sequential unconstrained minimization techniques such as the one described in section 6.1 are popular because they are generally reliable and easy to implement. The interior penalty function SUMT is particularly desirable since the method generates a sequence of steadily improving feasible designs that funnel down the middle of the feasible region of the design space toward the optimum¹¹⁶. On the other hand, sequential unconstrained minimization techniques tend to require a large number of evaluations of the objective function and the constraints necessitating the use of approximations to these functions when their evaluation is computationally expensive¹¹⁷. Furthermore, the pseudo-objective function, Φ , of Eq. (6.2.1) tends to be numerically ill-conditioned as the design vector, \vec{X} , approaches a constraint boundary where constraints become active ($g \cong 0$). The method of feasible directions^{118,119}, another popular optimal design algorithm, is especially suited to the search for an optimum design at or near constraint boundaries.

Feasible directions is a direct method, requiring separate treatment of the objective function and constraints without grouping them together into a single pseudo-objective function. From a point on the boundary of the feasible domain, the method of feasible directions is applied to determine a search direction, \vec{S} , that produces a design that reduces the objective function, F , (making \vec{S} a *usable* direction) while keeping the design as far from the constraint boundary as possible (making \vec{S} a *feasible* direction). Hence, a constrained maximization subproblem can be defined having the elements of \vec{S} as the unknown variables. This problem is stated as

$$\begin{aligned}
 &\text{maximize} && \beta \\
 &\text{subject to} && -\vec{S} \cdot \vec{\nabla} g_j + \theta_j \beta \leq 0 \quad j \in I_A \\
 & && \vec{S} \cdot \vec{\nabla} F + \beta \leq 0 \\
 & && \theta_j \geq 0 \\
 & && \vec{S} \quad \text{bounded}
 \end{aligned} \tag{6.3.1}$$

where I_A is the set of constraints that are active ($g_j \cong 0$) at \vec{X}^q , the current design, $\vec{\nabla}g_j$ is the gradient of the j^{th} active constraint, $\vec{\nabla}F$ is the gradient of the objective function, and the θ_j are "push-off" factors that determine how far X^{q+1} will be from the constraint boundary upon a move along \vec{S} with $\alpha = 1.0$ (see Eq. (6.2.3)). For highly nonlinear constraints, a large value of θ_j may be necessary to prevent a small move (small step size α) along \vec{S} from producing a design that violates adjacent constraints. For linear constraints, $\theta_j = 0$ is reasonable since a move in a direction tangent to a linear constraint can be made without violating that constraint. The constraint " \vec{S} bounded" has traditionally been imposed by requiring

$$-1.0 \leq S_i \leq 1.0 \quad i = 1, 2, \dots, n_{dv}. \quad (6.3.2)$$

Eqs. (6.3.2) and (6.3.1) define a linear (convex) constrained minimization problem for the elements of the search direction vector, \vec{S} , that can be solved by the simplex method (see section 3.6 of Ref. 9), a very efficient technique for solving linear programming problems. Unfortunately, as discussed in section 6.5 of Ref. 120, bounding \vec{S} as shown in Eq. (6.3.2) biases the search direction - a significant drawback. This drawback can be avoided by bounding the Euclidean norm of \vec{S} , instead of the individual terms of \vec{S} , in the following way

$$\vec{S} \cdot \vec{S} \leq 1.0. \quad (6.3.3)$$

While replacing Eq. (6.3.2) with Eq. (6.3.3) adds a nonlinear constraint to Eq. (6.3.1), Zoutendijk¹¹⁸ has shown that this constraint can be re-written in a form that renders Eq. (6.3.1) solvable using linear programming techniques.

The method of feasible directions is one design optimization option in the ADS¹²¹ design synthesis computer program, which is used in the present study. Once Eq. (6.3.1) is solved for \vec{S} , a one-dimensional search for α^* must be performed as noted in section 6.2. The option in ADS chosen to perform this one-dimensional search is the Golden Section search algorithm for minimization of constrained functions of one vari-

able. Iterations involving calculations of \vec{S} from Eqs. (6.3.1) (6.3.3) and the determination of α^* continue until convergence is achieved.

6.4 Design Variables

Design variables can generally be classified as either continuous or discrete. Continuous design variables are allowed to take on any value between their specified upper and lower bounds; however, discrete design variables are constrained to take on only certain specific values between these limits. As was mentioned in section 1.1, a wide variety of design variables is available to the designer of laminated composite structure. These design variables include number of plies with the same fiber orientation within each layer of the laminate (or layer thicknesses), laminae fiber orientation angles, and the lengths of the various segments comprising the stiffening rings. Treatment of segment lengths as continuous variables generally does not cause any difficulty during fabrication since most parts can be readily machined to virtually any length. Treatment of lamina fiber orientation angles as continuous variables is also reasonable; however, in some instances it may be more cost-effective to limit the choice of angles to a specific set such as 90° , $\pm 45^\circ$, and 0° . Treatment of the number of plies within a lamina as a continuous variable may not be reasonable in designs where the structure is to be fabricated from prepreg having a specific ply thickness since non-integer values call for fractions of plies.

If lamina thicknesses, fiber orientation angles, and ring segment lengths were all treated as design variables in the structural sizing of an eight layer cylinder with a single ring stiffener made of an eight layer flange and an eight layer web, the number of design variables would be very large. The approach taken in the present study is to use only a small subset of the total number of design variables available, leaving problems involving larger, more complicated sets of design variables for future study. By starting with a small set of design variables and working toward larger sets, it may become evident at some point in the process that a further increase in the number of design variables, with the associated increase in the complexity of the problem, may not be cost-effective.

In the present study, lamina fiber orientation angles are not considered as design

variables. Since structural weight is the objective function to be minimized, the objective function is independent of the lamina fiber orientation angles. This independence can create computational difficulties in some cases. Furthermore, the work of Onoda⁷⁴ and Fukunaga and Vanderplaats¹²² indicates that lamination parameters may be preferable to fiber orientation angles as design variables. As shown in Refs. 74 and 122, the laminate constitutive equations can be written in terms of these lamination parameters which are harmonic functions of the fiber orientation angles. Another simplification used in the present study is that the number of plies with the same fiber orientation within each layer of the laminate will be treated as continuous design variables since this is sufficient for theoretical purposes. The use of discrete design variables introduces additional complexity into the problem that is beyond the scope of the present study. For fabrication purposes, the number of plies in each lamina can be rounded to integer values. While recent developments¹²³ may render this practice of rounding obsolete, further evaluation of methods such as those presented in Ref. 123 is warranted before such methods are applied to the solution of nonlinear problems such as the one of the present study.

A problem in which lamina thicknesses are design variables is one example of a sizing optimization problem. Other than a reasonable choice for upper and lower bounds on these design variables, no other special considerations are needed. In the present study, ring segment lengths are also considered as design variables. Problems in which ring segment lengths are design variables, however, are more closely related to shape optimization problems since a change in these design variables causes a change in the position of the boundaries of the various shell branches. Use of these design variables does not complicate the analysis of the prebuckled equilibrium configuration since this analysis is based on exact, closed-form solutions to the governing equations. However, caution must be exercised in the buckling analysis since the buckling loads are calculated based on the finite element method. After each design iteration, the finite element mesh must change in order to accommodate the new shell

branch boundary positions. In the present study, a simple remeshing rule that translates finite element node positions as a function of shell branch boundary changes is used. It is assumed that the number of nodes within each shell branch remains equal to the value set at the beginning of the design cycle. Care is taken in specifying upper and lower bounds for the segment lengths that prevent distortion of the finite element mesh to the point where the calculated buckling loads are no longer accurate.

In summary, the various design variables to be used in the present study are

1. Cylindrical shell lamina thicknesses
2. Ring flange lamina thicknesses
3. Ring web lamina thicknesses
4. Ring flange lengths
5. Ring web radial depths.

6.5 Stress Constraints

The loads imposed upon the ring-stiffened cylinder must not produce stresses within the structure that exceed the strength of the material from which the structure is fabricated. Since the stresses in each lamina of each branch of the prebuckled shell are continuous functions of the coordinates ξ_1 and ξ_3 (see Fig. 3.3.1), the requirement that the structure not be overstressed represents an infinite number of constraints. In general, however, only a small subset (if any) of these constraints will be active in the final optimal design. Generally, stress constraints corresponding only to points having coordinates ξ_1 and ξ_3 where these constraints exhibit a local minimum are retained. In the present study, such points are at the coordinates $\xi_3 = \xi_3^i$ and $\xi_3 = \xi_3^{i+1}$ (see Figs. 3.2.1 and 3.2.2) of the individual lamina comprising the cylinder skin adjacent to ring flanges and the clamped boundaries and ring webs at their most inboard edges.

Many different failure criteria exist that may be used as the basis for definition of the stress constraints. The simplest of these criteria, maximum stress or maximum strain, fails to account for the interaction among the various stress components acting at a single point. The Tsai-Wu¹²⁴ tensor polynomial approach is a popular failure criterion that accounts for this interaction that has, in some cases, been used to accurately predict experimentally observed failures. As pointed out by Hashin¹²⁵ however, the Tsai-Wu criterion fails to account for the fact that failure in composites can occur in one or more very different failure modes that might not be well represented by a single smooth function such as that of Tsai-Wu. Hashin proposes a failure criteria based on four separate failure modes: fiber tension, fiber compression, matrix tension, and matrix compression. Rosen, et. al.¹²⁶ extended Hashin's work by noting that the two matrix modes are more accurately characterized by four distinct matrix modes: two in-plane modes and two interlaminar modes dominated by interlaminar shear and normal stresses. The criteria of Rosen, et. al. have been chosen as the basis of the stress constraints in the present study. These constraints are : at each specified point within a

specified shell branch having coordinates ξ_1 and ξ_3

$$\text{If } \sigma_{11} \geq 0; \text{ then } 1.0 - \frac{\sigma_{11}}{\sigma_{11}^{AT}} \geq 0 \quad (6.5.1)$$

$$\text{If } \sigma_{11} < 0; \text{ then } 1.0 - \frac{\sigma_{11}}{\sigma_{11}^{AC}} \geq 0 \quad (6.5.2)$$

$$\text{If } \sigma_{22} \geq 0; \text{ then } 1.0 - \left(\frac{\sigma_{22}}{\sigma_{22}^{AT}} \right)^2 - \left(\frac{\tau_{12}}{\tau_{12}^A} \right)^2 \geq 0 \quad (6.5.3)$$

$$\text{If } \sigma_{22} < 0; \text{ then } 1.0 - \left[1.0 - \left(\frac{\sigma_{22}^{AC}}{2\tau_{12}^A} \right)^2 \right] \frac{\sigma_{22}}{\sigma_{22}^{AC}} - \left(\frac{\sigma_{22}}{2\tau_{12}^A} \right)^2 - \left(\frac{\tau_{12}}{\tau_{12}^A} \right)^2 \geq 0 \quad (6.5.4)$$

$$\text{If } \sigma_{33} \geq 0; \text{ then } 1.0 - \left(\frac{\sigma_{33}}{\sigma_{33}^{AT}} \right)^2 - \left[\frac{(\tau_{13}^2 + \tau_{23}^2)}{(\tau_{23}^A)^2} \right] \geq 0 \quad (6.5.5)$$

$$\text{If } \sigma_{33} < 0; \text{ then } 1.0 - \left[1.0 - \left(\frac{\sigma_{33}^{AC}}{2\tau_{23}^A} \right)^2 \right] \frac{\sigma_{33}}{\sigma_{33}^{AC}} - \left(\frac{\sigma_{33}}{2\tau_{23}^A} \right)^2 - \left[\frac{(\tau_{13}^2 + \tau_{23}^2)}{(\tau_{23}^A)^2} \right] \geq 0 \quad (6.5.6)$$

where the σ_{ij} are normal stresses with respect to the ij directions in the local *material* coordinate system (see Figs. 3.2.1 and 3.2.2), the τ_{ij} are shear stresses with respect to the ij coordinate directions, and the σ_{ij}^{AT} , σ_{ij}^{AC} , and τ_{ij}^A are allowable tensile normal, compressive normal (note that allowable compressive stresses are assumed to be negative values), and shear stresses, respectively, determined from simple unidirectional coupon tests. Eqs. (6.5.1) and (6.5.2) characterize fiber direction tensile and compressive failure modes respectively. Eqs. (6.5.3) and (6.5.4) characterize in-plane matrix tensile and compressive failure modes respectively while Eqs. (6.5.5) and (6.5.6) characterize interlaminar tensile and compressive failure modes respectively. Note that Eqs. (6.5.5) and (6.5.6) may also be used to characterize failure in the ring flange/cylinder skin attachment area.

6.6 Buckling Constraints

The true "buckling" constraint is that the axisymmetric equilibrium configuration of the ring-stiffened cylinder must remain stable under the imposed loads. The most popular way of writing this constraint mathematically is to constrain the lowest buckling load parameter to be greater than or equal to 1.0. In other words

$$1.0 - \lambda_{cr} \geq 0. \quad (6.6.1)$$

As was discussed in section 2.3.2, it is not sufficient to impose only the single constraint, Eq. (6.6.1), without considering buckling modes having larger buckling load parameters due to the possible occurrence of mode coalescence and/or mode switching. In the case of buckling of a cylindrical shell, it may be difficult to predict a priori how many of these higher modes must be accounted for.

In section 5.1 it was mentioned that the efficiency of the buckling analysis is highly dependent upon the speed with which, for a specified value of the circumferential wave number n_i (see section 5.1), the sequence of linear algebraic eigenvalue problems (Eq. (5.5.4)) are solved for the load parameter increments ($\Delta\lambda$). Also mentioned in section 5.1 is the fact that the efficiency of the solution of Eq. (5.5.4) drops substantially when $[K(n_i) + K_G(n_i; \lambda)]$ is not positive definite. Such a situation would arise if, for a specified value of n_i , critical load parameters related to modes higher than those associated with the smallest critical load parameter must be calculated. It was observed during the course of this study that, with the commercial eigensolvers available, the solution of Eq. (5.5.4) could not be performed with sufficient computational speed to make the optimal sizing algorithm practical.

Calculating the precise value of λ at which the structure will buckle along with the associated mode shape whenever the optimization subroutine calls for a buckling constraint evaluation is inefficient because it provides the optimizer with more information than is actually needed. A new constraint more directly related to the *stability*

(or lack thereof) of the axisymmetric equilibrium configuration can be formulated that lends itself to much faster evaluation than the constraint based on the buckling eigenvalue formulation. This new constraint does not require the solution of an eigenvalue problem; rather, it ensures that the matrix $[K(n_i) + K_G(n_i; \lambda)]$ remains positive definite, guaranteeing the stability of the axisymmetric equilibrium configuration. The constraint is formulated in sections 6.6.1 and 6.6.2 below.

6.6.1 LDL^T Decomposition of $[K(n_i) + K_G(n_i; \lambda)]$

It was mentioned in section 2.3.4 that Ringertz⁸³ presents a technique for imposing buckling constraints on designs of stiffened panels, characterized by a geometrically nonlinear prebuckling equilibrium configuration and analyzed using a commercially available finite element program, without solving a nonlinear eigenvalue problem. He develops the equivalent constraint

$$\sum_{i=1}^N \ln(\gamma_i) \geq 0 \quad (6.6.1.1)$$

where N is the order of the global stiffness and geometric stiffness matrices ($[K]$ and $[K_G]$) of the finite element model and the γ_i are the eigenvalues of $[K + K_G]$. Unfortunately, this constraint formulation still requires the solution of an N^{th} order eigenvalue problem for all N eigenvalues, which can be computationally expensive for large problems. Haftka¹²⁷ presents an alternate technique for establishing stability constraints without solving an eigenvalue problem. His method relies on the symmetry of $[K + K_G]$ ($[K(n_i) + K_G(n_i; \lambda)]$ in the present study). This property allows $[K(n_i) + K_G(n_i; \lambda)]$ to be factored as

$$[K(n) + K_G(n; \lambda)] = [L][D][L]^T \quad (6.6.1.2)$$

where $[L]$ is a lower triangular matrix with all diagonal terms equal to 1 and $[D]$ is a diagonal matrix. The matrix $[K(n_i) + K_G(n_i; \lambda)]$ is positive definite if and only if all

of the diagonal terms, d_i , of the matrix $[D]$ are positive. In other words

$$d_i \geq 0 \quad i = 1, 2, \dots, N. \quad (6.6.1.3)$$

The computation of LDL^T appears on pages 9 through 30 of Ref. 128 and is outlined in Appendix E. As is shown in Appendix E, the banded nature of the matrix $[K(n_i) + K_G(n_i; \lambda)]$ allows for very rapid factorization of this matrix even when its order is very large.

6.6.2 Equivalent Constraint Formulation

Haftka¹²⁷ imposed the nonnegativity requirement on all of the terms of the $[D]$ matrix, shown in Eq. (6.6.1.3), as buckling constraints in the sizing of a wing bay of the space shuttle orbiter. For the problem Haftka considered, Eq. (6.6.1.3) yielded about 50 separate constraints. Similar application of Eq. (6.6.1.3) to the problem considered in the present study would result in a prohibitively large number of inequality constraints. It can be shown that if the matrix $[M]$ is factored into an upper triangular matrix, $[M^*]$, using Gaussian Elimination then

$$[M^*] = [D][L]^T; \quad (6.6.2.1)$$

hence, the LDL^T factorization can actually be produced using Gaussian Elimination. If $[M^*]$ is made up of N -by- N square submatrices, then this Gaussian Elimination procedure is generally referred to as "Potter's Method". Blum and Fulton¹⁰⁷ state that if $[m^k]$ represents the k th submatrix ($k = 1, 2, \dots, N$) appearing along the diagonal of the upper triangular matrix, $[M^*]$, then all of the zero's of the determinant of the original matrix, $[M]$, are contained in the determinant of $[m^N]$, the last submatrix appearing along the diagonal of $[M^*]$. Since the order of the submatrices is not restricted, then $[m^k]$ can be 1-by-1 yielding the term-by-term Gaussian Elimination of Eq. (6.6.2.1) and the corresponding LDL^T factorization. The diagonal matrix $[D]$ is then a matrix of 1-by-1 "submatrices" corresponding to the $[m^k]$ submatrices of Potter's Method. This

means that if $[K(n_i) + K_G(n_i; \lambda)]$ is factored as shown in Eq. (6.6.1.2), then all of the zero's of the determinant of $[K(n_i) + K_G(n_i; \lambda)]$ are contained in the very last term of the $[D]$ matrix in Eq. (6.6.1.2). This means that, for a given value of n , as λ approaches λ_n (see section 5.1) from above, the first term of the $[D]$ matrix to reach zero will be the very last term, d_N . During the course of the present study, this has been observed in practice.

Starting from an initially feasible (all constraints satisfied) design, the structural optimization algorithm developed for the present study is formulated to produce a sequence of steadily improved feasible designs. Approximations for either the objective function or the constraints are avoided making it highly unlikely that convergence to an infeasible design during any portion of the optimization process will occur. Since the initial design and all subsequent improved designs are feasible, the axisymmetric equilibrium configurations of all these designs are stable and the $[K(n_i) + K_G(n_i; \lambda)]$ associated with these designs for all circumferential wave numbers, n , are positive definite. Furthermore, the first term of the $[D]$ matrix in the LDL^T decomposition of these $[K(n_i) + K_G(n_i; \lambda)]$ matrices to reach zero when $\lambda = \lambda_n$ (buckling occurs for the specified value of n_i) is the very last term, d_N , meaning that of all the constraints delineated in Eq. (6.6.1.3), $d_N \geq 0$ represents the *critical* constraint. From an initially feasible design, during movement in the design space to an improved design where the λ_n associated with some values n_i are reduced, no other term of the $[D]$ matrix associated with these n_i will reach zero without d_N reaching zero first. Hence, from the initially feasible design, the calculation of the search direction, \vec{S} , yielding an improved design can be based on a single stability constraint for each specified value of n_i , namely

$$d_N(n_i) \geq 0 \quad i = n_1, n_2, \dots, n_t \quad (6.6.2.2)$$

where t is the total number of values of n to be considered in the constraint set and the n_i are the prescribed circumferential wave numbers.

Given a feasible design, then, when determining a search direction, \vec{S} , all terms

of the $[D]$ matrix except the last one, d_N , can be ignored in the formulation of the stability constraints for each n_i . However, these other terms cannot be ignored during the one dimensional search for the step length, α^* (see Eq. (6.2.3)) because the function $d_N(n_i; \lambda)$ has poles at values of λ that are zeroes of these other terms. The function $d_N(n_i; \lambda)$ exhibits a jump discontinuity at these poles and thus can jump from negative to positive without passing through zero when $\lambda > \lambda_n$. During the one-dimensional search, a candidate value of α^* may move the design into the infeasible domain. If d_N is the only value returned to the optimization subroutine upon a call from the one-dimensional search routine at this value of α^* , the discontinuity exhibited by d_N in the infeasible domain could cause a positive value of the stability constraint to be returned to the optimizer even though the design is infeasible. Fortunately, if the design is infeasible, then at least one term of the $[D]$ matrix must be negative. Such negative terms can be used to augment the simple stability constraints specified in Eq. (6.6.2.2) during the one-dimensional search to ensure that a negative stability constraint value is returned to the optimizer whenever a candidate α^* produces an infeasible design. An equivalent exterior constraint is proposed that includes all of the negative terms in the $[D]$ matrix. At a candidate design, if n_{dn} is the number of these negative terms, not including the last term, d_N , then the equivalent stability constraint, for each specified circumferential wave number, used in the present study is

$$g_j^b = \begin{cases} d_N, & \text{if } n_{dn} = 0; \\ -|d_N| - \left[\sum_{l=1}^{n_{dn}} (d_l)^2 \right]^{1/2}, & \text{if } n_{dn} > 0. \end{cases} \quad (6.6.2.3)$$

The formulation of this constraint is based on the equivalent exterior constraint suggested by Haftka, Gürdal, and Kamat (Eq. 7.4.3 on page 239 of Ref. 9) for constraints that vary continuously with time. The idea of replacing a large number of constraints with a single equivalent constraint grew out of the fact that specifying a constraint at each time step would yield a prohibitively large number of constraints. A similar problem would occur in the present study if constraints were written for each diagonal term

of the $[D]$ matrix as the number of elements in the finite element model of the ring-stiffened cylinder became large.

Use of the equivalent constraint defined in Eq. (6.6.2.3) in optimization algorithms that operate in the infeasible region of the design space is not recommended. Furthermore, even if the equivalent constraint formulation is abandoned in favor of the specification of a constraint for every diagonal term of the $[D]$ matrix of the LDL^T decomposition of $[K(n_i) + K_G(n_i; \lambda)]$ shown in Eq. (6.6.1.3), use of an optimization algorithm that may converge to intermediate designs that are infeasible is still not recommended. This is because in the infeasible region of the design space the derivatives of the d_i with respect to the design variables, used to determine the search direction \vec{S} , are discontinuous.

It was also discovered that in the feasible region of the design space the derivatives of $d_N(n_i)$ with respect to the design variables are extremely large when λ is close to $\lambda_n(n_i)$. For example, for some designs when $\lambda - \lambda_n(n_i) \approx 0.001$ it was observed that the derivatives, $\partial d_N / \partial X_i$, were approximately 100000 while the value of the constraint was approximately 500. A constraint value of 500 does not appear to justify considering that constraint as active until it is recognized that very small reductions of the design variables (number of plies, length of ring flanges, etc.) produce immediate violation of the constraint. Hence, one final modification to the stability constraints was made to allow for a generous buffer zone preceding $g_j^b = 0$ where designs having stability constraints falling in this zone were considered infeasible. Thus the final form of the stability constraints used in the present study is

$$g_j^b - g_{buff}^b \geq 0 \quad j = 1, 2, \dots, t \quad (6.6.2.4)$$

where t is the number of critical and near-critical circumferential wave numbers for which constraints of the form shown in Eqs. (6.6.2.2) and (6.6.2.3) are written, g_j^b is given in Eq. (6.6.2.3), and g_{buff}^b is the value of g^b less than which the stability constraint is to be considered violated. A good value to assign to g_{buff}^b is dependent upon the particular problem being solved.

6.7 Sensitivity Analysis

During the execution of the optimal sizing algorithm, the optimization subroutine requires the values of the derivatives of F , g_j^b , and g_j^s (see Eq. (6.1.1)) with respect to the design variables X_i in order to determine the search direction \vec{S} (see Eq. (6.2.3)). In the present study, derivatives of the total structural weight with respect to the design variables, $(\partial F/\partial X_i)$, are evaluated in closed form. Derivatives of the behavioral (stress and stability) constraints are evaluated approximately using the following forward finite difference formulae

$$\frac{\partial g_j^s}{\partial X_i} \approx \frac{g_j^s(X_i + \Delta X_i) - g_j^s(X_i)}{\Delta X_i} \quad (6.7.1)$$

$$\frac{\partial g_j^b}{\partial X_i} \approx \frac{g_j^b(X_i + \Delta X_i) - g_j^b(X_i)}{\Delta X_i} \quad (6.7.2)$$

where ΔX_i is a small perturbation of the i th design variable. The calculation of the derivatives shown in Eqs. (6.7.1) and (6.7.2) requires $n_{dv}+1$ structural analyses where n_{dv} is the total number of design variables.

6.8 Convergence Criteria

In sections 6.1 through 6.7, the structural optimization problem that is the focus of the present study is formulated and methods are proposed for its solution. Since these methods are iterative in nature, criteria must be specified to determine convergence and the iteration cessation point. During the progress of the optimization algorithm, convergence criteria are needed for both the optimum step size, α^* , and the optimal design itself. In the present study, it is assumed that the convergence criteria for α^* that are set internally in both NEWSUMT-A¹¹⁴ and ADS¹²¹ are adequate; however, consideration of convergence criteria for the optimal design that are more precise than those used in these optimization programs is warranted. Such criteria are the subject of this section.

Convergence of the optimal design indicates when no further search directions, \vec{S} , need to be calculated and the calculation of new designs can be stopped. The most popular criteria used to indicate convergence, used in both NEWSUMT-A and ADS, are based on the absolute or relative change in the objective function after two or more iterations. For example, if after three iterations the objective function has changed by no more than some specified absolute or relative value the optimization process ceases. Use of such criteria is certainly justified in order to terminate a constrained minimization experiencing computational difficulties; however, further criteria are needed to establish the proximity of the candidate design to a true local optimum. More accurate determination of this proximity is particularly important when the relative merits and deficiencies of several optimum designs are to be assessed in a study meant to reveal design trends. If the absolute or relative change in the objective function is the only criterion used to establish the optimality of a candidate design, it is impossible to distinguish designs that converged due to their proximity to a true local minimum from designs that have not. Problems associated with numerical ill-conditioning may keep the optimizer from finding a search direction that reduces the objective function even though the current design is far from a local optimum. Hence, further criteria must be

applied in order to determine when a local optimum has been located.

Unless both the objective function and the feasible domain are both *convex* (see section 5.1.2 of Ref. 9), many local optima may exist in the design space. In the case of a nonconvex problem it is not possible to mathematically establish the global optimality of a locally optimum design without considering *all* local optima in the design space. However, rigorous criteria do exist to establish local optimality of a candidate design using information at the point in the design space defined by that design only. For inequality constrained problems, such as the one investigated in the present study, the *necessary* conditions for local optimality are

1. If a constraint, g , is not active ($g > 0$), its corresponding Lagrange Multiplier, Λ , is zero.
2. All of the Lagrange Multipliers associated with the set of g_j , $j = 1, 2, \dots, n_a$ active constraints ($g_j = 0$) are non-negative and

$$\vec{\nabla} \mathcal{L} = \vec{\nabla} F - \sum_{j=1}^{n_a} \Lambda_j \vec{\nabla} g_j = 0 \quad (6.8.1)$$

where \mathcal{L} is the Lagrangian function, $\vec{\nabla}$ is the gradient vector (derivatives with respect to the design variables), and Λ_j is the Lagrange Multiplier associated with the j th active constraint. These necessary conditions for optimality are known as the Kuhn-Tucker conditions.

Performing the dot product of both sides of Eq. (6.8.1) with a search direction, \vec{S} , and rearranging terms yields

$$\vec{S} \cdot \vec{\nabla} F = \sum_{j=1}^{n_a} \Lambda_j \vec{S} \cdot \vec{\nabla} g_j. \quad (6.8.2)$$

If $\vec{S} \cdot \vec{\nabla} F$ (or $\vec{S} \cdot \vec{\nabla} g_j$) > 0 then a move along \vec{S} increases F (or g_j). If $\vec{S} \cdot \vec{\nabla} F$ (or $\vec{S} \cdot \vec{\nabla} g_j$) < 0 then a move along \vec{S} decreases F (or g_j). Note that if the Λ_j are all positive and Eq. (6.8.2) is satisfied, it is impossible to have $\vec{S} \cdot \vec{\nabla} F < 0$ and all $\vec{S} \cdot \vec{\nabla} g_j > 0$. Since $g_j = 0$ for all active constraints, satisfaction of Eq.

(6.8.2) means that if $\vec{S} \cdot \vec{\nabla} F < 0$, then at least one constraint will be violated if a move along \vec{S} is made. One remaining possibility is a move in a direction, \vec{S} , along the local tangent to the objective function and the active constraints where

$$\vec{S} \cdot \vec{\nabla} F = \vec{S} \cdot \vec{\nabla} g_j = 0 \quad j = 1, 2, \dots, n_a. \quad (6.8.3)$$

In some cases, a move along a direction \vec{S} satisfying Eq. (6.8.3) may reduce F without violating any of the active constraints. The possible existence of such a search direction renders satisfaction of the Kuhn-Tucker conditions an *insufficient* proof of local optimality. Sufficiency can only be established by considering higher order derivatives of the objective function and constraints with respect to design variables (see Eqs. (5.1.14) through (5.1.16) of Ref. 9). A formal check of the sufficiency conditions is seldom performed in practice (and will not be performed in the present study) since it involves the calculation of these higher order derivatives. Furthermore, considering the theories upon which the optimization algorithms outlined in sections 6.2 and 6.3 are based, the chance that the algorithm could miss such a search direction and converge prematurely are small. Hence, in the present study, candidate designs satisfying the Kuhn-Tucker conditions will be considered to be local optima, with the caveat that the check for sufficiency of the Kuhn-Tucker conditions as proof of local optimality will not be made.

In practice, locating a design satisfying the Kuhn-Tucker conditions *exactly* is neither feasible nor necessary. Rather, satisfaction of these conditions to within some tolerance is more appropriate. In the present study, satisfaction of the Kuhn-Tucker conditions will be assumed if

$$\frac{\left| \frac{\partial F}{\partial X_i} - \sum_{j=1}^{n_a} \Lambda_j \frac{\partial g_j}{\partial X_i} \right|}{\left| \frac{\partial F}{\partial X_i} \right|} \leq \epsilon_{KT_i} \quad i = 1, 2, \dots, n_{dv} \quad (6.8.4)$$

where ϵ_{KT_i} is a small specified tolerance.

Eq. (6.8.4) requires the calculation of the Lagrange multipliers, Λ_j . In the present study, a least squares approach is used. First, Eq. (6.8.1) is rewritten as

$$\{G\} - [N] \{\Lambda\} = \{0\} \quad (6.8.5)$$

where

$$\{G\} = \vec{\nabla} F \quad (6.8.6)$$

and

$$n_{ij} = \frac{\partial g_j}{\partial X_i} \quad i = 1, 2, \dots, n_{dv} \quad j = 1, 2, \dots, n_a. \quad (6.8.7)$$

A residual vector, $\{u\}$, is defined such that

$$\{u\} = [N] \{\Lambda\} - \{G\}. \quad (6.8.8)$$

Next, the square of the norm of $\{u\}$, $\|\{u\}\|^2$, is minimized by differentiating it with respect to the Λ_j and setting the result of each differentiation to zero. This minimization yields

$$2[N]^T [N] \{\Lambda\} - 2[N]^T \{G\} = \{0\}. \quad (6.8.9)$$

Hence,

$$\{\Lambda\} = ([N]^T [N])^{-1} [N]^T \{G\} \quad (6.8.10)$$

Eq. (6.8.10) is the best solution in the least square sense; however, if the Kuhn-Tucker conditions (Eq. (6.8.5)) are satisfied it should be the *exact* solution. These Lagrange multipliers indicate the cost of the constraints, g_j , in terms of their affect on the objective function, F . Small values of Λ_j indicate that the constraint, g_j associated with that Λ_j can be made more restrictive without a significant associated increase in F .

When $n_a = 1$ (only one constraint is active) then satisfaction of the Kuhn-Tucker conditions is evaluated by considering the "cost-effectiveness" with respect to a change in each design variable given by

$$\frac{\partial F / \partial X_i}{\partial g / \partial X_i} \quad i = 1, 2, \dots, n_{dv} \quad (6.8.11)$$

where g is the active constraint. The Kuhn-Tucker conditions are satisfied when the cost-effectiveness with respect to each design variable is the same. As in Eq. (6.8.4), satisfaction of the Kuhn-Tucker conditions for the case of a single active constraint in the present study will be assumed when the cost-effectiveness with respect to each design variable is equal to within some tolerance, ϵ_{KT} .

Chapter 7

RESULTS AND DISCUSSION

7.1 Buckling Analysis Case Study

During the development of the numerical analysis outlined in Chapters 4 and 5, care was taken to insure that the results generated with the analysis of the present study matched previously published results. Several case studies of the buckling of imperfect, anisotropic unstiffened cylinders, the results of which were reported by Booton³⁵, were performed using this analysis. The calculated buckling loads matched the buckling loads reported by Booton precisely. Case studies of the buckling of an orthotropic annular plate subjected to outer edge compression were also performed with the analysis of the present study and compared to results published by Uthge-nannt and Brand¹²⁹ and Ramaiah¹³⁰. The buckling loads and mode shapes predicted using the analysis of the present study matched those reported by these authors precisely. A more general case study of the buckling of an anisotropic annular plate (an annular plate made of a composite laminate exhibiting bending-stretching coupling, twisting-stretching coupling, bending-twisting coupling or some combination of these couplings) subjected to outer edge compression was also performed using the analysis of the present study. No previously published results of such a case study could be found in the literature; hence, the buckling loads and mode shapes generated with the analysis of the present study were compared with buckling loads and mode shapes generated using the STAGS¹⁰⁶ general purpose finite element program. Geometries and orthotropic material properties used by Ramaiah¹³⁰ were chosen for this study; furthermore, $[+45/-45]_T$ and $[0/90]_T$ laminates of this orthotropic material were considered. Buckling loads and mode shapes generated with the analysis of the present study and STAGS matched precisely.

Before proceeding with an optimal sizing study, it is worthwhile to first consider a case study of the buckling behavior of a ring-stiffened cylinder subjected to vari-

ous loadings and including imperfections of various magnitudes. The results of such a case study can be used to help evaluate and understand the optimal ring-stiffened cylinders generated with the sizing algorithm. For the cylindrical shell depicted in Fig. 7.1.1, buckling loads were generated for several combinations of axial compression (P), torsion (T) and internal pressure (p). The corresponding unstiffened cylindrical shell was also considered for comparison. In all cases, the cylinder length (L) was 60.0 in., the cylinder radius was 18.08 in. and the shell wall was assumed to be a $[-45_4/45_4/90_4/0_4]_S$ laminate of graphite-epoxy prepreg tape having material properties shown in Table 1.1.1 For the ring-stiffened cases, the flange length (L_F) was 2.0 in., the web height (H_W) was 5.0 in., and the flanges, webs and cylinder end tabs (having length $L_F/2$) were all assumed to be made of a $[45/0/45]_T$ laminate of graphite-epoxy woven cloth material having properties shown in Table 7.1.2.

The buckling interaction diagram for perfect and imperfect unstiffened shells with and without pressure is shown in Fig. 7.1.2. For the two unpressurized cases, results were also generated using the analysis code published in the report by Booton³⁵. The pressurized case was not analyzed using Booton's code since it does not have the capability of computing buckling loads of cylinders loaded with constant pressure. The results, identified as Ref. 35 in Fig. 7.1.2, match the corresponding results generated using the present analysis very well. The arrows in Fig. 7.1.2 indicate percent changes in the buckling load of proportional load cases having the same ratio of N_X/N_{XY} , moving from the base of the arrow to the tip. As can be seen in the figure, the presence of an initial imperfection in the unpressurized shell having a maximum amplitude equal to 25% of the total shell thickness (t_S) results in a 54% drop in buckling load under pure compression but only a maximum 3.5% drop under pure torsion. The addition of a 60.0 psi internal pressure to the imperfect shell then raises the torsional buckling load a maximum of 110%; however, it raises the axial compression buckling load of the imperfect shell by only 22%.

A similar buckling interaction diagram for the ring-stiffened shell for four cases

of pressure and imperfection combinations is shown in Fig. 7.1.3. Three of the four buckling loci in Fig. 7.1.3 correspond to those shown for the unstiffened shell in Fig. 7.1.2 (the pressurized, perfect case was added to provide a theoretical upper bound interaction curve). For the unpressurized shell under pure torsion, the presence of the imperfection causes at most a 1% decrease in the buckling load as compared to that of the perfect structure; the addition of internal pressure raises the buckling load of the imperfect structure by 48%. Under pure compression, imperfections account for a 68% drop in buckling load compared to the perfect structure; addition of pressure then raises the buckling load of the imperfect cylinder subjected to axial compression 77% above the buckling load of the unpressurized, imperfect cylinder. Note that in the unstiffened shell, internal pressure was more effective in raising the buckling load under pure torsion than under pure compression while in the stiffened shell, the opposite is true. This difference in the effect of internal pressure on the buckling load of the unstiffened cylinder versus the ring-stiffened cylinder can be explained using Figs. 7.1.4 through 7.1.6 which show the effect on the buckling load of adding ring stiffeners to the unstiffened shell. In these figures, proportional load cases with the same N_X/N_{XY} ratio are linked by arrows pointing from the critical combination of N_X and N_{XY} at buckling of the unstiffened shell to the corresponding combination for the stiffened shell.

For the perfect, unpressurized cylinders (Fig. 7.1.4) adding rings produced up to an 85% increase in the torsional buckling load but virtually no increase in the axial compression buckling load. Rings are much more effective in resisting the formation of the long, skewed waveforms associated with torsional buckling than the shorter, less skewed waveforms associated with axial compression buckling. For the unpressurized, imperfect cylinder (Fig. 7.1.5), the results are nearly the same as the perfect cylinder in the case of pure torsion; however, under pure compression the ring-stiffened cylinder buckles at a load *below* that of the corresponding unstiffened cylinder. This lower buckling load can be explained by comparing plots of the buckling mode shapes of the imperfect and perfect cylinders for a single proportional load case. This load case is

labeled case "A" in Figs 7.1.4 through 7.1.6 and the mode shapes appear in Figs. 7.1.7 and 7.1.8. The buckling mode shapes of the cylindrical shell and ring webs show that the ring webs of the imperfect cylinder (see Fig. 7.1.8) buckle while the cylindrical shell does not buckle between the rings. On the other hand, the perfect cylinder (see Fig. 7.1.7) buckles in the panel length between the rings while the ring webs do not buckle. The outward radial Poisson expansion of the perfect, ring-stiffened cylinder results in the ring webs being stabilized by hoop tension loading; however, in the imperfect shell this is not necessarily true. Plots of prebuckling radial displacement of both the perfect and imperfect unpressurized ring-stiffened cylinders depicted in Fig. 7.1.1 are shown in Fig. 7.1.9 for loading case "A". For the perfect cylinder, the prebuckling radial displacement is positive everywhere; however, the imperfect shell wall exhibits regions where the net displacement is directed radially *inward*. The inward displacement is due to the nonlinear coupling of the axial compression load with the geometric imperfection where this imperfection is directed radially inward. Two of these regions are adjacent to the area where the ring attaches to the shell. Hence, the ring webs become loaded in hoop *compression* which is a destabilizing load. Since the webs are long and thin (the most likely configuration predicted by an optimum sizing code based on the analysis of the perfect structure), the hoop compression load causes them to buckle prematurely. Referring to Figs. 7.1.4 and 7.1.5, note that for cases where the addition of rings raises the buckling loads in both figures, the amount of increase exhibited by the imperfect cylinder was smaller than that exhibited by the perfect cylinder, except, of course, when the cylinder is loaded in pure torsion and therefore lacks any sensitivity to the axisymmetric imperfection considered in the present study. Furthermore, referring to Figs. 7.1.5 and 7.1.6, note that for cases where the addition of rings raises the buckling loads in both figures, the amount of increase exhibited by the pressurized cylinder was substantially smaller than that exhibited by the unpressurized cylinder.

7.2 Description of Optimal Sizing Case Studies and

Discussion of Algorithm Performance

Optimal design case studies were performed using the three cylindrical shell configurations depicted in Fig. 7.2.1. The first configuration is an unstiffened cylinder, the second configuration is a cylinder stiffened by two uniformly spaced steps in thickness (or straps), and the final configuration is a cylinder stiffened by two uniformly spaced "T"-shaped rings. All three cylindrical shell configurations are 45.00 in. long and have a 15.00 in. radius to the inner surface of the cylinder wall. Furthermore, the shell wall in all three configurations is a $[-45_{N_{45}} / +45_{N_{45}} / 90_{N_{90}} / 0_{N_0}]_s$ laminate of graphite-epoxy prepreg tape having the assumed orthotropic material properties listed in Table 7.1.1. The straps are assumed to be of length L_f and made of a $[45_{N_f} / 0_{N_f} / 45_{N_f}]_T$ laminate of graphite-epoxy cloth having the assumed orthotropic material properties listed in Table 7.1.2. The flanges and the webs of the "T"-shaped rings are assumed to be fabricated from the same cloth material as the straps and are assumed to be laminated in the same stacking sequence. These rings are assumed to have a flange length of L_f , and a web radial depth of H_W . It is also assumed that both the strap stiffeners and the "T" ring stiffeners are secondarily bonded to the shell wall using a 0.005 in. thick layer of ductile adhesive having the isotropic material properties listed in Table 7.1.3. A description of the six possible design variables, N_{45} , N_{90} , N_0 , N_f , L_f , and H_W are listed in Table 7.2.1 along with their specified upper and lower bounds and their initial design values.

Several combinations of mechanical loading (axial compression and torsion), internal pressure, and initial imperfection amplitudes have been considered. These combinations are listed in Table 7.2.2, where "LD ID" identifies each combination, P (N_X) is the axial loading, T (N_{XY}) is the torsional (shear) loading, p is the internal pressure loading, and μ is the maximum geometric imperfection amplitude written as a fraction of the total cylinder wall thickness t_s . Note that as the total cylinder wall thickness changes from one optimization iteration to the next, the absolute magnitude of the im-

perfection amplitude changes as well. An imperfect, pure torsion case was not considered since the shell is not sensitive to the axisymmetric imperfection considered in the present study in the absence of any axial compression loading. The magnitudes of the loads were chosen to approximate, at 1/8 scale, loadings typical of those occurring in various regions of the fuselage of a modern commercial transport aircraft. Note that each of the three shell configurations considered in the case study was sized for a *subset* of the cases listed in Table 7.2.2 rather than all 14 cases. Useful design trends can be established without considering all 14 cases.

It should be reiterated at this point that the optimal designs generated in the present study may be *local* optima rather than global optima. Hence, a possibility exists that, for a given configuration illustrated in Fig. 7.2.1 and LD ID listed in Table 7.2.2, it is possible that a design having a lower weight than the design reported as “optimal” may exist. No attempt is made, in the present study, to locate the global optima. Rather, from a point in the feasible domain of the design space (see Table 7.2.1 for the initial values of the various design variables that characterize this point), a search is performed in order to locate an adjacent local minimum.

Finding locally optimum designs that satisfied the Kuhn-Tucker conditions (see section 6.8) was difficult. It was found that, in many cases, such designs could not be located using NEWSUMT-A or the feasible directions algorithm in ADS alone; rather, it was discovered that the best results were achieved using a combination of these two algorithms. Design trends were blurred or hidden entirely until satisfaction of the Kuhn-Tucker conditions was enforced by repeated application of the penalty function and feasible directions algorithm. From an initially feasible design indicated in Table 7.2.1, NEWSUMT-A was used first. If the design that NEWSUMT-A converged to did not satisfy the Kuhn-Tucker conditions, then starting at this design, the method of feasible directions algorithm in ADS was used. In many cases, ADS had to be restarted two or three times before a design satisfying the Kuhn-Tucker conditions was located. The rationale for this approach was that it is known that performance of

the penalty function methods in the neighborhood of constraint boundaries can be poor due to ill-conditioning of the pseudo-objective function (Eq. (6.2.1)), while the method of feasible directions is written specifically for performing the search for a local optimum from designs lying directly on the constraint boundary. Performance of both NEWSUMT-A and ADS was controlled using the maximum number of iterations (15) convergence criterion, rather than the relative change in objective function criterion.

In many cases, NEWSUMT-A converged to a design satisfying the Kuhn-Tucker conditions when the optimal design problem was characterized by cylinder wall layer thickness design variables (N_{45} , N_{90} , and N_0) only. Even when more cylinder wall layer thickness design variables were added to the problem, NEWSUMT-A still converged to a design satisfying the Kuhn-Tucker conditions. However, in every case considered in the present study where the optimal design problem included both cylinder wall layer thickness design variables along with ring sizing design variables (N_f , L_f , and H_w) NEWSUMT-A converged to a non-optimal design requiring the subsequent application of the method of feasible directions in ADS. Attempts were made to improve the performance of the NEWSUMT-A algorithm by scaling the design variables and the constraints (see pages 97-100 and 136-137 of Ref. 11), to no avail. The necessity of having to restart the method of feasible directions periodically is thought to be related to the way the design variables, objective function, and the constraints are scaled in ADS. Scaling is performed only at the beginning of the first iteration of the method of feasible directions. Periodic re-scaling of the design variables, objective function, and constraints during iterations of the method of feasible directions subsequent to the first iteration would no doubt improve the algorithm. In any case, with this combination of NEWSUMT-A and ADS, the optimal designs to be reported in the section 7.3 were generated. All of these results satisfy the Kuhn-Tucker conditions to within a tolerance, ϵ_{KT} , (see Eq. (6.8.4)), of 7%. In certain cases, satisfaction of the Kuhn-Tucker conditions was forced to be tighter than 7%; however, the changes in the optimal values design variables resulting from this tighter tolerance were insignificant.

In order to speed the performance of the optimal sizing algorithm the stress constraints, described in section 6.5, were not included in the constraint set. It was assumed that for the loadings listed in Table 7.2.2, the stress constraints would not be critical in comparison to the stability constraints. Results of a thorough stress analysis of the optimal designs, to be reported in section 7.4, indicate that including only stability and side constraints in the constraint set was a reasonable approach. Generally, considering buckling modes associated with 7 or 8 different circumferential wave numbers in the stability constraint set was sufficient to allow for the possible occurrence of mode switching and mode coalescence. Close to the optimum, the number of different buckling modes considered in the constraint set could be reduced to as few as 3 or 4.

The finite element model used in the stability analysis contains elements with a maximum length of 1.0 in. in which the in-plane buckling displacements are interpolated quadratically. A minimum of two elements was used in the ring flanges and a minimum of three elements was used in the ring webs. This choice was based on a convergence study of the buckling loads of several cylinders, both stiffened and unstiffened, and several annular plates. Convergence of the finite element analysis for buckling typically occurred when the number of elements in the finite element mesh was sufficient to accurately represent the critical buckling mode shape of the ring-stiffened cylinder. Since the prebuckling equilibrium equations governing the response in each structural segment are solved in closed form, the effects of a finite element mesh on the prebuckling load distribution did not have to be considered. Hence, a detailed mesh at the boundaries and where the shell meets a ring flange was not needed. For the 45.00 in. long, 15.00 in. radius cylinder with rings having L_f and H_w dimensions shown in Table 7.2.1, the finite element meshes used in the present study are reasonable.

7.3 Optimal Design Case Study Results

The results of the optimal design studies of the unstiffened, strap-stiffened, and "T" ring-stiffened cylinders appear in Tables 7.3.1, 7.3.2, and 7.3.3 respectively. In these tables, LD ID refers to the cases listed in Table 7.2.2, t_s is the optimal total thickness of the cylinder wall of the optimal shell, % ± 45 , %90, and %0 represent the optimal distributions of the thicknesses of layers having $\pm 45^\circ$, 90° , and 0° fiber orientation angles, respectively, as a percentage of t_s , NORM. WT. is the optimal weight of the shell divided by the weight of the corresponding perfect ($\mu = 0$), unpressurized ($p = 0$) optimal unstiffened cylinder (Table 7.3.1, LD ID 1, 4, 7, 10, and 13), t_f is the optimal total thickness of the strap in Table 7.3.2 or the "T" ring flange in Table 7.3.3, L_F is the optimal length of the strap in Table 7.3.2 or the "T" ring flange in Table 7.3.3, H_W is the optimal radial depth of the web of the "T" ring in Table 7.3.3, and % RING WT. is the total weight of the rings expressed as a percent of the weight of the optimal ring-stiffened cylinder. In Tables 7.3.4, 7.3.5, and 7.3.6, the active constraints and the Lagrange multipliers corresponding to these active constraints associated with the optimal designs shown in Tables 7.3.1, 7.3.2, and 7.3.3 are listed. Under the heading "Stability Constraints", the circumferential wave numbers of the buckling mode shapes associated with the active stability constraints are presented. While lower bound side constraints, X^l , were active in several optimal designs, in no case was an active upper bound side constraint, X^u , observed. Note that in some cases (Table 7.3.5, LD ID 8, 10, and 14) stability constraints associated with more than one circumferential wave number were active at the final optimal design. Also note the magnitudes of the Lagrange multipliers associated with the active stability constraints. The small values reflects the observation, noted in section 6.6.2, that the gradients of the stability constraints become very large as these constraints become active and that generous "buffer zones" around these constraints (more generous, perhaps, than those used in the present study) can be used.

Before proceeding to a critical evaluation of the optimal designs, an example of

the existence of more than one local minima in the design space is presented. This is the optimal unstiffened cylinder design associated with LD ID 13 in Table 7.3.1. Both of these designs satisfy the Kuhn-Tucker conditions; furthermore, as an additional check, stability analyses were performed on new designs located at 10 equally spaced points along the vector connecting the two optimal designs within the design space. At each one of these design points, except, of course, the end points, at least one stability constraint was violated. This indicates that the two designs are, indeed, local optima. Note, from Table 7.3.1, that the two designs are very different; however, the weights of these designs (both normalized with respect to the weight of the lighter design) differ by only 2%. This reflects a feature of the problem that was observed many times during the course of the search for the optimal designs - that many non-optimal designs (non-optimal meaning designs that did not satisfy the Kuhn-Tucker conditions) that have weights within a few (5) percent of the weight of the true optimal design exist in the design space. This characteristic of the design space, sometimes referred to as "flatness", indicates that it is possible to change the optimal design to a non-optimal design, perhaps due to some requirement not considered in the present study, without paying a substantial weight penalty.

7.3.1 Unstiffened Cylinder Case Studies

The optimal thickness distributions of the $\pm 45^\circ$, 90° , and 0° layers of the unstiffened cylinders, listed in Table 7.3.1, are plotted in Figs. 7.3.1 through 7.3.3 as percent of the total shell wall thickness t_s versus LD ID number. No results are listed for LD ID 14 since the straps in optimal strap-stiffened design associated with this LD ID (Table 7.3.2) virtually vanished. The numbers in parentheses in Figs. 7.3.1 through 7.3.3 indicate the ratio of torsional (shear) loading (N_{XY}) to axial loading (N_X). Note, from Table 7.2.2, that this relative amount of torsional (shear) loading to axial compressive loading, also denoted by the ratio $N_{XY} : N_X$, increases with increasing value of the LD ID appearing along the horizontal axis of each of the three figures (7.3.1 through

7.3.3). For the perfect, unpressurized cylinders addressed in Fig. 7.3.1, the optimal designs are made up mostly of $\pm 45^\circ$ and 0° layers in all cases except LD ID 1 - pure axial compression. However, as illustrated in Fig. 7.3.2, when the initial imperfection is accounted for the thickness of the 90° layer is substantially greater than the 90° layer thickness in the corresponding perfect cylinder optimal design. As shown in Fig. 7.3.3, the optimal designs in the imperfect, pressurized case also have substantially thicker 90° layers than the corresponding perfect, unpressurized optimal cylinders and almost no 0° layers. Hence, the addition of internal pressure to the imperfect cylinder does not "negate" the effect of the imperfections on the optimal designs. Also, while the sizing of the perfect shell indicates striking differences in the optimal design of cylinders subjected to pure axial compression compared to those subjected to some amount of torsional loading, these differences are much less striking when initial imperfections are accounted for. For combined axial compression and torsional loading (LD ID 4, 7 and 10 in Fig. 7.3.1, LD ID 5, 8 and 11 in Fig. 7.3.2, and LD ID 6, 9 and 12 in Fig. 7.3.3.), the inclusion of initial imperfections results in the optimal cylinder appearing less like the optimal design of the cylinder subjected to pure torsion and more like that of a cylinder subjected to pure compression.

Fig. 7.3.4 depicts the effects of imperfections and internal pressurization on the optimal weights of the unstiffened cylinders. Only the LD ID numbers associated with the perfect, unpressurized configuration is indicated on the horizontal axis of this figure. For example, LD ID 1 identifies the perfect, unpressurized cylinder loaded in pure compression; however, the optimal weights of the imperfect, unpressurized (LD ID 2), and imperfect, pressurized (LD ID 3) cylinders are also identified by LD ID 1 since the mechanical loading (axial compression) is the same for LD ID 1, 2, and 3. For each value of LD ID, the optimal weights are normalized with respect to the optimal weight of the perfect, unpressurized cylinder associated with that value of LD ID. In all of the cases shown, the optimal weights (and thus the optimal total cylinder wall thicknesses) of the imperfect, unpressurized cylinders are substantially (10% or more)

greater than the optimal weight of the corresponding perfect, unpressurized cylinder. This weight difference is a function of the relative amount of torsional to axial loading ($N_{XY} : N_X$) that the cylinder is subjected to. The higher this ratio, the lower the difference. For example, when $N_{XY} : N_X$ is 0 (LD ID 1) the difference is almost 50%; however, when $N_{XY} : N_X$ is 1:1, the difference is 10%. This observation quantifies, in terms of optimal weight, what the buckling interaction curve of Fig. 7.1.2 quantifies in terms of buckling loads - that the imperfection sensitivity of the cylinder increases as the ratio of axial compression loading to torsional loading increases. The effects of pressurization on the optimal designs of the imperfect cylinders, also depicted in Fig. 7.3.4, will be discussed after a brief explanation of the observed effects of imperfections on the optimal designs.

The facts that the inclusion of the initial geometric imperfection results in both an increase in the total cylinder wall thickness and a substantial increase in the percent thickness of the 90° layers can be explained by considering the particular solution (Eq. (4.1.32)) to the equation governing the prebuckling radial displacement of the cylinder wall (Eq. (4.1.27)). The contribution to this particular solution from the initial imperfection is

$$\bar{w}_p^o(X) = \bar{A} \cos \omega X \quad (7.3.1.1)$$

where

$$\bar{A} = \frac{\mu \omega^2 \bar{N}_X}{a_1 \omega^4 - a_2 \omega^2 + a_3}. \quad (7.3.1.2)$$

For the balanced, symmetric cylinder wall laminate considered in the present study, replacing the terms in Eq. (7.3.1.2) with the dimensional terms listed in Table 1 yields

$$\bar{A} = \frac{\mu N_X L^2}{N_X L^2 + 2\sqrt{D_{11}^*/A_{22}^*} \bar{Z} t_s} \quad (7.3.1.3)$$

or

$$\bar{A} = \frac{\mu N_X}{N_X + (2/R)\sqrt{D_{11}[A_{22} - (A_{12}^2/A_{11})]}} \quad (7.3.1.4)$$

To reduce the radial shell wall deformations induced by the initial imperfection in the presence of the axial load, the denominator of Eq. (7.3.1.4) should be as large as possible. This can be accomplished by increasing the axial bending stiffness, D_{11} , of the cylinder wall, the hoop membrane stiffness, A_{22} , of the cylinder wall, or a combination of the two. This is why the optimal designs of the imperfect shells are thicker than the corresponding perfect designs and that most of this additional thickness is made up of 90° layers. The increase in the size of the 90° layer raises the hoop membrane stiffness and moves the $\pm 45^\circ$ layers further away from the middle surface of the cylinder wall.

A final trend indicated in Fig. 7.3.4 is that the optimal weights of the pressurized, imperfect cylinders are substantially smaller than the optimal weights of corresponding unpressurized, imperfect cylinder. For LD ID 10 ($N_{XY} : N_X = 1 : 1$), the optimal weight of the pressurized, imperfect cylinder is 28% smaller than the unpressurized *perfect* cylinder; however, for LD ID 1 ($N_{XY} : N_X = 0$) the optimal weight of the imperfect, pressurized cylinder is only 10% smaller than the optimal weight of the unpressurized, imperfect cylinder. This information again quantifies, in terms of optimal weight, what is quantified in terms of buckling loads in the buckling interaction curves of Fig. 7.1.2 - that the added capability of the cylinder to resist buckling due to the addition of internal pressure increases with an increase in the ratio $N_{XY} : N_X$.

7.3.2 Ring-Stiffened Cylinder Case Study

7.3.2.1 Discussion of Optimal Design Detail Trends

The optimal sizing results for the strap-stiffened cylinders, reported in Table 7.3.2, are plotted in Figs. 7.3.5 through 7.3.7. The optimal sizing results for the "T" ring-stiffened cylinders, reported in Table 7.3.3, are plotted in Figs. 7.3.8 through 7.3.10. The additional ring weight parameter plotted in Figs. 7.3.5 through 7.3.7 and Figs. 7.3.8 through 7.3.10 indicates the weight of the rings (straps or "T"s) of the optimal designs as a percentage of the total weight of the optimal ring-stiffened cylinder de-

sign.

Figs. 7.3.5 through 7.3.7 and Figs. 7.3.8 through 7.3.10 indicate that the trends in the distribution of the cylinder wall layers thicknesses are similar to those trends observed in the case study of the unstiffened cylinders that was discussed in detail in section 7.3.1. The only measurable difference between the unstiffened and ring-stiffened cylinder wall layer thickness distributions is that the optimal ring-stiffened cylinders have a larger percentage of $\pm 45^\circ$ layers than the corresponding optimal unstiffened cylinders do.

As shown in Table 7.3.2, in every design where a ring of substantial stiffness is called for, the optimal strap design has a length of the lower bound value of 1.00 in. and, as shown in Table 7.3.3, the optimal "T" ring design is one with a thin narrow flange (generally a flange with a lower bound length of 1.00 in.) and a thin deep web. A plot of the total ring weights of the optimal strap-stiffened and "T" ring-stiffened cylinders as a percent of the total weight of the optimal ring-stiffened cylinder, shown in Fig. 7.3.11, illustrates that for all but LD ID 9, the optimal strap designs are many times heavier than the optimal "T" ring designs. All of these observations indicate that the rings are sized for optimal bending stiffness. This occurs because the critical buckling mode shapes of the cylindrical shell, the formation of which the rings must be designed to resist, are generally asymmetric. Such a buckled configuration, should it occur, would result in substantial bending of the rings.

Another issue that can be addressed with the results of these optimal sizing case studies is whether or not the presence of initial imperfections in the cylinder wall impact the designs of the rings in the optimal cylinder significantly. Looking at Fig. 7.3.8, the plot of the optimal designs for the perfect, unpressurized, "T" ring-stiffened cylinders, it is clear that the percent ring weight increases with increasing $N_{XY} : N_X$; however, this trend is not so clear in Fig. 7.3.9, the plot of optimal designs of the corresponding imperfect, unpressurized cylinders. To see why this is so, the ring weight percentages in the optimal "T" ring-stiffened cylinders sized for three different val-

ues of $N_{XY} : N_X$ are plotted in Fig. 7.3.12 for both the perfect, unpressurized and imperfect, unpressurized configurations. It is clear from this figure that the presence of imperfections in the cylinder wall can result in significant ring weight increases in the optimal cylinders when compared to designs where imperfections are ignored. For example, for a ratio $N_{XY} : N_X$ of 1:4, the weight of the "T" rings of the optimal perfect, unpressurized cylinder is only 0.500% the total weight of the structure while the weight of the "T" rings of the optimal imperfect, unpressurized cylinder is 1.3% of the total weight of the optimal structure - an increase of 160%! It is postulated that this increase in the percent ring weights in the optimal imperfect cylinders is most likely due to the ability of the imperfections to trigger premature buckling of the ring webs. This ability is illustrated in Figs. 7.1.7 through 7.1.9 and discussed in section 7.1.

7.3.2.2 Discussion of Optimal Weight Trends

In Figs. 7.3.13 and 7.3.14, the optimal weights of the ring-stiffened cylinders have been normalized with respect to the optimal weights of the corresponding perfect, unpressurized, *unstiffened* cylinders. The effects of imperfections and pressurization on the optimal total weights of the ring-stiffened cylinders, illustrated in Figs. 7.3.13 and 7.3.14, are the same as the effects of these parameters on the optimal total weights of the corresponding unstiffened cylinders illustrated in Fig. 7.3.4.

The buckling interaction curves of Figs. 7.1.4 through 7.1.6 indicate that the addition of rings can increase the capability of an unstiffened cylinder to resist buckling substantially when some amount of torsional loading is present. This phenomenon is quantified in terms of the weight saved in the optimal designs of the cylinder as shown in Fig. 7.3.15. In this figure, the percent difference in weight between the optimal strap-stiffened or "T" ring-stiffened cylinders and the corresponding optimal unstiffened cylinders is plotted for various values of LD ID. As to be expected from a consideration of Fig. 7.3.11, the "T" ring-stiffened cylinders are substantially more efficient than the corresponding strap-stiffened cylinders. Furthermore, the addition of ring-stiffening

yields significant weight savings even when the ratio of torsional load to axial load is small. For example, LD ID 5 corresponds to an imperfect cylinder having a ratio $N_{XY} : N_X$ of only 1:4; however, the addition of rings to the unstiffened cylindrical shell subjected to this loading still produces a 6% savings in weight. Of course, as shown in Fig. 7.3.15, the weight savings are many times greater in cases where the cylinder is loaded by more substantial amounts of torsion. This reflects the observation made about Figs. 7.1.4 through 7.1.6 in section 7.1 - that the effect of adding rings to the unstiffened cylinder on the buckling resistance of the structure increases with an increase in the ratio $N_{XY} : N_X$. For example, adding "T" ring-stiffeners to the imperfect cylinder loaded by torsion and axial compression in the ratio $N_{XY} : N_X$ of 1:1 (LD ID 11) yields a weight savings of 17%!

Two other observations made in section 7.1 concerning Figs. 7.1.4 through 7.1.6 were that the net increases in the buckling loads that occurred when rings were added to the perfect, unpressurized, unstiffened cylinder were reduced when imperfections were accounted for in the analysis, and that these net increases were drastically reduced when the imperfect cylinder was pressurized. This is reflected in the overall drop in the amount by which the optimal weight of the ring-stiffened cylinder differs from the weight of the corresponding optimal unstiffened cylinder, as is illustrated in Fig. 7.3.15 when a weight savings associated with a perfect, unpressurized configuration (LD ID 4,7, and 10) is compared to the weight savings associated with an imperfect-unpressurized (LD ID 5,8, and 11) or imperfect-pressurized configuration (LD ID 6 or 9). This drop in weight savings for three "T" ring-stiffened cases is more clearly illustrated in Fig. 7.3.16. For example, LD ID 7 corresponds to a perfect, unpressurized cylinder subjected to axial compression and torsional loading in the ratio $N_{XY} : N_X$ of 1:2. For this LD ID, adding the two "T" ring stiffeners produces an optimal weight savings of 16%; however, in the corresponding imperfect case (LD ID 8), the weight savings is reduced to 11%. When the internal pressure is included (LD ID 9) the total weight savings due to the addition of the "T" ring stiffeners is only about 5%. The

lack of effect the rings have in increasing the buckling resistance of the imperfect, pressurized cylinders is also demonstrated by comparing the percent ring weights of the optimal imperfect, pressurized cylinders (Fig. 7.3.7 for the strap-stiffened cylinders and Fig. 7.3.10 for the "T" ring-stiffened cylinders) to the percent ring weights of the optimal perfect and imperfect, unpressurized cylinders (Figs. 7.3.5 and 7.3.6 for the strap-stiffened cylinders and Figs. 7.3.8 and 7.3.9 for the "T" ring-stiffened cylinders). The percent ring weights of the optimal imperfect, pressurized cylinders are substantially smaller in each case than the percent ring weights of the corresponding perfect and imperfect unpressurized cylinders.

7.4 Stress Constraints

In this section, the stress constraints described in section 6.5 are addressed. Under the assumption that the stability constraints described in section 6.6 would be critical for design, the stress constraints were ignored during the optimal sizing of the cylinders described in section 7.3. It is appropriate at this point, therefore, to perform a stress analysis of the optimal cylinders in order to check the validity of the assumption of stability constraint criticality. This stress analysis is based on a lamina stress analysis of the cylinder skin (see Appendix A), a lamina stress analysis of the ring webs (interlaminar stresses ignored), and an analysis of the through-the-thickness normal (or "peel") stresses and transverse shear stresses in the adhesive used to bond the straps (or "T" rings) to the cylinder wall. Initial geometric imperfections in the cylinder wall are ignored for stress analysis purposes. Imperfections are ignored because the initial imperfection shape used in the present study, Eq. (4.1.25), was chosen because of the strong coupling demonstrated to exist between this imperfection and asymmetric buckling mode shapes, not necessarily because of its true representation of real imperfection distributions. Lamina stresses are calculated at the extreme surfaces of each layer of the cylinder skin or ring webs at stations spaced 0.10 in. apart. Adhesive stresses are calculated at stations approximately 0.05 in. apart along the length of the strap or the flange connecting the "T" ring to the cylinder wall. At each station, the stress constraints (Eqs. (6.5.1) through (6.5.6)) are evaluated as is appropriate. At the ring/skin interface, the interlaminar failure constraints of Eqs. (6.5.5) and (6.5.6) are evaluated with respect to the allowable stresses of the adhesive, listed in Table 7.1.3 along with the rest of the assumed material properties of this adhesive, and the allowable stresses of the inner-most cylinder skin layer of graphite-epoxy tape, listed in Table 7.1.1, to which the adhesive is applied. Before proceeding to a discussion of the results of the stress analysis of the optimal cylinder designs, a brief discussion of the nature of the stresses in the ring flange/cylinder skin interface is presented.

7.4.1 Ring Flange/Cylinder Skin Interface Stresses

In order to investigate the nature of the stresses in the ring flange/cylinder skin interface, a "T" ring-stiffened cylinder having the same configuration as the one used as the initial design for the "T" ring-stiffened cylinder optimal sizing case studies described in section 7.3.2 is considered. This cylinder is 45.0 in. long, has an inner surface radius of 15.00 in., and is made of a $[-45_s/45_s/90_s/0_s]_s$ laminate of graphite-epoxy tape having the material properties listed in Table 7.1.1. It is stiffened by two equally spaced rings as shown in Fig. 7.2.1. Two different ring configurations are considered. The first configuration has $L_f = 2.0$ in., $H_w = 3.0$ in., and $N_f = 1$ ($t_f = 0.042$ in.) (see Table 7.2.1). This first configuration was chosen to approximate a ring having a long, thin attachment flange. The second configuration has $L_f = 1.0$ in., $H_w = 3.0$ in., and $N_f = 4$ ($t_f = 0.168$ in.). This second configuration was chosen to approximate a ring having a short, thick attachment flange. The ring-stiffened shell is assumed to be subjected to an axial compression load of 250000. lbs., a torsional load of 1875000. in.-lbs., and an internal pressure load of 70.0 psi.

The resulting distributions of adhesive through-the-thickness normal (or "peel") stresses, $\sigma_{ZZ} = \sigma_{33}$, and transverse shear stresses, $\tau_{XZ} = \tau_{13}$ and $\tau_{YZ} = \tau_{23}$ (see Fig.4.4.1) for the two ring configurations are plotted in Figs. 7.4.1, 7.4.2, and 7.4.3 respectively for one of the ring stiffeners. The web of this ring is located at $x = -7.50$ in., the two edges of the long flange are located at $x = -8.50$ in. and $x = -6.50$ in., and the two edges of the short flange are located at $x = -8.00$ in. and $x = -7.00$ in. In their analysis of skin/stiffener interface stresses in composite stiffened panels, Wang and Biggers⁵⁰ demonstrated that at the free edges of the flanges that attach the stiffener to the panel skin, these adhesive stresses peak sharply in a narrow region adjacent to the free edge of the flange. Figs. 7.4.1 through 7.4.3 demonstrate that this is also true of the stresses in the ring flange/cylinder skin interface region. The peel stresses (Fig. 7.4.1) also peak in a region directly below the point where the ring web and flange are joined, as is to be expected since the stiff web restrains the flange/skin combination

from outward radial expansion under the action of the internal pressure. There is a significant difference in the distribution of the through-the-thickness normal stress beneath the long, thin ring flange and the short, thick flange. The long, thin flange only tends to separate from the cylinder skin directly beneath the ring web, while the short, thick flange shows a very strong tendency to separate from the cylinder skin in a narrow region near the free edge of the flange. These observations are consistent with those reported by Wang and Biggers⁵⁰ for the flat stiffened panels.

The τ_{XZ} transverse shear stress distributions illustrated in Fig. 7.4.2 also show peak values occurring in a narrow region near the free edge of the flange. Actually, τ_{XZ} beneath the free edge of the flange should be zero; however, the simplified treatment of the adhesive as a set of shear springs in the present study does not allow for enforcement of the condition $\tau_{XZ} = 0$ at this edge. In their study of tubular lap joints, Adams and Peppiatt⁹³ used a more detailed model of the adhesive to show that the transverse shear stress corresponding to τ_{XZ} in the present study actually peaks very close to the edge of the adhesive then drops to zero at the edge very suddenly. Hence, while the simplified adhesive model used in the present study does not allow for enforcement of $\tau_{XZ} = 0$ at the edge of the adhesive, it does appear to allow for reasonable prediction of this adhesive stress up to, but not including, this edge.

As shown in Fig. 7.4.2, the stress state adjacent to the free edge of the long, thin flange is substantially more severe than the stress state adjacent to the free edge of the short, thick flange. This result is consistent with the observation made by Wang and Biggers⁵⁰ that to minimize the maximum value of this τ_{XZ} shear stress, a minimum practical flange length should be used. The τ_{YZ} transverse shear distributions appear in Fig. 7.4.3. Once again, the peak values occur in a narrow region adjacent to the free edge of the flange. The curves plotted in Fig 7.4.3 show that the difference in the distributions of the τ_{YZ} transverse shear stress beneath the long, thin flange and the short, thick flange is not as pronounced as the corresponding difference in the distributions of the τ_{XZ} transverse shear stress. Furthermore, the peak stress at the free

edge of the short, thick flange is about 50% higher than the peak stress at the free edge of the long, thin flange. This is also consistent with the observations of Wang and Biggers⁵⁰. They showed that the τ_{YZ} stress distribution is not sensitive to the flange length and that the peak τ_{YZ} transverse shear stress increases with along with an increase in flange thickness. The conflicting effects of the various ring flange parameters on the various adhesive stresses indicate that a ring flange design may exist producing optimal ring/skin joint strength.

7.4.2 Results of Stress Analyses of Optimal Cylinders

The results of the stress analyses of the optimal strap-stiffened and "T" ring-stiffened cylinders are listed in Tables 7.4.1 and 7.4.2 respectively. The optimal cylinder design is identified by LD ID in the first column. Stress analyses were not performed on the optimal unstiffened cylinders since the optimal layer thickness distributions of the corresponding optimal ring-stiffened cylinders were very similar and the cylinder wall total thicknesses of the ring-stiffened cylinders were all smaller than the corresponding unstiffened cylinders. In Tables 7.4.1 and 7.4.2, the minimum values of the constraints associated with a cylinder skin lamina fiber direction failure (Eqs. (6.5.1) and (6.5.2)), an in-plane lamina matrix cracking failure (Eqs. (6.5.3) and (6.5.4)), and an interlaminar-type failure (Eqs. (6.5.5) and (6.5.6)) in the ring/skin interface region are listed. Also listed are the locations of the minimum values of the cylinder skin lamina fiber direction and in-plane matrix cracking stress constraints in terms of the normalized meridional coordinate X ($X = \pm 0.500$ at the extreme ends of the cylinder) and the cylinder wall laminate layer where these minimum constraint values occur. A "T" is used to indicate that an in-plane tension failure constraint (Eq. (6.5.1) or (6.5.3)) is critical while a "C" is used to indicate that an in-plane compression failure constraint (Eq. (6.5.2) or (6.5.4)) is critical. The letters "AT" indicate that an adhesive tension failure constraint (Eq. (6.5.5)) is critical. The letters "AC" indicate that an adhesive compression failure constraint (Eq. (6.5.6)) is critical. Stresses in the ring

webs did not produce constraint values smaller than the values listed in Table 7.4.2 in any case. Furthermore, the interlaminar stresses in the cylinder skin calculated using the method outlined in section A.2 of Appendix A were small in every case considered. Interlaminar shear stresses, calculated using the method of section A.2, were less than 2000 psi in each case; furthermore, the maximum calculated through-the-thickness tensile normal stress, calculated using this method, was 100 psi.

In Tables 7.4.1 and 7.4.2, positive minimum constraint values indicate stress constraint satisfaction; negative constraint values indicate stress constraint violation. The dashes indicate constraints equal to 1.0 for all practical purposes. In all but one case (LD ID 14 of the optimal strap-stiffened cylinder designs), the optimal cylinder designs lie well within the feasible domain defined by the stress constraints alone. Furthermore, except for LD ID 13, critical constraint values typically occur either at the clamped ends of the cylinder or in the cylinder wall bending boundary layer adjacent to these ends. The cylinders corresponding to LD ID 13 are loaded in pure torsion; the minimum constraint values occur in the cylinder skin at $X = 0.178$. This is adjacent to the edge of a strap or ring flange.

The large positive values of the stress constraints indicate that the assumption of stability constraint criticality was reasonable in every case except the strap-stiffened cylinder associated with LD ID 14. In this case, which is for the cylinder subjected to torsion and internal pressure without axial loading, an in-plane matrix cracking constraint at the clamped end of the cylinder is violated. All other stress constraint values are large positive numbers. In his study of pressurized cylindrical panels, Boitnott⁵⁴, observed during his experiments that he could not detect any damage in the graphite-epoxy panels until the pressures reached values substantially higher than those predicted to produce in-plane matrix cracking failures. Hence, a comparison of the optimal designs of the strap-stiffened cylinders in which in-plane matrix cracking constraints are satisfied with those in which these constraints are violated, with all other constraints satisfied, is of some interest. The strap-stiffened cylinder was re-sized for

LD ID 14 with additional constraints added to prevent violation of the in-plane matrix cracking constraints at the clamped end. The new optimal design, satisfying all stress constraints, and the design from Table 7.3.2, in which the in-plane matrix cracking stress constraint is violated, appear below.

Design Variable	Matrix Cracking	No Matrix Cracking
t_s	0.05053 in.	0.07815 in.
% ± 45	97.269	64.985
% 90	0.974	35.002
% 0	1.757	0.013
t_f	0.0059 in.	0.0000 in.
L_f	1.000 in.	1.000 in.
Buckling λ_{cr}	1.000	1.32
Norm. Wt.	1.000	1.469

Note that the weights of the optimal designs are normalized with respect to the weight of the optimal strap-stiffened cylinder design violating the in-plane matrix cracking constraint (the lower weight design). Also note that the stability constraint for the design satisfying the in-plane matrix cracking stress constraint is not active. To satisfy the in-plane matrix cracking constraint, a 90° layer that is significantly larger than the 90° layer in the optimal design where this constraint is violated is needed. Furthermore, it is readily apparent that a significant penalty in optimal weight is associated with enforcing the satisfaction of the in-plane matrix cracking constraint in this case.

7.4.3 Internal Pressure To Failure

The final portion of the present study involves an investigation of the stress failures occurring in the optimal ring-stiffened cylinder design of Tables 7.3.2 and 7.3.3 due to the application of their design mechanical loads (axial compression and torsion) along with internal pressures that are higher than those for which the cylinder was sized. This investigation is performed by predicting, for each optimal strap-stiffened

and "T" ring-stiffened cylinder, the value of internal pressure at which a stress failure is first likely to occur. The results of this study are listed in Table 7.4.3 for the optimal strap-stiffened cylinders and in Table 7.4.4 for the optimal "T" ring-stiffened cylinders. The form of these tables is the same as the form of Tables 7.4.1 and 7.4.2, except the constraint values listed are for the cylinders subjected to the mechanical loads associated with the LD ID indicated in the first column and the internal pressure to failure indicated in the second column. Furthermore, the letters "CT" indicate that an inter-laminar tension failure constraint (Eq. (6.5.5)), at the innermost layer of the cylinder wall to which the adhesive bond is applied, is critical.

Wang and Biggers⁵⁰ mention that the stresses in the flange/skin interface region of flat stiffened graphite-epoxy panels are particularly sensitive to the laminate stacking sequence of the stiffener flange. Hence, for the three cases in Table 7.4.3 where the indicated first failure in the optimal strap-stiffened cylinders is predicted to occur due to high adhesive through-the-thickness normal and transverse shear stresses (LD ID 8, 10, and 13) a new pressure to failure was calculated for the shell having straps with the stacking sequence $[0_N, /45_N, /45_N,]_T$ instead of $[45_N, /0_N, /45_N,]_T$. Note that the new strap laminate is unsymmetric. A check of the buckling loads of the optimal cylinders having straps with the new stacking sequence indicated that the effect of this change on the buckling load was negligible. In all three cases, the internal pressure to failure of the cylinders with the unsymmetrically laminated straps increased. These increases are illustrated in Fig. 7.4.4. The failure pressures in this figure are normalized with respect to the failure pressure of the cylinders with symmetrically laminated straps. Note that for LD ID 8 and 10 the internal pressures to failure of the cylinders with the unsymmetrically laminated straps are 120% and 40% higher, respectively, than the internal pressures to failure of the cylinders with the symmetrically laminated straps. The increase in failure pressure of the cylinder sized for torsional mechanical loading only (LD ID 13) is not as high as the cylinders sized for both axial compression and torsional loading. The failure pressures of the cylinders with the unsymmet-

rically laminated straps are higher since the edges of the straps curl into the cylinder skin as the strap stretches in the hoop direction due to the bending-stretching coupling exhibited by the unsymmetric laminate. This curling forces the flange to conform more with the cylinder skin as it tends to separate from the strap due to local bending under the combined action of axial compression and internal pressure loading. This lowers the peel stress in the adhesive substantially.

For cases in Tables 7.4.3 and 7.4.4 where the first predicted failure was due to in-plane matrix cracking, internal pressures to failure were also calculated where this failure mode was ignored. The results of this study for the strap-stiffened cylinders appear in Fig. 7.4.5 and for the "T" ring-stiffened cylinders in Fig. 7.4.6. The substantial increase in failure pressure illustrated in all cases, along with the result discussed in section 7.4.2 illustrating the potential weight penalty associated with satisfying in-plane matrix cracking strength constraints in stress constraint-critical optimal designs, indicates that serious study of the effects of in-plane matrix cracking on the failure of pressurized structure is warranted.

Chapter 8

CONCLUDING REMARKS AND RECOMMENDATIONS FOR FURTHER WORK

8.1 Concluding Remarks

A structural analysis has been developed to predict prebuckling deformations, prebuckling stresses and buckling loads of anisotropic cylinders with secondarily bonded ring stiffeners, subjected to axial compression, torsion, and internal pressure. The structure is modeled as a branched shell. A nonlinear axisymmetric prebuckling equilibrium state is assumed which is amenable to exact solution within each branch. A simple analytical model, characterized by the approximate treatment of the adhesive layer as a series of uniformly distributed shear and extensional elastic springs, is employed to predict prebuckling stresses in the ring flange/ cylinder skin interface region. Stress resultants and stress couples generated using the exact solutions are applied as boundary conditions to this model. Buckling displacements are represented by a Fourier series in the circumferential coordinate and the finite element method in the cylindrical shell axial coordinate or ring web radial coordinate.

Several case studies were conducted using this structural analysis in order to assess the effects of imperfections, pressurization, and ring stiffening on the buckling loads and mode shapes of a cylindrical shell. It was demonstrated that a nonlinear prebuckling analysis is needed to accurately predict buckling loads and capture the buckling mode shapes of ring-stiffened cylindrical shells. It was found that the effect of rings on the buckling resistance of the cylinder is very sensitive to the relative magnitudes of axial compression loading, torsional loading, and internal pressure loading to which the structure is subjected. The rings become more effective as the relative magnitude of the torsional loading to axial compression loading is increased. The rings become less effective when the amount of internal pressure loading is increased.

The structural analysis was then implemented in an optimal sizing algorithm. An equivalent stability constraint, formulated based on the LDL^T decomposition of the

sum of the global finite element stiffness and geometric stiffness matrices, was used in order to avoid having to repeatedly solve the nonlinear eigenvalue problem associated with the calculation of buckling loads and mode shapes. Using a combination of indirect (penalty function) and direct (feasible direction) optimization methods, optimal designs of a 15.0 in. radius, 45.00 in. long ring-stiffened cylinders were determined. These optimal designs were characterized by up to six design variables and satisfied the Kuhn-Tucker conditions. In one case, two local optima were demonstrated to exist in the design space. While the designs of these two optima were much different, their weights differed by only 2%. The presence of the axisymmetric initial imperfection in the cylinder wall can affect the optimal lamina thickness distributions of the cylinder wall, the optimal ring sizes, and the optimal weights of the ring-stiffened cylinder significantly. The optimization algorithm effectively locates designs which minimize the effects of the nonlinear deformations caused by the axisymmetric imperfection. Weight savings associated with the addition of two rings to the unstiffened cylinder were shown to be 5% for cylinders loaded with torsional and axial compression loading in the ratio of 1:4; however, this weight savings increased to 17% for cylinders loaded with torsional and axial compression loading in the ratio of 1:1. Accounting for internal pressurization in the optimal sizing of the imperfect cylinders produced designs having significantly smaller rings than the corresponding unpressurized cylinders. As discussed in section 2.2.1, Hutchinson²⁵ indicated that the presence of internal pressure tended to "iron out" the effects of certain imperfection shapes on the axial buckling load. Hence, a designer of the pressurized, imperfect cylinder may be tempted to propose a design closely resembling the optimal perfect, unpressurized cylinder. However, it has been shown that the optimal cylinder wall lamina thickness distributions of the pressurized, imperfect cylinders more closely resemble the optimal lamina thickness distributions of the imperfect, unpressurized cylinders rather than the optimal lamina thickness distributions of the perfect, unpressurized cylinders. Assuming the presence of internal pressure "irons out" the effects of initial imperfections on the optimal de-

sign is flawed. The optimal designs of these imperfect, pressurized cylinders are substantially lighter than the optimal designs of the corresponding imperfect, unpressurized cylinders when torsion makes up a significant fraction of the combined load state that the cylinder is subjected to.

Locations of regions exhibiting peak stresses varied from case to case. Stresses in the adhesive layer bonding the ring stiffeners to the cylinder wall peak sharply in a narrow region adjacent to the free edge of the ring flange. The through-the-thickness normal stress also peaks beneath the ring web. Cylinder wall lamina stresses tend to be greatest at the clamped ends of the cylinder or in the adjacent shell wall bending boundary layer. In all but one optimal sizing problem considered in the present study, the assumption of criticality of the stability constraints and neglect of the stress constraints during the optimal sizing of the cylinders produced designs that nevertheless satisfied all of the stress constraints as well as the stability constraints. In one case, neglect of the stress constraints resulted in an optimal design that violated an in-plane matrix cracking constraint at the clamped end of the cylinder. Subsequent re-sizing of the cylinder to satisfy this constraint resulted in an optimal design that was 49% heavier than the optimal design produced when the in-plane matrix cracking stress constraint was ignored.

Ultimate strengths of the optimal ring-stiffened cylinder designs were evaluated based on a calculation of the internal pressure necessary to produce a violation of one of the stress constraints. It was demonstrated that by using an unsymmetrically laminated ring flange, a substantial increase in the strength of the ring flange/cylinder wall joint is produced.

8.2 Recommendations for Further Work

Lacking in the present study is a series of experiments designed to verify the observed design trends and response phenomena. The complexity involved in fabricating composite ring-stiffened cylindrical shell specimens and designing and building test fix-

ture equipment to apply combined axial compression, torsional, and internal pressure loads to the specimens put such a detailed experimental investigation beyond the scope of the present study. However, this study does form the groundwork for further investigation into the analysis and design of more complex shell structures. With a minimum amount of modification to the existing analysis, ring-stiffened cylinders of honeycomb sandwich construction could be studied. Such a modification would allow for the investigation of a proposed design concept for shells having diameters and subjected to loads more closely approximating the scale of actual aerospace hardware such as an aircraft fuselage. Permitting more extensive modification of the existing analysis, the first limiting assumption that should be relaxed is that of axisymmetry of the prebuckled equilibrium configuration.

The assumption of an asymmetric prebuckled equilibrium configuration would allow for more general types of loading, including bending, that are more typical of loads encountered by aerospace vehicle structures and would allow for consideration of asymmetric material properties, which may be particularly important in the case of the analysis of the laminated annular plate (see Fig. 3.2.2). Fabrication of composite ring stiffeners having axisymmetric material properties may not be cost-effective. The effects of circumferential variation of the material properties on the buckling loads of these structures should be investigated further. Relaxation of the assumption of prebuckling axisymmetry would also permit the investigation of the response of the cylindrical shell with random, asymmetric initial imperfections that are more representative of imperfection shapes present in actual structure than the axisymmetric imperfection considered in the present study. It is suggested that the effects of such imperfections on the prebuckling stress state, particularly in the ring flange/cylinder skin interface region, be investigated along with the effects of random, asymmetric imperfections on the structural stability and the optimal designs of ring-stiffened cylinders.

Discrete longitudinal stiffening could also be incorporated into the model if the assumption of an axisymmetric prebuckling equilibrium configuration is relaxed. This

is another design concept typical of large aerospace vehicles. Fundamental to an understanding of such a concept is the knowledge of how to design the structure with cylinder skins that are postbuckled. Assuming the vehicle is to be designed to have postbuckled skins, a geometrically nonlinear analysis of the vehicle structure with postbuckled skins is warranted. Assuming that no buckling from this geometrically nonlinear equilibrium state is to be allowed, stability constraints could be established using the methods of the present study. However, should the structure be fabricated with secondarily bonded or co-cured stiffeners, the presence of postbuckled skins would almost certainly necessitate a more detailed consideration of stress constraints in the skin/stiffener interface than that of the present study.

From the standpoint of optimal design, consideration should be given to the investigation of the convergence problems discovered during the course of the present study so that a more robust optimal design algorithm can be developed. Tailoring of the ring flange stiffness to reduce the flange/skin interface stresses should be investigated as well as adding more numerous and complex design variables to the investigation. As the technology needed for the location of globally optimum designs matures (see, for example, Hajela¹³¹) these techniques should be applied to the optimal design of stiffened shell structures since it is known that the optimal sizing of these structures is characterized by the existence of a large number of local optima. Development of a hybrid algorithm of a global optimization technique and a method similar to one of the two outlined in the present study would likely be a most efficient approach.

REFERENCES

- ¹ Jackson, A. C., Campion, M. C., and Pei, G., "Study of Utilization of Advanced Composites in Fuselage Structures of Large Transports," NASA CR-172404, Sept. 1984.
- ² Dickson, J. N., and Biggers, S. B., "Design and Analysis of a Stiffened Composite Fuselage Panel," NASA CR-159302, Aug. 1980.
- ³ Bushnell, D., "Panel Optimization With Integrated Software (POIS) PANDA-Interactive Program For Preliminary Minimum Weight Design," AFWAL-TR-81-3073, July 1981.
- ⁴ Bushnell, D., "PANDA2 - Program For Minimum Weight Design Of Stiffened, Composite, Locally Buckled Panels ," AFWAL-TR-86-3056, Sept. 1986.
- ⁵ Niu, M. C. Y., *Airframe Structural Design*, Connilit Press Ltd., Hong Kong, 1988, pg. 377.
- ⁶ Bushnell, D., "Buckling of Shells: Pitfall For Designers," *AIAA Journal*, Vol. 19, Sept. 1981, pp. 1183-1226.
- ⁷ Starnes, J. H., Jr., Knight, N. F., Jr. and Rouse, M., "Postbuckling Behavior of Selected Flat, Stiffened, Graphite-Epoxy Panels Loaded in Compression," *AIAA Journal*, Vol. 23, Aug. 1985, pp. 1237-1246.
- ⁸ Schmit, L. A., Jr., "Structural Design By Systematic Synthesis," *Proceedings of the 2nd National Conference on Electrical Computation*, Structural Div. ASCE, 1960, pp. 105-132.
- ⁹ Haftka, R.T., Gürdal, Z., and Kamat, M.P., *Elements of Structural Optimization*, Kluwer Academic Publishers, Boston, Massachusetts, 1989.
- ¹⁰ Leissa, A. W., "Vibration Of Shells," NASA SP-288, 1960.
- ¹¹ Flügge, W., "*Die Stabilität der Kreiszyinderschale*," *Ingenieur-Archiv*, Bd 3, 1932, pp. 463-506.

- ¹² Sanders, J. L., "Nonlinear Theories For Thin Shells," *Quarterly of Applied Mathematics*, Vol. 21, Apr. 1963, pp. 21-36.
- ¹³ Donnell, L. H., "Stability Of Thin-walled Tubes Under Torsion," NACA TR-479, 1933.
- ¹⁴ Donnell, L. H., "A New Theory For Buckling Of Thin Cylinders Under Axial Compression And Bending," *Trans. ASME*, Vol. 56, 1935, pp. 795-806.
- ¹⁵ Marguerre, K., "Zur Theorie Der Gekrümmten Platten Mit Grosser Formänderung," *Proceedings of the 5th International Congress on Applied Mechanics*, 1938, pp. 93-101.
- ¹⁶ Hoff, N. J., "The Accuracy of Donnell's Equations," *Journal of Applied Mechanics*, Vol. 22, Sept. 1955, pp. 329-334.
- ¹⁷ Dong, S. B., Pister, K. S., and Taylor, R. L., "On the Theory of Laminated Anisotropic Shells and Plates," *Journal of the Aerospace Sciences*, Vol. 29, Aug. 1962, pp. 969-975.
- ¹⁸ Wu, C. H., "Buckling of Anisotropic Circular Cylindrical Shells," Ph.D. Dissertation, Case Western Reserve Univ., June 1971.
- ¹⁹ Simitses, G. J., Shaw, D., and Sheinman, I., "Stability of Cylindrical Shells by Various Nonlinear Shell Theories," *ZAMM Z. Angew. Math. u. Mech.*, Vol. 65, 1985, pp. 159-166.
- ²⁰ Simitses, G. J., Sheinman, I., and Shaw, D., "The Accuracy of Donnell's Equations for Axially Loaded, Imperfect Orthotropic Cylinders," *Computers and Structures*, Vol. 20, 1985, pp. 939-945.
- ²¹ Seide, P., and Weingarten, V. I., "On the Buckling of Circular Cylindrical Shells Under Pure Bending," *Journal of Applied Mechanics*, Vol. 28, 1961, pp. 112-116.
- ²² Crate, H., Batdorf, S. B., and Baab, G. W., "The Effect of Internal Pressure on the Buckling Stress of Thin-walled Cylinders Under Torsion," NACA ARR-L4E27,

1946.

- ²³ Donnell, L. H., and Wan, C. C., "On the Buckling Thin Cylinders and Columns Under Axial Compression," *Journal of Applied Mechanics*, Vol. 17, Mar. 1950, pp. 73-83.
- ²⁴ Koiter, W. T., "The Effect of Axisymmetric Imperfections on the Buckling of Cylindrical Shells Under Axial Compression," Lockheed Technical Report N63 21285, Aug. 1963.
- ²⁵ Hutchinson, J. "Axial Buckling of Pressurized Imperfect Cylindrical Shells," *AIAA Journal*, Vol. 3, Aug. 1965, pp. 1461-1466.
- ²⁶ Thurston, G. A., "A New Method for Computing Axisymmetric Buckling of Spherical Caps," *Journal of Applied Mechanics*, Vol. 38, Mar. 1971, pp. 179-184.
- ²⁷ Stein, M., "The Influence Of Prebuckling Deformations and Stresses on the Buckling of Perfect Cylinders," NACA TR R-190, Feb. 1964.
- ²⁸ Almroth, B. O., "Influence of Imperfections and Edge Restraint on the Buckling of Axially Compressed Cylinders," NASA CR-432, Apr. 1966.
- ²⁹ Tennyson, R. C., Muggeridge, D. B., and Caswell, R. D., "New Design Criteria for Predicting Buckling of Cylindrical Shells Under Axial Compression," *Journal of Spacecraft*, Vol. 8, Oct. 1971, pp. 1062-1067.
- ³⁰ Ambartsumyan, S. A., "Theory of Anisotropic Shells," NASA TT F-118, 1964.
- ³¹ Cheng, S., and Ho, B. P. C., "Stability of Heterogenous Aelotropic Shells Under Combined Loading," *AIAA Journal*, Vol. 1, Apr. 1963, pp. 892-898.
- ³² Holston, A., Jr., "Buckling of Inhomogeneous Anisotropic Cylindrical Shells By Bending," *AIAA Journal*, Vol. 6, Oct. 1968, pp. 1837-1841.
- ³³ Card, M. F., "The Sensitivity of Buckling of Axially Compressed Fiber Reinforced Cylindrical Shells to Small Geometric Imperfections," Ph.D. Dissertation, Virginia Polytechnic Institute and State University, June 1969.

- ³⁴ Tennyson, R. C., Chan, K. H., and Muggeridge, D. B., "The Effect of Axisymmetric Shape Imperfections on the Buckling of Laminated Anisotropic Circular Cylinders," *CASI Trans.*, Vol. 4, Sept. 1971, pp. 131-139.
- ³⁵ Booton, M., "Buckling of Imperfect Anisotropic Cylinders Under Combined Loading," UTIAS Report No. 203, Toronto, Aug. 1976.
- ³⁶ Jones, R. M., and Hennemann, J. C., "Effect of Prebuckling Deformations on Buckling of Laminated Composite Circular Cylindrical Shells," *Proceedings of the AIAA/ASME/ASCE/AHS 19th Structures, Structural Dynamics, and Materials Conference*, 1978, pp. 370-379.
- ³⁷ Simites, G. J., Shaw, D., and Sheinman, L., "Imperfection Sensitivity of Laminated Cylindrical Shells in Torsion and Axial Compression," *Composite Structures*, Vol. 4, 1985, pp. 335-360.
- ³⁸ van der Neut, A., "The General Instability of Stiffened Cylindrical Shells Under Axial Compression," Nationaal Luchtvaartlaboratorium, Amsterdam, Report No. S. 314, 1947.
- ³⁹ Stein, M., Sanders, J. L., and Crate, H., "Critical Stress of Ring-Stiffened Cylinders in Torsion," NACA Report No. 989, 1950.
- ⁴⁰ Block, D. L., "Influence of Ring Stiffeners on Instability of Orthotropic Cylinders in Axial Compression," NASA-TN-D-2482, Oct. 1964.
- ⁴¹ Haftka, R., and Singer, J., "Buckling of Discretely Ring-Stiffened Cylindrical Shells," *Israel Journal of Technology*, Vol. 6, 1968, pp. 125-137.
- ⁴² Baruch, M., and Singer, J., "Effect of Eccentricity of Stiffeners on the General Instability of Stiffened Cylindrical Shells Under Hydrostatic Pressure," *Journal of Mechanical Engineering Sciences*, Vol. 5, 1963, pp. 23-27.
- ⁴³ Block, D. L., Card, M. F., and Mikulus, M. M., "Buckling of Eccentrically Stiffened Orthotropic Cylinders," NASA TN D-2960, 1965.

- ⁴⁴ Hutchinson, J. W., and Amazigo, J. C., "Imperfection Sensitivity of Eccentrically Stiffened Cylindrical Shells," *AIAA Journal*, Vol. 5, March 1967, pp. 392-401.
- ⁴⁵ Bushnell, D., "Evaluation of Various Analytical Models for Buckling and Vibration of Stiffened Shells," *AIAA Journal*, Vol. 11, Sept. 1973, pp. 1283-1291.
- ⁴⁶ Bushnell, D., "Stress, Stability, and Vibration of Complex Branched Shells of Revolution," NASA CR-2116, Oct. 1972.
- ⁴⁷ Jones, R. M., "Buckling of Circular Cylindrical Shells With Multiple Orthotropic Layers and Eccentric Stiffeners," *AIAA Journal*, Vol. 6, Dec. 1968, pp. 2301-2305.
- ⁴⁸ Jones, R. M., and Morgan, H. S., "Buckling of Stiffened Laminated Composite Circular Cylindrical Shells With Different Moduli In Tension and Compression," AFOSR-TR-75-0547, Feb. 1975.
- ⁴⁹ Wang, J. T. S., and Hsu, T. M., "Discrete Analysis of Stiffened Composite Cylindrical Shells," *AIAA Journal*, Vol. 23, Nov. 1985, pp. 1753-1761.
- ⁵⁰ Wang, J. T. S., and Biggers, S. B., "Skin/Stiffener Interface Stresses In Composite Stiffened Panels," NASA CR-172261, Jan. 1984.
- ⁵¹ Tsai, H. C., "Prediction of Skin-Stiffener Separation of Integrally Stiffened Composite Panels Under Combined Loads," NADC Report NADC-86052-60, Jan. 1986.
- ⁵² Hyer, M. W., Loup, D. C., and Starnes, J. H., Jr., "Stiffener/Skin Interactions In Pressure-Loaded Composite Panels," *AIAA Journal*, Vol. 28, Mar. 1990, pp. 532-537.
- ⁵³ Hyer, M. W. and Cohen, D., "Calculation of Stresses in Stiffened Composite Panels," *AIAA Journal*, Vol. 26, July 1988, pp. 853-857.
- ⁵⁴ Boitnott, R. L., "Nonlinear Response and Failure of Internally Pressurized Composite Cylindrical Panels," Ph.D. Dissertation, Virginia Polytechnic Institute and State University, March 1985.

- ⁵⁵ Hyman, B. I., and Lucas, A. W., Jr., "An Optimum Design For the Instability of Cylindrical Shells Under Lateral Pressure," *AIAA Journal*, Vol. 9, Apr. 1971, pp. 738-740.
- ⁵⁶ Singer, J., and Baruch, M., "Recent Studies On Optimization For Elastic Stability of Cylindrical And Conical Shells," *Proceedings of the 5th Congress of the International Council of the Aeronautical Sciences*, Sept. 1966, pp. 751-782.
- ⁵⁷ Burns, A. B., "Optimum Stiffened Cylinders For Combined Axial Compression and Internal or External Pressure," *Journal of Spacecraft*, Vol. 8, Oct. 1971, pp. 1062-1067.
- ⁵⁸ Kicher, T. P., "Structural Synthesis of Integrally Stiffened Cylinders," *Journal of Spacecraft and Rockets*, Vol. 5, 1968, pp. 62-67.
- ⁵⁹ Schmit, L. A., Jr., Morrow, W. M. II, and Kicher, T. P., "A Structural Synthesis Capability For Integrally Stiffened Cylindrical Shells," *Proceedings of the AIAA/ASME/ASCE/AHS 9th Structures, Structural Dynamics, and Materials Conference*, AIAA Paper No. 68-327, 1968.
- ⁶⁰ Simites, G. J., and Ungbhakorn, V., "Weight Optimization of Stiffened Cylinders Under Axial Compression," *Computers and Structures*, Vol. 5, 1975, pp. 305-314.
- ⁶¹ Simites, G. J., and Aswani, M., "Minimum Weight Design of Stiffened Cylinders Under Hydrostatic Pressure," *Proceedings of the AIAA 13th Aerospace Sciences Meeting*, AIAA Paper No. 75-138, Jan. 1975.
- ⁶² Simites, G. J., and Giri, J., "Minimum Weight Design of Stiffened Cylinders Subject To Pure Torsion," *Computers and Structures*, Vol. 7, 1977, pp. 667-677.
- ⁶³ Simites, G. J., and Giri, J., "Minimum Weight Design of Stiffened Cylinders Subject To Torsion Combined With Axial Compression and Without Lateral Pressure," *Computers and Structures*, Vol. 8, 1978, pp. 19-30.
- ⁶⁴ Simites, G. J., and Sheinman, L., "Optimization of Geometrically Imperfect Cylinders," *Computers and Structures*, Vol. 9, 1979, pp. 101-110.

- drical Shells Under Axial Compression," *Computers and Structures*, Vol. 9, 1978, pp. 377-381.
- ⁶⁵ Bronwicky, A. J., Nelson, R. B., Felton, L. P., and Schmit, L. A., Jr., "Optimization of Ring-Stiffened Shells," *AIAA Journal*, Vol. 13, Oct. 1975, pp. 1319-1325.
 - ⁶⁶ Pappas, M., "Improved Synthesis Capability For T-Ring Stiffened Cylindrical Shells Under Hydrostatic Pressure," *Computers and Structures*, Vol. 6, 1976, pp. 339-343.
 - ⁶⁷ Pappas, M., "Optimal Frequency Separation of Cylindrical Shells," *AIAA Journal*, Vol. 16, Sept. 1978, pp. 999-1001.
 - ⁶⁸ Kunoo, K., and Yang, T. Y., "Minimum Weight Design of Cylindrical Shells With Multiple Stiffener Sizes," *AIAA Journal*, Vol. 16, Jan. 1978, pp. 35-40.
 - ⁶⁹ Pappas, M., and Moradi, J., "Optimal Design of Ring-Stiffened Cylindrical Shells Using Multiple Stiffener Sizes," *AIAA Journal*, Vol. 18, Aug. 1980, pp. 1020-1022.
 - ⁷⁰ Qiu, R., "Weight Optimization of Stiffened Cylinders Under Axial Compression," *Computers and Structures*, Vol. 21, 1985, pp. 945-952.
 - ⁷¹ Tasi, J., "Effect of Heterogeneity on the Stability of Composite Cylindrical Shells Under Axial Compression," *AIAA Journal*, Vol. 4, June 1966, pp. 1058-1062.
 - ⁷² Hirano, Y., "Optimization of Laminated Composite Cylindrical Shells For Axial Buckling," *Transactions of the Japan Society For Aeronautical and Space Sciences*, Vol. 25, May 1982, pp. 154-162.
 - ⁷³ Nshanian, Y. S., and Pappas, M., "Optimal Laminated Composite Shells For Buckling and Vibration," *AIAA Journal*, Vol. 21, Mar. 1983, pp. 430-437.
 - ⁷⁴ Onoda, J., "Optimal Laminate Configurations of Cylindrical Shells For Buckling," *AIAA Journal*, Vol. 23, July 1985, pp. 1093-1097.
 - ⁷⁵ Sun, G., "A Practical Approach To Optimal Design of Laminated Cylindrical Shells For Buckling," *Composites Science and Technology*, Vol. 36, 1989, pp.

243-253.

- ⁷⁶ Hu H., and Wang S. S., "Optimization For Buckling Resistance of Fiber-Composite Laminate Shells With And Without Cutouts," *Proceedings of the AIAA / ASME/ASCE/AHS 31st Structures, Structural Dynamics, and Materials Conference*, 1990, pp. 1300-1312.
- ⁷⁷ Chao, T. L., "Minimum Weight Design of Stiffened Fiber Composite Cylinders," AFML-TR-69-251, Sept. 1969.
- ⁷⁸ Agarwal, B. L., "Minimum Weight Design of Axially Compressed Unstiffened and Stiffened Composite Cylinders," Ph.D. Dissertation, University of Cincinnati, 1975.
- ⁷⁹ Hansen, J. S., and Tennyson R.C., "Optimum Design For Buckling of Laminated Cylinders", *Collapse: The Buckling of Structures in Theory and Practice*, University Press, Cambridge, 1982, pp. 410-429.
- ⁸⁰ Narusberg, V. L., Rikards, R. B., and Teters, G. A., "Optimization of a Reinforced Plastic Shell With Allowance For Geometrically Nonlinear Factors," *Mekhanika Polimerov*, Vol. 6, Dec. 1978, pp. 1079-1083.
- ⁸¹ Gajewski, A., and Zyczkowski, M., *Optimal Structural Design Under Stability Constraints*, Kluwer Academic Publishers, Boston, 1988.
- ⁸² Sun, G., and Hansen, J. S., "Optimal Design of Laminated Composite Circular Cylindrical Shells Subjected To Combined Loads," *Journal of Applied Mechanics*, Vol. 55, Mar. 1989, pp. 136-142.
- ⁸³ Ringertz, U. T., "Optimal Design of Nonlinear Shell Structures," The Aeronautical Research Institute of Sweden Report, FFA-TN 1991-18, 1991.
- ⁸⁴ Jones, R. M., *Mechanics of Composite Materials*, Scripta Book Company, Washington D.C., 1975, pp. 31-57 and pp. 147-156.
- ⁸⁵ Frederick, D. and Chang, T. S., *Continuum Mechanics*, Scientific Publishers, Cambridge, 1965, pp. 99-102.

- ⁸⁶ Lekhnitskii, S. G., *Anisotropic Plates*, Second Edition, Gordon and Breach, New York, 1968, pp. 369-373
- ⁸⁷ Bryant, R. H., "Solutions For Axially Symmetric Orthotropic Annular Plates," *Journal of Aircraft*, Vol. 7, Dec. 1970, pp. 570-572.
- ⁸⁸ Padovan, J., "Static Solution of Monoclinic Laminated Circular Plates," *AIAA Journal*, Vol. 12, June 1974, pp. 862-863.
- ⁸⁹ Boyce, W. E., and DiPrima, R. C., *Elementary Differential Equations and Boundary Value Problems*, John Wiley and Sons, Inc., New York, 1977, pp. 272-275 and pp. 324-328.
- ⁹⁰ Goland, M., and Reissner, E., "The Stresses In Cemented Joints," *Transactions of ASME*, Vol. 11, Mar. 1944, pp. A-17-A-26.
- ⁹¹ Lubkin, J. L., and Reissner, E., "Stress Distribution And Design Data For Adhesive Lap Joints Between Circular Tubes," *Transactions of ASME*, Vol. 78, Mar. 1956, pp. 1213-1221.
- ⁹² Terekhova, L. P., and Skoryi, I. A., "Stresses In Bonded Joints Of Thin Cylindrical Shells," *Strength of Materials*, Translated from *Problemy Prochnosti* No. 10, Oct. 1972, pp. 108-111.
- ⁹³ Adams, R. D., and Peppiatt, N. A., "Stress Analysis Of Adhesive Bonded Tubular Lap Joints," *Journal of Adhesion*, Vol. 9, Oct. 1977, pp. 1-18.
- ⁹⁴ Updike, D. P., and Yuceoglu, U., "Tubular Lap Joints in Composite Cylindrical Shells Under External Bending and Shear," *Proceedings of the Fourth International Conference on Composite Materials*, Tokyo, Japan, Oct. 1982, pp. 297-304.
- ⁹⁵ Chon, C. T., "Analysis of Tubular Lap Joint in Torsion," *Journal of Composite Materials*, Vol. 16, July 1982, pp. 268-284.
- ⁹⁶ Hart-Smith, C. J., "Adhesive-Bonded Single-Lap Joints," NASA CR-112236, Jan. 1973.

- ⁹⁷ Kalnins, A., "Analysis of Shells Of Revolution Subject To Symmetric and Non-symmetric Loads," *Transactions of A S M E*, Vol. 86, Sept. 1964, pp. 467-476.
- ⁹⁸ Corvelli, N., "Design Of Bonded Joints In Composite Materials," *Proceedings of the NASA / G W U / A S M Symposium On Welding, Bonding and Fastening*, Williamsburg, Virginia, June 1972, pp. 1-4.
- ⁹⁹ Budiansky, B., and Radkowski, P. P., "Numerical Analysis of Unsymmetrical Bending of Shells of Revolution," *A I A A Journal*, Vol. 1, Aug. 1963, pp. 1833-1842.
- ¹⁰⁰ Cohen, G., "Computer Analysis of Asymmetrical Deformation of Orthotropic Shells of Revolution," *A I A A Journal*, Vol. 2, May 1964, pp. 932-934.
- ¹⁰¹ Cohen, G., "Computer Analysis of Axisymmetric Buckling of Ring-Stiffened Orthotropic Shells of Revolution," *A I A A Journal*, Vol. 6, Jan. 1968, pp. 141-149.
- ¹⁰² Jordan, P. F., and Shelley, P. E., "Stabilization of Unstable Two-Point Boundary Value Problems," *A I A A Journal*, Vol. 4, No. 5, 1966, pp. 923-924.
- ¹⁰³ Cohen, G., "Numerical Integration of Shell Equations Using The Field Method," *Journal of Applied Mechanics*, Vol. 41, Mar. 1974, pp. 261-266.
- ¹⁰⁴ Cohen, G., "FASOR - A Program For Stress, Buckling and Vibration of Shells of Revolution," *Adv. Eng. Software*, Vol. 3, 1981, pp. 155-162.
- ¹⁰⁵ Potters, M. L., "A Matrix Method For The Solution of a Second Order Difference Equation in Two Variables," *Mathematic Centrum*, Amsterdam, Holland, Report MR 19, 1955.
- ¹⁰⁶ Almroth, B. O., Brogan, F. A. and Stanley, G. M. "Users Manual For STAGS," NASA CR-165670, 1978.
- ¹⁰⁷ Blum, R. E., and Fulton, R. E., "A Modification of Potter's Method For Solving Eigenvalue Problems Involving Tridiagonal Matrices," *A I A A Journal*, Vol. 4, Dec. 1966, pp. 2251-2252.

- 108 Keller, H. B., "Numerical Solution of Two Point Boundary Value Problems," No. 24 in the CBMS-NSF Regional Conference Series in Applied Mathematics, SIAM Publishers, 1976, pp. 39-48.
- 109 Thurston, G. A., "Roots of Lambda Matrices," *Journal of Applied Mechanics*, Vol. 45, Dec. 1978, pp. 859-863.
- 110 Sun, G., "Optimization of Laminated Cylinders For Buckling," UTIAS Report No. 317, Toronto, May. 1987, pp. 24-32.
- 111 Meirovitch, L., *Computational Methods in Structural Dynamics*, Sijthoff and Noordhoff, 1980, pp. 50-72.
- 112 Reddy, J. N., *An Introduction To The Finite Element Method*, McGraw Hill, New York, 1984, pp. 65
- 113 Haftka, R. T., and Starnes, J. H., Jr., "Applications of a Quadratic Extended Interior Penalty Function For Structural Optimization," *AIAA Journal*, Vol. 14, June, 1976, pp. 718-724.
- 114 Grandhi, R. V., Thareja, R., and Haftka, R. T., "NEWSUMT-A : A General Purpose Program For Constrained Optimization Using Constraint Approximations," *Journal of Mechanisms, Transmission, and Automation In Design*, Vol. 107, 1985, pp. 94-99.
- 115 Fiacco, A. V., and McCormick, G. P., *Nonlinear Programming: Unconstrained Minimization Techniques*, John Wiley and Sons, Inc., New York, 1968, pp. 39-52.
- 116 Cassis, J. H., and Schmit, L. A., Jr., "On Implementation Of The Extended Interior Penalty Function," *International Journal For Numerical Methods in Engineering*, Vol. 10, Jan., 1976, pp. 3-23.
- 117 Schmit, L. A., Jr., and Farshi, B., "Some Approximation Concepts For Structural Synthesis," *AIAA Journal*, Vol. 12, May, 1974, pp. 692-699.

- ¹¹⁸ Zoutendijk, M., *Methods of Feasible Directions*, Elsevier Publishing Co., Amsterdam, 1960.
- ¹¹⁹ Vanderplaats, G. N., and Moses, F., "Structural Optimization By Methods Of Feasible Directions," *Journal of Computers and Structures*, Vol. 3, July, 1973, pp. 739-755.
- ¹²⁰ Vanderplaats, G. N., *Numerical Optimization Techniques For Engineering Design: With Applications*, McGraw Hill, New York, 1984.
- ¹²¹ Vanderplaats, G. N., "ADS - A Fortran Program For Automated Design Synthesis: Version 1.10," NASA CR-177985, Sept. 1985.
- ¹²² Fukunaga, H., and Vanderplaats, G. N., "Stiffness Optimization Of Orthotropic Laminated Composites Using Lamination Parameters," *AIAA Journal*, Vol. 29, April, 1991, pp. 641-646.
- ¹²³ Olsen, G. R., and Vanderplaats, G. N., "Method for Nonlinear Optimization With Discrete Design Variables," *AIAA Journal*, Vol. 27, Nov., 1989, pp. 1584-1589.
- ¹²⁴ Tsai, S. W., and Wu, E. M., "A General Theory Of Strength For Anisotropic Materials," *Journal of Composite Materials*, Vol. 5, Jan., 1971, pp. 58-80.
- ¹²⁵ Hashin, Z., "Failure Criteria For Unidirectional Fiber Composites," *Journal of Applied Mechanics*, Vol. 47, June 1980, pp. 329-334.
- ¹²⁶ Rosen, B. W., Nagarkar, A. P., Pipes, R. B., and Walsh, R., "Research Study To Define The Critical Failure Mechanisms In Notched Composites Under Compression Fatigue Loading," Material Science Corp. Report No. MSC TFR 1201/1801, Contract No. N00019-79-C-0633, March, 1981, pp. 5-8. and pp. 33-35
- ¹²⁷ Haftka, R. T., "Design For Temperature And Thermal Buckling Constraints Employing A Noneigenvalue Formulation," *Journal of Spacecraft*, Vol. 20, July-Aug. 1983, pp. 363-367.
- ¹²⁸ Wilkinson, J. H., and Reinsch, C., *Linear Algebra*, Springer-Verlag, Berlin, 1971.

- ¹²⁹ Uthgenannt, E. B., and Brand, R. S., "Buckling of Orthotropic Annular Plates," *AIAA Journal*, Vol. 8, Nov. 1970, pp. 2102-2104.
- ¹³⁰ Ramaiah, G. K., "Buckling of Polar Orthotropic Annular Plates Under In-Plane Compressive Forces," *Journal of Applied Mechanics*, Vol. 48, Sept. 1981, pp. 643-653.
- ¹³¹ Hajela, P., "Genetic Search - An Approach To The Nonconvex Optimization Problem," *AIAA Journal*, Vol. 28, July 1990, pp. 1205-1210.

Table 1
NOMENCLATURE

A_{ij}	$\sum_k (\overline{Q}_{ij})_k (\xi_3^k - \xi_3^{k-1})$
$[A^*]$	$[A]^{-1}$
\overline{A}_{ij}	$t_s^2 A_{ij} / D_{11}^*$
\overline{A}_{ij}^*	$A_{ij}^* (D_{11}^*)^* / t_s^2$
B_{ij}	$\frac{1}{2} \sum_k (\overline{Q}_{ij})_k [(\xi_3^k)^2 - (\xi_3^{k-1})^2]$
$[B^*]$	$-[A]^{-1}[B]$
\overline{B}_{ij}	$t_s B_{ij} / D_{11}^*$
\overline{B}_{ij}^*	B_{ij} / t_s
D_{ij}	$\frac{1}{3} \sum_k (\overline{Q}_{ij})_k [(\xi_3^k)^3 - (\xi_3^{k-1})^3]$
$[D^*]$	$[D] - [B][A]^{-1}[B]$
$D_{11}^*, (D_{11}^*)^*$	D_{11}, D_{11}^* of cylinder wall
\overline{D}_{ij}	D_{ij} / D_{11}^*
\overline{D}_{ij}^*	$D_{ij}^* / (D_{11}^*)^*$

E_{11}, E_{22}	Orthotropic moduli
ecc	Ring web/cylinder middle surface eccentricity
\overline{ecc}	ecc/L
G_{12}	Orthotropic shear modulus
h	Total laminate thickness or adhesive layer thickness
H_W	Ring web height
L	Cylinder length
M_{11}, M_{22}, M_{12}	Stress couples
$M'_{11}, M'_{22}, M'_{12}$	Buckling stress couples
$\overline{M}_{11}, \overline{M}_{22}, \overline{M}_{12}$	$M_{11}L^2/(D_{11}^*t_s), M_{22}L^2/(D_{11}^*t_s),$ $M_{12}L^2/(D_{11}^*t_s)$
$\overline{M}'_{11}, \overline{M}'_{22}, \overline{M}'_{12}$	$M'_{11}L^2/(D_{11}^*t_s), M'_{22}L^2/(D_{11}^*t_s),$ $M'_{12}L^2/(D_{11}^*t_s)$
N_{11}, N_{22}, N_{12}	Stress resultants
N_X, N_{XY}	Applied axial and shear stress resultants

$N'_{11}, N'_{22}, N'_{12}$	Buckling stress resultants
$\bar{N}_{11}, \bar{N}_{22}, \bar{N}_{12}$	$N_{11}L^2/(D_{11}^*)^s, N_{22}L^2/(D_{11}^*)^s, N_{12}L^2/(D_{11}^*)^s$
$\bar{N}'_{11}, \bar{N}'_{22}, \bar{N}'_{12}$	$N'_{11}L^2/D_{11}^s, N'_{22}L^2/D_{11}^s, N'_{12}L^2/D_{11}^s$
$\hat{\bar{N}}_{11}$	Nondimensional applied axial compression load
n	Number of circumferential waves
P	Applied axial compression load
p	Pressure
\bar{p}	$pRL^2/(D_{11}^*)^s$
Q_{11}	$E_{11}/(1 - \nu_{12}\nu_{21})$
Q_{22}	$E_{22}/(1 - \nu_{12}\nu_{21})$
Q_{12}	$\nu_{21}E_{11}/(1 - \nu_{12}\nu_{21}) = \nu_{12}E_{22}/(1 - \nu_{12}\nu_{21})$
Q_{66}	G_{12}
\bar{Q}_{11}	$Q_{11} \cos^4 \theta + 2(Q_{12} + 2Q_{66}) \sin^2 \theta \cos^2 \theta +$ $Q_{22} \sin^4 \theta$

\overline{Q}_{22}	$Q_{11} \sin^4 \theta + 2(Q_{12} + 2Q_{66}) \sin^2 \theta \cos^2 \theta + Q_{22} \cos^4 \theta$
\overline{Q}_{12}	$(Q_{11} + Q_{22} - 4Q_{66}) \sin^2 \theta \cos^2 \theta + Q_{12}(\sin^4 \theta + \cos^4 \theta)$
\overline{Q}_{66}	$(Q_{11} + Q_{22} - 2Q_{12} - 2Q_{66}) \sin^2 \theta \cos^2 \theta + Q_{66}(\sin^4 \theta + \cos^4 \theta)$
\overline{Q}_{16}	$(Q_{11} - Q_{12} - 2Q_{66}) \sin \theta \cos^3 \theta + (Q_{12} - Q_{22} + 2Q_{66}) \sin^3 \theta \cos \theta$
\overline{Q}_{26}	$(Q_{11} - Q_{12} - 2Q_{66}) \sin^3 \theta \cos \theta + (Q_{12} - Q_{22} + 2Q_{66}) \sin \theta \cos^3 \theta$
R, R_s	Radius to middle surface of cylinder
R_f	Radius to middle surface of ring flange
t_s	Total thickness of cylindrical shell wall
T	Applied torsional load
u_1	Axial displacement (cylinder) Radial displacement (ring web)
u'_1	Buckling axial displacement (cylinder) Buckling radial displacement (ring web)

\bar{u}_1	u_1/t_s
\bar{u}'_1	Lu'_1/t_s^2
u_2	Circumferential displacement (cylinder) Circumferential displacement (ring web)
u'_2	Buckling circumferential displacement (cylinder) Buckling circumferential displacement (ring web)
\bar{u}_2	u_2/t_s
\bar{u}'_2	Lu'_2/t_s^2
u_3	Radial displacement (cylinder) Normal displacement (ring web)
u'_3	Buckling radial displacement (cylinder) Buckling radial displacement (ring web)
\bar{u}_3	u_3/t_s
\bar{u}'_3	u'_3/t_s
V_{11}	Kirchhoff shear stress resultant

\bar{V}_{11}	$V_{11}L^3/(D_{11}^*t_s)$
Q'_{11}	Buckling Kirchhoff shear stress resultant
\bar{Q}'_{11}	$Q'_{11}L^3/(D_{11}^*t_s)$
w_o	Cylinder initial geometric imperfection
\bar{w}_o	w_o/t_s
\bar{Z}	L^2/Rt_s
β	nL/R
γ_{xy}, γ_{12}	Shear strain with respect to load-oriented (global) axes
$\bar{\gamma}_{xy}, \bar{\gamma}_{12}$	$\gamma_{xy}(L/t_s)^2, \gamma_{12}(L/t_s)^2$
$\hat{\gamma}_{12}$	Mechanical shear strain with respect to load-oriented (global) axes of imperfect cylinder
$\hat{\bar{\gamma}}_{12}$	$\hat{\gamma}_{12}(L/t_s)^2$
$\epsilon_{xx}, \epsilon_{yy}, \epsilon_{11}, \epsilon_{22}$	Normal strains with respect to load-oriented (global) axes
$\bar{\epsilon}_{xx}, \bar{\epsilon}_{yy}, \bar{\epsilon}_{11}, \bar{\epsilon}_{22}$	$\epsilon_{xx}(L/t_s)^2, \epsilon_{yy}(L/t_s)^2, \epsilon_{11}(L/t_s)^2, \epsilon_{22}(L/t_s)^2$

$\hat{\epsilon}_{11}, \hat{\epsilon}_{22}$	Mechanical normal strains with respect to load-oriented (global) axes of imperfect cylinder
$\hat{\bar{\epsilon}}_{11}, \hat{\bar{\epsilon}}_{22}$	$\hat{\epsilon}_{11}(L/t_s)^2, \hat{\epsilon}_{22}(L/t_s)^2$
$\kappa_{xx}, \kappa_{yy}, \kappa_{11}, \kappa_{22}$	Curvatures with respect to load-oriented (global) axes
$\bar{\kappa}_{xx}, \bar{\kappa}_{yy}, \bar{\kappa}_{11}, \bar{\kappa}_{22}$	$\kappa_{xx}(L^2/t_s), \kappa_{yy}(L^2/t_s), \kappa_{11}(L^2/t_s), \kappa_{22}(L^2/t_s)$
$\hat{\kappa}_{11}, \hat{\kappa}_{22}$	Mechanical curvatures with respect to load-oriented (global) axes of imperfect cylinder
$\hat{\bar{\kappa}}_{11}, \hat{\bar{\kappa}}_{22}$	$\hat{\kappa}_{11}(L^2/t_s), \hat{\kappa}_{22}(L^2/t_s)$
ξ_1	Axial coordinate (cylinder) Radial coordinate (ring web)
ξ_2	Circumferential coordinate (cylinder) Circumferential coordinate (ring web)
ξ_3	Radial coordinate (cylinder) Normal coordinate (ring web)
ξ_3^k, ξ_3^{k-1}	Thickness coordinates of surfaces of k^{th} lamina
$\bar{\xi}_1, \bar{\xi}_2, \bar{\xi}_3$	$\xi_1/L, \xi_2/L, \xi_3/L$

ϕ	Cone angle
θ	Lamina fiber orientation angle
λ	Load parameter
λ_{cr}	Theoretical buckling load parameter of ring-stiffened cylinder
μ	Imperfection amplitude / t_s
ν_{12}, ν_{21}	Major and minor Poisson's ratios
χ	Stress function (ring web)
ω	Axisymmetric imperfection frequency
Π	Total potential energy
$\bar{\Pi}$	$\Pi L^2 / D_{11}^* t_s^2$
$\sigma_{xx}, \sigma_{yy}, \sigma_{zz}$	Normal stresses with respect to load-oriented (global) axes
$\tau_{yz}, \tau_{xz}, \tau_{xy}$	Shear stresses with respect to load-oriented (global) axes
$[\]^T, (\{ \})^T$	Transpose of matrix $[\]$ (vector $\{ \}$)

$()^o$	Indicates $()$ is a plate or shell midplane quantity
$()^{cyl}$ or $()^s$	Indicates $()$ pertains to the cylinder wall
$()^{web}$	Indicates $()$ pertains to the ring web
$()^P$	Indicates $()$ pertains to the initial imperfection
$()^e$	Indicates $()$ pertains to finite element e
$(\dot{})$	$\partial() / \partial \lambda$
$(\vec{})$	Indicates $()$ is a vector quantity
F	Objective function (total structural weight)
X_i	Design variable
g_j^b	Stability constraint
g_j^s	Stress constraint
X_i^l, X_i^u	Lower, upper bounds on design variables
n_{dv}	Number of design variables
n_{gb}	Number of stability constraints

n_{gs}	Number of stress constraints
Φ	Pseudo-objective function
r_p	Penalty parameter
$P(g)$	Penalty function
\vec{S}	Search direction
α	Step length along \vec{S}
σ_{ij}^{AT}	Allowable tensile normal stress
σ_{ij}^{AC}	Allowable compressive normal stress
τ_{ij}^A	Allowable shear stress
λ_n	Critical load parameter for a buckling mode with n circumferential waves
Λ	Lagrange multiplier
ϵ_{KT_i}	Tolerance on satisfaction of Kuhn-Tucker conditions for i th design variable

Table 7.1.1

Assumed Material Properties of Graphite-Epoxy Tape

Property	Value	Property	Value	Property	Value
E_1	18.5 Msi	σ_{11}^{AT}	211. Ksi	σ_{33}^{AT}	6.1 Ksi
E_2	1.64 Msi	σ_{11}^{AC}	-204. Ksi	σ_{33}^{AC}	-21.4 Ksi
G_{12}	0.87 Msi	σ_{22}^{AT}	6.1 Ksi	τ_{13}^A	± 13.8 Ksi
ν_{12}	0.30	σ_{22}^{AC}	-21.4 Ksi	τ_{23}^A	± 9.0 Ksi
t_{ply}	0.005 in.	τ_{12}^A	± 13.8 Ksi		
ρ	0.057 lb/in ³				

Table 7.1.2

Assumed Material Properties of Graphite-Epoxy Woven Cloth

Property	Value	Property	Value	Property	Value
E_1	10.1267 Msi	σ_{11}^{AT}	211. Ksi	σ_{33}^{AT}	6.1 Ksi
E_2	10.1267 Msi	σ_{11}^{AC}	-204. Ksi	σ_{33}^{AC}	-21.4 Ksi
G_{12}	0.87 Msi	σ_{22}^{AT}	211. Ksi	τ_{13}^A	± 13.8 Ksi
ν_{12}	0.04886	σ_{22}^{AC}	-204. Ksi	τ_{23}^A	± 13.8 Ksi
t_{ply}	0.014 in.	τ_{12}^A	± 13.8 Ksi		
ρ	0.057 lb/in ³				

Table 7.1.3

Assumed Material Properties of Ductile Adhesive

Property	Value	Property	Value	Property	Value
E_1	0.500 Msi	σ_{11}^{AT}	10. Ksi	σ_{33}^{AT}	10. Ksi
E_2	0.500 Msi	σ_{11}^{AC}	-10. Ksi	σ_{33}^{AC}	-10. Ksi
G_{12}	0.185 Msi	σ_{22}^{AT}	10. Ksi	τ_{13}^A	± 6.0 Ksi
ν_{12}	0.35	σ_{22}^{AC}	-10. Ksi	τ_{23}^A	± 6.0 Ksi
ρ	0.057 lb/in ³	τ_{12}^A	± 6.0 Ksi		
G_{sec}/G_{tan}	0.29				

Table 7.2.1

Description of Design Variables, Side Constraints, and Initial Designs

Design Variable	Description	Lower Bound	Upper Bound	Initial Design
N_f	Number of plies in the strap (or ring flange and web). Strap (or ring flange and web) is a $[45N_f/0N_f/45N_f]_T$ cloth laminate.	0.001	10.0	1.0
L_f	Strap length (or ring flange length).	1.000	4.0	2.000
H_w	Ring web radial depth.	0.10	6.0	3.000
N_{45}	Number of 45° plies in the skin.	0.001	none	5.0
N_{90}	Number of 90° plies in the skin.	0.001	none	5.0
N_0	Number of 0° plies in the skin. Skin is a $[-45N_{45}/45N_{45}/90N_{90}/0N_0]_S$ tape laminate.	0.001	none	5.0

Table 7.2.2
Load / Imperfection Case Identification

LD ID	P (lbs.)	T (lb. - in.)	N _x (lb / in.)	N _{xy} (lb / in.)	μ (w_o/t_s)	p (psi)
1	-250000.	0.0	-2652.	0.0	0.0	0.0
2	-250000.	0.0	-2652.	0.0	0.25	0.0
3	-250000.	0.0	-2652.	0.0	0.25	70.0
4	-250000.	938000.	-2652.	663.	0.0	0.0
5	-250000.	938000.	-2652.	663.	0.25	0.0
6	-250000.	938000.	-2652.	663.	0.25	70.0
7	-250000.	1875000.	-2652.	1326.	0.0	0.0
8	-250000.	1875000.	-2652.	1326.	0.25	0.0
9	-250000.	1875000.	-2652.	1326.	0.25	70.0
10	-94000.	1410000.	-997.	997.	0.0	0.0
11	-94000.	1410000.	-997.	997.	0.25	0.0
12	-94000.	1410000.	-997.	997.	0.25	70.0
13	0.0	1625000.	0.0	1149.	0.0	0.0
14	0.0	1625000.	0.0	1149.	0.0	70.0

Table 7.3.1
Optimal Designs of Unstiffened Cylinders

LD ID	t_s (in.)	% ± 45	% 90	% 0	NORM. WT.
1	0.09966	41.322	44.120	14.558	1.000
2	0.14774	45.332	51.361	3.307	1.481
3	0.13322	51.244	48.748	0.008	1.335
4	0.12044	64.400	2.424	33.176	1.000
5	0.16085	57.085	29.880	13.035	1.337
6	0.13780	55.990	44.003	0.007	1.145
7	0.14608	76.159	0.007	23.834	1.000
8	0.17649	67.375	25.900	6.725	1.209
9	0.14745	66.434	33.374	0.192	1.009
10	0.12140	74.388	0.009	25.603	1.000
11	0.13516	43.965	29.320	26.715	1.114
12	0.08758	67.775	30.217	2.008	0.721
13*	0.12057	76.447	0.008	23.545	1.000
13*	0.12230	40.722	27.094	32.184	1.020

* : 2 local optima located

Table 7.3.2
Optimal Designs of Strap-Stiffened Cylinders

LD ID	t_s (in.)	% ± 45	% 90	% 0	t_f (in.)	L_f (in.)	NORM WT.	% RING WT.
1	0.09966	41.322	44.120	14.558	0.0000	1.000	1.000	0.000
2	0.14483	49.823	47.513	2.664	0.0158	2.6442	1.476	1.255
3	0.13332	54.444	45.481	0.075	0.0017	1.000	1.339	0.055
5	0.15141	64.812	27.211	7.977	0.0868	1.6315	1.313	3.951
8	0.15241	70.863	27.818	1.319	0.2930	1.0000	1.133	7.756
9	0.14200	74.376	25.617	0.007	0.0342	1.9693	0.995	2.044
10	0.09350	89.332	.011	10.657	0.2242	1.0000	0.852	9.519
11	0.10814	75.243	16.111	8.646	0.2511	1.0000	0.983	9.239
12	0.08594	70.580	23.739	5.681	0.0274	1.0000	0.719	1.388
13	0.08960	85.908	0.011	14.081	0.2249	1.0000	0.826	9.919
14	0.05053	97.269	0.974	1.757	0.0059	1.000	0.422	0.510

Table 7.3.3
Optimal Designs of "T"-Ring Stiffened Cylinders

LD ID	t_s (in.)	% 45	% 90	% 0	t_f (in.)	L_f (in.)	H_w (in.)	NORM WT.	% RING WT.
4	0.10785	63.441	16.624	19.935	0.0033	1.0000	3.0011	0.902	0.501
5	0.14900	62.502	37.474	0.024	0.0114	1.6524	2.4485	1.258	1.301
6	0.13466	57.345	42.611	0.044	0.0026	1.0000	3.5326	1.124	0.352
7	0.12179	81.440	5.386	13.174	0.0077	1.0000	2.6837	0.843	0.950
8	0.15408	64.230	30.839	4.931	0.0204	1.8397	2.4425	1.083	2.322
9	0.13733	71.984	28.008	0.008	0.0140	2.3243	2.7283	0.964	2.121
10	0.09546	87.698	0.010	12.292	0.0114	1.0000	1.9743	0.800	1.482
11	0.11019	69.206	14.753	16.041	0.0135	1.0053	2.4512	0.926	1.733
13	0.09022	83.669	0.011	16.320	0.0138	1.0000	1.9295	0.764	1.861

Table 7.3.4

Active Constraints and Corresponding Lagrange Multipliers
For Unstiffened Cylinder Designs

LD ID	STABILITY CONSTRAINTS	STABILITY Λ^s	X^L CONSTRAINTS	X^L Λ^s
1	$n = 10$	1.420E-5	-	-
2	$n = 7$	1.476E-5	-	-
3	$n = 8$	0.160E-5	N_0	0.263
4	$n = 7$	3.813E-4	-	-
5	$n = 6$	1.227E-4	-	-
6	$n = 7$	0.860E-5	N_0	0.121
7	$n = 7$	1.399E-4	N_{90}	0.302
8	$n = 6$	4.602E-5	-	-
9	$n = 7$	4.485E-5	-	-
10	$n = 7$	4.930E-5	N_{90}	0.271
11	$n = 6$	6.993E-4	-	-
12	$n = 8$	1.333E-5	-	-
13*	$n = 7$	2.726E-5	N_{90}	0.2648
13*	$n = 7$	4.802E-5	-	-

* : 2 local optima found

Table 7.3.5

Active Constraints and Corresponding Lagrange Multipliers
For Strap-Stiffened Cylinder Designs

LD ID	STABILITY CONSTRAINTS	STABILITY Λ^S	X^L CONSTRAINTS	X^L Λ^S
1	$n = 10$	1.420E-5	N_f, L_f	0.868, 0.055
2	$n = 7$	6.484E-5	-	-
3	$n = 8$	0.154E-5	L_f	0.071
5	$n = 6$	3.916E-5	-	-
8	$n = 6, n = 7$	3.330E-5, 1.390E-4	L_f	1.2922
9	$n = 7$	1.500E-5	N_0	0.0786
10	$n = 9, n = 10$	1.170E-5, 0.328E-5	L_f, N_0	1.088, 0.473
11	$n = 8$	0.982E-5	L_f	1.152
12	$n = 8$	0.528E-5	L_f	0.110
13	$n = 10$	4.500E-5	N_{90}, L_f	0.975, 0.351
14	$n = 11, n = 14$	0.908E-6, 1.170E-5	L_f	0.053

Table 7.3.6

Active Constraints and Corresponding Lagrange Multipliers
For "T" Ring-Stiffened Cylinder Designs

LD ID	STABILITY CONSTRAINTS	STABILITY Λ^S	X^L CONSTRAINTS	X^L Λ^S
4	$n = 9$	1.132E-5	L_f	0.099
5	$n = 7$	7.286E-6	-	-
6	$n = 8$	0.587E-6	L_f, N_0	0.065, 0.161
7	$n = 9$	1.016E-5	L_f	0.102
8	$n = 7$	1.312E-5	-	-
9	$n = 7$	1.180E-5	N_0	0.115
10	$n = 10$	1.310E-5	L_f, N_{90}	0.055, 0.356
11	$n = 8$	0.993E-5	L_f	0.019
13	$n = 10$	1.187E-6	L_f, N_{90}	0.090, 0.331

Table 7.4.1
Minimum Stress Constraint Values
For Strap-Stiffened Cylinder Optimal Designs

LD ID	Fiber Mode	Fiber Mode Location X / Layer	Matrix Mode	Matrix Mode Location X / Layer	Strap/Skin Mode
1	0.536 (C)	0.462 / 0°	0.626 (C)	0.500 / ±45°	-
2	0.563 (C)	0.447 / 0°	0.639 (C)	0.500 / ±45°	0.697 (AC)
3	0.430 (C)	0.447 / 0°	0.320 (C)	0.500 / ±45°	-
5	0.667 (C)	0.449 / 0°	0.769 (C)	0.500 / ±45°	0.405 (AC)
8	0.591 (C)	0.438 / 0°	0.695 (C)	0.500 / ±45°	0.318 (AT)
9	0.461 (C)	0.440 / 0°	0.433 (C)	0.500 / ±45°	0.436 (AC)
10	0.728 (C)	0.500 / ±45°	0.861 (C)	0.451 / ±45°	0.622 (AT)
11	0.762 (C)	0.500 / ±45°	0.889 (C)	0.500 / ±45°	0.785 (AT)
12	0.533 (C)	0.500 / ±45°	0.283 (T)	0.500 / ±45°	0.871 (AC)
13	0.867 (C)	0.178 / ±45°	0.920 (T)	0.178 / ±45°	0.801 (AC)
14	0.410 (C)	0.500 / ±45°	-2.74 (T)	0.500 / ±45°	0.954 (AC)

(T) : Tension (AT) : Adhesive Tension
(C) : Compression (AC) : Adhesive Compression

Table 7.4.2
Minimum Stress Constraint Values
For "T" Ring-Stiffened Cylinder Optimal Designs

LD ID	Fiber Mode	Fiber Mode Location X / Layer	Matrix Mode	Matrix Mode Location X / Layer	Flange/Skin Mode
4	0.608 (C)	0.453 / 0°	0.676 (C)	0.455 / ±45°	0.984 (AT)
5	0.553 (C)	0.440 / 0°	0.645 (C)	0.500 / ±45°	0.848 (AC)
6	**	**	**	**	**
7	0.570 (C)	0.447 / 0°	0.581 (C)	0.447 / ±45°	0.964 (AT)
8	0.628 (C)	0.500 / ±45°	0.729 (C)	0.500 / ±45°	0.782 (AC)
9	**	**	**	**	**
10	0.738 (C)	0.500 / ±45°	0.877 (C)	0.451 / ±45°	0.972 (AT)
11	0.780 (C)	0.500 / ±45°	0.903 (C)	0.500 / ±45°	0.965 (AC)
13	0.865 (C)	0.178 / ±45°	0.917 (C)	0.178 / ±45°	0.966 (AT)

(T) : Tension (AT) : Adhesive Tension
(C) : Compression (AC) : Adhesive Compression
** : See Table 7.4.4 (Pressure to failure)

Table 7.4.3
Internal Pressure To Failure
For Strap-Stiffened Cylinder Optimal Designs

LD ID	Pressure (psi)	Fiber Mode Constraint	Fiber Mode Location X / Layer	Matrix Mode Constraint	Matrix Mode Location X / Layer	Strap/Skin Mode Constraint
1	131.2	0.408 (C)	0.462 / 0°	-.001 (C)	0.464 / ±45°	-
2	227.1	0.437 (C)	0.447 / 0°	0.001 (C)	0.500 / ±45°	0.651 (AC)
3	161.3	0.363 (C)	0.447 / 0°	-.001 (C)	0.500 / ±45°	-
5	210.7	0.447 (C)	0.500 / ±45°	0.004 (T)	0.500 / ±45°	0.649 (AC)
8	83.7	0.510 (C)	0.500 / ±45°	0.498 (C)	0.500 / ±45°	0.002 (CT)
8*	185.0	0.380 (C)	0.500 / ±45°	0.007 (T)	0.500 / ±45°	0.069 (CT)
9	160.9	0.349 (C)	0.500 / ±45°	-0.003 (T)	0.500 / ±45°	0.393 (AC)
9†	426.3	0.000 (C)	0.500 / ±45°	-4.714 (T)	0.500 / ±45°	0.257 (AC)
10	23.8	0.662 (C)	0.500 / ±45°	0.568 (T)	0.444 / 0°	0.000 (CT)
10*	33.3	0.635 (C)	0.500 / ±45°	0.398 (T)	0.444 / 0°	0.000 (CT)
11	75.2	0.622 (C)	0.500 / ±45°	0.398 (T)	0.500 / ±45°	0.000 (CT)
11*	101.0	0.574 (C)	0.500 / ±45°	0.064 (T)	0.500 / ±45°	0.000 (CT)
12	87.4	0.495 (C)	0.500 / ±45°	0.006 (T)	0.500 / ±45°	0.874 (AC)
12†	312.6	0.005 (C)	0.500 / ±45°	-7.680 (T)	0.500 / ±45°	0.955 (AT)
13	57.4	0.703 (C)	0.500 / ±45°	0.140 (T)	0.500 / ±45°	0.000 (CT)
13*	64.8	0.681 (C)	0.500 / ±45°	-0.023 (T)	0.500 / ±45°	-0.007 (CT)
14	26.2	0.646 (C)	0.500 / ±45°	-0.002 (T)	0.500 / ±45°	0.961 (AC)

(T) : Tension (AT) : Adhesive Tension (CT) : Adherend Tension

(C) : Compression (AC) : Adhesive Compression

* : Strap laminate changed to $[0_{N_f}/45_{N_f}/45_{N_f}]_T$

† : Matrix cracking failure ignored

Table 7.4.4
Internal Pressure To Failure
For 'T' Ring-Stiffened Cylinder Optimal Designs

LD ID	Pressure (psi)	Fiber Mode Constraint	Fiber Mode Location X / Layer	Matrix Mode Constraint	Matrix Mode Location X / Layer	Flange/Skin Mode Constraint
4	69.0	0.495 (C)	0.453 / 0°	.000 (T)	0.453 / 0°	0.986 (CT)
5	221.7	0.375 (C)	0.500 / ±45°	-.001 (C)	0.500 / ±45°	0.810 (AC)
6	178.2	0.357 (C)	0.447 / 0°	-.001 (C)	0.453 / ±45°	0.946 (AC)
7	40.46	0.490 (C)	0.447 / 0°	.001 (T)	0.444 / 0°	0.970 (AT)
8	201.8	0.398 (C)	0.500 / ±45°	.001 (T)	0.500 / ±45°	0.767 (AC)
8 [†]	550.0	0.000 (C)	0.500 / ±45°	-5.651 (T)	0.500 / ±45°	0.866 (AT)
9	163.8	0.327 (C)	0.500 / ±45°	.001 (T)	0.500 / ±45°	0.699 (AT)
10	55.1	0.589 (C)	0.500 / ±45°	.014 (T)	0.442 / 0°	0.979 (AT)
10 [†]	184.4	-0.004 (T)	0.442 / 90°	-5.603 (T)	0.442 / 90°	0.900 (AT)
11	107.4	0.583 (C)	0.500 / ±45°	.001 (T)	0.500 / ±45°	0.972 (AC)
13	64.4	0.683 (C)	0.500 / ±45°	0.000 (T)	0.442 / ±45°	0.964 (AT)
13 [†]	243.2	-0.001 (T)	0.429 / 90°	-8.052 (T)	0.500 / ±45°	0.850 (AT)

(T) : Tension (AT) : Adhesive Tension (CT) : Adherend Tension

(C) : Compression (AC) : Adhesive Compression

[†] : Matrix cracking failure ignored

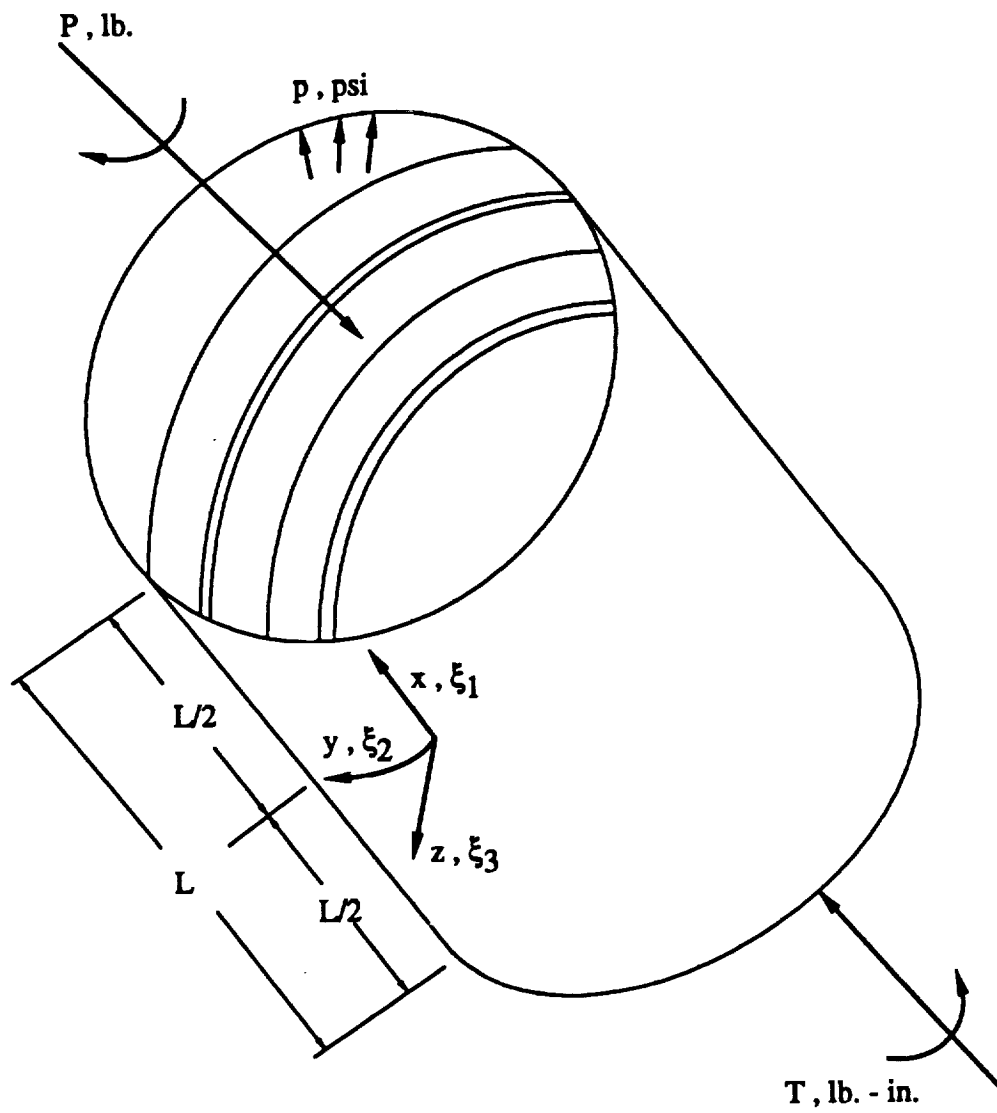


Figure 1.1.1
Ring-Stiffened Cylinder And Imposed Loads

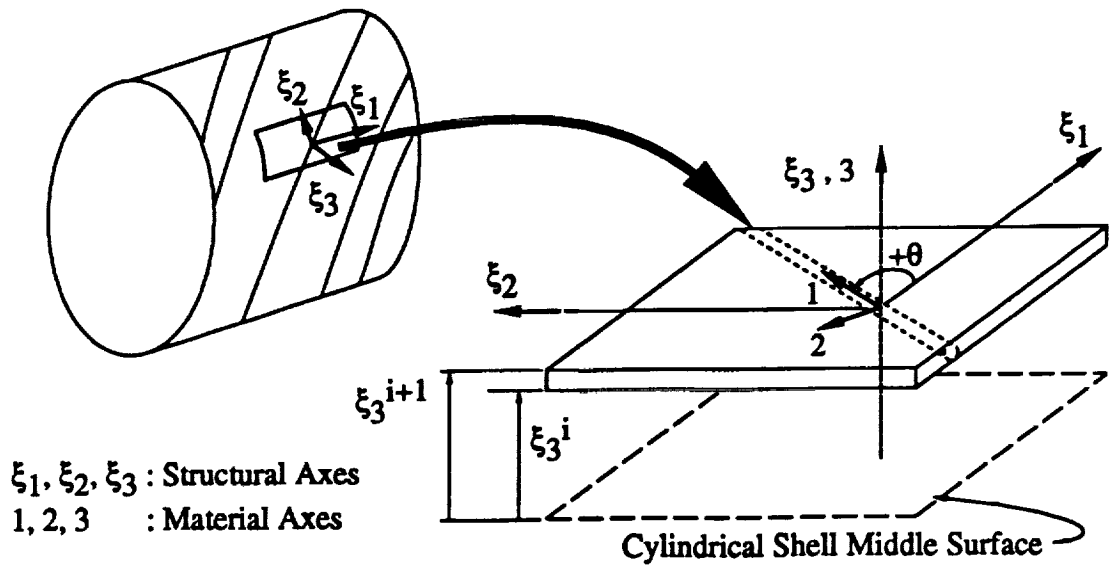


Figure 3.2.1
 Typical Cylindrical Shell Lamina

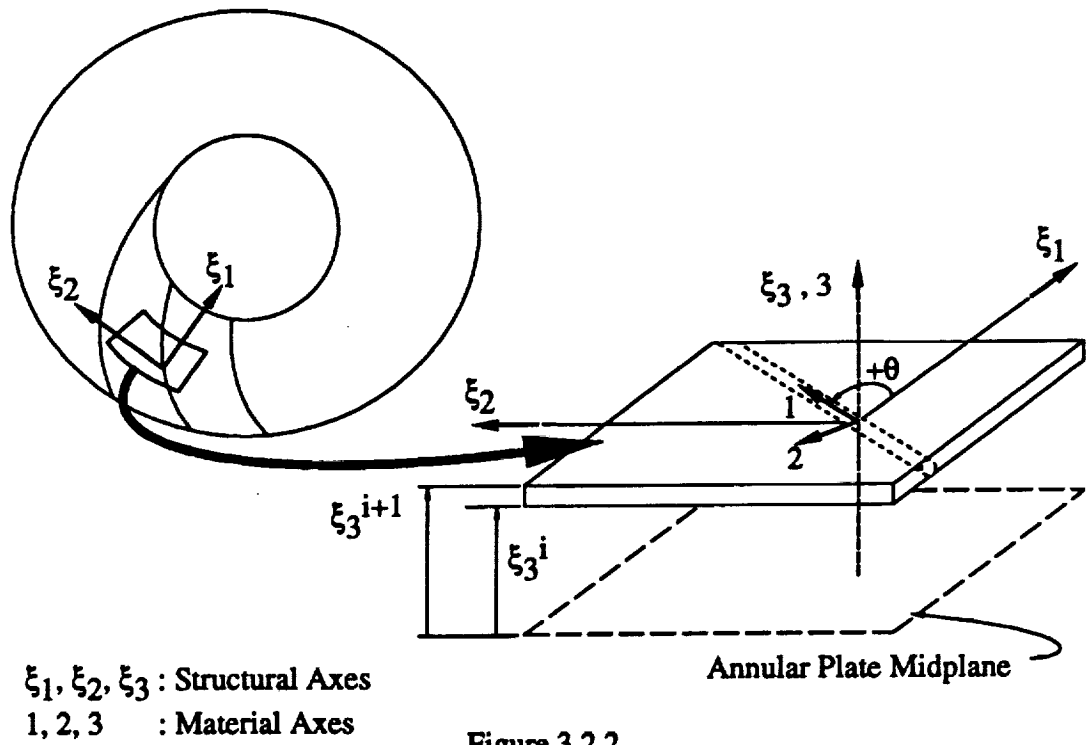


Figure 3.2.2
 Typical Annular Plate Lamina

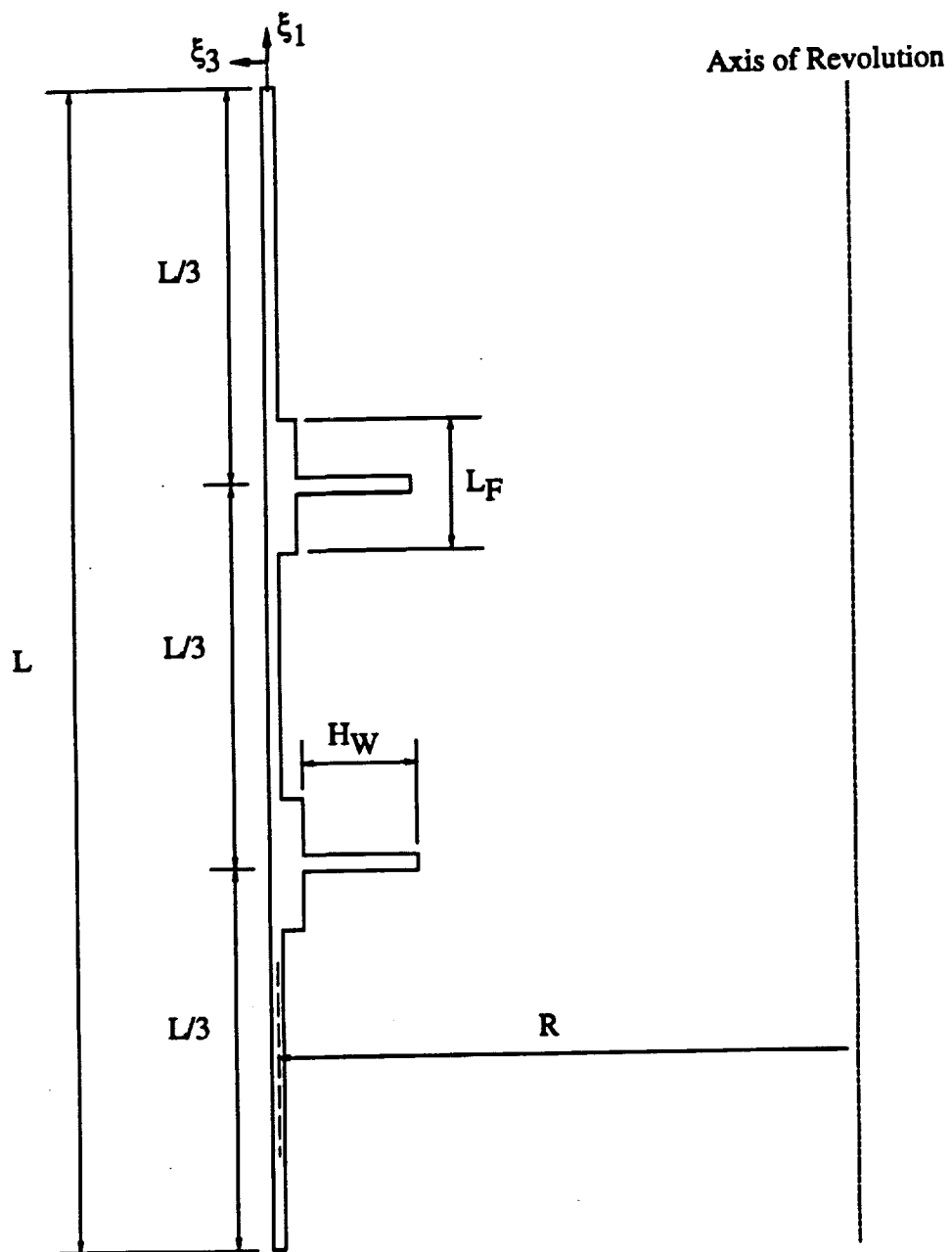


Figure 3.2.3
Cross Section of Ring-Stiffened Cylinder

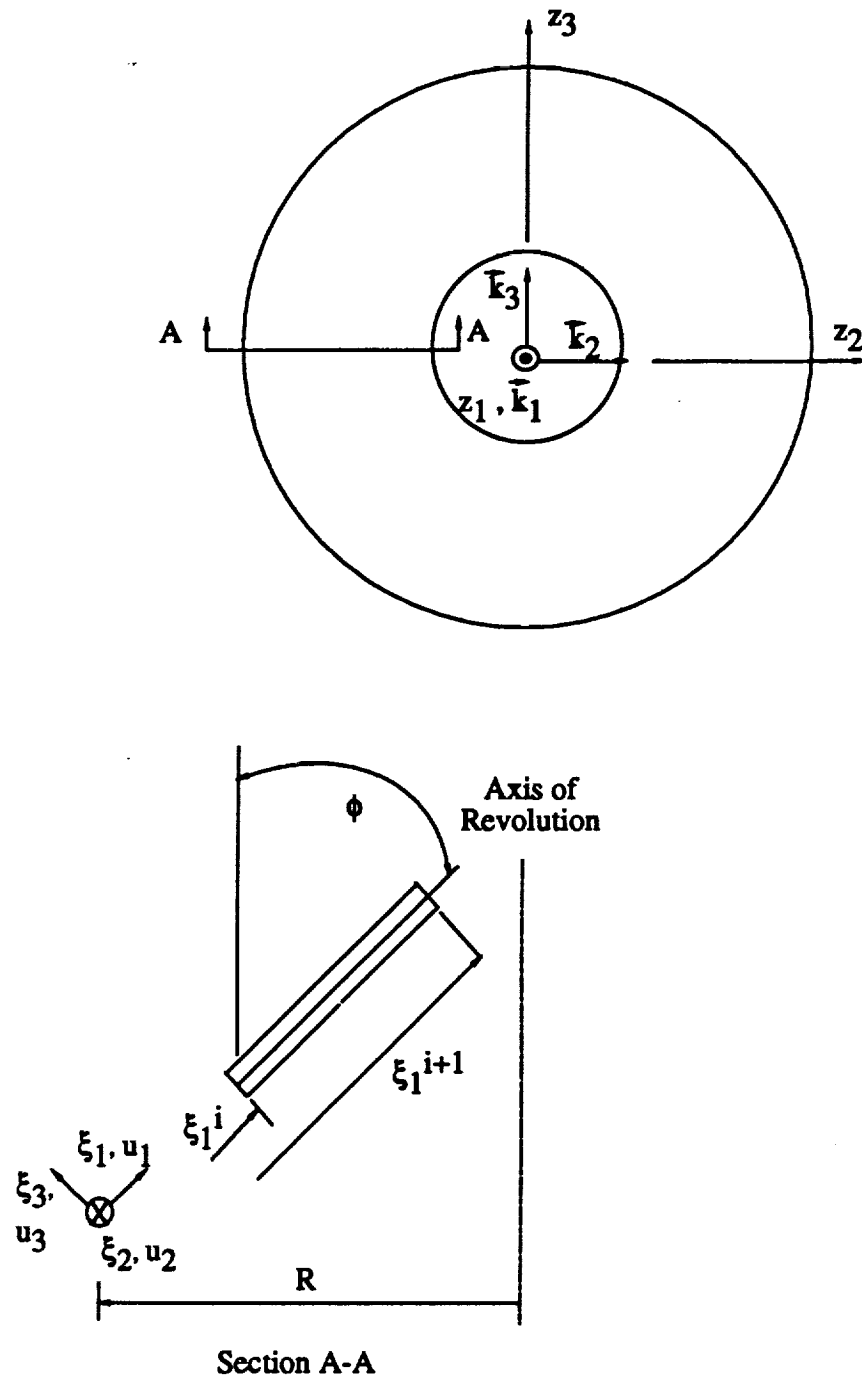


Figure 3.3.1
Typical Conical Shell Segment

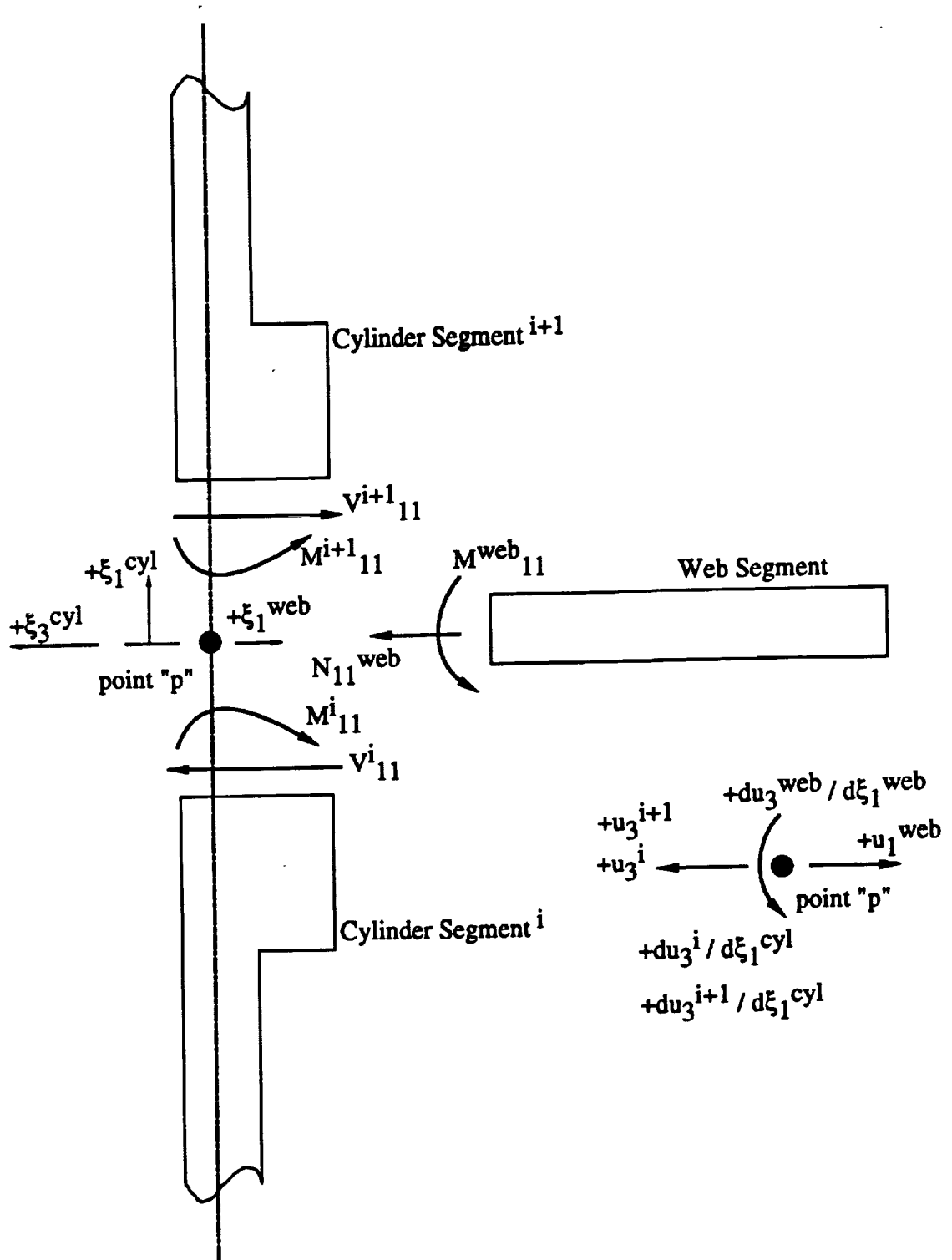


Figure 4.3.1
Prebuckling Equilibrium And Compatibility

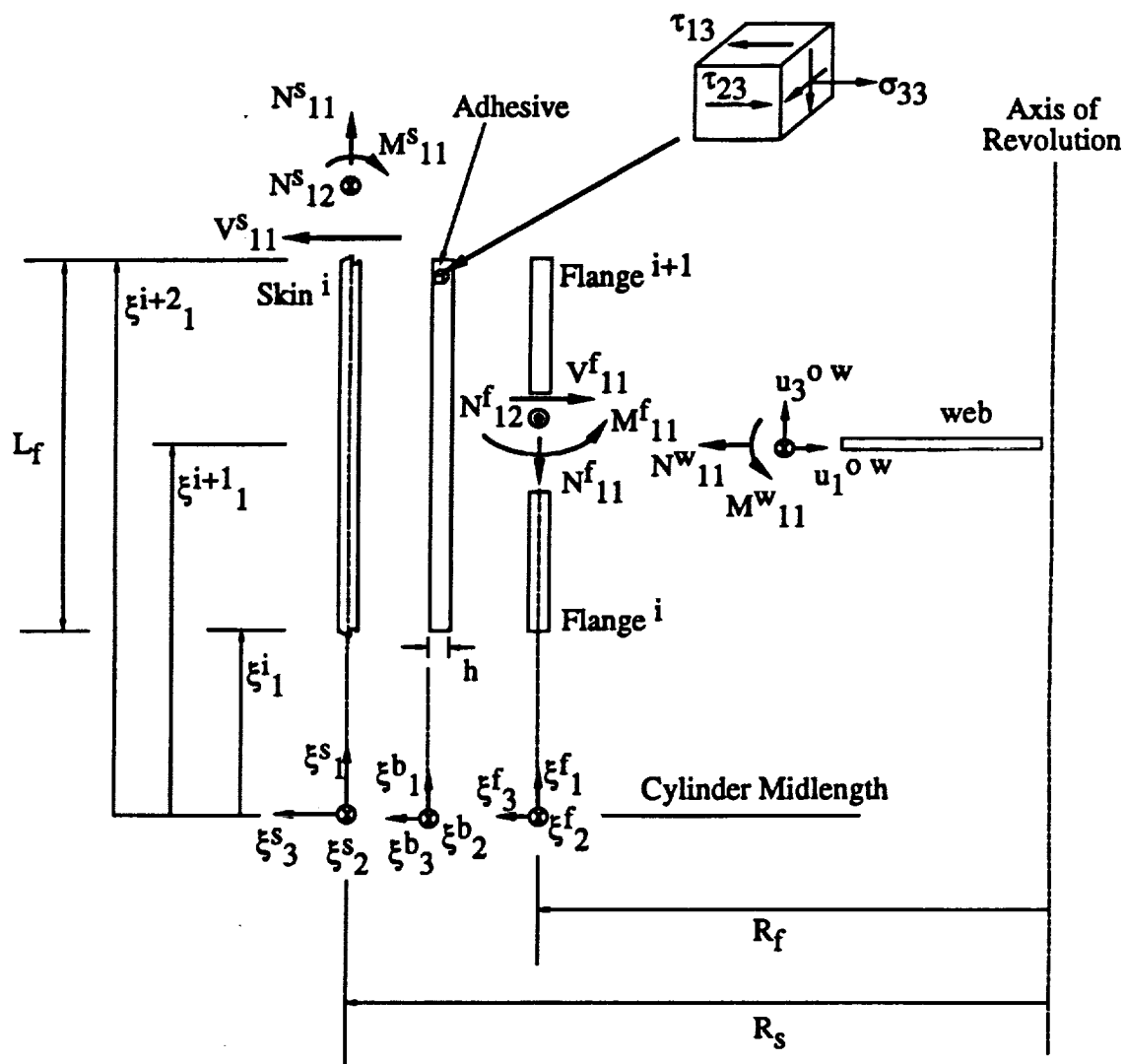
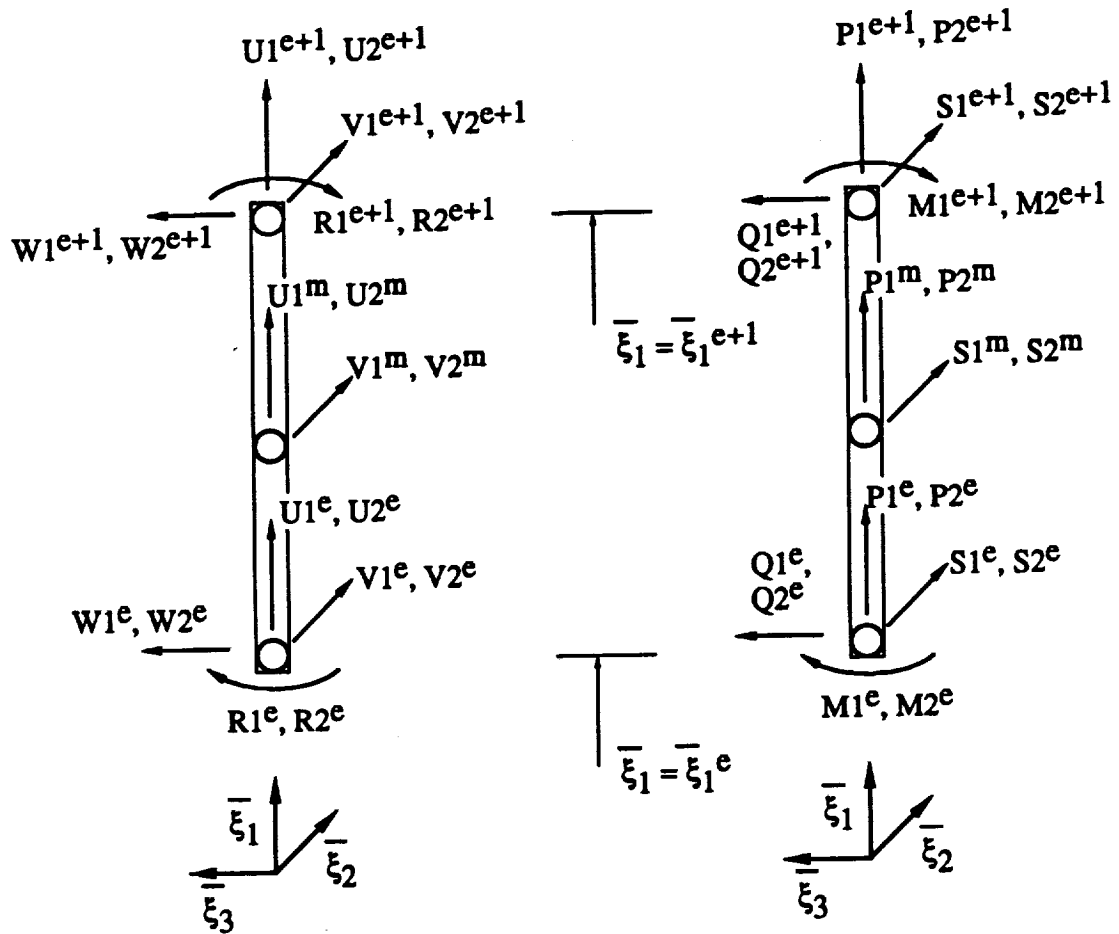


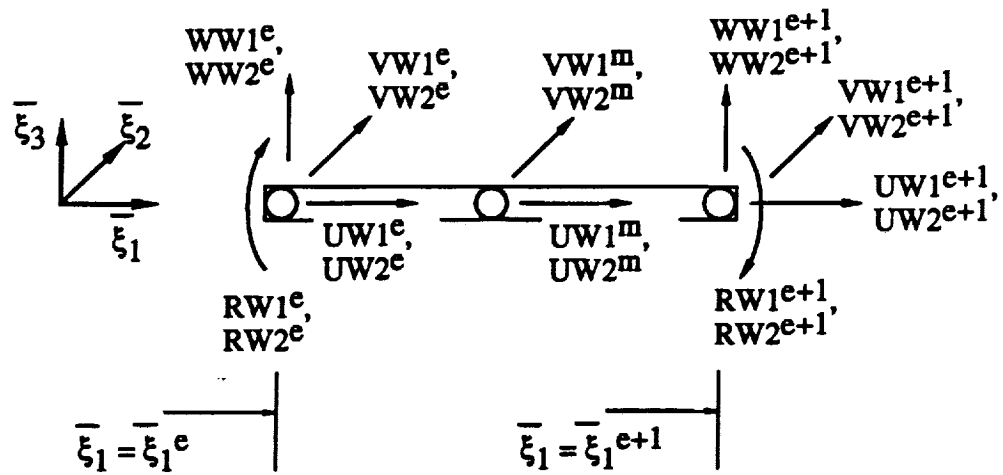
Figure 4.4.1
Ring / Shell Bonded Joint



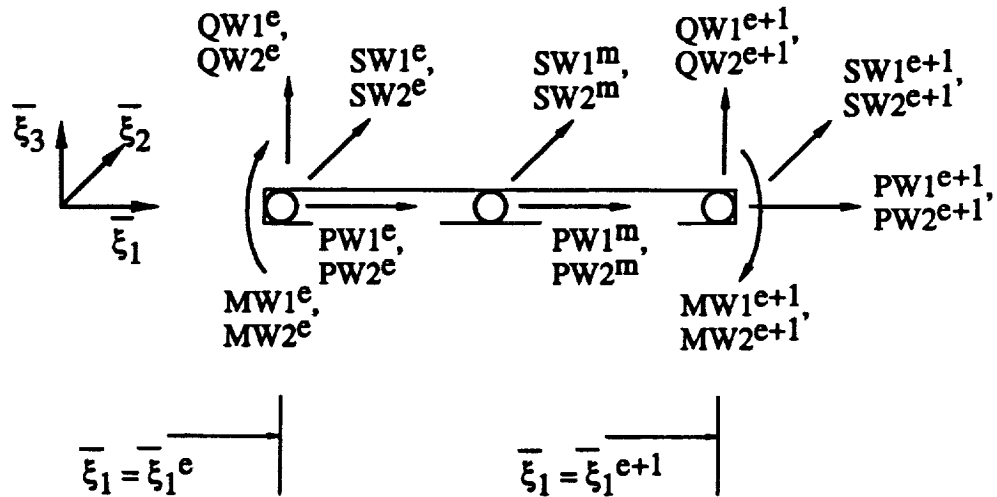
a. Generalized Nondimensional Nodal Buckling Displacements and Rotations

b. Generalized Nondimensional Nodal Buckling Forces and Moments

Figure 5.2.1
Cylindrical Shell Finite Element



a. Generalized Nondimensional Nodal Buckling Displacements and Rotations



b. Generalized Nondimensional Nodal Buckling Forces and Moments

Figure 5.3.1
Annular Plate Finite Element

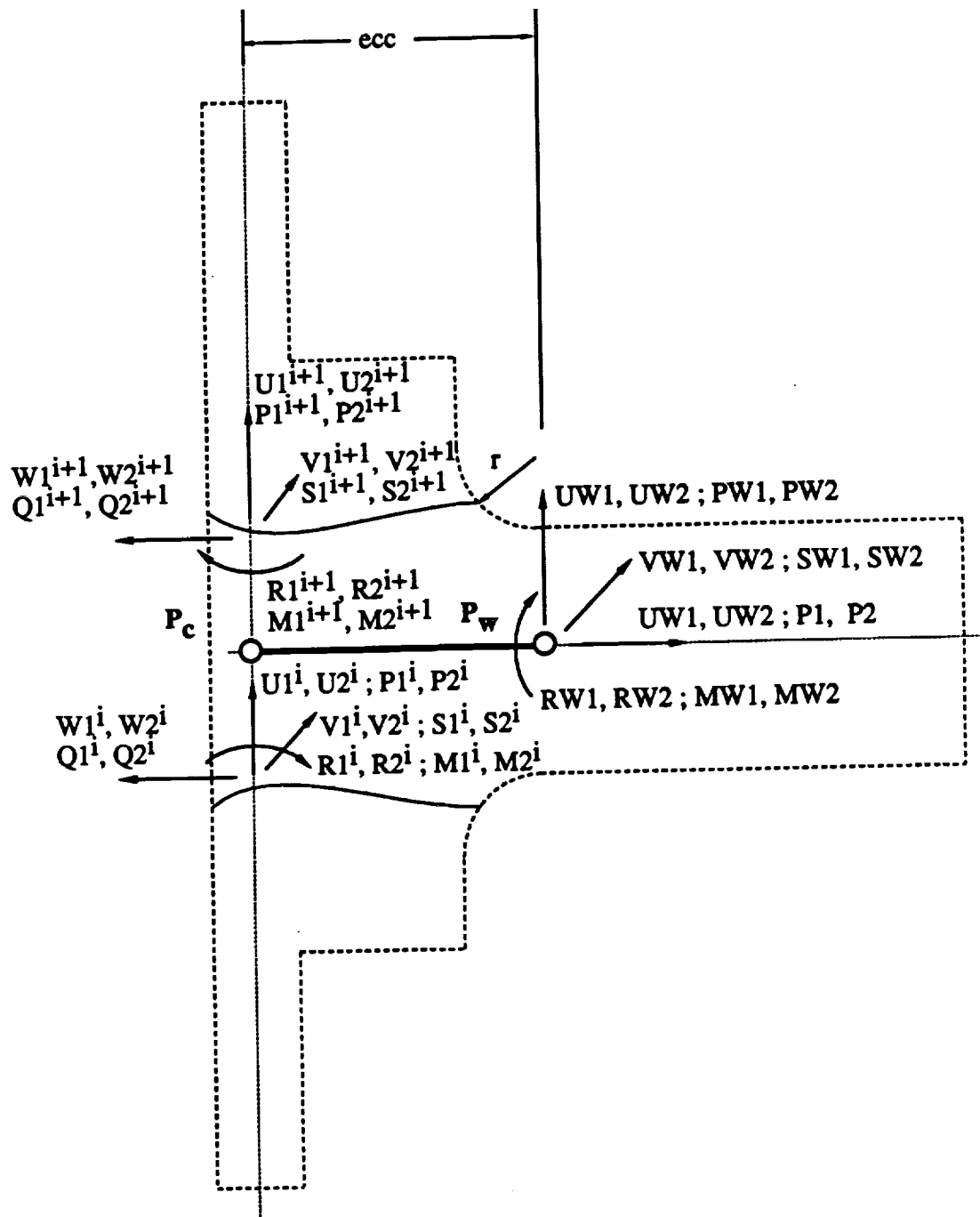


Figure 5.4.1
Cylindrical Shell Finite Element / Annular Plate Finite Element Junction

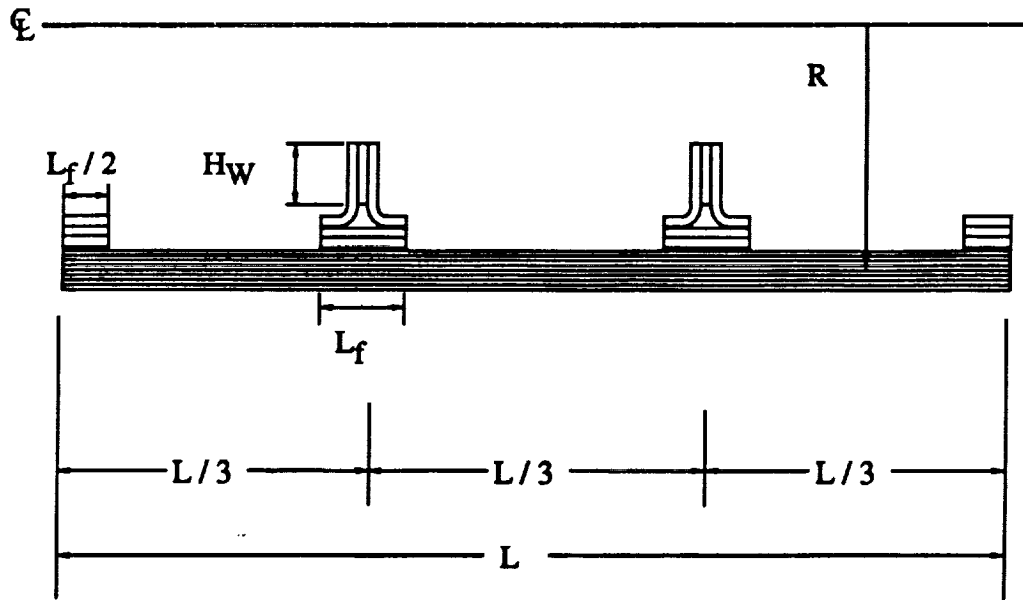


Figure 7.1.1
Buckling Analysis Example Problem

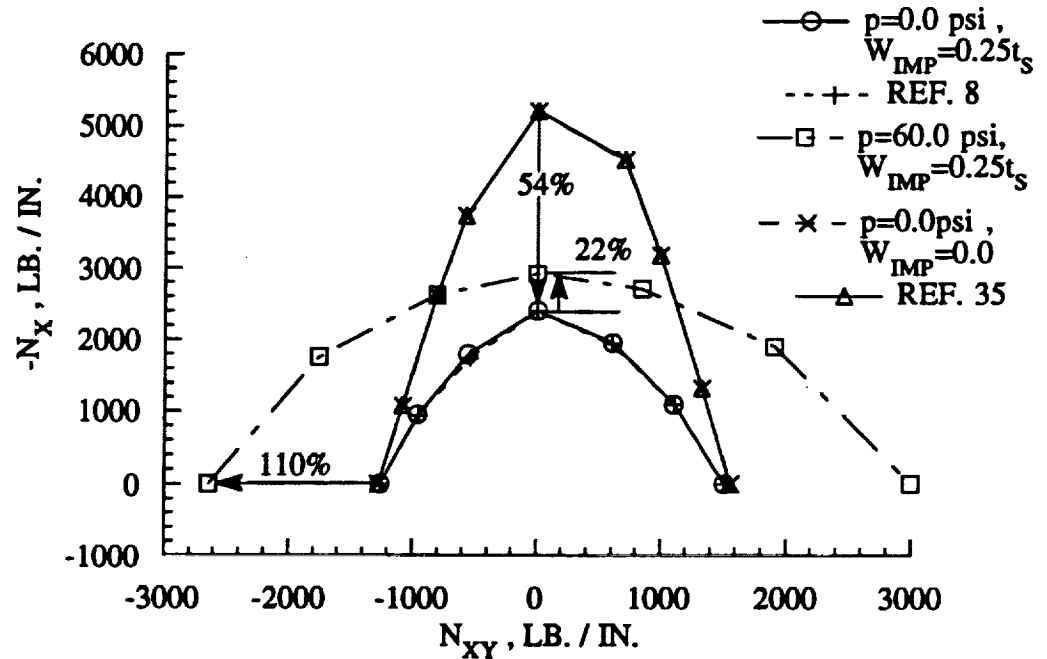


Figure 7.1.2
Buckling Interaction Diagram For Unstiffened Cylinder

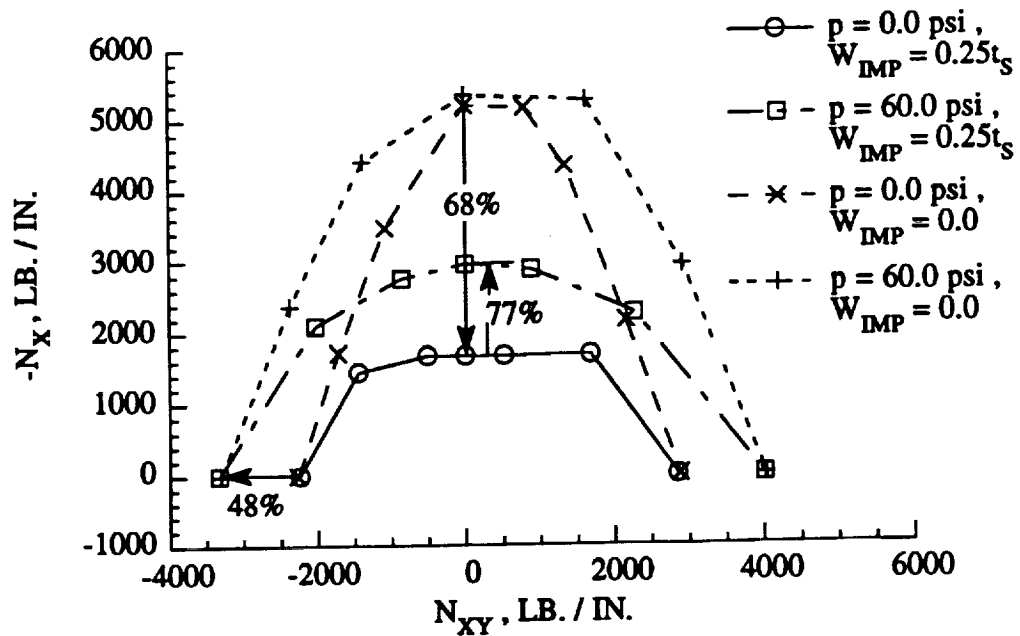


Figure 7.1.3
Buckling Interaction Diagram For Ring-Stiffened Cylinder

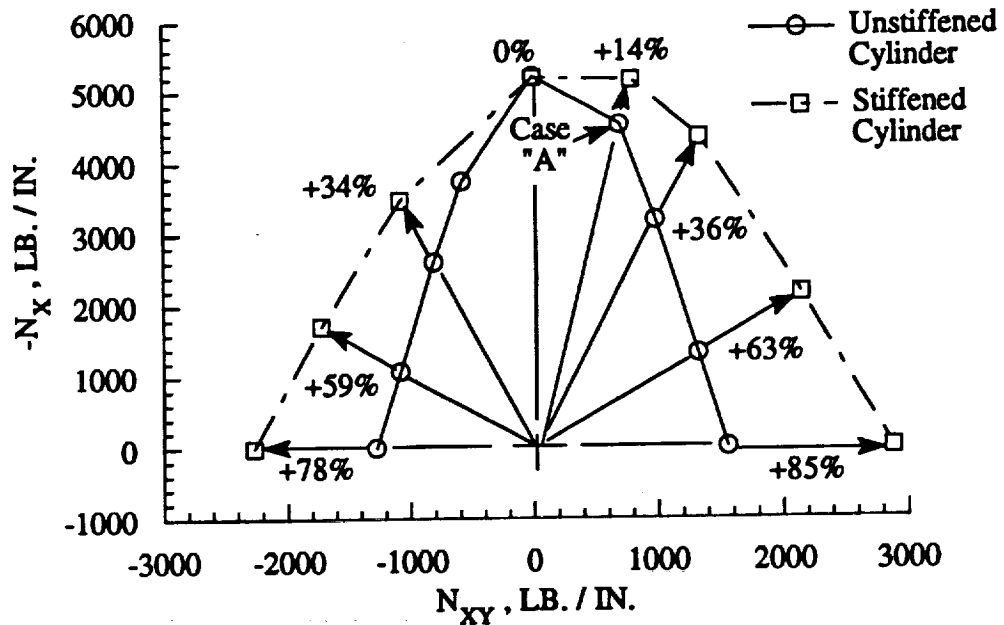


Figure 7.1.4
Effect Of Adding Rings To Unpressurized, Perfect Cylinder

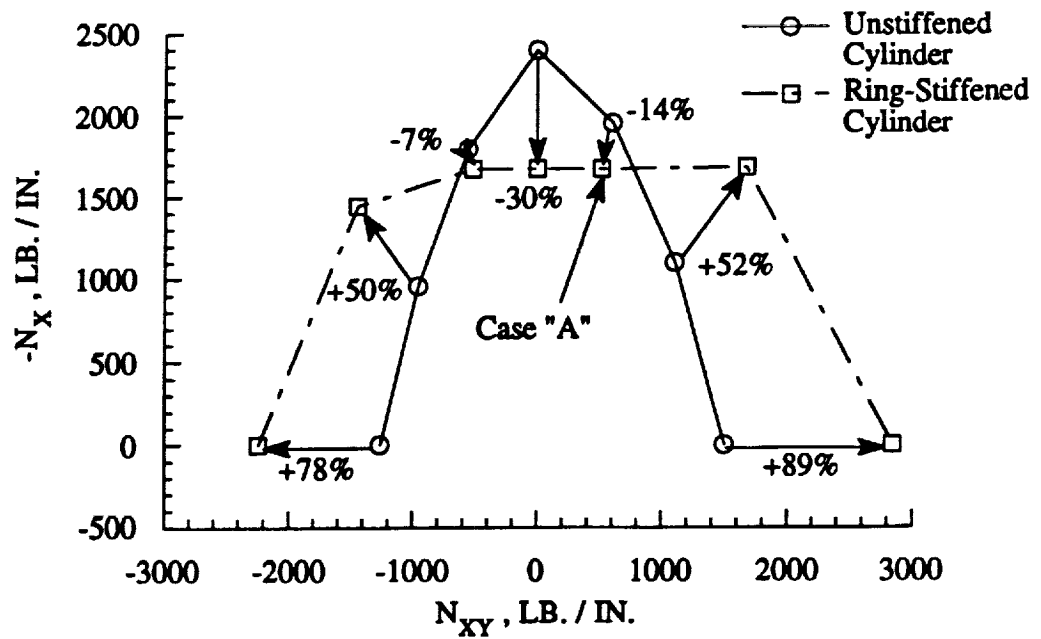


Figure 7.1.5
Effect Of Adding Rings To Unpressurized, Imperfect Cylinder

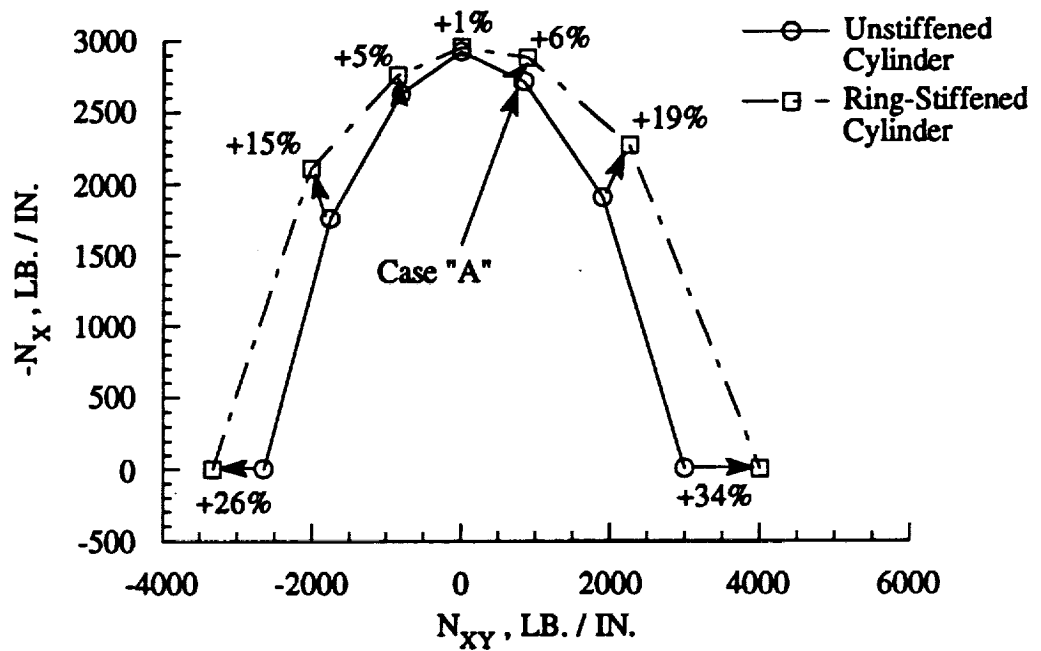


Figure 7.1.6
Effect Of Adding Rings To Imperfect, Pressurized Cylinder

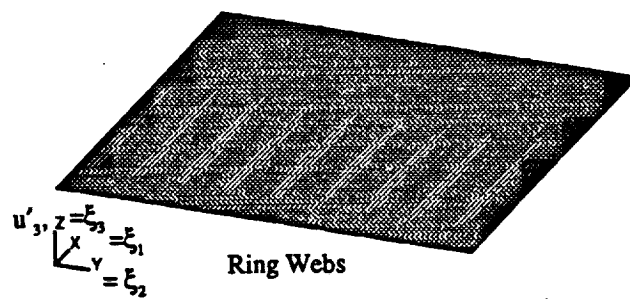
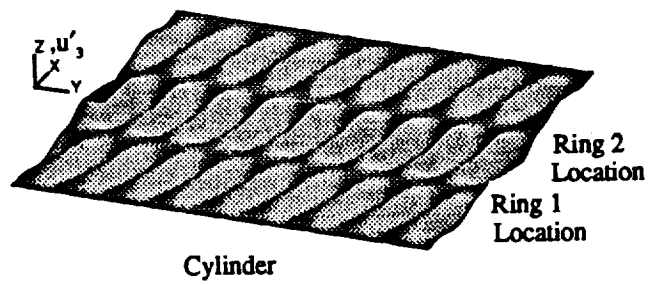


Figure 7.1.7

Case "A" Buckling Mode Shape Of Perfect Ring-Stiffened Cylinder

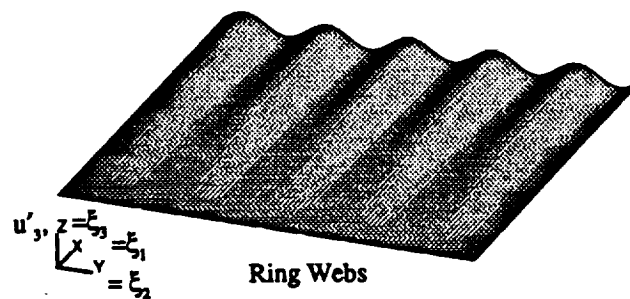
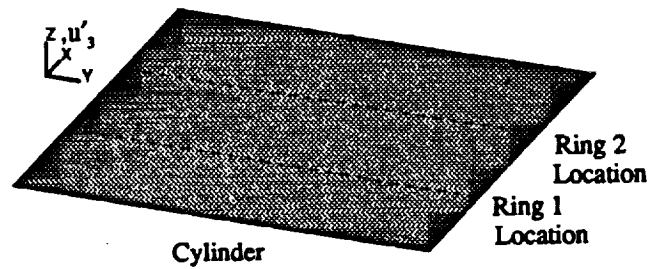


Figure 7.1.8

Case "A" Buckling Mode Shape Of Imperfect Ring-Stiffened Cylinder

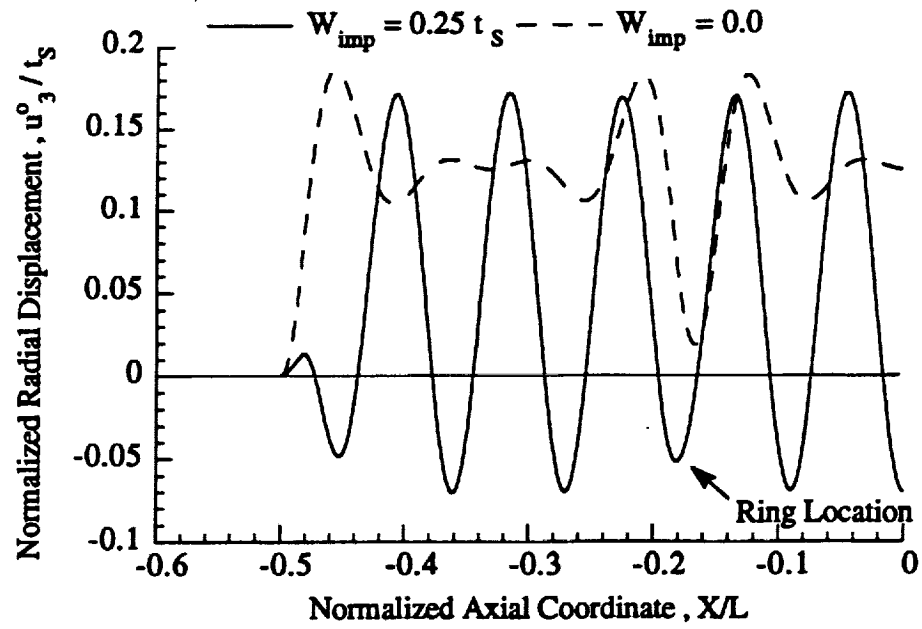


Figure 7.1.9
Case "A" Normalized Prebuckling Radial Displacement

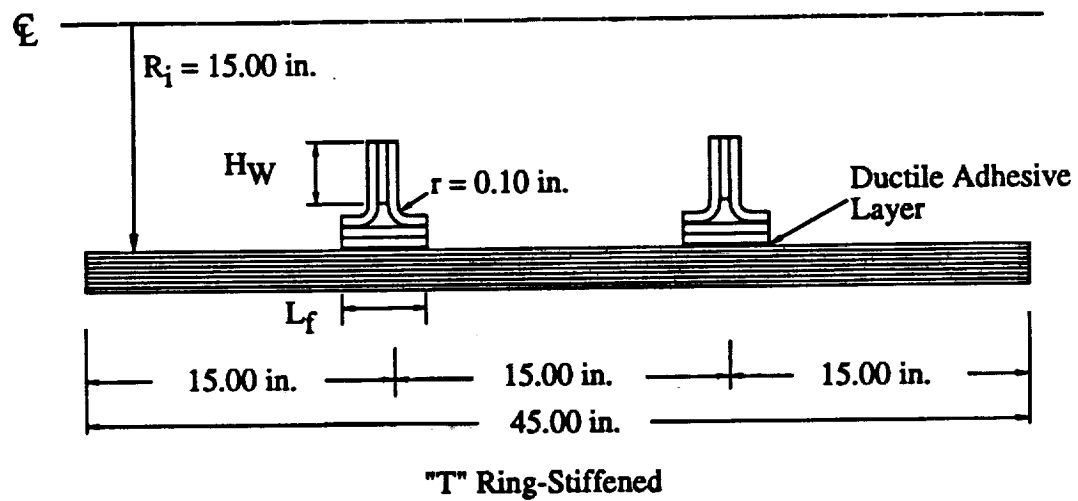
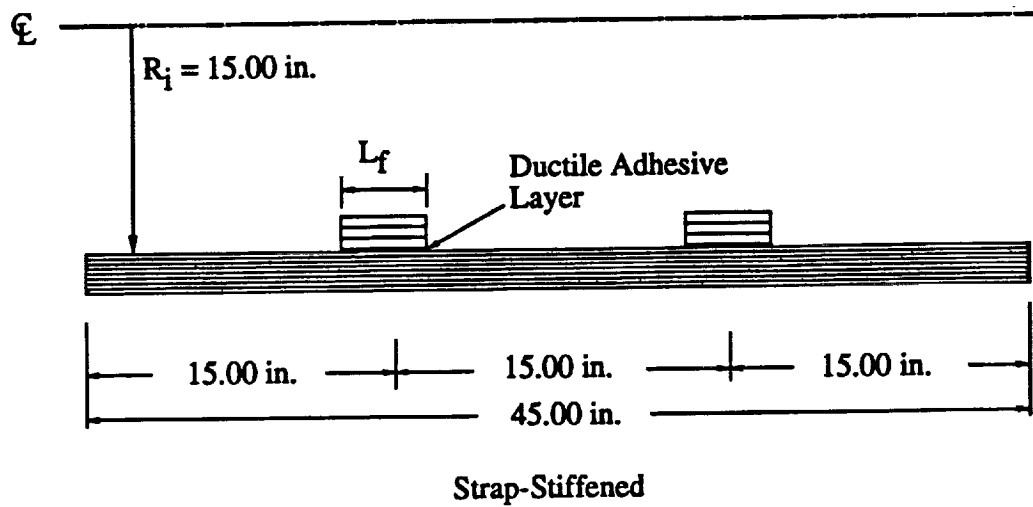
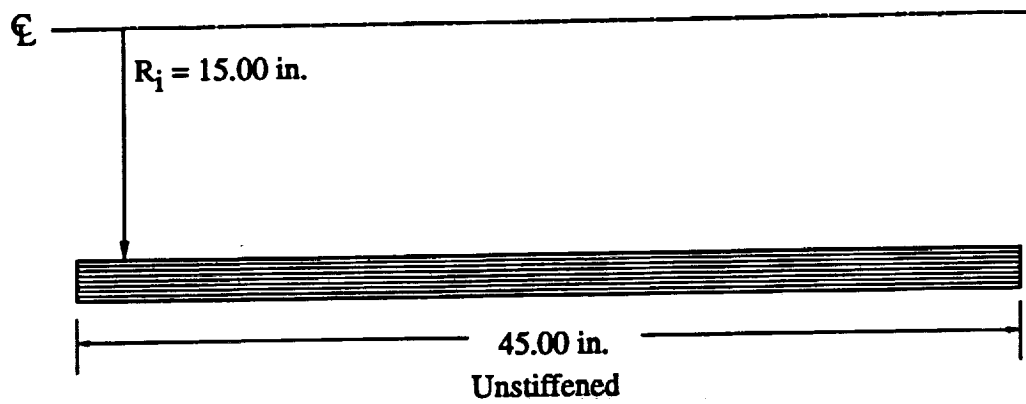


Figure 7.2.1
Optimal Sizing Case Study Configurations

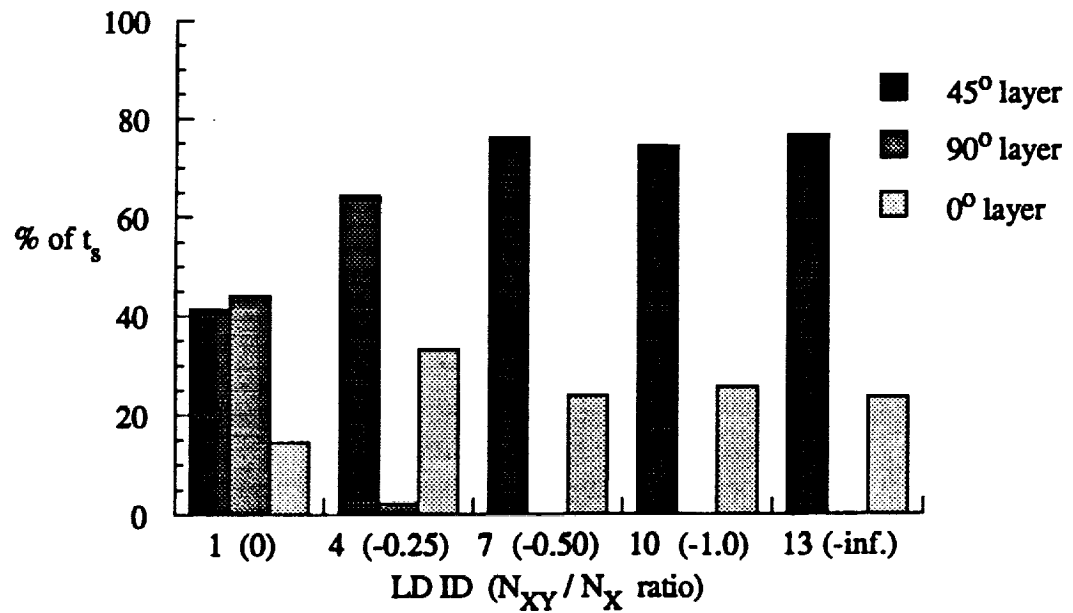


Figure 7.3.1
Effect of Mechanical Loading on Optimal Designs
of Perfect, Unpressurized, Unstiffened Cylinders

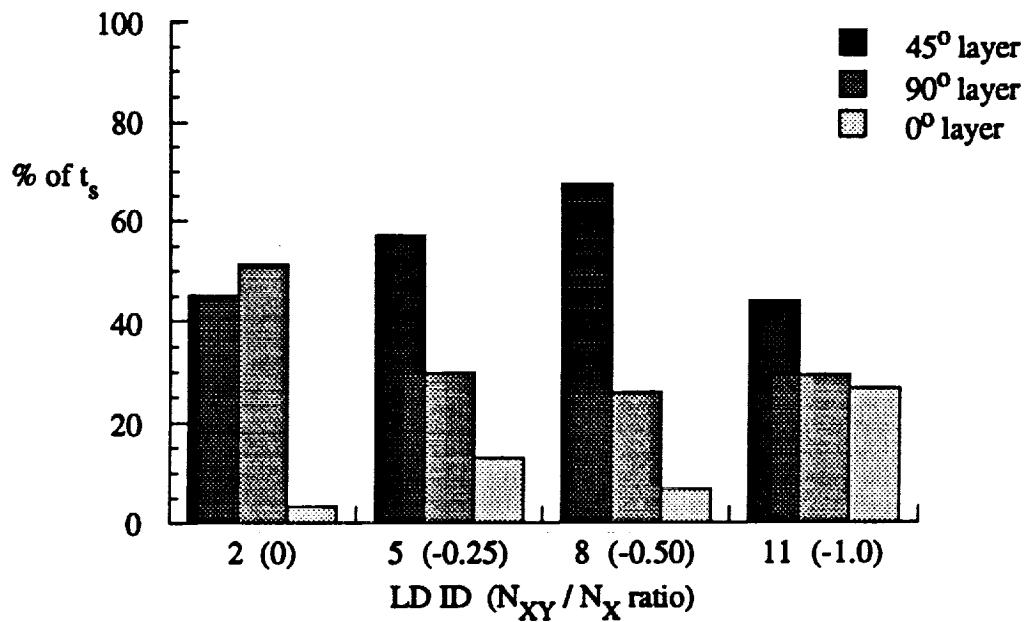


Figure 7.3.2
Effect of Mechanical Loading on Optimal Designs
of Imperfect, Unpressurized, Unstiffened Cylinders

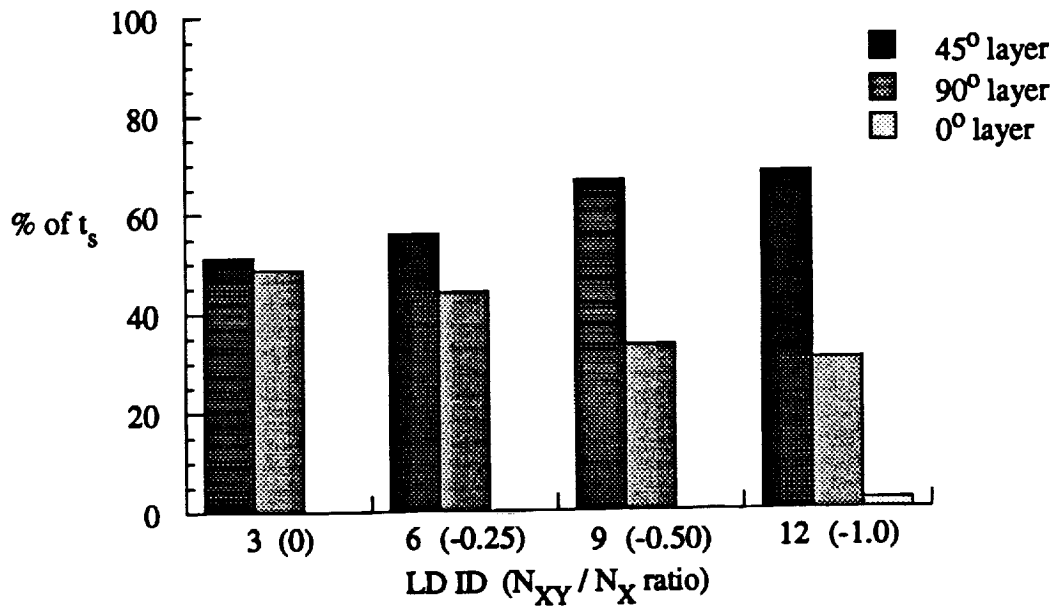


Figure 7.3.3
Effect of Mechanical Loading on Optimal Designs
of Imperfect, Pressurized, Unstiffened Cylinders

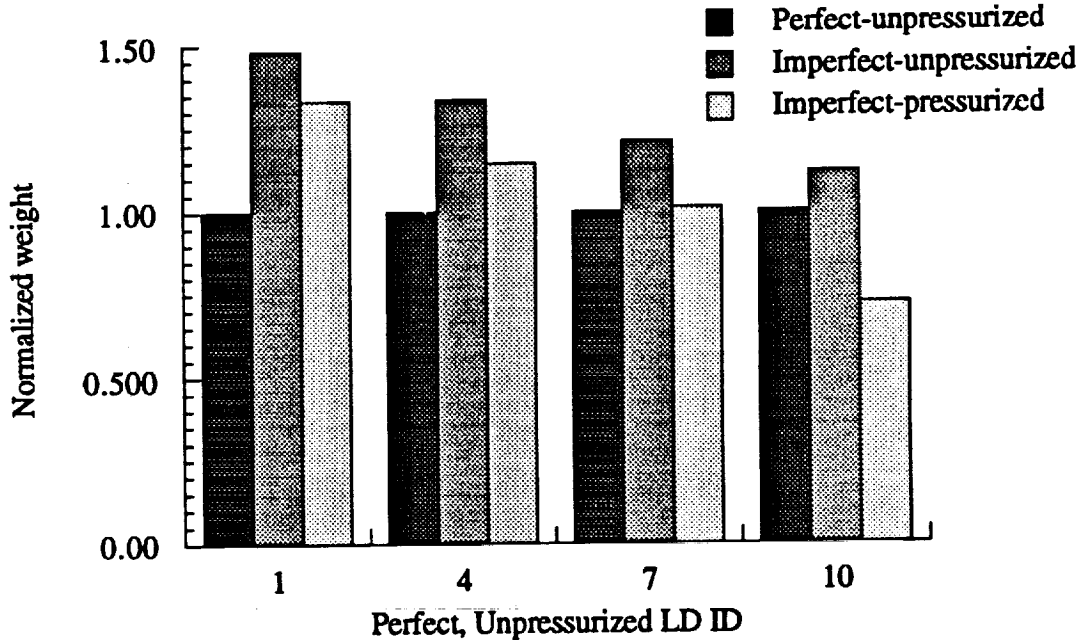


Figure 7.3.4
Effect of Imperfections and Pressurization on
Weights of Optimal Unstiffened Cylinders

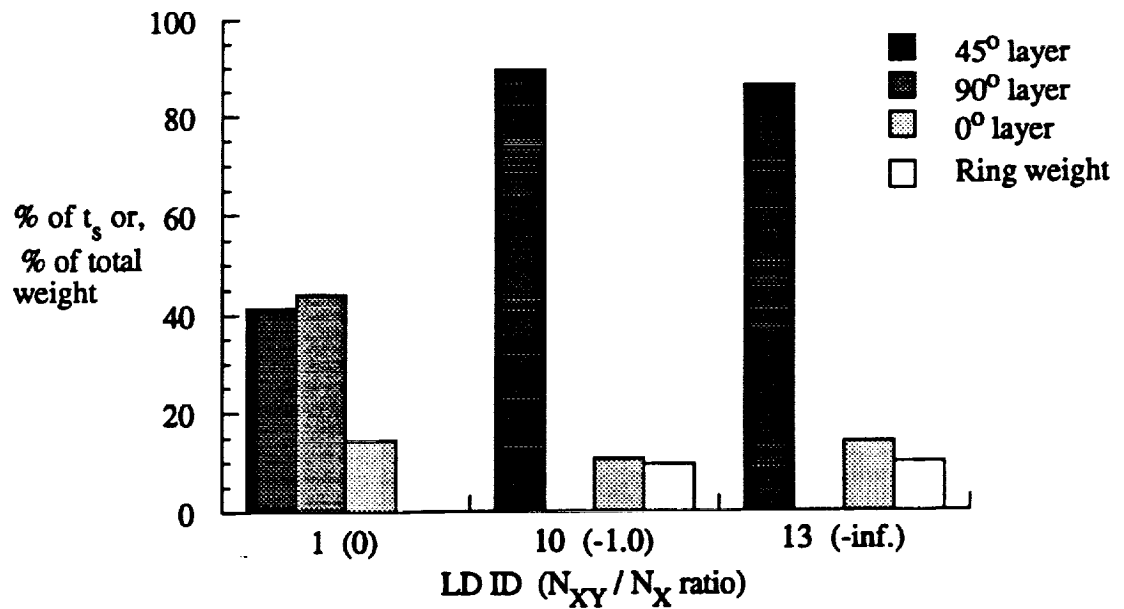


Figure 7.3.5
Effect of Mechanical Loading on Optimal Designs
of Perfect, Unpressurized, Strap-Stiffened Cylinders

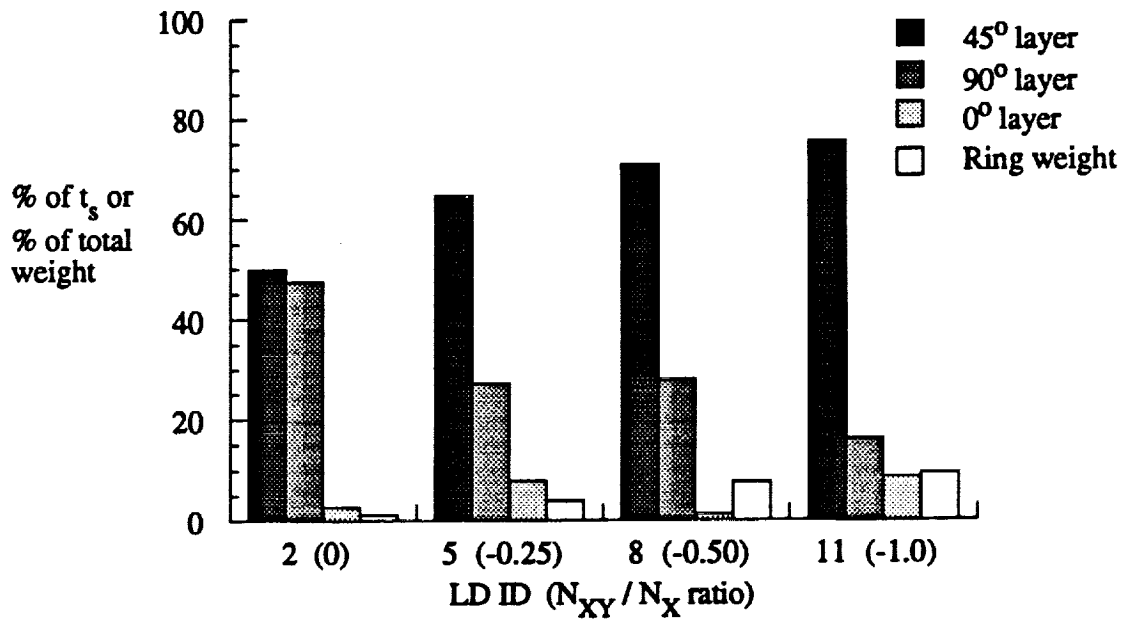


Figure 7.3.6
Effect of Mechanical Loading on Optimal Designs
of Imperfect, Unpressurized, Strap-Stiffened Cylinders

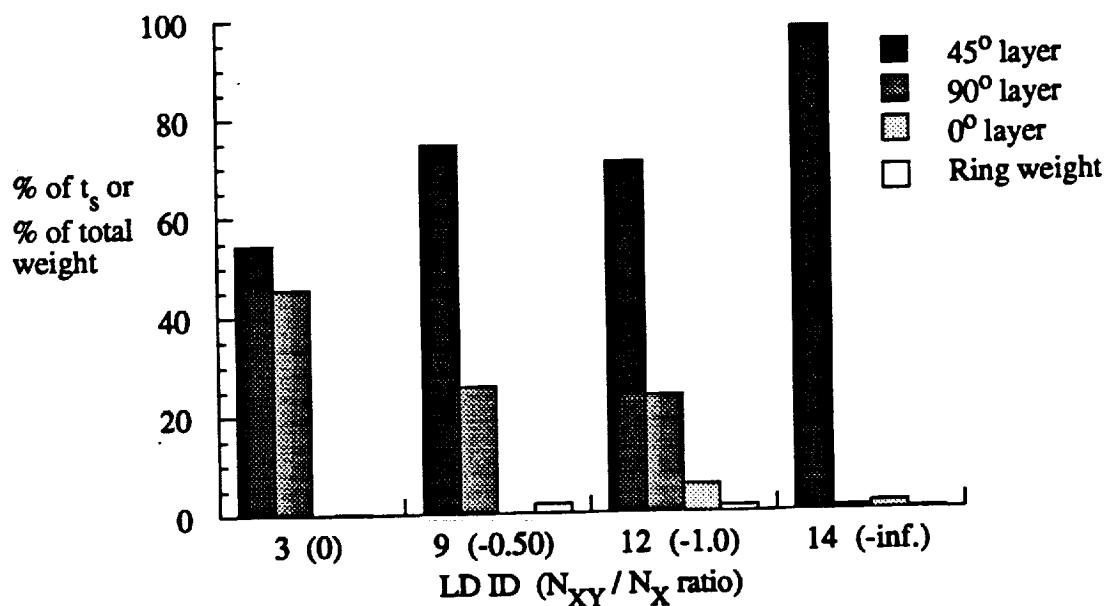


Figure 7.3.7
Effect of Mechanical Loading on Optimal Designs
of Imperfect, Pressurized, Strap-Stiffened Cylinders

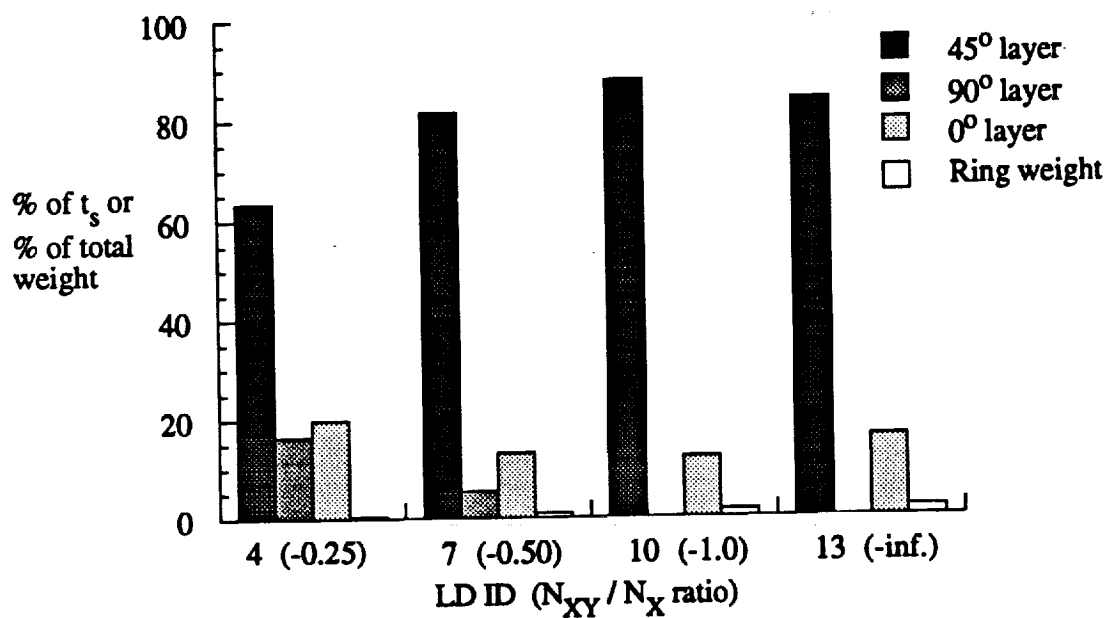


Figure 7.3.8
Effect of Mechanical Loading on Optimal Designs
of Perfect, Unpressurized "T" Ring-Stiffened Cylinders

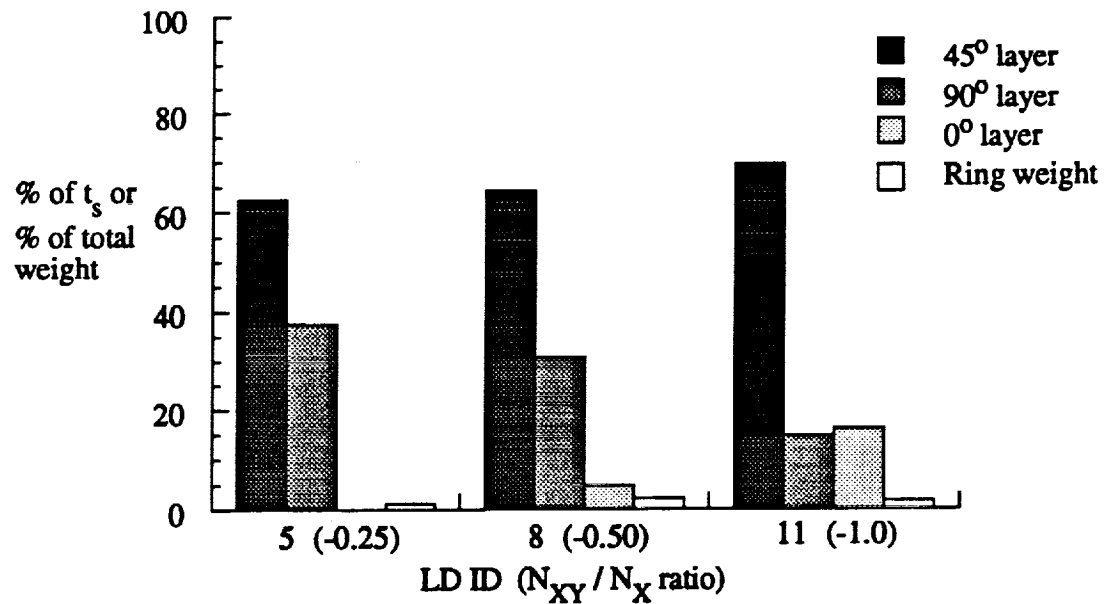


Figure 7.3.9
Effect of Mechanical Loading on Optimal Designs
of Imperfect, Unpressurized, "T" Ring-Stiffened Cylinders

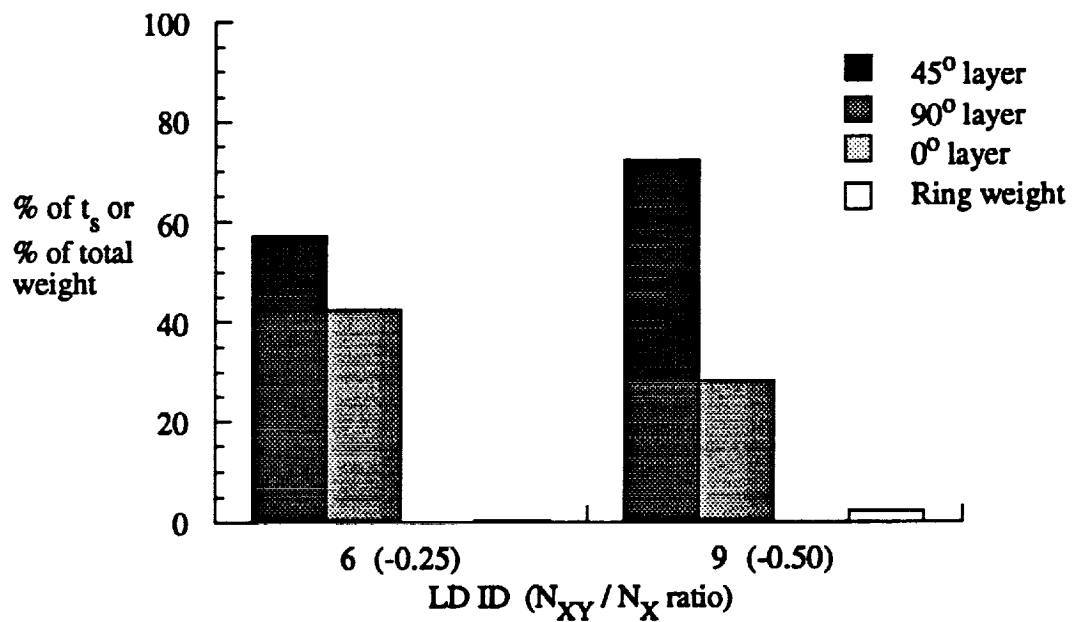


Figure 7.3.10
Effect of Mechanical Loading on Optimal Designs
of Imperfect, Pressurized, "T" Ring-Stiffened Cylinders

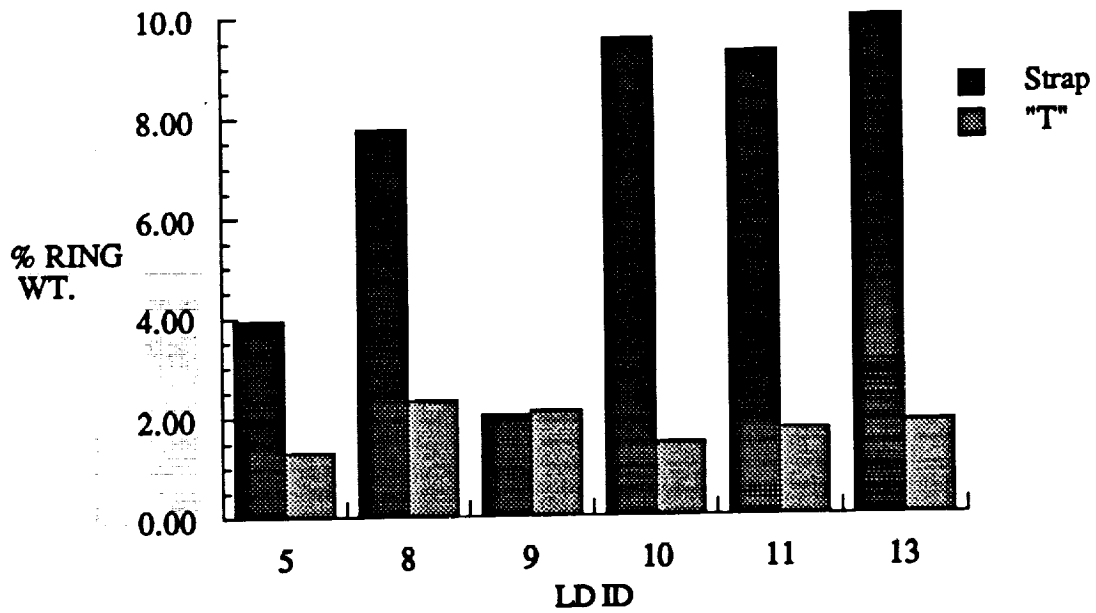


Figure 7.3.11
Comparison of Strap-Stiffener Weights With
"T" Ring-Stiffener Weights

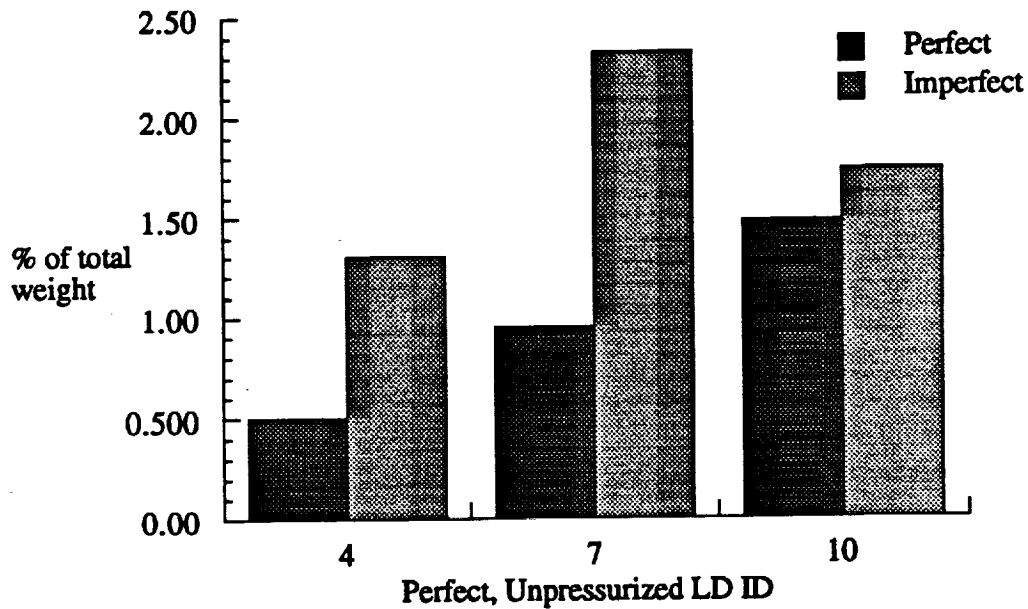


Figure 7.3.12
Effect of Imperfections On Ring Weights of
Optimal Unpressurized "T" Ring-Stiffened Cylinders

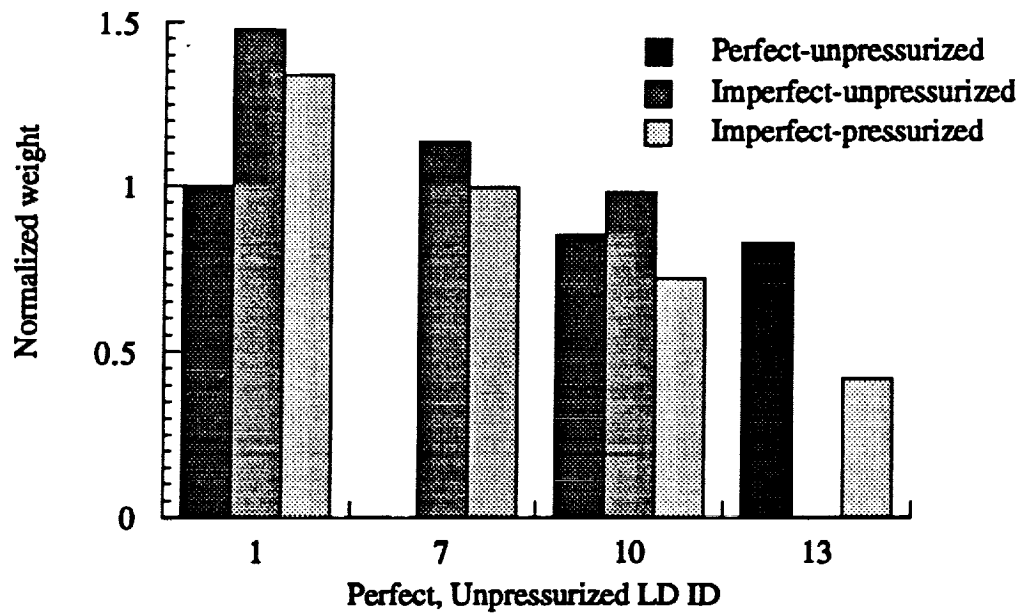


Figure 7.3.13
Effect of Imperfections and Pressurization on
Weights of Optimal Strap-Stiffened Cylinders

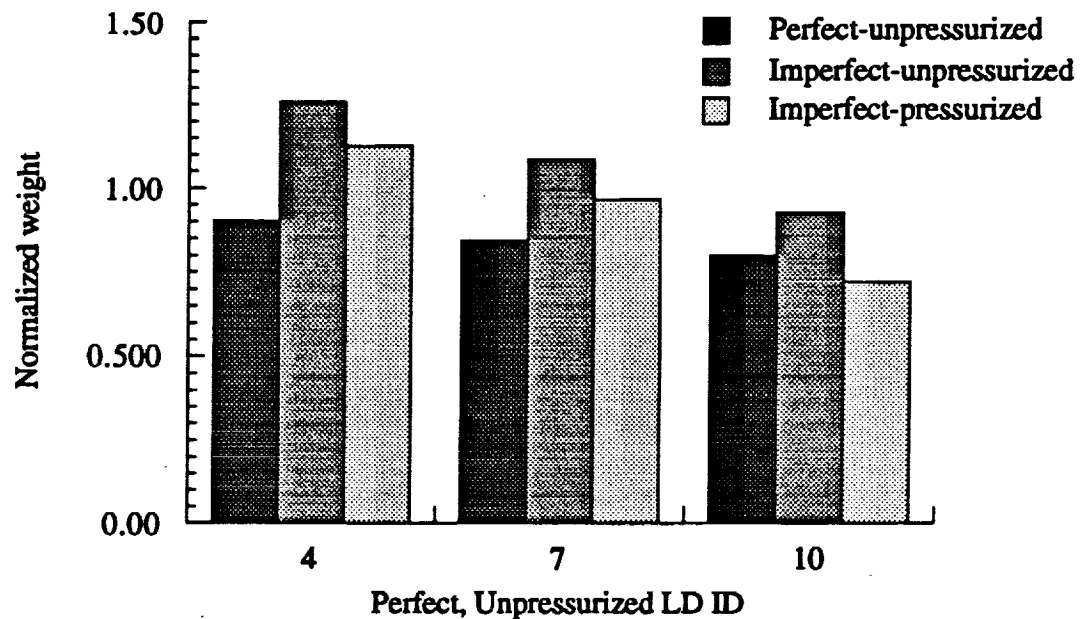


Figure 7.3.14
Effect of Imperfections and Pressurization on Weights
of Optimal "T" Ring-Stiffened Cylinders

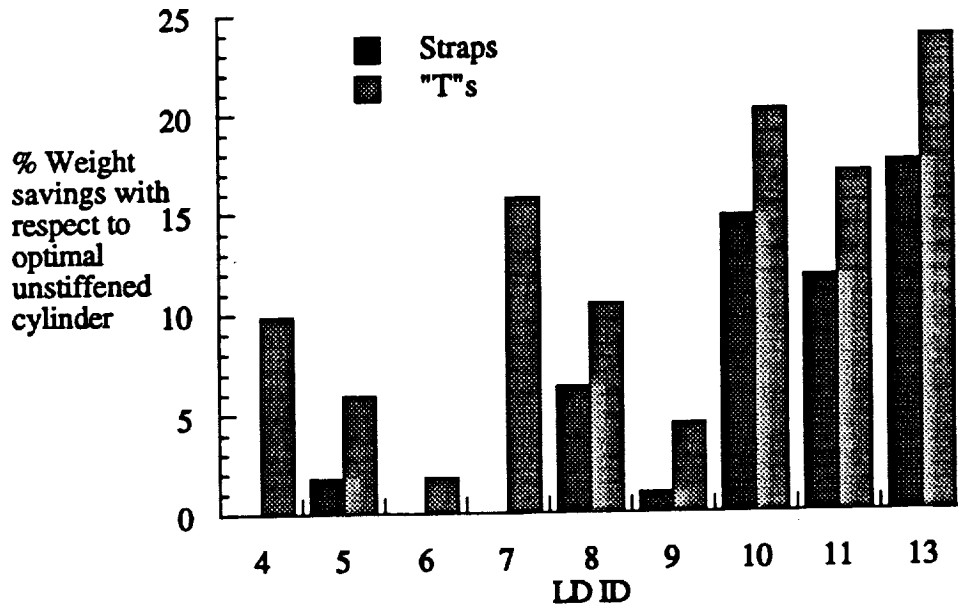


Figure 7.3.15
Weight Savings Due To Addition Of Rings

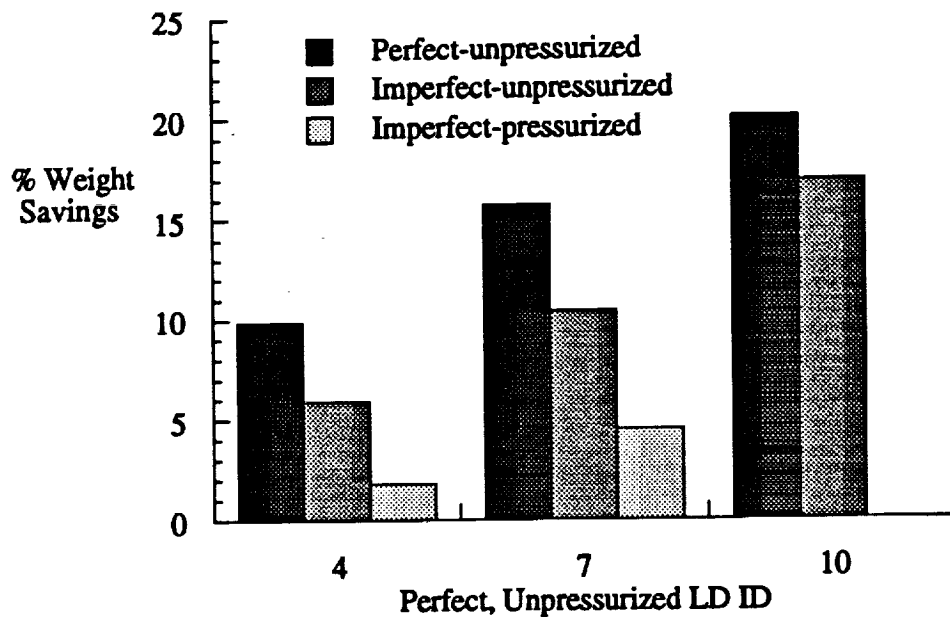


Figure 7.3.16
Effect Of Imperfections and Pressurization on
Weight Savings Due To Addition of "T" Ring-Stiffeners

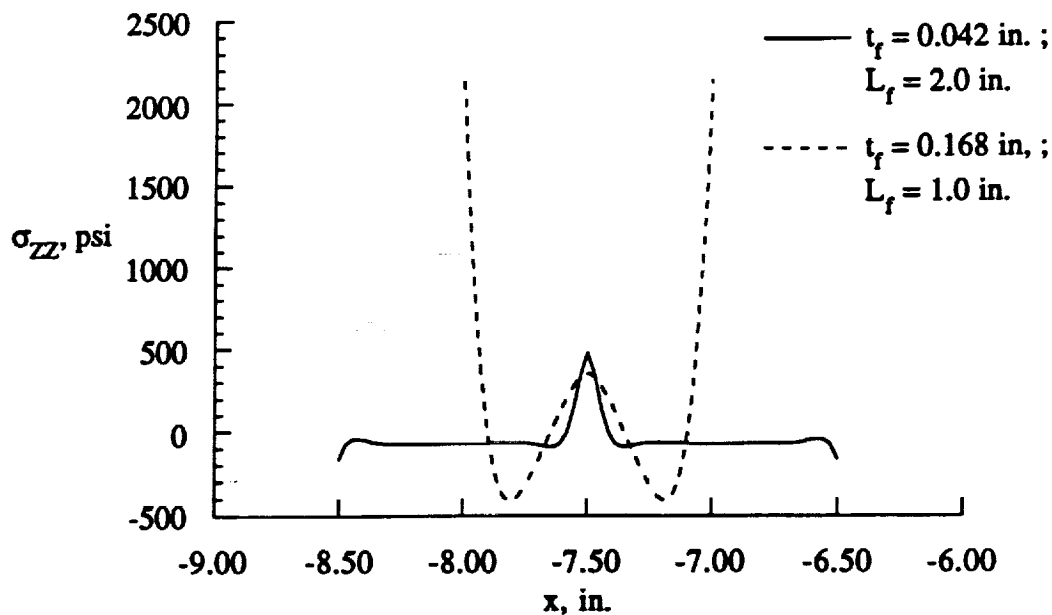


Figure 7.4.1
Typical Ring Flange/Cylinder Skin Adhesive σ_{zz} Peel Stress Distributions

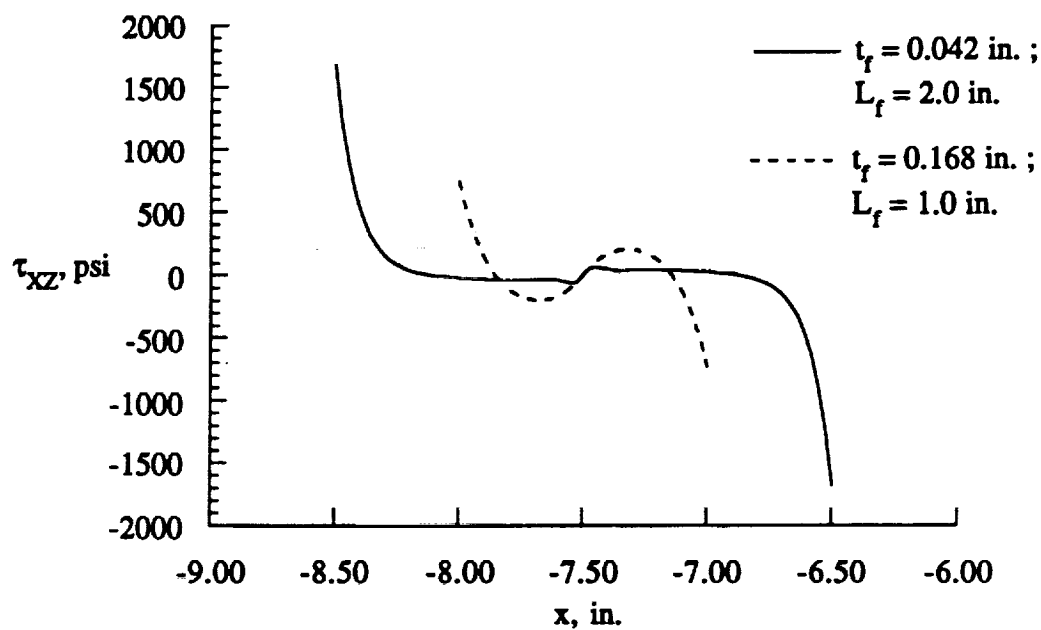


Figure 7.4.2
Typical Ring Flange/Cylinder Skin Adhesive τ_{xz} Shear Stress Distributions

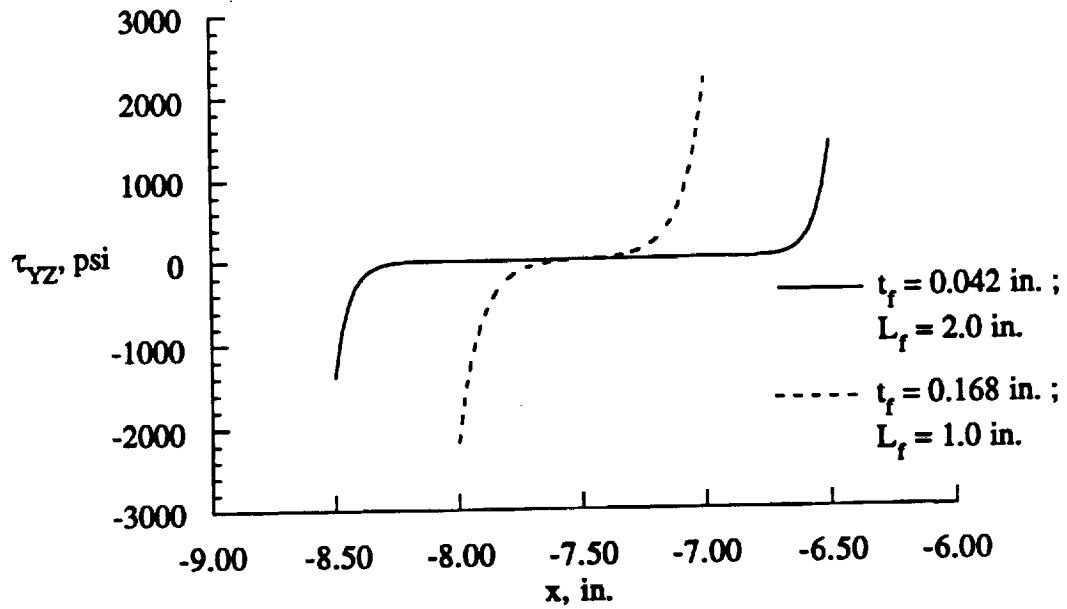


Figure 7.4.3
Typical Ring Flange/ Cylinder Skin Adhesive τ_{YZ} Shear Stress Distributions

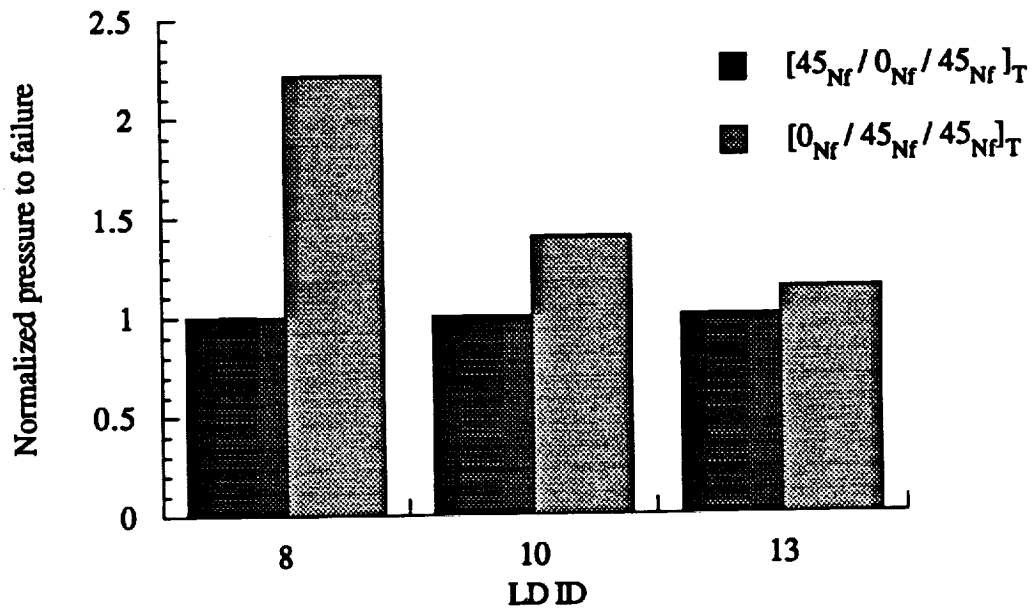


Figure 7.4.4
Effect of Strap Stacking Sequence On Internal Pressure To Failure of Optimal Strap-Stiffened Cylinders

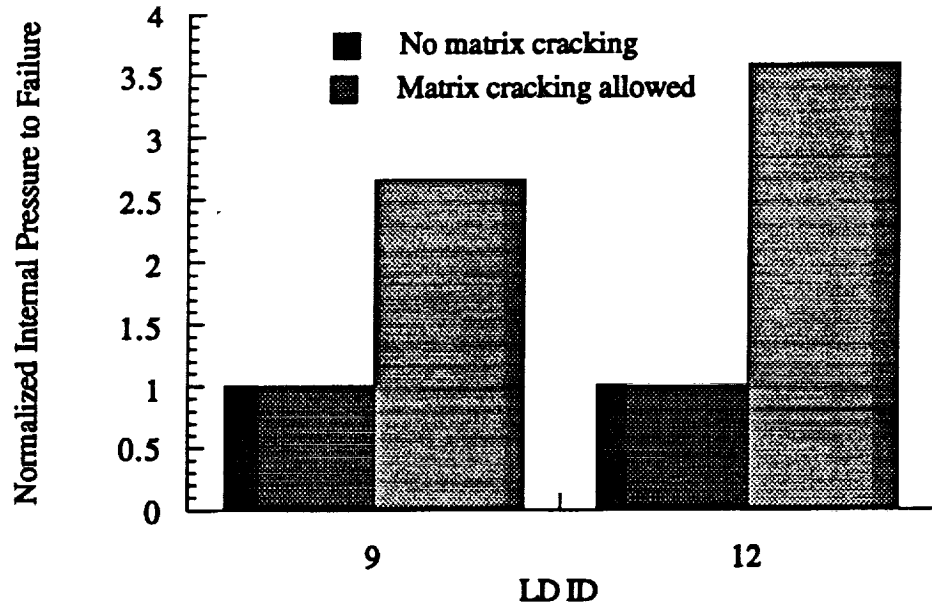


Figure 7.4.5
Effect of Neglect of Matrix Cracking Failure On Internal Pressure To Failure of Optimal Strap-Stiffened Cylinders

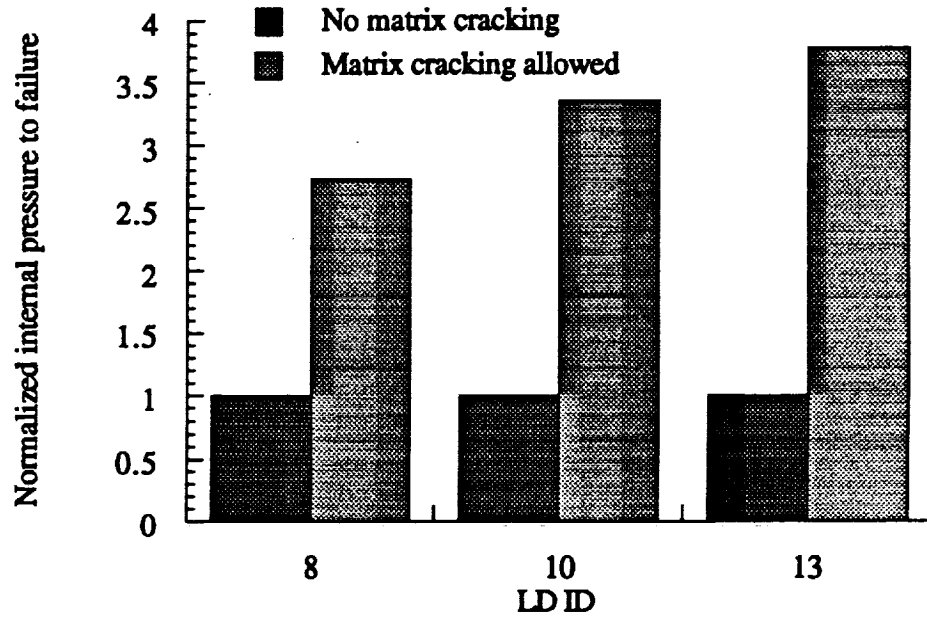


Figure 7.4.6
Effect of Neglect of Matrix Cracking On Internal Pressure To Failure of Optimal "T" Ring-Stiffened Cylinders

Appendix A

LAMINA STRESS ANALYSIS OF PREBUCKLED CYLINDRICAL SHELL

A.1 Tangential Stresses

Fig. 3.2.1 shows a typical cylindrical shell lamina with fiber orientation angle θ , global (structural) coordinate axes ξ_1, ξ_2, ξ_3 and material coordinate axes 123. Assuming a state of plane stress exists within the lamina, the tangential stress components in global coordinates are given by

$$\{\sigma\}_{glb} = \begin{Bmatrix} \sigma_{xx} \\ \sigma_{yy} \\ \tau_{xy} \end{Bmatrix} = \begin{bmatrix} \bar{Q}_{11} & \bar{Q}_{12} & \bar{Q}_{16} \\ \bar{Q}_{12} & \bar{Q}_{22} & \bar{Q}_{26} \\ \bar{Q}_{16} & \bar{Q}_{26} & \bar{Q}_{66} \end{bmatrix} \begin{Bmatrix} \epsilon_{xx} \\ \epsilon_{yy} \\ \gamma_{xy} \end{Bmatrix} \quad (A.1.1)$$

where σ_{xx}, σ_{yy} and τ_{xy} are stresses and $\epsilon_{xx}, \epsilon_{yy}$ and γ_{xy} are strains with respect to the $\xi_1\xi_1, \xi_2\xi_2$ and $\xi_1\xi_2$ coordinate directions respectively and the \bar{Q}_{ij} are the lamina reduced stiffnesses in the global coordinate system (see Jones⁸⁴). The lamina strains in the global coordinate system are given by

$$\begin{Bmatrix} \epsilon_{xx} \\ \epsilon_{yy} \\ \gamma_{xy} \end{Bmatrix} = \begin{Bmatrix} \epsilon_{xx}^o \\ \epsilon_{yy}^o \\ \gamma_{xy}^o \end{Bmatrix} + \xi_3 \begin{Bmatrix} \kappa_{xx} \\ \kappa_{yy} \\ \kappa_{xy} \end{Bmatrix} \quad (A.1.2)$$

For the cylindrical shell considered in this study, strains at any point, ξ_3 , through the thickness of the laminate are given by the axisymmetric form of Eqs. (3.3.1.3) through (3.3.1.5)

$$\begin{Bmatrix} \epsilon_{xx} \\ \epsilon_{yy} \\ \gamma_{xy} \end{Bmatrix} = \left(\frac{t_s}{L}\right)^2 \begin{Bmatrix} \bar{\epsilon}_{11}^o \\ \bar{\epsilon}_{22}^o \\ \bar{\gamma}_{12}^o \end{Bmatrix} + \frac{\xi_3}{t_s} \left(\frac{t_s}{L}\right)^2 \begin{Bmatrix} \bar{\kappa}_{11} \\ 0 \\ 0 \end{Bmatrix} \quad (A.1.3)$$

where $\bar{\epsilon}_{11}^o, \bar{\epsilon}_{22}^o$ and $\bar{\gamma}_{12}^o$ are nondimensional middle surface strains, $\bar{\kappa}_{11}$ is the nondimensional middle surface curvature defined in Eq. (4.1.19), L is the length and R is the middle surface radius of the cylinder. Substituting Eqs. (4.1.19) and (4.1.21) into (4.1.18) then substituting the resulting expressions for $\bar{\epsilon}_{11}^o, \bar{\epsilon}_{22}^o$ and $\bar{\gamma}_{12}^o$ into Eq. (A.1.3) results in

$$\epsilon_{xx} = \left(\frac{L}{t_s}\right)^2 \left(EX_1 \bar{N}_X + EX_2 \bar{N}_{XY} + EX_3 \bar{w}^o + EX_4 \frac{d^2 \bar{w}^o}{dX^2} \right) - \frac{\xi_3}{t_s} \left(\frac{t_s}{L}\right)^2 \quad (A.1.4)$$

$$\epsilon_{yy} = \left(\frac{L}{t_s}\right)^2 (EY\bar{w}^o) \quad (A.1.5)$$

$$\gamma_{xy} = \left(\frac{L}{t_s}\right)^2 \left(GXY_1 \bar{N}_X + GXY_2 \bar{N}_{XY} + GXY_3 \bar{w}^o + GXY_4 \frac{d^2 \bar{w}^o}{dX^2} \right) \quad (A.1.6)$$

where \bar{w}^o is the nondimensional displacement of the middle surface of the cylindrical shell in the ξ_3 direction defined in Eq. (4.1.5) and

$$\begin{aligned} EX_1 &= \left(\frac{t_s}{L}\right)^2 \left(\bar{A}_{11}^* - \frac{\bar{A}_{12}^* \bar{A}_{12}^*}{\bar{A}_{22}^*} \right) & GXY_1 &= \left(\frac{t_s}{L}\right)^2 \left(\bar{A}_{16}^* - \frac{\bar{A}_{26}^* \bar{A}_{12}^*}{\bar{A}_{22}^*} \right) \\ EX_2 &= \left(\frac{t_s}{L}\right)^2 \left(\bar{A}_{16}^* - \frac{\bar{A}_{12}^* \bar{A}_{26}^*}{\bar{A}_{22}^*} \right) & GXY_2 &= \left(\frac{t_s}{L}\right)^2 \left(\bar{A}_{66}^* - \frac{\bar{A}_{26}^* \bar{A}_{26}^*}{\bar{A}_{22}^*} \right) \\ EX_3 &= \frac{\bar{A}_{12}^* t_s}{\bar{A}_{22}^* R} & GXY_3 &= \frac{\bar{A}_{26}^* t_s}{\bar{A}_{22}^* R} \\ EX_4 &= -\left(\frac{t_s}{L}\right)^2 \left(\bar{B}_{11}^* - \frac{\bar{A}_{12}^* \bar{B}_{21}^*}{\bar{A}_{22}^*} \right) & GXY_4 &= -\left(\frac{t_s}{L}\right)^2 \left(\bar{B}_{61}^* - \frac{\bar{A}_{26}^* \bar{B}_{21}^*}{\bar{A}_{22}^*} \right) \\ EY &= \frac{t_s}{R} \end{aligned} \quad (A.1.7)$$

Substitution of Eqs. (A.1.4) through (A.1.6) into Eq. (A.1.1) yields the stresses with respect to the global coordinate system ξ_1, ξ_2, ξ_3 .

$$\sigma_{xx} = C_o \left(\frac{d^2 \bar{w}^o}{dX^2} \right) \xi_3 + C_1 \left(\frac{d^2 \bar{w}^o}{dX^2} \right) + C_2 \bar{w}^o + C_3 \bar{N}_X + C_4 \bar{N}_{XY} \quad (A.1.8)$$

$$\sigma_{yy} = D_o \left(\frac{d^2 \bar{w}^o}{dX^2} \right) \xi_3 + D_1 \left(\frac{d^2 \bar{w}^o}{dX^2} \right) + D_2 \bar{w}^o + D_3 \bar{N}_X + D_4 \bar{N}_{XY} \quad (A.1.9)$$

$$\tau_{xy} = D_o \left(\frac{d^2 \bar{w}^o}{dX^2} \right) \xi_3 + D_1 \left(\frac{d^2 \bar{w}^o}{dX^2} \right) + D_2 \bar{w}^o + D_3 \bar{N}_X + D_4 \bar{N}_{XY} \quad (A.1.10)$$

where

$$\begin{aligned} C_o &= -\bar{Q}_{11} \left(\frac{t_s}{L^2} \right) & D_o &= -\bar{Q}_{12} \left(\frac{t_s}{L^2} \right) \\ C_1 &= \bar{Q}_{11} EX_4 + \bar{Q}_{16} GXY_4 & D_1 &= \bar{Q}_{12} EX_4 + \bar{Q}_{26} GXY_4 \\ C_2 &= \bar{Q}_{11} EX_3 + \bar{Q}_{12} EY + \bar{Q}_{16} GXY_3 & D_2 &= \bar{Q}_{12} EX_3 + \bar{Q}_{22} EY + \bar{Q}_{26} GXY_3 \\ C_3 &= \bar{Q}_{11} EX_1 + \bar{Q}_{16} GXY_1 & D_3 &= \bar{Q}_{12} EX_1 + \bar{Q}_{26} GXY_1 \\ C_4 &= \bar{Q}_{11} EX_2 + \bar{Q}_{16} GXY_2 & D_4 &= \bar{Q}_{12} EX_2 + \bar{Q}_{26} GXY_2 \end{aligned}$$

$$\begin{aligned}
E_o &= -\bar{Q}_{16} \left(\frac{t_z}{L^2} \right) \\
E_1 &= \bar{Q}_{16} EX_4 + \bar{Q}_{66} GXY_4 \\
E_2 &= \bar{Q}_{16} EX_3 + \bar{Q}_{26} EY + \bar{Q}_{66} GXY_3 \\
E_3 &= \bar{Q}_{16} EX_1 + \bar{Q}_{66} GXY_1 \\
E_4 &= \bar{Q}_{16} EX_2 + \bar{Q}_{66} GXY_2
\end{aligned} \tag{A.1.11}$$

and it is understood that the material properties used in these equations are evaluated at the coordinate, ξ_3 , where stresses are to be calculated. The stresses in the (ξ_1, ξ_2, ξ_3) coordinate system, $\{\sigma\}_{glb}$, can be transformed to stresses in the $(1, 2, 3)$ material coordinate system, $\{\sigma\}_{mat}$, using the following equation

$$\{\sigma\}_{mat} = [T_1]\{\sigma\}_{glb} \tag{A.1.12}$$

where

$$[T_1] = \begin{bmatrix} \cos^2 \theta & \sin^2 \theta & 2 \sin \theta \cos \theta \\ \sin^2 \theta & \cos^2 \theta & -2 \sin \theta \cos \theta \\ -\sin \theta \cos \theta & \sin \theta \cos \theta & \cos^2 \theta - \sin^2 \theta \end{bmatrix}. \tag{A.1.13}$$

A.2 Interlaminar Stresses

Consistant with DMV theory, the axisymmetric elasticity equilibrium equations for a single lamina of the imperfect cylindrical shell depicted in Fig 3.2.1 are (see page 24 of Ref. 54)

$$\frac{\partial \sigma_{zz}}{\partial \xi_1} + \frac{\partial \tau_{zz}}{\partial \xi_3} = 0 \quad (\text{A.2.1})$$

$$\frac{\partial \tau_{zy}}{\partial \xi_1} + \frac{\partial \tau_{yz}}{\partial \xi_3} = 0 \quad (\text{A.2.2})$$

$$\begin{aligned} \frac{\partial \tau_{zz}}{\partial \xi_1} + \frac{\partial \sigma_{zz}}{\partial \xi_3} - \frac{\sigma_{yy}}{R} + \frac{\partial \sigma_{zz}}{\partial \xi_1} \left(\frac{du_3^o}{d\xi_1} + \frac{dw_o}{d\xi_1} \right) \\ + \sigma_{zz} \left(\frac{d^2 u_3^o}{d\xi_1^2} + \frac{d^2 w_o}{d\xi_1^2} \right) = 0 \end{aligned} \quad (\text{A.2.3})$$

where $\sigma_{zz}, \sigma_{yy}, \tau_{zy}, \tau_{zz}, \tau_{yz}$ and σ_{zz} are stresses with respect to the $\xi_1\xi_1, \xi_2\xi_2, \xi_1\xi_2, \xi_1\xi_3, \xi_2\xi_3$, and $\xi_3\xi_3$ coordinate directions respectively, u_3^o is the displacement of the middle surface of the cylinder in the ξ_3 direction, w_o is the initial geometric imperfection and R is the middle surface radius of the cylinder. Nondimensionalizing ξ_1, u_3^o and w_o as shown in Table 1 yields

$$\left(\frac{1}{L} \right) \frac{\partial \sigma_{zz}}{\partial \bar{\xi}_1} + \frac{\partial \tau_{zz}}{\partial \xi_3} = 0 \quad (\text{A.2.4})$$

$$\left(\frac{1}{L} \right) \frac{\partial \tau_{zy}}{\partial \bar{\xi}_1} + \frac{\partial \tau_{yz}}{\partial \xi_3} = 0 \quad (\text{A.2.5})$$

$$\begin{aligned} \left(\frac{1}{L} \right) \frac{\partial \tau_{zz}}{\partial \bar{\xi}_1} + \frac{\partial \sigma_{zz}}{\partial \xi_3} - \frac{\sigma_{yy}}{R} \\ + \frac{\partial \sigma_{zz}}{\partial \bar{\xi}_1} \left(\frac{t_s}{L^2} \right) \left(\frac{d\bar{w}^o}{d\bar{\xi}_1} + \frac{d\bar{w}_o}{d\bar{\xi}_1} \right) + \sigma_{zz} \left(\frac{t_s}{L^2} \right) \left(\frac{d\bar{w}^o}{d\bar{\xi}_1} + \frac{d\bar{w}_o}{d\bar{\xi}_1} \right) = 0. \end{aligned} \quad (\text{A.2.6})$$

where L is the length and t_s is the total thickness of the cylinder. Substituting Eqs. (A.1.8) through (A.1.10) into Eqs. (A.2.4) through (A.2.6), performing the integration with respect to ξ_3 and solving for the interlaminar stresses τ_{zz}, τ_{yz} and σ_{zz} gives

$$\tau_{zz} = TXZ_1(X)\xi_3^2 + TXZ_2(X)\xi_3 + F(X) \quad (\text{A.2.7})$$

$$\tau_{yz} = TYZ_1(X)\xi_3^2 + TYZ_2(X)\xi_3 + G(X) \quad (\text{A.2.8})$$

$$\sigma_{zz} = SZ_1(X)\xi_3^3 + SZ_2(X)\xi_3^2 + SZ_3(X)\xi_3 + H(X) \quad (\text{A.2.9})$$

where $X = \bar{\xi}_1$ as shown in Eq. (4.1.4) and

$$TXZ_1(X) = -\left(\frac{C_0}{2L}\right) \frac{d^3 \bar{w}^o}{dX^3} \quad (\text{A.2.10})$$

$$TXZ_2(X) = -\left(\frac{C_1}{L}\right) \frac{d^3 \bar{w}^o}{dX^3} - \left(\frac{C_2}{L}\right) \frac{d\bar{w}^o}{dX} \quad (\text{A.2.11})$$

$$TYZ_1(X) = -\left(\frac{E_0}{2L}\right) \frac{d^3 \bar{w}^o}{dX^3} \quad (\text{A.2.12})$$

$$TYZ_2(X) = -\left(\frac{E_1}{L}\right) \frac{d^3 \bar{w}^o}{dX^3} - \left(\frac{E_2}{L}\right) \frac{d\bar{w}^o}{dX} \quad (\text{A.2.13})$$

$$SZ_1(X) = \left(\frac{C_0}{6L^2}\right) \frac{d^4 \bar{w}^o}{dX^4} \quad (\text{A.2.14})$$

$$\begin{aligned} SZ_2(X) = & \left(\frac{C_1}{2L^2}\right) \frac{d^4 \bar{w}^o}{dX^4} - \left[\left(\frac{t_s C_0}{2L^2}\right) \left(\frac{d\bar{w}^o}{dX} + \frac{d\bar{w}_o}{dX}\right)\right] \frac{d^3 \bar{w}^o}{dX^3} \\ & + \left[\frac{C_2}{2L^2} + \frac{D_0}{2R} - \left(\frac{t_s C_0}{2L^2}\right) \left(\frac{d^2 \bar{w}^o}{dX^2} + \frac{d^2 \bar{w}_o}{dX^2}\right)\right] \frac{d^2 \bar{w}^o}{dX^2} \end{aligned} \quad (\text{A.2.15})$$

$$\begin{aligned} SZ_3(X) = & -\left[\left(\frac{t_s C_1}{L^2}\right) \left(\frac{d\bar{w}^o}{dX} + \frac{d\bar{w}_o}{dX}\right)\right] \frac{d^3 \bar{w}^o}{dX^3} \\ & + \left[\frac{D_1}{R} - \left(\frac{t_s C_1}{L^2}\right) \left(\frac{d^2 \bar{w}^o}{dX^2} + \frac{d^2 \bar{w}_o}{dX^2}\right)\right] \frac{d^2 \bar{w}^o}{dX^2} \\ & - \left[\left(\frac{t_s C_2}{L^2}\right) \left(\frac{d\bar{w}^o}{dX} + \frac{d\bar{w}_o}{dX}\right)\right] \frac{d\bar{w}^o}{dX} \\ & + \left[\frac{D_2}{R} - \left(\frac{t_s C_2}{L^2}\right) \left(\frac{d^2 \bar{w}^o}{dX^2} + \frac{d^2 \bar{w}_o}{dX^2}\right)\right] \bar{w}^o \\ & + \left[\frac{D_3}{R} - \left(\frac{t_s C_3}{L^2}\right) \left(\frac{d^2 \bar{w}^o}{dX^2} + \frac{d^2 \bar{w}_o}{dX^2}\right)\right] \bar{N}_X \\ & + \left[\frac{D_4}{R} - \left(\frac{t_s C_4}{L^2}\right) \left(\frac{d^2 \bar{w}^o}{dX^2} + \frac{d^2 \bar{w}_o}{dX^2}\right)\right] \bar{N}_{XY} - \left(\frac{1}{L}\right) \frac{dF}{dX} \end{aligned} \quad (\text{A.2.16})$$

The nondimensional radial displacement, \bar{w}^o , is given Eqs. (4.1.32), (4.1.38) and (4.1.39) and the nondimensional initial geometric imperfection, \bar{w}_o , is given in Eq. (4.1.25). The functions of integration $F(X)$, $G(X)$, and $H(X)$ can be determined using the appropriate surface traction on one side of the laminate and enforcing interlaminar continuity of the stresses given in Eqs. (A.2.7) through (A.2.9). For the cylindrical shell under internal pressure, the appropriate boundary conditions on the innermost surface of the first lamina are

$$\tau_{xz} = \tau_{yz} = 0 \quad \text{and} \quad \sigma_{zz} = -p \quad (\text{A.2.17})$$

where p is the (positive) value of internal pressure. The functional form of $F(X)$, $G(X)$, and $H(X)$ can be determined easily since the solutions for τ_{xz} , τ_{yz} and σ_{zz} given in Eqs. (A.2.7) through (A.2.9) are separated in X and ξ_3 . The necessary calculations are straightforward but algebraically intensive; hence, they are omitted here for brevity. Since integration of Eqs. (A.2.4) through (A.2.6) through the entire laminate thickness must produce the shell equations used in section 4.1, the surface tractions on the exterior of the outermost surface of the outermost lamina must be zero. This provides a useful check on the calculations. The resulting interlaminar stresses can be written with respect to the material coordinate system using the following transformation equations

$$\tau_{13} = \tau_{xz} \cos \theta - \tau_{yz} \sin \theta \quad (\text{A.2.18})$$

$$\tau_{23} = \tau_{xz} \sin \theta + \tau_{yz} \cos \theta \quad (\text{A.2.19})$$

$$\sigma_{33} = \sigma_{zz} \quad (\text{A.2.20})$$

Appendix B

FORMULATION OF EQUILIBRIUM EQUATIONS GOVERNING THE RESPONSE OF A RING FLANGE AND ATTACHED SKIN AS A SYSTEM OF FIRST ORDER ORDINARY DIFFERENTIAL EQUATIONS

While the nondimensional equations governing the tangential equilibrium of the frame flange, Eqs. (4.4.38) and (4.4.39), and the tangential equilibrium of the attached skin, Eqs. (4.4.41) and (4.4.42), are of order two with respect to the nondimensional tangential displacements \bar{u}_1^o and \bar{u}_2^o , the equations governing the radial equilibrium, Eqs. (4.4.40) and (4.4.43), are of order three with respect to these quantities. The third order derivatives can be eliminated by first differentiating Eqs. (4.4.38) and (4.4.39) with respect to $\bar{\xi}_1$. This yields

$$\begin{aligned} \bar{B}_{11}^f \left(\frac{L}{t_s} \right) \frac{d^3 \bar{u}_1^{of}}{d\bar{\xi}_1^3} = & au_1^f \frac{d^4 \bar{u}_3^f}{d\bar{\xi}_1^4} + (au_2^f - au_3^f) \frac{d^2 \bar{u}_3^f}{d\bar{\xi}_1^2} - au_4^f \frac{d^2 \bar{u}_3^s}{d\bar{\xi}_1^2} \\ & - au_5^f \frac{d\bar{u}_1^f}{d\bar{\xi}_1} + au_5^f \frac{d\bar{u}_1^s}{d\bar{\xi}_1} + au_6^f \frac{d\bar{u}_2^f}{d\bar{\xi}_1} - au_6^f \frac{d\bar{u}_2^s}{d\bar{\xi}_1} \end{aligned} \quad (B.1)$$

and

$$\begin{aligned} \bar{B}_{16}^f \left(\frac{L}{t_s} \right) \frac{d^3 \bar{u}_2^{of}}{d\bar{\xi}_1^3} = & av_1^f \frac{d^4 \bar{u}_3^f}{d\bar{\xi}_1^4} + (av_2^f - av_3^f) \frac{d^2 \bar{u}_3^f}{d\bar{\xi}_1^2} - av_4^f \frac{d^2 \bar{u}_3^s}{d\bar{\xi}_1^2} \\ & - av_5^f \frac{d\bar{u}_1^f}{d\bar{\xi}_1} + av_5^f \frac{d\bar{u}_1^s}{d\bar{\xi}_1} + av_6^f \frac{d\bar{u}_2^f}{d\bar{\xi}_1} - av_6^f \frac{d\bar{u}_2^s}{d\bar{\xi}_1}. \end{aligned} \quad (B.2)$$

Differentiating Eqs. (4.4.41) and (4.4.42) with respect to $\bar{\xi}_1$ gives

$$\begin{aligned} \bar{B}_{11}^s \left(\frac{L}{t_s} \right) \frac{d^3 \bar{u}_1^{os}}{d\bar{\xi}_1^3} = & au_1^s \frac{d^4 \bar{u}_3^s}{d\bar{\xi}_1^4} + (au_2^s + au_4^s) \frac{d^2 \bar{u}_3^s}{d\bar{\xi}_1^2} + au_3^s \frac{d^2 \bar{u}_3^f}{d\bar{\xi}_1^2} \\ & + au_5^s \frac{d\bar{u}_1^f}{d\bar{\xi}_1} - au_5^s \frac{d\bar{u}_1^s}{d\bar{\xi}_1} - au_6^s \frac{d\bar{u}_2^f}{d\bar{\xi}_1} + au_6^s \frac{d\bar{u}_2^s}{d\bar{\xi}_1} \end{aligned} \quad (B.3)$$

and

$$\begin{aligned} \bar{B}_{16}^s \left(\frac{L}{t_s} \right) \frac{d^3 \bar{u}_2^{os}}{d\bar{\xi}_1^3} = & av_1^s \frac{d^4 \bar{u}_3^s}{d\bar{\xi}_1^4} + (av_2^s + av_4^s) \frac{d^2 \bar{u}_3^s}{d\bar{\xi}_1^2} + av_3^s \frac{d^2 \bar{u}_3^f}{d\bar{\xi}_1^2} \\ & + av_5^s \frac{d\bar{u}_1^f}{d\bar{\xi}_1} - av_5^s \frac{d\bar{u}_1^s}{d\bar{\xi}_1} - av_6^s \frac{d\bar{u}_2^f}{d\bar{\xi}_1} + av_6^s \frac{d\bar{u}_2^s}{d\bar{\xi}_1} \end{aligned} \quad (B.4)$$

where (see Eqs. (4.4.29) through (4.4.33))

$$\begin{aligned}
au_1^f &= \frac{\bar{B}_{11}^f(\bar{B}_{11}^f \bar{A}_{66}^f - \bar{B}_{61}^f \bar{A}_{16}^f)}{\bar{A}_{11}^f \bar{A}_{66}^f - \bar{A}_{16}^f \bar{A}_{16}^f} & au_1^s &= \frac{\bar{B}_{11}^s(\bar{B}_{11}^s \bar{A}_{66}^s - \bar{B}_{61}^s \bar{A}_{16}^s)}{\bar{A}_{11}^s \bar{A}_{66}^s - \bar{A}_{16}^s \bar{A}_{16}^s} \\
au_2^f &= (\bar{Z}_f) \frac{\bar{B}_{11}^f(\bar{A}_{26}^f \bar{A}_{16}^f - \bar{A}_{12}^f \bar{A}_{66}^f)}{\bar{A}_{11}^f \bar{A}_{66}^f - \bar{A}_{16}^f \bar{A}_{16}^f} & au_2^s &= (\bar{Z}_f) \frac{\bar{B}_{11}^s(\bar{A}_{26}^s \bar{A}_{16}^s - \bar{A}_{12}^s \bar{A}_{66}^s)}{\bar{A}_{11}^s \bar{A}_{66}^s - \bar{A}_{16}^s \bar{A}_{16}^s} \\
au_3^f &= \frac{\bar{B}_{11}^f \bar{K}_{Bf} \bar{A}_{66}^f}{\bar{A}_{11}^f \bar{A}_{66}^f - \bar{A}_{16}^f \bar{A}_{16}^f} & au_3^s &= \frac{\bar{B}_{11}^s \bar{K}_{Bf} \bar{A}_{66}^s}{\bar{A}_{11}^s \bar{A}_{66}^s - \bar{A}_{16}^s \bar{A}_{16}^s} \\
au_4^f &= \frac{\bar{B}_{11}^f \bar{K}_{Bs} \bar{A}_{66}^f}{\bar{A}_{11}^f \bar{A}_{66}^f - \bar{A}_{16}^f \bar{A}_{16}^f} & au_4^s &= \frac{\bar{B}_{11}^s \bar{K}_{Bs} \bar{A}_{66}^s}{\bar{A}_{11}^s \bar{A}_{66}^s - \bar{A}_{16}^s \bar{A}_{16}^s} \\
au_5^f &= \frac{\bar{B}_{11}^f \bar{C}_{13}^B \bar{A}_{66}^f}{\bar{A}_{11}^f \bar{A}_{66}^f - \bar{A}_{16}^f \bar{A}_{16}^f} & au_5^s &= \frac{\bar{B}_{11}^s \bar{C}_{13}^B \bar{A}_{66}^s}{\bar{A}_{11}^s \bar{A}_{66}^s - \bar{A}_{16}^s \bar{A}_{16}^s} \\
au_6^f &= \frac{\bar{B}_{11}^f \bar{C}_{13}^B \bar{A}_{16}^f}{\bar{A}_{11}^f \bar{A}_{66}^f - \bar{A}_{16}^f \bar{A}_{16}^f} & au_6^s &= \frac{\bar{B}_{11}^s \bar{C}_{13}^B \bar{A}_{16}^s}{\bar{A}_{11}^s \bar{A}_{66}^s - \bar{A}_{16}^s \bar{A}_{16}^s} \\
& & \bar{Z}_f &= \frac{L^2}{R_f t_s}
\end{aligned}$$

(B.5)

and

$$\begin{aligned}
av_1^f &= -\frac{\bar{B}_{16}^f(\bar{B}_{11}^f \bar{A}_{16}^f - \bar{B}_{61}^f \bar{A}_{11}^f)}{\bar{A}_{11}^f \bar{A}_{66}^f - \bar{A}_{16}^f \bar{A}_{16}^f} & av_1^s &= -\frac{\bar{B}_{16}^s(\bar{B}_{11}^s \bar{A}_{16}^s - \bar{B}_{61}^s \bar{A}_{11}^s)}{\bar{A}_{11}^s \bar{A}_{66}^s - \bar{A}_{16}^s \bar{A}_{16}^s} \\
av_2^f &= -\left(\frac{L^2}{R_f t_s}\right) \frac{\bar{B}_{16}^f(\bar{A}_{26}^f \bar{A}_{11}^f - \bar{A}_{12}^f \bar{A}_{16}^f)}{\bar{A}_{11}^f \bar{A}_{66}^f - \bar{A}_{16}^f \bar{A}_{16}^f} & av_2^s &= -\bar{Z} \frac{\bar{B}_{16}^s(\bar{A}_{26}^s \bar{A}_{11}^s - \bar{A}_{12}^s \bar{A}_{16}^s)}{\bar{A}_{11}^s \bar{A}_{66}^s - \bar{A}_{16}^s \bar{A}_{16}^s} \\
av_3^f &= -\frac{\bar{B}_{16}^f \bar{K}_{Bf} \bar{A}_{16}^f}{\bar{A}_{11}^f \bar{A}_{66}^f - \bar{A}_{16}^f \bar{A}_{16}^f} & av_3^s &= -\frac{\bar{B}_{16}^s \bar{K}_{Bf} \bar{A}_{16}^s}{\bar{A}_{11}^s \bar{A}_{66}^s - \bar{A}_{16}^s \bar{A}_{16}^s} \\
av_4^f &= -\frac{\bar{B}_{16}^f \bar{K}_{Bs} \bar{A}_{16}^f}{\bar{A}_{11}^f \bar{A}_{66}^f - \bar{A}_{16}^f \bar{A}_{16}^f} & av_4^s &= -\frac{\bar{B}_{16}^s \bar{K}_{Bs} \bar{A}_{16}^s}{\bar{A}_{11}^s \bar{A}_{66}^s - \bar{A}_{16}^s \bar{A}_{16}^s} \\
av_5^f &= -\frac{\bar{B}_{16}^f \bar{C}_{13}^B \bar{A}_{11}^f}{\bar{A}_{11}^f \bar{A}_{66}^f - \bar{A}_{16}^f \bar{A}_{16}^f} & av_5^s &= -\frac{\bar{B}_{16}^s \bar{C}_{13}^B \bar{A}_{16}^s}{\bar{A}_{11}^s \bar{A}_{66}^s - \bar{A}_{16}^s \bar{A}_{16}^s} \\
av_6^f &= -\frac{\bar{B}_{16}^f \bar{C}_{13}^B \bar{A}_{16}^f}{\bar{A}_{11}^f \bar{A}_{66}^f - \bar{A}_{16}^f \bar{A}_{16}^f} & av_6^s &= -\frac{\bar{B}_{16}^s \bar{C}_{13}^B \bar{A}_{11}^s}{\bar{A}_{11}^s \bar{A}_{66}^s - \bar{A}_{16}^s \bar{A}_{16}^s}
\end{aligned}$$

(B.6)

Now substituting Eqs. (B.1) through (B.6) into Eqs. (4.4.38) through (4.4.43) and collecting terms yields

$$e1_1^f \frac{d^2 \bar{u}_1^f}{d\bar{\xi}_1^2} + e1_2^f \frac{d^2 \bar{u}_2^f}{d\bar{\xi}_1^2} + e1_3^f \frac{d^3 \bar{u}_3^f}{d\bar{\xi}_1^3} + e1_4^f \frac{d\bar{u}_3^f}{d\bar{\xi}_1} + e1_5^f \bar{u}_1^f + e1_6^f \frac{d\bar{u}_3^f}{d\bar{\xi}_1} + e1_7^f \bar{u}_1^f = 0 \quad (B.7)$$

$$e2_1^f \frac{d^2 \bar{u}_1^f}{d\bar{\xi}_1^2} + e2_2^f \frac{d^2 \bar{u}_2^f}{d\bar{\xi}_1^2} + e2_3^f \frac{d^3 \bar{u}_3^f}{d\bar{\xi}_1^3} + e2_4^f \frac{d\bar{u}_3^f}{d\bar{\xi}_1} + e2_5^f \bar{u}_2^f + e2_6^f \bar{u}_2^f = 0 \quad (B.8)$$

$$\begin{aligned} & e3_1^f \frac{d^4 \bar{u}_3^f}{d\bar{\xi}_1^4} + e3_2^f \frac{d^2 \bar{u}_3^f}{d\bar{\xi}_1^2} + e3_3^f \bar{u}_3^f + e3_4^f \frac{d\bar{u}_1^f}{d\bar{\xi}_1} + e3_5^f \frac{d\bar{u}_2^f}{d\bar{\xi}_1} \\ & + e3_6^f \frac{d^2 \bar{u}_3^f}{d\bar{\xi}_1^2} + e3_7^f \bar{u}_3^f + e3_8^f \frac{d\bar{u}_1^f}{d\bar{\xi}_1} + e3_9^f \frac{d\bar{u}_2^f}{d\bar{\xi}_1} = -\bar{p} \end{aligned} \quad (B.9)$$

$$e1_1^s \frac{d^2 \bar{u}_1^s}{d\bar{\xi}_1^2} + e1_2^s \frac{d^2 \bar{u}_2^s}{d\bar{\xi}_1^2} + e1_3^s \frac{d^3 \bar{u}_3^s}{d\bar{\xi}_1^3} + e1_4^s \frac{d\bar{u}_3^s}{d\bar{\xi}_1} + e1_5^s \bar{u}_1^s + e1_6^s \frac{d\bar{u}_3^s}{d\bar{\xi}_1} + e1_7^s \bar{u}_1^f = 0 \quad (B.10)$$

$$e2_1^s \frac{d^2 \bar{u}_1^s}{d\bar{\xi}_1^2} + e2_2^s \frac{d^2 \bar{u}_2^s}{d\bar{\xi}_1^2} + e2_3^s \frac{d^3 \bar{u}_3^s}{d\bar{\xi}_1^3} + e2_4^s \frac{d\bar{u}_3^s}{d\bar{\xi}_1} + e2_5^s \bar{u}_2^s + e2_6^s \bar{u}_2^f = 0 \quad (B.11)$$

$$\begin{aligned} & e3_1^s \frac{d^4 \bar{u}_3^s}{d\bar{\xi}_1^4} + e3_2^s \frac{d^2 \bar{u}_3^s}{d\bar{\xi}_1^2} + e3_3^s \bar{u}_3^s + e3_4^s \frac{d\bar{u}_1^s}{d\bar{\xi}_1} + e3_5^s \frac{d\bar{u}_2^s}{d\bar{\xi}_1} \\ & + e3_6^s \frac{d^2 \bar{u}_3^f}{d\bar{\xi}_1^2} + e3_7^s \bar{u}_3^f + e3_8^s \frac{d\bar{u}_1^f}{d\bar{\xi}_1} + e3_9^s \frac{d\bar{u}_2^f}{d\bar{\xi}_1} = -\hat{N}_{11} \frac{d^2 \bar{w}_0}{d\bar{\xi}_1^2} \end{aligned} \quad (B.12)$$

where

$$\begin{aligned} e1_1^f &= \bar{A}_{11}^f \left(\frac{L}{t_s} \right) & e1_1^s &= \bar{A}_{11}^s \left(\frac{L}{t_s} \right) \\ e1_2^f &= \bar{A}_{16}^f \left(\frac{L}{t_s} \right) & e1_2^s &= \bar{A}_{16}^s \left(\frac{L}{t_s} \right) \\ e1_3^f &= -\bar{B}_{11}^f & e1_3^s &= -\bar{B}_{11}^s \\ e1_4^f &= \bar{A}_{12}^f \left(\frac{L^2}{R_f t_s} \right) + \bar{K}_{Bf} & e1_4^s &= \bar{A}_{12}^s \left(\frac{L^2}{R_s t_s} \right) - \bar{K}_{Bs} \\ e1_5^f &= \bar{C}_{13}^B & e1_5^s &= \bar{C}_{13}^B \\ e1_6^f &= \bar{K}_{Bs} & e1_6^s &= -\bar{K}_{Bf} \\ e1_7^f &= -\bar{C}_{13}^B & e1_7^s &= -\bar{C}_{13}^B \end{aligned} \quad (B.13)$$

$$\begin{aligned}
e2_1^f &= \overline{A}_{16}^f \left(\frac{L}{t_s} \right) & e2_1^s &= \overline{A}_{16}^s \left(\frac{L}{t_s} \right) \\
e2_2^f &= \overline{A}_{66}^f \left(\frac{L}{t_s} \right) & e2_2^s &= \overline{A}_{66}^s \left(\frac{L}{t_s} \right) \\
e2_3^f &= -\overline{B}_{61}^f & e2_3^s &= -\overline{B}_{61}^s \\
e2_4^f &= \overline{A}_{26}^f \left(\frac{L^2}{R_f t_s} \right) & e2_4^s &= \overline{A}_{26}^s \left(\frac{L^2}{R_s t_s} \right) \\
e2_5^f &= \overline{C}_{13}^B & e2_5^s &= \overline{C}_{13}^B \\
e2_6^f &= -\overline{C}_{13}^B & e2_6^s &= -\overline{C}_{13}^B
\end{aligned}$$

(B.14)

$$\begin{aligned}
e3_1^f &= -\overline{D}_{11}^f + au_1^f + av_1^f \\
e3_2^f &= \left(\overline{B}_{12}^f + \overline{B}_{12}^f \right) \left(\frac{L^2}{R_f t_s} \right) + au_2^f - au_3^f + av_2^f - av_3^f \\
e3_3^f &= -\overline{A}_{22}^f \left(\frac{L^2}{R_f t_s} \right)^2 + \overline{C}_{33}^B \\
e3_4^f &= -\overline{A}_{12}^f \left(\frac{L^3}{R_f t_s^2} \right) - au_5^f - av_5^f \\
e3_5^f &= -\overline{A}_{26}^f \left(\frac{L^3}{R_f t_s^2} \right) + au_6^f + av_6^f \\
e3_6^f &= -au_4^f - av_4^f \\
e3_7^f &= -\overline{C}_{33}^B \\
e3_8^f &= au_5^f + av_5^f \\
e3_9^f &= -au_6^f - av_6^f
\end{aligned}$$

(B.15)

$$\begin{aligned}
e3_1^s &= -\overline{D}_{11}^s + au_1^s + av_1^s \\
e3_2^s &= \left(\overline{B}_{12}^s + \overline{B}_{12}^s \right) \left(\frac{L^2}{R_s t_s} \right) + \widehat{N}_{11} + au_2^s + au_4^s + av_2^s + av_4^s \\
e3_3^s &= -\overline{A}_{22}^s \left(\frac{L^2}{R_s t_s} \right)^2 + \overline{C}_{33}^B \\
e3_4^s &= -\overline{A}_{12}^s \left(\frac{L^3}{R_s t_s^2} \right) - au_5^s - av_5^s
\end{aligned}$$

$$\begin{aligned}
e3_5^s &= -\overline{A}_{26}^s \left(\frac{L^3}{R_s t_s^2} \right) + au_6^s + av_6^s \\
e3_6^s &= au_3^s + av_3^s \\
e3_7^s &= -\overline{C}_{33}^B \\
e3_8^s &= au_5^s + av_5^s \\
e3_9^s &= -au_6^s - av_6^s.
\end{aligned} \tag{B.16}$$

After eliminating the second terms in Eqs. (4.4.38) and (4.4.41) and the first terms in Eqs. (4.4.39) and (4.4.42) and dividing each of the resulting set of six equations through by the coefficient of the highest order derivative appearing in each equation, the system can be cast in the desired form (Eq. (4.4.45)) where

$$\{U\} = \begin{Bmatrix} \overline{u}_1^{of} \\ (\overline{u}_1^{of})' \\ \overline{u}_2^{of} \\ (\overline{u}_2^{of})' \\ \overline{u}_3^{of} \\ (\overline{u}_3^{of})' \\ (\overline{u}_3^{of})'' \\ (\overline{u}_3^{of})''' \\ \overline{u}_1^{os} \\ (\overline{u}_1^{os})' \\ \overline{u}_2^{os} \\ (\overline{u}_2^{os})' \\ \overline{u}_3^{os} \\ (\overline{u}_3^{os})' \\ (\overline{u}_3^{os})'' \\ (\overline{u}_3^{os})''' \end{Bmatrix} \tag{B.17}$$

and ' indicates differentiation with respect to $\bar{\xi}_1$. The resulting nonzero terms of the

16-by-16 matrix $[B]$ are

$$B_{1,2} = 1.0$$

$$B_{2,1} = -\frac{e1_5^f e2_2^f}{e1_1^f e2_2^f - e1_2^f e2_1^f}$$

$$B_{2,3} = -\frac{e2_5^f e1_2^f}{e1_1^f e2_2^f - e1_2^f e2_1^f}$$

$$B_{2,6} = -\frac{e1_4^f e2_2^f - e2_4^f e1_2^f}{e1_1^f e2_2^f - e1_2^f e2_1^f}$$

$$B_{2,8} = -\frac{e1_3^f e2_2^f - e2_3^f e1_2^f}{e1_1^f e2_2^f - e1_2^f e2_1^f}$$

$$B_{2,9} = -\frac{e1_7^f e2_2^f}{e1_1^f e2_2^f - e1_2^f e2_1^f}$$

$$B_{2,11} = -\frac{e2_6^f e1_2^f}{e1_1^f e2_2^f - e1_2^f e2_1^f}$$

$$B_{2,14} = -\frac{e1_6^f e2_2^f}{e1_1^f e2_2^f - e1_2^f e2_1^f}$$

$$B_{3,4} = 1.0$$

$$B_{4,1} = -\frac{e1_5^f e2_1^f}{e1_1^f e2_2^f - e1_2^f e2_1^f}$$

$$B_{4,3} = -\frac{e2_5^f e1_1^f}{e1_1^f e2_2^f - e1_2^f e2_1^f}$$

$$B_{4,6} = -\frac{e1_1^f e2_4^f - e1_4^f e2_1^f}{e1_1^f e2_2^f - e1_2^f e2_1^f}$$

$$B_{4,8} = -\frac{e1_1^f e2_3^f - e2_1^f e1_3^f}{e1_1^f e2_2^f - e1_2^f e2_1^f}$$

$$B_{4,9} = -\frac{e1_7^f e2_1^f}{e1_1^f e2_2^f - e1_2^f e2_1^f}$$

$$B_{4,11} = -\frac{e2_6^f e1_1^f}{e1_1^f e2_2^f - e1_2^f e2_1^f}$$

$$B_{4,14} = -\frac{e1_6^f e2_1^f}{e1_1^f e2_2^f - e1_2^f e2_1^f}$$

$$B_{5,6} = 1.0$$

$$B_{6,7} = 1.0$$

$$B_{7,8} = 1.0$$

$$B_{8,2} = -\frac{e3_4^f}{e3_1^f}$$

$$B_{8,4} = -\frac{e3_5^f}{e3_1^f}$$

$$B_{8,5} = -\frac{e3_3^f}{e3_1^f}$$

$$B_{8,7} = -\frac{e3_2^f}{e3_1^f}$$

$$B_{8,10} = -\frac{e3_8^f}{e3_1^f}$$

$$B_{8,12} = -\frac{e3_9^f}{e3_1^f}$$

$$B_{8,13} = -\frac{e3_2^f}{e3_1^f}$$

$$B_{8,15} = -\frac{e3_6^f}{e3_1^f}$$

$$\begin{aligned}
B_{9,10} &= 1.0 \\
B_{10,9} &= -\frac{e1_5^s e2_2^s}{e1_1^s e2_2^s - e1_2^s e2_1^s} \\
B_{10,11} &= -\frac{e2_5^s e1_2^s}{e1_1^s e2_2^s - e1_2^s e2_1^s} \\
B_{10,14} &= -\frac{e1_4^s e2_2^s - e2_4^s e1_2^s}{e1_1^s e2_2^s - e1_2^s e2_1^s} \\
B_{10,16} &= -\frac{e1_3^s e2_2^s - e2_3^s e1_2^s}{e1_1^s e2_2^s - e1_2^s e2_1^s} \\
B_{10,1} &= -\frac{e1_7^s e2_2^s}{e1_1^s e2_2^s - e1_2^s e2_1^s} \\
B_{10,3} &= -\frac{e2_6^s e1_2^s}{e1_1^s e2_2^s - e1_2^s e2_1^s} \\
B_{10,6} &= -\frac{e1_8^s e2_2^s}{e1_1^s e2_2^s - e1_2^s e2_1^s} \\
B_{11,12} &= 1.0 \\
B_{12,9} &= -\frac{e1_5^s e2_1^s}{e1_1^s e2_2^s - e1_2^s e2_1^s} \\
B_{12,11} &= -\frac{e2_5^s e1_1^s}{e1_1^s e2_2^s - e1_2^s e2_1^s} \\
B_{12,14} &= -\frac{e1_1^s e2_4^s - e1_4^s e2_1^s}{e1_1^s e2_2^s - e1_2^s e2_1^s} \\
B_{12,16} &= -\frac{e1_1^s e2_3^s - e2_1^s e1_3^s}{e1_1^s e2_2^s - e1_2^s e2_1^s} \\
B_{12,1} &= -\frac{e1_7^s e2_1^s}{e1_1^s e2_2^s - e1_2^s e2_1^s} \\
B_{12,13} &= -\frac{e2_6^s e1_1^s}{e1_1^s e2_2^s - e1_2^s e2_1^s} \\
B_{12,16} &= -\frac{e1_8^s e2_1^s}{e1_1^s e2_2^s - e1_2^s e2_1^s} \\
B_{13,14} &= 1.0 \\
B_{14,15} &= 1.0 \\
B_{15,16} &= 1.0 \\
B_{16,10} &= -\frac{e3_4^s}{e3_1^s} \\
B_{16,12} &= -\frac{e3_5^s}{e3_1^s} \\
B_{16,13} &= -\frac{e3_3^s}{e3_1^s} \\
B_{16,15} &= -\frac{e3_2^s}{e3_1^s} \\
B_{16,2} &= -\frac{e3_8^s}{e3_1^s} \\
B_{16,4} &= -\frac{e3_9^s}{e3_1^s} \\
B_{16,5} &= -\frac{e3_2^s}{e3_1^s} \\
B_{16,7} &= -\frac{e3_6^s}{e3_1^s}
\end{aligned} \tag{B.18}$$

Finally, neglecting the presence of any initial geometric imperfection, the only nonzero term of the vector $\{F\}$ is

$$F_{8,1} = -\frac{\bar{P}}{e3_1^s} \tag{B.19}$$

Appendix C

ELEMENT STIFFNESS AND GEOMETRIC STIFFNESS MATRICES FOR A CYLINDRICAL SHELL FINITE ELEMENT

As described in section 2 of Chapter 5, the finite element model of the second variation of the nondimensional total potential energy for the cylindrical shell finite element can be written as

$$\delta^2 \bar{\Pi}^e = \frac{\pi R}{L} \{W^e\}^T [K^e] \{W^e\} + \frac{\pi R}{L} \{W^e\}^T [K_G^e] \{W^e\} + \delta^2 \bar{\Pi}_{load}^e \quad (C.1)$$

where $\delta^2 \bar{\Pi}_{load}^e$ is the second variation of the nondimensional total potential energy of the loads applied to the boundaries ($\bar{\xi} = \bar{\xi}^e$) and ($\bar{\xi} = \bar{\xi}^{e+1}$) and $\{W^e\}$ is the vector of nondimensional element nodal buckling displacements and rotations (see Eq. (5.2.49)) where

$$\{W^e\} = \{ \{U1\} \quad \{V1\} \quad \{W1\} \quad \{U2\} \quad \{V2\} \quad \{W2\} \}^T. \quad (C.2)$$

$[K^e]$ is the element stiffness matrix given by

$$[K^e] = \int_{\bar{\xi}_1^e}^{\bar{\xi}_1^{e+1}} [B1]^T [C] [B1] d\bar{\xi}_1 \quad (C.3)$$

where

$$[B1] = \begin{bmatrix} \frac{d}{d\bar{\xi}_1} \{\Phi_1\}^T & \{0\}^T & \{0\}^T & \{0\}^T & \{0\}^T & \{0\}^T \\ \{0\}^T & \{0\}^T & \bar{Z}\{\Omega_1\}^T & \{0\}^T & -\beta\{\Psi_2\}^T & \{0\}^T \\ \{0\}^T & \frac{d}{d\bar{\xi}_1} \{\Psi_1\}^T & -\beta\{\Phi_2\}^T & \{0\}^T & \{0\}^T & \{0\}^T \\ \{0\}^T & \{0\}^T & -\frac{d^2}{d\bar{\xi}_1^2} \{\Omega_1\}^T & \{0\}^T & \{0\}^T & \{0\}^T \\ \{0\}^T & \{0\}^T & \beta^2 \{\Omega_1\}^T & \{0\}^T & \{0\}^T & \{0\}^T \\ \{0\}^T & \{0\}^T & \{0\}^T & \{0\}^T & \{0\}^T & 2\beta \frac{d}{d\bar{\xi}_1} \{\Omega_2\}^T \\ \{0\}^T & \{0\}^T & \{0\}^T & \frac{d}{d\bar{\xi}_1} \{\Phi_2\}^T & \{0\}^T & \{0\}^T \\ \{0\}^T & \beta\{\Psi_1\}^T & \{0\}^T & \{0\}^T & \{0\}^T & \bar{Z}\{\Omega_2\}^T \\ \beta\{\Phi_1\}^T & \{0\}^T & \{0\}^T & \{0\}^T & \frac{d}{d\bar{\xi}_1} \{\Psi_2\}^T & \{0\}^T \\ \{0\}^T & \{0\}^T & \{0\}^T & \{0\}^T & \{0\}^T & -\frac{d^2}{d\bar{\xi}_1^2} \{\Omega_2\}^T \\ \{0\}^T & \{0\}^T & \{0\}^T & \{0\}^T & \{0\}^T & \beta^2 \{\Omega_2\}^T \\ \{0\}^T & \{0\}^T & -2\beta \frac{d}{d\bar{\xi}_1} \{\Omega_1\}^T & \{0\}^T & \{0\}^T & \{0\}^T \end{bmatrix} \quad (C.4)$$

and $\{\Phi_1\}$, $\{\Phi_2\}$, $\{\Psi_1\}$, $\{\Psi_2\}$, $\{\Omega_1\}$ and $\{\Omega_2\}$ are the interpolation functions given in Eq. (5.2.49), β is given in Eq. (5.2.44), $\bar{Z} = L^2/(Rt_s)$ where L is the length, R is the radius to the middle surface, and t_s is the total thickness of the cylindrical shell.

The matrix $[C]$ is

$$[C] = \begin{bmatrix} [c] & [0] \\ [0] & [c] \end{bmatrix}. \quad (C.5)$$

where $[c]$ is given in Eq. (5.2.39). $[K_G^e]$ is the elemental geometric stiffness matrix given by

$$[K_G^e] = \sum_{j=1}^4 [K_G^j] \quad (C.6)$$

where

$$[K_G^1] = \begin{bmatrix} [0] & [0] & [0] & [0] & [0] & [0] \\ [0] & [0] & [0] & [0] & [0] & [0] \\ [0] & [0] & [K_G^{11}] & [0] & [0] & [K_G^{12}] \\ [0] & [0] & [0] & [0] & [0] & [0] \\ [0] & [0] & [0] & [0] & [0] & [0] \\ [0] & [0] & [K_G^{12}]^T & [0] & [0] & [K_G^{22}] \end{bmatrix} \quad (C.7)$$

$$[K_G^{11}] = \int_{\bar{\xi}_1^*}^{\bar{\xi}_1^{*+1}} \left[\bar{N}_{11} \left\{ \frac{d\Omega_1}{d\bar{\xi}_1} \right\} \left\{ \frac{d\Omega_1}{d\bar{\xi}_1} \right\}^T + \bar{N}_{22} \beta^2 \{\Omega_1\} \{\Omega_1\}^T \right] d\bar{\xi}_1 \quad (C.8)$$

$$[K_G^{12}] = \int_{\bar{\xi}_1^*}^{\bar{\xi}_1^{*+1}} \bar{N}_{12} \beta \left[\left\{ \frac{d\Omega_2}{d\bar{\xi}_1} \right\} \{\Omega_1\}^T - \left\{ \frac{d\Omega_1}{d\bar{\xi}_1} \right\} \{\Omega_2\}^T \right] d\bar{\xi}_1 \quad (C.9)$$

$$[K_G^{22}] = \int_{\bar{\xi}_1^*}^{\bar{\xi}_1^{*+1}} \left[\bar{N}_{11} \left\{ \frac{d\Omega_2}{d\bar{\xi}_1} \right\} \left\{ \frac{d\Omega_2}{d\bar{\xi}_1} \right\}^T + \bar{N}_{22} \beta^2 \{\Omega_2\} \{\Omega_2\}^T \right] d\bar{\xi}_1 \quad (C.10)$$

and

$$[K_G^2] = \int_{\bar{\xi}_1^*}^{\bar{\xi}_1^{*+1}} [B2]^T [C] [B1] d\bar{\xi}_1 \quad (C.11)$$

$$[K_G^3] = \int_{\bar{\xi}_1^*}^{\bar{\xi}_1^{*+1}} [B1]^T [C] [B2] d\bar{\xi}_1 \quad (C.12)$$

$$[K_G^4] = \int_{\bar{\xi}_1^*}^{\bar{\xi}_1^{*+1}} [B2]^T [C] [B2] d\bar{\xi}_1 \quad (C.13)$$

where \bar{N}_{11} and \bar{N}_{12} are the applied nondimensional axial and torsional loads and \bar{N}_{22} is the prebuckling nondimensional hoop stress resultant. $[B2]$ is given by

$$[B2] = \begin{bmatrix} \{0\}^T \{0\}^T \left[\frac{d\bar{u}_3^0}{d\xi_1} + \frac{d\bar{w}_0}{d\xi_1} \right] \frac{d}{d\xi_1} \{\Omega_1\}^T \{0\}^T \{0\}^T & \{0\}^T \\ \{0\}^T \{0\}^T & \{0\}^T \{0\}^T \{0\}^T \\ \{0\}^T \{0\}^T & \{0\}^T \{0\}^T - \left[\frac{d\bar{u}_3^0}{d\xi_1} + \frac{d\bar{w}_0}{d\xi_1} \right] \beta \{\Omega_2\}^T \\ \{0\}^T \{0\}^T & \{0\}^T \{0\}^T \{0\}^T \\ \{0\}^T \{0\}^T & \{0\}^T \{0\}^T \{0\}^T \\ \{0\}^T \{0\}^T & \{0\}^T \{0\}^T \{0\}^T \\ \{0\}^T \{0\}^T & \{0\}^T \{0\}^T \left[\frac{d\bar{u}_3^0}{d\xi_1} + \frac{d\bar{w}_0}{d\xi_1} \right] \frac{d}{d\xi_1} \{\Omega_2\}^T \\ \{0\}^T \{0\}^T & \{0\}^T \{0\}^T \{0\}^T \\ \{0\}^T \{0\}^T \left[\frac{d\bar{u}_3^0}{d\xi_1} + \frac{d\bar{w}_0}{d\xi_1} \right] \beta \{\Omega_1\}^T & \{0\}^T \{0\}^T \{0\}^T \\ \{0\}^T \{0\}^T & \{0\}^T \{0\}^T \{0\}^T \\ \{0\}^T \{0\}^T & \{0\}^T \{0\}^T \{0\}^T \\ \{0\}^T \{0\}^T & \{0\}^T \{0\}^T \{0\}^T \end{bmatrix} \quad (C.14)$$

where \bar{u}_3^0 is the nondimensional prebuckling radial displacement and \bar{w}_0 is the nondimensional initial geometric imperfection given in Eq. (4.1.25). Note that $[K^e]$ and $[K_G^e]$ are symmetric and $[K^e]$ is positive definite. The dimension of these matrices depends upon the type of interpolation used for \bar{U}_1 , \bar{U}_2 , \bar{V}_1 and \bar{V}_2 ; it is 16-by-16 for Lagrange linear interpolations, 20-by-20 for Lagrange quadratic interpolations and 24-by-24 for Lagrange cubic interpolations.

Appendix D

ELEMENT STIFFNESS AND GEOMETRIC STIFFNESS MATRICES FOR
AN ANNULAR PLATE FINITE ELEMENT

As described in section 3 of chapter 5, the finite element model of the second variation of the nondimensional total potential energy for the annular plate finite element can be written as

$$\delta^2 \bar{\Pi}^e = \frac{\pi R}{L} \{W^e\}^T [K^e] \{W^e\} + \frac{\pi R}{L} \{W^e\}^T [K_G^e] \{W^e\} + \delta^2 \bar{\Pi}_{load}^e \quad (D.1)$$

where $\delta^2 \bar{\Pi}_{load}^e$ is the second variation of the nondimensional total potential energy of the loads applied to the boundaries ($\bar{\xi} = \bar{\xi}^e$) and ($\bar{\xi} = \bar{\xi}^{e+1}$) and $\{W^e\}$ is the vector of nondimensional element nodal buckling displacements and rotations (see Eq. (5.3.24)) where

$$\{W^e\} = \{ \{UW1\} \quad \{VW1\} \quad \{WW1\} \quad \{UW2\} \quad \{VW2\} \quad \{WW2\} \}^T. \quad (D.2)$$

$[K^e]$ is the element stiffness matrix given by

$$[K^e] = \int_{\bar{\xi}_1^e}^{\bar{\xi}_1^{e+1}} [B1]^T [C] [B1] \left(1 - \frac{L}{R} \bar{\xi}_1\right) d\bar{\xi}_1 \quad (D.3)$$

where

$$[B1] = [[B1A][B1B]] \quad (D.4)$$

$$[B1A] = \begin{bmatrix} \frac{d}{d\xi_1}\{\Phi_1\}^T & \{0\}^T & \{0\}^T \\ -L\{\Phi_1\}^T/R\bar{s} & \{0\}^T & \{0\}^T \\ \{0\}^T & \frac{d}{d\xi_1}\{\Psi_1\}^T + L\{\Psi_1\}^T/R\bar{s} & \{0\}^T \\ \{0\}^T & \{0\}^T & -\frac{d^2}{d\xi_1^2}\{\Omega_1\}^T \\ \{0\}^T & \{0\}^T & \{B1A\}_{5,3} \\ \{0\}^T & \{0\}^T & \{0\}^T \\ \{0\}^T & \{0\}^T & \{0\}^T \\ \{0\}^T & \beta\{\Psi_1\}^T/\bar{s} & \{0\}^T \\ \beta\{\Phi_1\}^T/\bar{s} & \{0\}^T & \{0\}^T \\ \{0\}^T & \{0\}^T & \{0\}^T \\ \{0\}^T & \{0\}^T & \{0\}^T \\ \{0\}^T & \{0\}^T & \{B1A\}_{12,3} \end{bmatrix} \quad (D.5)$$

$$[B1B] = \begin{bmatrix} \{0\}^T & \{0\}^T & \{0\}^T \\ \{0\}^T & -\beta\{\Psi_2\}^T/\bar{s} & \{0\}^T \\ -\beta\{\Phi_2\}^T/\bar{s} & \{0\}^T & \{0\}^T \\ \{0\}^T & \{0\}^T & \{0\}^T \\ \{0\}^T & \{0\}^T & \{0\}^T \\ \{0\}^T & \{0\}^T & \{B1B\}_{6,3} \\ \frac{d}{d\xi_1}\{\Phi_2\}^T & \{0\}^T & \{0\}^T \\ -L\{\Phi_2\}^T/R\bar{s} & \{0\}^T & \{0\}^T \\ \{0\}^T & \frac{d}{d\xi_1}\{\Psi_2\}^T + L\{\Psi_2\}^T/R\bar{s} & \{0\}^T \\ \{0\}^T & \{0\}^T & -\frac{d^2}{d\xi_1^2}\{\Omega_2\}^T \\ \{0\}^T & \{0\}^T & \{B1B\}_{11,3} \\ \{0\}^T & \{0\}^T & \{0\}^T \end{bmatrix} \quad (D.6)$$

$$\bar{s} = 1 - \frac{L}{R} \bar{\xi}_1 \quad (D.7)$$

$$\{B1A\}_{5,3} = \frac{\beta^2}{\bar{s}^2} \{\Omega_1\}^T + \frac{L}{R\bar{s}} \left\{ \frac{d\Omega_1}{d\bar{\xi}_1} \right\}^T \quad (D.8)$$

$$\{B1A\}_{12,3} = \frac{-2\beta L}{R\bar{s}^2} \{\Omega_1\}^T - \frac{2\beta}{\bar{s}} \left\{ \frac{d\Omega_1}{d\bar{\xi}_1} \right\}^T \quad (D.9)$$

$$\{B1B\}_{6,3} = \frac{2\beta L}{R\bar{s}^2} \{\Omega_2\}^T + \frac{2\beta}{\bar{s}} \left\{ \frac{d\Omega_2}{d\bar{\xi}_1} \right\}^T \quad (D.10)$$

$$\{B1B\}_{11,3} = \frac{\beta^2}{\bar{s}^2} \{\Omega_2\}^T + \frac{L}{R\bar{s}} \left\{ \frac{d\Omega_2}{d\bar{\xi}_1} \right\}^T \quad (D.11)$$

and $\{\Phi_1\}$, $\{\Phi_2\}$, $\{\Psi_1\}$, $\{\Psi_2\}$, $\{\Omega_1\}$ and $\{\Omega_2\}$ are the interpolation functions given in Eq. (5.3.24), β is given in Eq. (5.3.23), L is the length and R is the radius of the middle surface of the cylindrical shell. The matrix $[C]$ is

$$[C] = \begin{bmatrix} [c] & [0] \\ [0] & [c] \end{bmatrix}. \quad (D.12)$$

where $[c]$ is given in Eq. (5.3.19). $[K_G^e]$ is the elemental geometric stiffness matrix given by

$$[K_G^e] = \sum_{j=1}^4 [K_G^j] \quad (D.13)$$

where

$$[K_G^1] = \begin{bmatrix} [K_G^{11}] & [0] & [0] & [0] & [K_G^{15}] & [0] \\ [0] & [K_G^{22}] & [0] & [K_G^{24}] & [0] & [0] \\ [0] & [0] & [K_G^{33}] & [0] & [0] & [K_G^{36}] \\ [0] & [K_G^{24}]^T & [0] & [K_G^{44}] & [0] & [0] \\ [K_G^{15}]^T & [0] & [0] & [0] & [K_G^{55}] & [0] \\ [0] & [0] & [K_G^{36}]^T & [0] & [0] & [K_G^{66}] \end{bmatrix} \quad (D.14)$$

$$[K_G^{11}] = \int_{\bar{\xi}_1}^{\bar{\xi}_1^{+1}} \left[N_{22} \frac{\beta^2}{\bar{s}} \{\Phi_1\} \{\Phi_1\}^T \right] (\bar{s}) d\bar{\xi}_1 \quad (D.15)$$

$$[K_G^{15}] = \int_{\bar{\xi}_1^*}^{\bar{\xi}_1^{*+1}} \left[\bar{N}_{22} \frac{\beta}{\bar{s}^2} \left(\frac{L}{R} \right) \{\Phi_1\} \{\Psi_2\}^T \right] (\bar{s}) d\bar{\xi}_1 \quad (D.16)$$

$$[K_G^{22}] = \int_{\bar{\xi}_1^*}^{\bar{\xi}_1^{*+1}} \left[\bar{N}_{22} \frac{1}{\bar{s}^2} \left(\frac{L}{R} \right)^2 \{\Psi_1\} \{\Psi_1\}^T \right] (\bar{s}) d\bar{\xi}_1 \quad (D.17)$$

$$[K_G^{24}] = \int_{\bar{\xi}_1^*}^{\bar{\xi}_1^{*+1}} \left[-\bar{N}_{22} \frac{\beta}{\bar{s}^2} \left(\frac{L}{R} \right) \{\Phi_2\} \{\Psi_1\}^T \right] (\bar{s}) d\bar{\xi}_1 \quad (D.18)$$

$$[K_G^{33}] = \int_{\bar{\xi}_1^*}^{\bar{\xi}_1^{*+1}} \left[\bar{N}_{11} \left\{ \frac{d\Omega_1}{d\bar{\xi}_1} \right\} \left\{ \frac{d\Omega_1}{d\bar{\xi}_1} \right\}^T + \bar{N}_{22} \frac{\beta^2}{\bar{s}^2} \{\Omega_1\} \{\Omega_1\}^T \right] (\bar{s}) d\bar{\xi}_1 \quad (D.19)$$

$$[K_G^{36}] = \int_{\bar{\xi}_1^*}^{\bar{\xi}_1^{*+1}} \bar{N}_{12} \frac{\beta}{\bar{s}} \left[\left\{ \frac{d\Omega_2}{d\bar{\xi}_1} \right\} \{\Omega_1\}^T - \left\{ \frac{d\Omega_1}{d\bar{\xi}_1} \right\} \{\Omega_2\}^T \right] d\bar{\xi}_1 \quad (D.20)$$

$$[K_G^{44}] = \int_{\bar{\xi}_1^*}^{\bar{\xi}_1^{*+1}} \left[\bar{N}_{22} \frac{\beta^2}{\bar{s}^2} \{\Phi_2\} \{\Phi_2\}^T \right] (\bar{s}) d\bar{\xi}_1 \quad (D.21)$$

$$[K_G^{55}] = \int_{\bar{\xi}_1^*}^{\bar{\xi}_1^{*+1}} \left[\bar{N}_{22} \frac{1}{\bar{s}^2} \left(\frac{L}{R} \right)^2 \{\Psi_2\} \{\Psi_2\}^T \right] (\bar{s}) d\bar{\xi}_1 \quad (D.22)$$

$$[K_G^{66}] = \int_{\bar{\xi}_1^*}^{\bar{\xi}_1^{*+1}} \left[\bar{N}_{11} \left\{ \frac{d\Omega_2}{d\bar{\xi}_1} \right\} \left\{ \frac{d\Omega_2}{d\bar{\xi}_1} \right\}^T + \bar{N}_{22} \frac{\beta^2}{\bar{s}^2} \{\Omega_2\} \{\Omega_2\}^T \right] (\bar{s}) d\bar{\xi}_1 \quad (D.23)$$

$$[K_G^2] = \int_{\bar{\xi}_1}^{\bar{\xi}_1^{*+1}} [B2]^T [C] [B1](\bar{s}) d\bar{\xi}_1 \quad (D.24)$$

$$[K_G^3] = \int_{\bar{\xi}_1}^{\bar{\xi}_1^{*+1}} [B1]^T [C] [B2](\bar{s}) d\bar{\xi}_1 \quad (D.25)$$

$$[K_G^4] = \int_{\bar{\xi}_1}^{\bar{\xi}_1^{*+1}} [B2]^T [C] [B2](\bar{s}) d\bar{\xi}_1 \quad (D.26)$$

where \bar{N}_{11} and \bar{N}_{22} are the nondimensional radial and circumferential prebuckling stress resultants. $[B2]$ is given by

$$[B2] = \begin{bmatrix} \{0\}^T & \{0\}^T & (\frac{d\bar{u}_3}{d\bar{\xi}_1}) \frac{d}{d\bar{\xi}_1} \{\Omega_1\}^T & \{0\}^T & \{0\}^T & \{0\}^T \\ \{0\}^T & \{0\}^T & \{0\}^T & \{0\}^T & \{0\}^T & \{0\}^T \\ \{0\}^T & \{0\}^T & \{0\}^T & \{0\}^T & \{0\}^T & -\frac{\rho}{s} (\frac{d\bar{u}_3}{d\bar{\xi}_1}) \{\Omega_2\}^T \\ \{0\}^T & \{0\}^T & \{0\}^T & \{0\}^T & \{0\}^T & \{0\}^T \\ \{0\}^T & \{0\}^T & \{0\}^T & \{0\}^T & \{0\}^T & \{0\}^T \\ \{0\}^T & \{0\}^T & \{0\}^T & \{0\}^T & \{0\}^T & \{0\}^T \\ \{0\}^T & \{0\}^T & \{0\}^T & \{0\}^T & \{0\}^T & (\frac{d\bar{u}_3}{d\bar{\xi}_1}) \frac{d}{d\bar{\xi}_1} \{\Omega_2\}^T \\ \{0\}^T & \{0\}^T & \{0\}^T & \{0\}^T & \{0\}^T & \{0\}^T \\ \{0\}^T & \{0\}^T & \frac{\rho}{s} (\frac{d\bar{u}_3}{d\bar{\xi}_1}) \{\Omega_1\}^T & \{0\}^T & \{0\}^T & \{0\}^T \\ \{0\}^T & \{0\}^T & \{0\}^T & \{0\}^T & \{0\}^T & \{0\}^T \\ \{0\}^T & \{0\}^T & \{0\}^T & \{0\}^T & \{0\}^T & \{0\}^T \\ \{0\}^T & \{0\}^T & \{0\}^T & \{0\}^T & \{0\}^T & \{0\}^T \end{bmatrix} \quad (D.27)$$

where \bar{u}_3^0 is the nondimensional prebuckling out-of-plane displacement. $[K^e]$ and $[K_G^e]$ are symmetric and $[K^e]$ is positive definite. The dimension of these matrices depends

upon the type of interpolation used for \overline{UW}_1 , \overline{UW}_2 , \overline{VW}_1 and \overline{VW}_2 ; it is 16-by-16 for Lagrange linear interpolations, 20-by-20 for Lagrange quadratic interpolations and 24-by-24 for Lagrange cubic interpolations.

Appendix E

LDL^T DECOMPOSITION OF A SYMMETRIC MATRIX

For the symmetric matrix $[M]$ there exists a factorization of $[M]$

$$[M] = [L][D][L]^T \quad (E.1)$$

where $[L]$ is a lower triangular matrix with all diagonal terms equal to 1.0 and $[D]$ is a diagonal matrix. If M_{ij} is an element of $[M]$ then from Eq. (E.1)

$$M_{ij} = \sum_{k=1}^j l_{ik} d_k l_{jk} \quad (E.2)$$

where l_{ij} is the ij th term of the $[L]$ matrix and d_k is the k th diagonal term of the $[D]$ matrix. Eq. (E.2) can be rewritten as

$$M_{ij} = l_{ij} d_j l_{jj} + \sum_{k=1}^{j-1} l_{ik} d_k l_{jk} \quad (E.3)$$

but,

$$l_{jj} = 1.0 \quad (E.4)$$

hence,

$$l_{ij} = \frac{M_{ij} - \sum_{k=1}^{j-1} l_{ik} d_k l_{jk}}{d_j}. \quad (E.5)$$

Setting $j = i$ in Eq. (E.3) yields

$$M_{ii} = l_{ii} d_i l_{ii} + \sum_{k=1}^{i-1} l_{ik} d_k l_{ik} \quad (E.6)$$

thus, using Eq. (E.4) with $j = i$,

$$d_i = M_{ii} - \sum_{k=1}^{i-1} l_{ik} d_k l_{ik}. \quad (E.7)$$

Now let

$$\tilde{M}_{ik} = l_{ik} d_k. \quad (E.8)$$

Substituting Eq. (E.8) into Eq. (E.7) produces

$$d_i = M_{ii} - \sum_{k=1}^{i-1} \tilde{M}_{ik} l_{ik}. \quad (E.9)$$

Substituting Eqs. (E.4) and (E.8) into Eq. (E.3) and solving for \tilde{M}_{ij} yields

$$\tilde{M}_{ij} = M_{ij} - \sum_{k=1}^{i-1} \tilde{M}_{ik} l_{ik}. \quad (E.10)$$

Also, substituting Eq. (E.8) into Eq. (E.5) yields

$$l_{ij} = \frac{M_{ij} - \sum_{k=1}^{j-1} \tilde{M}_{ik} l_{jk}}{d_j}. \quad (E.11)$$

Finally, solving for M_{ij} in Eq. (E.10) and substituting the result into Eq. (E.11) yields

$$l_{ij} = \frac{\tilde{M}_{ij}}{d_j}. \quad (E.12)$$

The banded nature of $[M]$ allows for very rapid factorization. From Eq. (E.9)

$$d_i = M_{ii} - \tilde{M}_{i1} l_{i1} - \tilde{M}_{i2} l_{i2} - \dots - \tilde{M}_{i(i-1)} l_{i(i-1)} \quad (E.13)$$

but from Eq. (E.10)

$$\begin{aligned} \tilde{M}_{i1} &= M_{i1} \\ \tilde{M}_{i2} &= M_{i2} - \tilde{M}_{i1} l_{21} \\ &\vdots \\ \tilde{M}_{i(i-1)} &= M_{i(i-1)} - \tilde{M}_{i1} l_{(i-1)1} - \tilde{M}_{i2} l_{(i-1)2} - \dots - \tilde{M}_{i(i-2)} l_{(i-1)(i-2)}. \end{aligned} \quad (E.14)$$

As a consequence of the symmetry of $[M]$, in any row i only terms up to the i th column are needed for the factorization. Furthermore, from Eq. (E.14) it can be seen that

if, say M_{i1} through M_{in} are all zero where $n < i - 1$, then \tilde{M}_{i1} through \tilde{M}_{in} are also all zero so that d_i can be written as

$$d_i = M_{ii} - \tilde{M}_{i(n+1)}l_{i(n+1)} - \tilde{M}_{i(n+2)}l_{i(n+2)} - \dots - \tilde{M}_{i(i-1)}l_{i(i-1)} \quad (E.15)$$

where $n + 1$ indicates the first nonzero column in row i of $[M]$. Hence, only terms within the *half bandwidth* of each row of $[M]$ need to be considered during the factorization. This liberty to ignore all terms outside of the half bandwidth of each row of $[M]$ in the calculation of $[D]$ yields a substantial savings in the amount of computer time needed to perform the LDL^T decomposition of $[M] = [K(n_i) + K_G(n_i; \lambda)]$ in section 6.6.1.

BIBLIOGRAPHIC DATA SHEET	1. Report No. VPI-E-92-16; CCMS-92-17	2.	3. Recipient's Accession No.
4. Title and Subtitle Analysis and Optimal Design of Pressurized, Imperfect, Anisotropic Ring-Stiffened Cylinders			5. Report Date June 1992
7. Author(s) R. Ley, Z. Gürdal, E. Johnson, and J. H. Starnes, Jr.			8. Performing Organization Report No. VPI-E-92-16, CCMS-92-
9. Performing Organization Name and Address Virginia Polytechnic Institute and State University Department of Engineering Science and Mechanics Blacksburg, VA 24061-0219			10. Project/Task/Work Unit No.
			11. Contract/Grant No. NAG-1-343 NASA-Va Tech Composites Prog
12. Sponsoring Organization Name and Address Aircraft Structures Branch National Aeronautics and Space Administration Langley Research Center Hampton, VA 23665-5225			13. Type of Report & Period Covered Interim Report 91 9/87-6/92
			14.
15. Supplementary Notes			
16. Abstract <p>Development of an algorithm to perform the structural analysis and optimal sizing of buckling resistant, imperfect anisotropic ring-stiffened cylinders subjected to axial compression, torsion, and internal pressure is presented. The structure is modeled as a branched shell. A nonlinear axisymmetric prebuckling equilibrium state is assumed which is amenable to a solution within each branch. Buckling displacements are represented by a Fourier series in the circumferential coordinate and finite elements in the axial or radial coordinate. A separate, more detailed analytical model is employed to predict prebuckling stresses in the flange/skin interface region.</p> <p>Results of case studies indicate that a nonlinear prebuckling analysis is needed to accurately predict buckling loads and mode shapes of these cylinders, that the rings have a greater influence on the buckling resistance as the relative magnitude of the torsional loading to axial compression loading is increased, but that this ring effectiveness decreases somewhat with internal pressure is added.</p> <p>The enforcement of stability constraints is treated in a way that does not require any eigenvalue analysis. Case studies performed using a combination of penalty function and feasible direction optimization methods indicate that the presence of the axisymmetric initial imperfection in the cylinder wall can significantly affect the optimal designs. Weight savings associated with the addition of two rings to the unstiffened cylinder and/or the addition of internal pressure is substantial when torsion makes up a significant fraction of the combined load state.</p> <p>Assumption of criticality of the stability constraints and neglect of the stress constraints during the optimal sizing of cylinders produced designs that nevertheless satisfied all of the stress constraints, in general, as well as the stability constraints. Subsequent re-sizing of one cylinder to satisfy a violated in-plane matrix cracking constraint resulted in an optimal design that was 49% heavier than the optimal design produced when this constraint was ignored.</p> <p>The additional internal pressure necessary to produce a violation of a stress constraint for each optimal design was calculated. Using an unsymmetrically laminated ring flange, a substantial increase in the strength of the flange/skin joint was observed.</p>			
17. Key Words and Document Analysis. 17a. Descriptors Nonlinear Prebuckling, Buckling of Imperfect Anisotropic Cylinders, Combined Loads, Ring Stiffeners, Optimal Design, Skin/Stiffener Stresses 17b. Identifiers/Open-Ended Terms 17c. COSATI Field/Group			
18. Availability Statement		19. Security Class (This Report) UNCLASSIFIED	21. No. of Pages 264
		20. Security Class (This Page) UNCLASSIFIED	22. Price

ORIGINAL PAGE IS
OF POOR QUALITY

VIRGINIA TECH CENTER FOR COMPOSITE MATERIALS AND STRUCTURES

The Center for Composite Materials and Structures is a coordinating organization for research and educational activity at Virginia Tech. The Center was formed in 1982 to encourage and promote continued advances in composite materials and composite structures. Those advances will be made from the base of individual accomplishments of the sixty-five full and associate members who represent eleven different departments in three colleges.

The Center functions through an Administrative Board which is elected yearly and a Director who is elected for a three-year term. The general purposes of the Center include:

- collection and dissemination of information about composites activities at Virginia Tech,
- contact point for other organizations and individuals,
- mechanism for collective educational and research pursuits,
- forum and agency for internal interactions at Virginia Tech.

The Center for Composite Materials and Structures is supported by a vigorous program of activity at Virginia Tech that has developed since 1963. During 1988-89 and 1989-90 fiscal years sponsored research project expenditures for investigation of composite materials and structures have totalled approximately five million dollars annually.

Various Center faculty are internationally recognized for their leadership in composite materials and composite structures through books, lectures, workshops, professional society activities, and research papers.

Research is conducted in a wide variety of areas including design and analysis of composite materials and composite structures, chemistry of materials and surfaces, characterization of material properties, development of new materials systems, and relations between damage and response of composites. Extensive laboratories are available for mechanical testing, nondestructive testing and evaluation, stress analysis, polymer synthesis and characterization, material surface characterization, component fabrication, and other specialties.

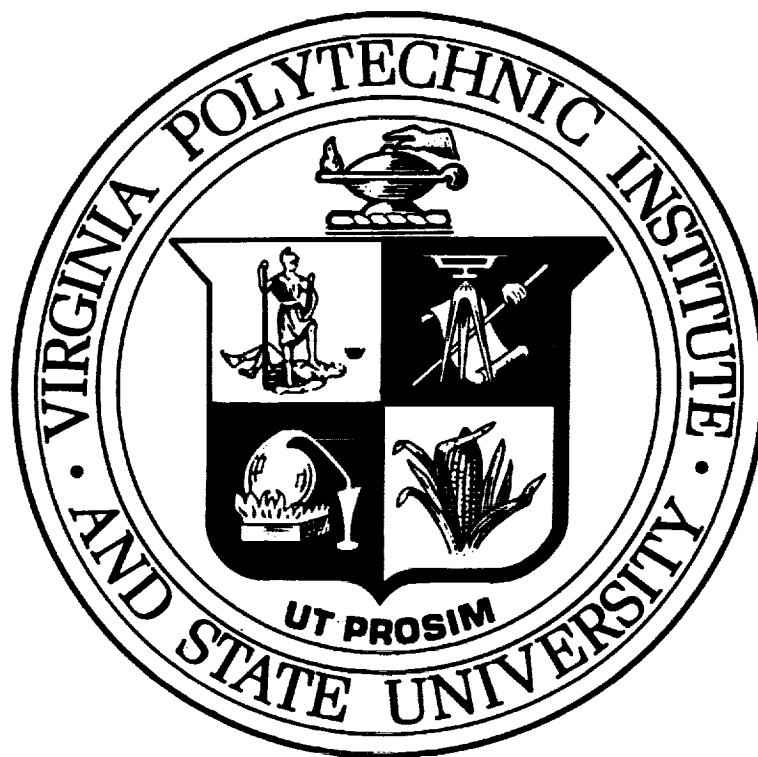
Educational activities include ten formal courses offered at the undergraduate and graduate levels dealing with the physics, chemistry, mechanics, and design of composite materials and structures. As of 1991, 129 Doctoral and 172 Master's students have completed graduate programs and are now active in industry, government, and education in the United States and abroad. The Center averaged 125 active student members during 1989-90 and 1990-91. Many Bachelor-level students have been trained in various aspects of composite materials and structures.

The Center has invested in the development of an administrative database (now fully operational for Center members) and a composite material properties database (now ready for data entry).

In addition to the CCMS Report Series, the Center sponsors a bi-monthly Seminar Series attended by faculty, staff, and students and the Center jointly sponsors a sesqui-annual Technical Review with the Center for Adhesive and Sealant Science which is well attended by government and corporate contacts.

MEMBERS OF THE CENTER		
Aerospace and Ocean Engineering	Electrical Engineering	Industrial and Systems Engineering
Raphael T. Haftka Eric R. Johnson Rakesh K. Kapania	Ioannis M. Besieris Richard O. Claus Douglas K. Lindner	Joel A. Nachlas
Chemical Engineering	Engineering Science and Mechanics	Materials Engineering
Donald G. Baird Garth L. Wilkes	Robert Czarnek David A. Dillard Normal E. Dowling John C. Duke, Jr. Daniel Frederick O. Hayden Griffin, Jr. Zafer Gurdal Robert A. Heller Edmund G. Henneke, II Michael W. Hyer Robert M. Jones Ronald D. Kriz Liviu Librescu Alfred C. Loos Don H. Morris John Morton Ali H. Nayfeh Daniel Post J. N. Reddy Kenneth L. Reifsnider C. W. Smith Wayne W. Stinchcomb Surot Thangjitham	Jesse J. Brown, Jr. Seshu B. Desu Ronald S. Gordon D. P. H. Hasselman Robert W. Hendricks Ronald G. Kander
Chemistry		Mathematics
John G. Dillard Harry W. Gibson James E. McGrath Thomas C. Ward James P. Wightman		Werner E. Kohler
Civil Engineering		Mechanical Engineering
Richard M. Barker Richard E. Weyers		Charles E. Knight Craig A. Rogers Curtis H. Stern
Clothing and Textiles		
Jeanette M. Cardamone		

Inquiries should be directed to:
Center for Composite Materials and Structures
Virginia Tech
Blacksburg, VA 24061-0257
Phone: (703) 231-4969
Fax: (703) 231-9452



Virginia Tech does not discriminate against employees, students or applicants on the basis of race, sex, handicap, age, veterans status, national origin, religion, political affiliation or sexual orientation.